Hook Load Fluctuations during Offshore Heavy Lifting

Thesis, MSc Offshore engineering

T. Hartmans

"A measurement-based validation of modelled hydrodynamics of a semi-submersible crane vessel, hoist wire system dynamic tension modelling, and assessment of the measuring equipment involved"

TU Delft

Hook Load Fluctuations during Offshore Heavy Lifting

Thesis, MSc Offshore engineering

by

T. Hartmans

to obtain the degree of Master of Science
at the Delft University of Technology,
to be defended publicly on Monday, September 12, 2016 at 14:30 PM.

Student number:	4024486	
Project duration:	November 2, 2015 – September 12, 2016	
Thesis committee:	Prof. dr. A. Metrikine,	TU Delft, chairman
	Dr. ir. J.M. de Oliveira Barbosa,	TU Delft, daily supervisor
	Dr. ir. K.N. van Dalen,	TU Delft
	Ir. A. Jongbloed,	Heerema Marine Contractors, senior supervisor
	Ir. J. Velema,	Heerema Marine Contractors, daily supervisor

TU Delft

Preface

This report is the result of my final work to obtain the degree of Master of Science, from Delft University of Technology. It is probably most interesting for readers who are in some way involved with offshore engineering. Basic principles and theories used are explained, which should enable those with other (technical) backgrounds to easily understand this report as well. Even though I have not managed to quantify the origins of discrepancies between measured and modelled hook load fluctuations, I think my efforts have shed some light on the topic.

Having had the opportunity to work on this project in cooperation with Heerema Marine Contractors (HMC) in Leiden is something that I am grateful for. My wish to do my graduation thesis on a topic concerning dynamics was somewhat unspecific. I could not have been more forunate than having HMC's Thialf, the largest semi-submersible crane vessel in the world, as its topic. Working on my thesis in the 'dynamic' environment of HMC's offices, filled with expertise and helpful individuals, was even better. I enjoyed most of the work required to complete this study, and needless to say I learnt a lot.

First of all, my gratitude goes out to my graduation committee. Prof. Metrikine and dr. de Oliveira Barbosa, who gave me new insights during meetings and helped me choose strategies in between, and my supervisors at HMC, Jorick and Arnold, who always took their time to think along and teach me how things are done at HMC. Furthermore, I would like to thank everyone who attended my 'brainstorm sessions' for their input, and everyone else working in the Marine Engineering department and elsewhere at HMC who contributed to this research in any way. In particular, the assistance of Ivan, Pandu and the Thialf's crew I received when obtaining the measurements used for this research was essential. Without their efforts, this thesis would have been quite different. Finally, I would like to thank my fellow graduate and intern students at HMC. We had a good time together.

I wish you an interesting reading experience.

T. Hartmans
Leiden, September 2016

Abstract

Heerema Marine Contractors (HMC) owns and operates several semi-submersible crane vessels (SSCVs), used for offshore heavy lift operations. In preparation of these operations, hydrodynamics analyses in the frequency domain are conducted using software developed in-house at HMC. These analyses result in Response Amplitude Operators (RAOs), which are used for estimating dynamic response to a certain sea state. Crane hook load fluctuations response modelled in this manner is generally larger than measured, however. Since hook load is often a limiting criterion, an overestimation of hook load fluctuations in the models could undesirably affect perceived operability. Three possible root causes for this discrepancy have been identified:

1. Modelled hydrodynamics are inaccurate
2. Measured dynamic tension does not represent dynamic hook load
3. Dynamic tension measuring equipment is inaccurate

In order to assess root cause (1.), a comparison study is conducted. Hydrodynamic rigid body models are created for four stages of a typical heavy lift operation: the free-floating, lift-off, free-hanging and set-down stages. Wave forcing, added mass and damping properties for the floating bodies are obtained from diffraction analyses performed using WAMIT. Model sensitivity to different hydrodynamic properties, obtained from single- vs. multi-body and infinite vs. actual water depth diffraction analyses, is tested as well. Measurements have been obtained for a project where a topsides module was lifted from a barge onto a jacket support structure. Measuring equipment included 6DoF motion sensors on the SSCV, module and in one of the SSCV's crane boom tips. Generally, modelled motion response is found to be quite accurate.

Originally, discrepancies between modelled and measured hook load fluctuations spectra were observed during the lift-off stage of a heavy lift operation. However, measured hook load fluctuations prove to be smaller than modelled for all stages considered. Hook load fluctuations are governed by relative vertical motions of the module and the SSCV's crane boom tip. Magnitude and phasing of these signals imply over- and underestimations of wire rope elasticity and damping properties respectively. Furthermore, the ratio between measured hook load fluctuations and hook load fluctuations corresponding to measured relative motions is quite different per stage. A stage dependent contribution of root causes (2.) and/or (3.) is therefore expected to add to the overall discrepancy.

In an attempt to obtain accurate crane wire rope elasticity properties from a simplified 2DoF dynamic crane model, natural frequencies during the free-hanging stage are searched for. Implementing these frequencies in the 2DoF system allows for two unknowns to be solved: a stiffness for the boom suspension wires, and an equivalent stiffness for the grommets and main hoist wires. Response peaks found within a frequency range corresponding to probable stiffnesses of the wire rope sections in the system are not very explicit. For the most probable and explicit response peaks found, no combination of stiffnesses exists for which this 2DoF model is solvable. These response peaks therefore cannot be explained by the modes searched for, and stiffness properties cannot be obtained from this model unfortunately. Therefore, elasticity properties for wire rope elements in the model are obtained from a stiffness test in literature. Subsequently, lift object vertical motions time traces are modelled, using imposed (measured) motions of the SSCV's crane tip as input. Alternative damping values are applied in order to minimize phasing between modelled and measured vertical motions of the lift object. This yields a supercritical damping value, whereas damping values are set at 1.5% of the critical damping in the models by default.

Applying the new elasticity and damping properties in the models results in a significant change in modelled hook load fluctuations. However, correspondence to measured hook load fluctuations does not necessarily increase, and discrepancies remain large. Furthermore, the measured signals used contain quite some noise, and root causes (2.) and/or (3.) are expected to add to the overall discrepancy observed. An assessment of root causes (2.) and (3.), and repetitions of this research for other lifts using more accurate measuring equipment are therefore recommended.

Contents

List of Tables

List of Figures

Acronyms

CoG Centre of Gravity. 10–15, 22, 23, 27, 63

DFT Discrete Fourier Transform. 10
DoF Degree of Freedom. 8–11, 22, 29, 32, 34, 35, 38, 39, 42–45, 48, 51, 53, 64
DP Dynamic Positioning. 2, 50

EoM Equation of Motion. 9, 11, 34, 38, 42

FFT Fast Fourier Transform. 10

GCS Global Coordinate System. 12–14, 19, 26, 36, 49, 50, 55, 63

HMC Heerema Marine Contractors. 1, 3, 4, 9–11, 16, 21, 22, 40, 48, 50, 51, 56, 57
HTV Heavy Transport Vessel. 2

LCS Local Coordinate System. 12–14, 22, 26, 27, 29, 49
LMP Load Measuring Pin. 5, 6, 24, 54, 56, 57

MBL Minimum Breaking Load. 40, 41
MRU Motion Response Unit. 23, 48–50, 52, 55, 83, 93–96

OD Outer Diameter. 40
ODE Ordinary Differential Equation. 42

PoI Point of Interest. 11, 13–15, 27, 63
PS portside. 12–15, 29, 30, 41, 45, 63, 64

RAO Response Amplitude Operator. 8, 9, 11, 17–20, 29, 48, 50, 51, 55

SB starboard. 6, 13–15, 19, 27, 29–31, 34, 38, 39, 41, 42, 45, 49–51, 63, 64
SSCV Semi-Submersible Crane Vessel. 1–4, 8–12, 16, 45, 48, 57, 59

WD Water Depth. 6, 18, 19
WRB Wave Rider Buoy. 8, 21, 25, 29

1

Introduction

1.1. Company introduction

Heerema Marine Contractors (HMC) is a world leading offshore construction company, which is specialized in design, transportation, installation and removal of all types of fixed and floating offshore structures, and subsea pipelines and infrastructure in both shallow and deep water. HMC owns and operates her own fleet, including three Semi-Submersible Crane Vessels (SSCVs) used for offshore heavy lift operations.

HMC's Thialf is the world's largest SSCV, with a lift capacity of 14,200 mT when both cranes are used in tandem. It can be seen installing a 5,300 mT topsides (the part of an offshore platform which contains the accommodation and production facilities) on the cover of this report. Measurements obtained during this heavy lift operation have been used extensively for this study.

1.2. Heavy lifting

1.2.1. Definition

When to denote a lift operation as 'heavy' is somewhat arbitrary; structures weighing a few tons can already be considered heavy, while record lifts of over 10,000 mT have been conducted in recent history. Most structures installed in offshore environments, like topsides and steel jacket foundations (towers that are often used to support topsides in water depths of up to 150-200 m), have a mass somewhere in this range. Therefore, the installation of such a structure in general is denoted a heavy lift operation. HMC operates in the heaviest segment of the offshore heavy lift market.

1.2.2. Semi-Submersible Crane Vessel & Crane layout

Within HMC, the majority of heavy lift operations are carried out by one of their earlier mentioned SSCVs. HMC's SSCVs are construction vessels with a very large deck area, equipped with two revolving cranes mounted at the stern of the vessels. The revolving cranes allow for the SSCVs to conduct more complex operations when used in tandem, like upending jackets. A SSCV is carried by two floaters (one on either side of the vessel), which are fully submerged during lift operations. The floaters are connected to the upper part of the vessel through vertical columns. Therefore, the deck area is much larger than the waterline area. A distinct advantage of this geometry is that wave forces on the SSCV are greatly reduced due to the smaller waterline area, while maintaining sufficient stability. As a result of this, SSCVs have favourable motions behaviour compared to conventional monohull (or ship-shaped) crane vessels. A disadvantage of this geometry is the decrease of vessel stability due to the reduced waterline area. Nevertheless, the transverse stability of SSCVs is still far greater than that of traditional monohull vessels in general.

HMC's Thialf is the SSCV on which this thesis is based. Some properties of the Thialf are lised in table 1.1 below:

Table 1.1: HMC's SSCV Thialf properties at 26.6m draught

Property	**Magnitude**	**Unit**
Displacement	170,460.5	m^3
Length	184.6	m
Width	88.4	m
SB crane capacity	7,100	mT
PS crane capacity	7,100	mT

Please refer to appendix A for drawings of the Thialf's cranes and a schematic overview of their hoist wire rope and sheaves arrangement.

1.2.3. Procedure

The procedure of an offshore heavy lift operation may vary, depending on the lift object and project location. In most cases, the lift object is transported to the project location on a barge or Heavy Transport Vessel (HTV). The barge or HTV is then moored at the stern of the SSCV, which maintains position using Dynamic Positioning (DP) or anchors. When a weather window (a certain period of time over which the environmental conditions are expected to be such that the operation can be executed in a safe manner) of sufficient length has opened, the actual lift operation can commence. It consists of several distinct stages, which are described below for a SSCV lifting a topsides of a barge onto a jacket:

1. Free-floating stage
   The grommets (steel wire rope in an endless loop), which are on one side connected to the topsides' lift points, are hung of the crane hooks at the other end. During this stage, grommets are kept slack. Therefore, there is no mechanical coupling and motions of the SSCV and barge cannot influence one another through rigging, but vessel motions could alter somewhat due to hydrodynamic interaction. Once it has been decided the lift can commence (depending on weather conditions), seafastening is cut and the operation can proceed to the lift-off stage.

2. Lift-off stage
   First, a certain tension is applied (fast) to the hoist wires and grommets by hoisting. This is done in order to avoid snap loads in the hoist wires and grommets resulting from vessel motions. Once this tension has been reached, the SSCV's trim is adjusted by pumping ballast water from its stern towards its bow and weight is further transferred from the barge to the SSCV by deballasting. Throughout this stage, vessel motions are mechanically coupled as a result of the SSCV being connected to the barge through taut grommets and hoist wires. When the weight of the topsides is almost entirely supported by the SSCV, it is hoisted in order to quickly get the lift object clear from the barge.

3. Free-hanging stage
   During this stage, the topsides is suspended from the SSCV's crane(s). Therefore, the SSCV and the barge do not influence the motions of one another anymore. During the free-hanging stage the SSCV sails towards the jacket where the suspended topsides is to be installed.

4. Set-down stage
   The set-down stage is similar to the lift-off stage, but reversed. First, the topsides is lowered to its final resting position on the jacket by hoisting. The hook load is further lowered by hoisting, such that the dynamic hook load cannot exceed the weight of the structure as a result of vessel motions. Further load transfer is achieved by means of ballasting the SSCV. Similar to the lift-off stage, the remainder of the load is transferred by hoisting rapidly in order to prevent snap loads from occurring, after which rigging is slack and the installation is complete.

A schematic sideview of a SSCV each stage in the lift procedure described above is shown in figure 1.1 below. Ballast water is depicted in blue. (2.) and (4.) depict early lift-off and set-down stages; the ballast water configurations have not changed yet compared to the free-floating (1.) and free-hanging (3.) stages respectively.

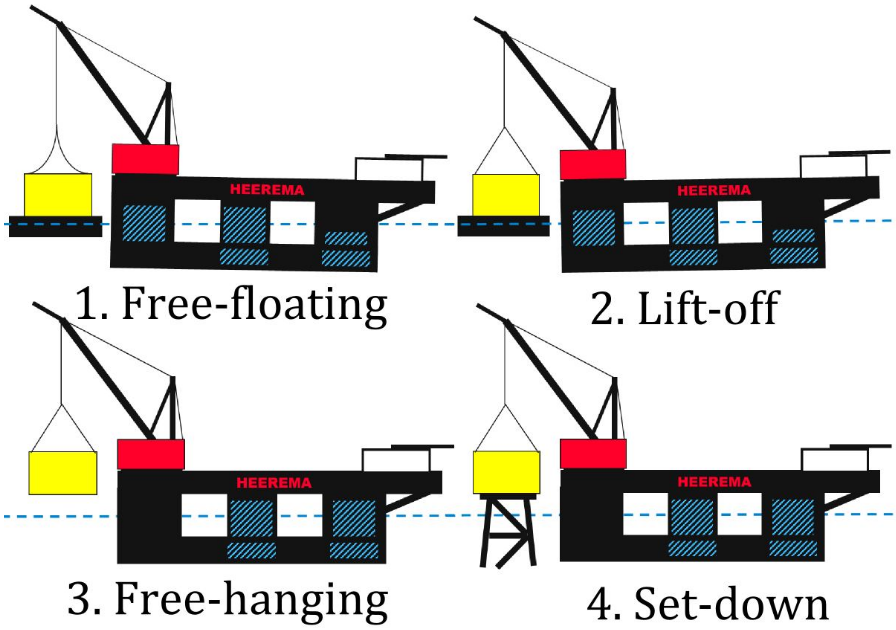

Figure 1.1: Heavy lift procedure

1.3. Motivation for study

1.3.1. Hydrodynamic lift analysis

For most heavy lift operations conducted by HMC, hydrodynamic analyses are conducted for the free-floating, lift-off and free-hanging stages described in the previous section. This is done in order to understand the general hydrodynamic behaviour of the system and determine the limiting sea states for which the lift can be performed in a safe manner. Combined with a wave forecast, the analyses' output can be used to estimate hydrodynamic response and check if no limiting criteria (for instance displacements or hook loads) are expected to be exceeded within the period of that forecast. Thus, it is a valuable tool for providing decision support for selecting a suitable weather window (and vessel heading if possible) for safely executing a lift. These analyses are generally performed using a software application developed in-house at HMC: Liftdyn (described in chapter 3).

1.3.2. Dynamic hook load

If a Liftdyn predicted motion or force response exceeds a limiting criterion, the lift will not be executed within the time window of the wave forecast, because that would pose a risk of failing equipment or even life threatening situations. The operation would then have to be postponed to a later time window, for which it is absolutely certain the operation can be executed in a safe manner. It is therefore of major importance that these estimated responses are reliable, or otherwise on the conservative side. On the other hand, this so-called 'waiting on weather' is unfavourable, since the operational costs of a large SSCV are very high. If these model calculations are over-conservative, this could result in an underestimated perceived operability, which in turn could lead to a decision to postpone a lift even though this is not necessary.

A limiting criterion which is often governing, is the hook load. During the lift-off stage of a heavy lift operation (and to a lesser extent the set-down stage), the SSCV is for several minutes effectively connected to a barge (or jacket) through taut hoist wires and grommets. Since the entire lifting system contains at least one floating body exposed to waves (the SSCV), energy originating from wave–floater interaction is transferred from one floating body to the other through the hoist wires and rigging, resulting in large fluctuations in the hook load.

1.3.3. Observed discrepancy

The magnitude of these hook load fluctuations has been proven difficult to predict using Liftdyn: while motions are found to be modelled quite accurately, offshore personnel observed that HMC's model predictions of hook load fluctuations are generally larger than the fluctuations measured. Recently, dynamic hook load comparison studies have been conducted by HMC for several projects in order to assess the observed discrepancy. Measured and Liftdyn modelled hook load fluctuations (energy) spectra are plotted together for two recent projects in figure 1.2 below:

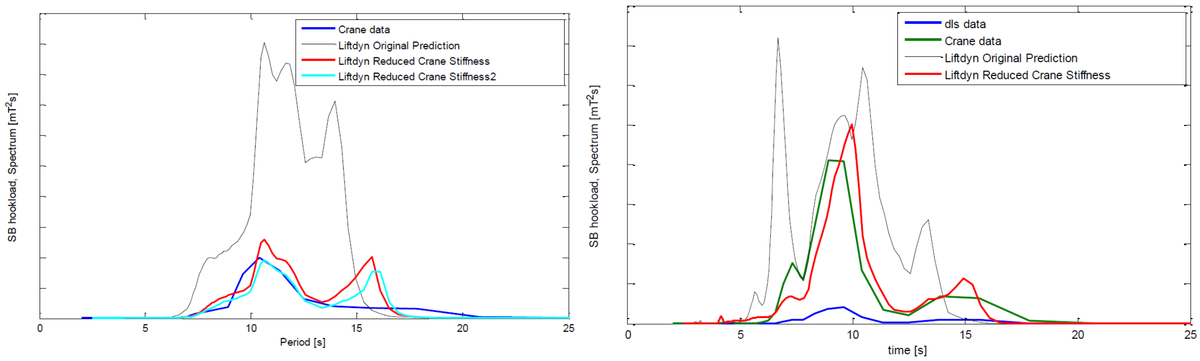

Figure 1.2: Measured and Liftdyn dynamic hook load spectra for two recent topsides installations

If the measured dynamic hook load indeed accurately represents the actual dynamic hook load, a reasonable explanation for the discrepancy between the measured and Liftdyn-calculated dynamic hook load would be an overestimation of the real system's stiffness in the model.

Therefore, the Young's modulues E [GPa] of hoist wires was reduced from 100 GPa to 35 GPa in the Liftdyn models ('Liftdyn Reduced Crane Stiffness' in figure 1.2). As expected, this results in a better correspondence to measured hook load fluctuations energy spectra. However, reducing the elasticity of hoist wires by a factor three (or even four, 'Liftdyn Reduced Crane Stiffness 2' in figure 1.2), does not leave the vessels' motions behaviour unaffected. For another comparison study, it was found that the modelled SSCV natural roll and the barge natural pitch periods had increased as a result of the reduced hoist wire stiffness [HMC, 2015]. Model predictions from models using the original hoist wires' elasticity of 100 GPa corresponded more accurately to measured motions. Also, the hoist wires' elasticity was altered such that model predictions fit measured values. An overestimation of stiffness does not necessarily have to be the cause of the discrepancy between modelled and measured hook loads. Even though steel wire rope has been in use for over a century, and its dynamic properties remain difficult to determine accurately up to the present day [Brown & Root Vickers, 1990], an elasticity as low as 35 GPa (compared to a stiffness of ca. 210 GPa for solid steel) is unlikely. Other causes for the discrepancy could be that modelled hydrodynamics are inaccurate, that the measured force is not representative for the actual dynamic hook load (as a result of measurement location or method) or that the measuring equipment itself is inaccurate.

1.3.4. Relevance

As the cause of the observed discrepancy between modelled and measured dynamic hook loads remains unclear, it is worthwhile to study the entire dynamic system which it is part of in order to gain better understanding of its origin. Since hook load fluctuations during lift-off are often governing for lift operations, the apparent model conservatism could undesirably affect perceived operability of the crane vessel. A better understanding of hook load fluctuations during the lift-off stage, recommendations for model adjustments (and increased confidence in the analyses resulting from them) or the measuring equipment involved would therefore be valuable to HMC.

1.3.5. Problem statement

"Heerema Marine Contractors' model predictions of hook load fluctuations during the lift-off stage of a heavy lift operation are generally larger than what is measured, which could undesirably affect apparent operability."

1.3.6. Goal

"The goal of this graduation thesis is to assess what causes the discrepancy between measured and modelled hook load fluctuations for offshore heavy lift operations, in order to improve engineering models or the confidence therein"

1.4. Approach

1.4.1. Determine root causes

Several possible root causes for the differences in measured and predicted hook load fluctuations have been identified. They are listed below:

1. Modelled hydrodynamics are inaccurate
   Simplifications of reality in Liftdyn models result in inaccurate calculated (relative) vessel motions and thus inaccurate dynamic hook loads.

2. Measured dynamic force does not represent dynamic hook load
   The hook load is not measured directly at the crane hook, but by two so-called Load Measuring Pins (LMPs), which act as axes for a sheave on either side of the reeved hoist wire system. Dynamic wire tensions at the LMPs might not be representative for the total dynamic hook load.

3. Hook load measuring equipment is inaccurate
   The dynamic tension at the LMP is inaccurately measured or registered.

A flowchart of the dynamic hook load validation that was made in the comparison studies mentioned in the previous section is given in figure 1.3 below, with the identified root causes depicted in red.

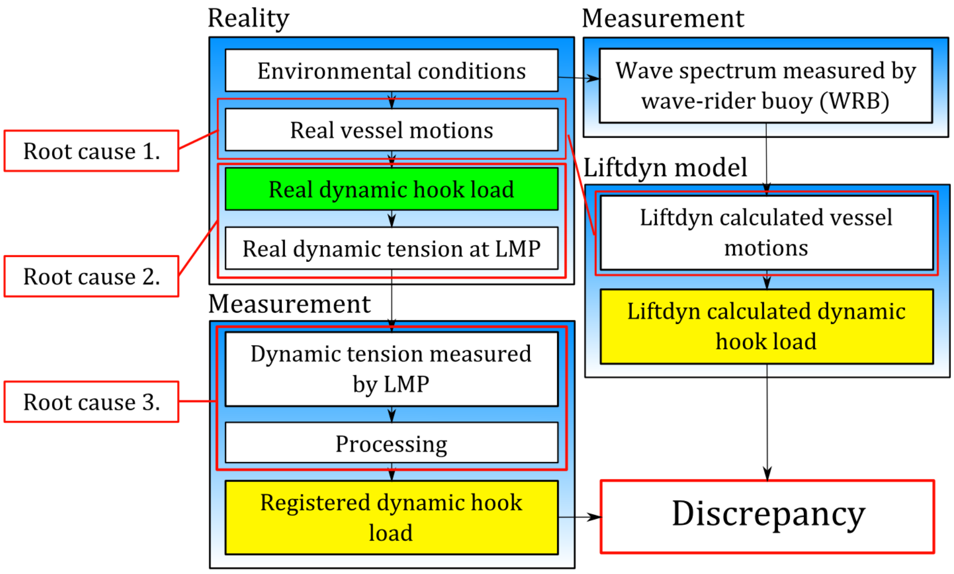

Figure 1.3: Dynamic hook load comparison flowchart & discrepancy root causes

1.4.2. Study method

The influence of each of the root causes described in the previous section on the observed discrepancy should be analysed individually. Root cause (1.) could be assessed through a comparison study of Liftdyn calculated motions response spectra with measured response spectra, root cause (2.) by means of a dynamic model of hoist wire tensions in the different segments, and root cause (3.) could be assessed by studying the properties of the LMP and its signal processing algorithm.

A detailed flowchart of the proposed method for assessing the influence of each root cause on the (measured) dynamic hook load is given in appendix A (figure A.3). Due to time constraints and lack of data, only root cause (1.) has been studied for this thesis.

As explained above, the motive for this study is the observed discrepancy between calculated and measured hook load fluctuations in the pre-tension stage during lift-off, which is considered a critical stage in the whole lift procedure. For comparison purposes, and for assessing vessel motions and hook load fluctuations in other stages of a heavy lift operation, models of the other stages described in the section above have been developed as well. The approach described in figure A.3 has been used for studying all four lift stages considered.

1.5. Report structure

Following this introduction, some theoretical background of the methods used for this study is covered in chapter 2. It includes the basics of rigid body dynamics in the frequency domain, (numerical) radiation and diffraction analysis, and data processing.

In chapter 3, Liftdyn software is explained, and the hydrodynamic models for all stages considered are defined. Furthermore, model sensitivity to hydraulic properties obtained from different diffraction analyses (infinite vs. actual Water Depth (WD) and single- vs. multi-body) is discussed.

The measurement campaign, which was expanded to include motion measurements of starboard (SB) crane boom especially for this thesis, is described in chapter 4. The techniques used for processing the measured motion sensor signals are presented as well.

Chapter 5 covers the results of the comparison study between measured and modelled motions and hook load fluctuations. Furthermore, hook load fluctuations that should occur (if assumed wire rope properties are correct) are calculated and presented in this chapter.

In chapter 6, several methods for obtaining accurate wire rope elasticity and damping properties are described. The dynamic properties thus obtained are applied to the wire rope sections in revised versions of the Liftdyn models presented in chapter 3. Furthermore, hook load fluctuations response modelled by these revised models are presented.

The measurements, methods used, and results presented in chapters 3, 4, 5 and 6 are discussed in chapter 7. Finally, conclusions and recommendations following from this discussion are given in chapter 8.

2

Theoretical background

This chapter provides the reader with some basic theoretical background of the methods used for hydrodynamic modelling and data processing. Reference is made to the relevant literature for more in-depth information on the theories applied in this study.

2.1. Time domain vs. Frequency domain

2.1.1. Fourier analysis

A wave elevation time signal (like ocean waves measured at a certain point, for example) can theoretically be approximated by the summation of a large number of regular waves, each with a different amplitude and phasing with respect to each other [Journée & Massie, 2001]:

$$\zeta_a(t) = \sum_{n=1}^{N} \zeta_{a,n} cos(\omega_n t + \epsilon_n) \tag{2.1}$$

where $\zeta_a(t)$ [m] is wave elevation of the irregular time signal, N is the number of regular waves it is comprised of, and $\zeta_{a,n}$ [m], ω_n [rad/s] and ϵ_n [rad] are the amplitude, frequency and phasing of a regular wave component. Once the number of regular waves the time signal contains becomes infinite (and thus the signal is not periodic anymore), this Fourier series expansion summation becomes an integral (using complex notation) [Blaauwendraad, 2010]:

$$\zeta_a(t) = \int_{-\infty}^{\infty} \zeta_a(\omega) e^{i\omega t} \, d\omega \tag{2.2}$$

where $\zeta_a(t)$ [m] is the wave elevation time signal, and $\zeta_a(\omega)$ [m] is wave elevation for the regular wave at that frequency. This is called the *Inverse Fourier Transformation*. Similarly, wave elevations for all frequency components can be found through the *Fourier Transformation*:

$$\zeta_a(\omega) = \int_{\infty}^{\infty} \zeta_a(t) e^{-i\omega t} \, dt \tag{2.3}$$

Elevations thus found (as a function of wave frequency), are wave elevations in the so-called 'frequency domain', as opposed to the measured wave elevation time signal, which is in the 'time domain'. From a wave field defined in the frequency domain, an infinite amount of wave time signals can be obtained, depending on their respective phasing ϵ_n. This means that, if no wave phasing data is available from a wave field defined in the frequency domain, an exact wave elevation time trace cannot be known.

Why analyses in the frequency domain are still useful, advantages and setbacks for analyses in either the frequency or time domain, and suitability for offshore applications of both methods is described in the section below.

2.1.2. Time domain vs. Frequency domain - Practicality for Offshore heave lifting

Wave conditions (or sea states) are difficult to accurately predict more than a couple of days or hours in advance. It is even harder (virtually impossible) to be able to exactly determine wave forcing on a floating body at a certain moment in time, since the metocean data available is often limited. Environmental data could be limited to a sea state forecast for the area, or at best measurements from one or several Wave Rider Buoys (Wave Rider Buoys (WRBs)) near the project location [Holthuijsen, 2006].

While data from modern WRBs contains wave elevation time traces and travelling directions at their location, these will already have changed somewhat at the vessel's location due to wave interaction. Also, calculating vessel motion responses as a result of real-time measured wave forcing would require a lot of computing power, which is not available onboard the SSCV performing the lift. Moreover, for this approach of modelling vessel motions to be a useful tool for deciding whether or not to commence an operation, it would have to be done hours in advance. A complex task like installing a heavy topsides on top of a jacket cannot simply be aborted or paused in the midst of operation. Due to all these uncertainties and restrictions, doing such a time domain simulation of future events in real time is not practical or possible with available equipment.

Therefore, it is desirable to have a tool with which this modelling can be done in a speedy manner, using the latest short-term weather forecast as input for the hydrodynamic forcing of the vessels in the model. Unlike the exact time trace of all the wave elevations and directions of propagation at a certain location, the wave spectrum (spectral density as a function of frequency, explained in the section below) at that location will change more gradually over time and can be more accurately predicted. Thus, being able to model vessel hydrodynamic responses based on knowledge of the forecasted or measured wave spectrum, enables one to make a decision with the resources available. The method used to perform such an analysis in the frequency domain is presented in the sections below.

The reader of this report is expected to be familiar with wave theory, wave spectra and the concepts time domain and frequency domain. Please refer to [Holthuijsen, 2006] for more information on these topics.

2.1.3. Frequency domain response & RAOs

Just as wave conditions can be represented by a wave spectrum, so can the hydrodynamic response of a vessel be depicted by a superposition of responses to all the harmonic waves the wave spectrum is composed of. Each of these waves will exert harmonic forces on the floating body under consideration, which will (depending on wave direction and vessel geometry) result in forces in all six Degree of Freedoms (DoFs). These forces result in vessel motions in all six DoFs. The reader of this report is expected to be familiar with these concepts regarding (hydro)dynamics [Journée & Massie, 2001].

For each of the DoFs of a vessel, a so-called Response Amplitude Operator (RAO) can be formulated that directly relates the magnitude of these responses to the wave height of an incoming harmonic wave. The RAO of a certain response is defined as follows :

$$RAO_z(\omega) = \frac{z_a(\omega)}{\zeta_a(\omega)} \tag{2.4}$$

where $z_a[unit]$ is the amplitude of an arbitrary response, and $\zeta_a[m]$ and $\omega[rad/s]$ are the amplitude and frequency of the incoming wave respectively. As such, the magnitude of an RAO is different for each incoming wave frequency and direction considered. In linear wave theory and linearized rigid body dynamics, the response is assumed to be linear with wave height, such that the RAO for a specific wave frequency remains the same for each incoming wave height at that frequency. According to this theory, one can use the RAO of a response to a unit wave height (of $1m$) to calculate the response for an arbitrary wave height at that wave frequency:

$$z_a(\omega) = RAO_z(\omega) \cdot \zeta_a(\omega) \tag{2.5}$$

As such, the response of a vessel to a single regular wave can be calculated. The total response of the vessel results from the superposition of responses resulting from all the regular waves the sea state contains. Since wave energy is proportional to amplitude squared, it is customary to use a wave energy (instead of elevation) spectrum. The wave energy spectrum is defined as follows:

$$S_\zeta(\omega)d\omega = \frac{1}{2}\zeta_a^2 \tag{2.6}$$

A response spectrum of an arbitrary response can then simply be obtained by multiplying the RAO squared with the measured wave energy spectrum:

$$S_z(\omega) = RAO_z^2(\omega) \cdot S_\zeta(\omega) \tag{2.7}$$

where $S_\zeta(\omega)$ and $S_z(\omega)$ [unit^{2}s] are the wave (energy) spectra of the incoming wave and the response respectively. Thus the response spectrum of a DoF can be calculated with knowledge of wave spectra only. A spectral representation of such a response can be used to statistically determine what is the chance it will exceed a limiting criterion within a project execution time window, which makes these RAOs useful tools for offshore decision support. A setback of this frequency domain approach is that each RAO is computed as if the responses have reached a steady state, while in reality some things (like wave spectra or, in the case of a heavy lift, the mean hook load) change over time. These properties will have to be assumed stationary (not changing over time). Anothter setback is that properties like damping and stiffness have to linearised, while in reality (non-linear) viscous damping occurs and hydromechanical restoring coefficients (which depend on waterline area) may vary. For the relatively simple vertical hull columns of HMC's SSCVs, this influence on restoring coefficients will be minor.

2.2. Liftdyn software

For heavy lift hydrodynamic analyses, the RAOs as explained in the previous section are calculated using an application called Liftdyn [HMC, 2009].

2.2.1. Rigid body dynamics

What Liftdyn basically does, is solving the Equation of Motions (EoMs) in order to obtain the steady-state response, for a whole range of incoming regular waves of different frequencies and directions:

$$(\mathbf{M+A})\underline{\ddot{x}} + \mathbf{B}\underline{\dot{x}} + \mathbf{C}\underline{x} = \underline{F}(t) \tag{2.8}$$

where (**M+A**), **B** and **C** are the (added) mass, damping and stiffness matrices respectively. Note that the symbols for damping and stiffness are those common in maritime engineering, whereas **C** and **K** are more common in civil engineering practices. The damping and stiffness matrices in this system contain both structural and hydraulic elements which makes the choice for symbol conventions somewhat arbitrarily. $\underline{\ddot{x}}$, $\underline{\dot{x}}$ and $\underline{x}$ are the accelerations, velocities and displacements of each DOF in the system, and $\underline{F}(t)$ represents the system's forcing (in this case hydrodynamic forcing through waves). The reader is expected to be familiar with how such a dynamic system can be solved. For reference, please refer to [Spijkers, Vrouwenvelder & Klaver, 2006].

2.2.2. Hydrodynamic forcing & WAMIT diffraction analysis

The right hand side of equation 2.8 consists of wave forcing. For each DoF and each incoming wave considered, these wave forcing functions need to be evaluated. A so-called diffraction analysis is conducted in order to compute added mass and damping of the bodies, and the wave forces acting on them. The software package for diffraction analyses used by HMC is Wave Analysis Massachusetts Institute of Technology [WAMIT, 2015]. The basis for calculating forces and moments on floating bodies resulting from waves in WAMIT, is by integrating water pressures over the wetted surface of a floating body. The pressures are obtained from the linearized Bernoulli equation:

$$p = -\rho \frac{\partial \Phi}{\partial t} - \rho g z \tag{2.9}$$

where Φ [m^2/s] is velocity potential. Boundary conditions are set at the vessel's hull, bottom of the sea and free surface. The velocity potential has three contributions:

- Φ_r; resulting from waves radiated from the oscillating body
- Φ_w; resulting from incoming waves on the fixed body
- Φ_d; resulting from waves reflected from the fixed body

How to calculate each of these components is omitted from this thesis [Journée & Massie, 2001].

In WAMIT, the user specifies a range of wave frequencies and directions for which the package should solve the diffraction analysis. Generally, a frequency range of 0-2 rad/s suffices for the SSCVs and barges operated by HMC, since higher frequency waves have an insignificant influence on the motions of these large vessels. As for wave direction, an analysis is usually made at fixed intervals in the range of $0-360°$, for instance at every 15°. The output of such a diffraction analysis contains, for each specified wave frequency, the added mass and damping for each of the vessel's six DoFs, and the forces with the corresponding phase differences (with respect to the incoming wave) acting on the rigid body's Centre of Gravity (CoG).

2.3. Data processing

All modelling and data processing for this study was conducted using Matlab. Two Matlab functions (developed in-house at HMC) were extensively used: one for obtaining spectra and one for filtering (noisy) measurements. They are briefly discussed here.

2.3.1. Fast Fourier Transform

How to obtain a wave spectrum from a measured time signal by means of a Fourier analysis has been briefly explained in section 2.1.1. Since wave spectra are obtained numerically (and measured time signals are discrete to begin with), the discrete version of equation 2.3 has to be applied. This is called the Discrete Fourier Transform (DFT):

$$S_\zeta(\omega) = \sum_{n=0}^{N} S_\zeta(t_n) e^{-i\omega t_n} \tag{2.10}$$

where ω [rad/s] is wave frequency and t_n [s] is the time for the step considered. In order to solve this DFT, the term $e^{-i\omega t_n}$ has to be evaluated for every step, which makes calculating the DFT a computationally intensive task. A so-called Fast Fourier Transform (FFT) [Cooley & Tukey, 1964] makes use of the symmetry in sine and cosine functions, such that this term only has to be determined for half the number of steps. Say the time signal the FFT is taken for has a length of $2N$. Equation 2.10 is therefore rewritten as follows:

$$S_\zeta(\omega) = \sum_{n=0}^{2N-1} S_\zeta(t_n) e^{-i\frac{2\pi}{2N-1} m t_n} = \sum_{n=0}^{2N} S_\zeta(t_n) w_{t_n,m}(2N), \quad m = 0, ..., 2N-1 \tag{2.11}$$

Split the time data $S_\zeta(t_n)$ in an even and an odd series:

$$S'_\zeta(r) = S_\zeta(2r), \quad r = 1, ..., N-1 \tag{2.12}$$

$$S''_\zeta(r) = S_\zeta(2r+1), \quad r = 1, ..., N-1 \tag{2.13}$$

Substituting (2.12) and (2.13) into (2.11) then yields:

$$S_\zeta(\omega) = \sum_{r=0}^{N-1} S'_\zeta(r) w_{r,m}(N) + w_{1,m}(N) \sum_{r=0}^{N-1} S''_\zeta(r) w_{r,m}(N) \tag{2.14}$$

Thereby, the term $w_{r,m}(N)$ only has to be calculated for half the number of steps. This reduces computation time by a factor of $\frac{N}{log_2 N}$, where N is the original number of steps in the time trace.

2.3.2. Bandpass filtering

Noise and slowly varying components (which are not of interest for this study) need to be removed from measured time signals. This is done by applying a 'bandpass filter', which takes out wave components outside of the desired frequency regime. After spectral representation of a time series has been obtained (by means of a FFT), all waves with frequencies outside of this regime are subtracted from the original time trace. Thus the time trace is filtered.

3
Hydrodynamic modelling

3.1. Introduction

In preparation of heavy lifts executed by HMC, hydrodynamic analyses are performed prior to project execution, in which the dynamic behaviour (as a result of wave forcing) of the vessels involved with the operation is modelled. For a certain project, there will be limiting criteria for which the operation can be executed in a safe manner, like maximum vessel motions or hook loads. Being able to model these responses to wave forcing in advance contributes greatly to the level of confidence one can have in the safe execution of an operation. As was explained earlier in chapter 2, the hydrodynamic analysis used calculates steady-state responses (to a unit wave height of 1 m) in the frequency domain, for a wide range of incoming wave directions and frequencies. The resulting RAOs, in combination with measured or forecasted wave spectra, can then be used for calculating response spectra. Within HMC, the computation of these RAOs is usually done using an application called Liftdyn: HMC's in-house developed software for hydrodynamic analyses in the frequency domain [HMC, 2009].

This chapter gives a brief introduction to Liftdyn, and describes the hydrodynamic models used for modelling each of the different heavy lift operation stages of the project for which measurements were obtained.

3.2. Liftdyn software

In Liftdyn, the user can build a model containing all the components of the lift system, like the SSCV, barge and topsides. These objects are modelled as rigid bodies. For each of these objects, a location, orientation, mass, CoG and radii of gyration can be set, which (along with wave forcing, added mass and hydraulic damping obtained from WAMIT) determine their dynamic behaviour. Apart from rigid bodies, so-called 'connectors' can be included in the model. These connectors are massless spring-dampers, acting along the line between two user-defined Point of Interests (PoIs) on two different rigid bodies. They are used to model all cable-like objects, like hoist wires and rigging. The PoIs can also be hinges, by fixing the constrained DoFs for two rigid bodies connected at a hinge. The dimensions of the rigid bodies can be included as well, but these are merely used for a visual representation of the object and have no influence on its dynamic behaviour, which is governed by the properties mentioned earlier. The Liftdyn user interface (displaying a visualisation of the model used for the dynamic analysis of the lift-off stage) can be seen in figure 3.1 below, with rigid bodies depicted in red and connectors in thick black lines.

Once the EoMs of the system have been solved, the user can obtain whatever RAOs he or she requires from the program, like forces in connectors or motions at pre-specified PoIs on a body, including their phase lead with respect to the incoming wave. Please refer to chapter 2 for background information on how the RAOs and their phase difference with respect to an incoming wave are calculated.

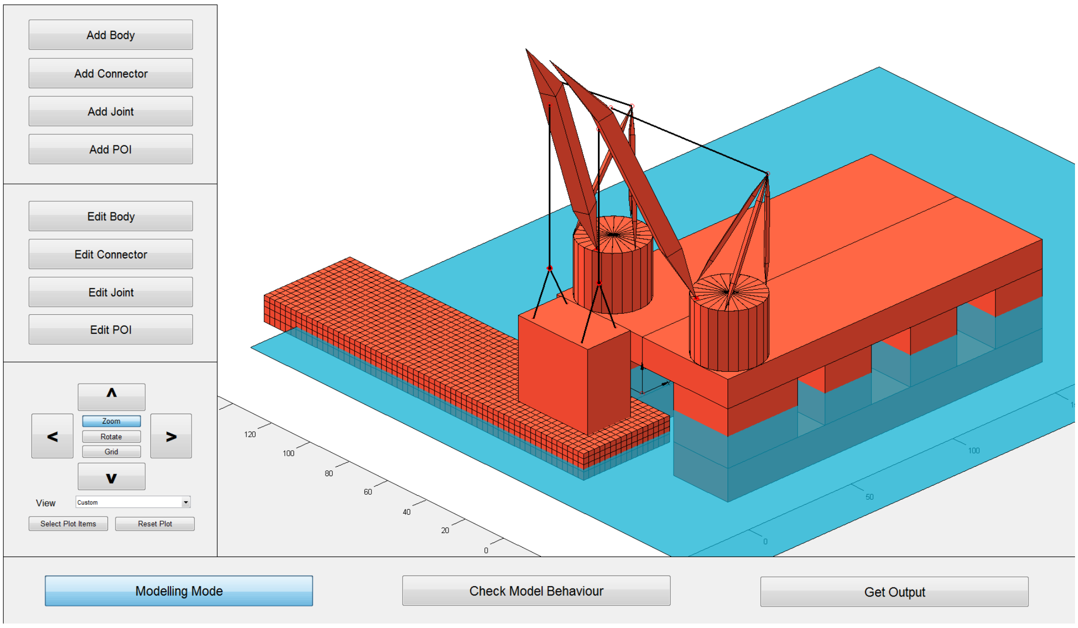

Figure 3.1: Liftdyn model, pre-tension stage

3.3. Liftdyn models

As mentioned earlier, measurements from a recent heavy lift operation were used for the comparison study presented in this thesis (see chapter 4). The Liftdyn models used to model the motions of the barge (H-542), SSCV (Thialf) and topsides are described in this section. It provides the reader with some key model parameter values. Please refer to appendix B for stage specific parameters for each of the stages considered.

For hydrodynamic forcing on the floating rigid bodies, please refer to section 3.4.

3.3.1. Axis systems definition

The global origin of the models is located in the Thialf's centerline at the stern, at the waterline, where the Global Coordinate System (GCS) x-, y- and z-axes are pointing towards the bow, portside (PS) and upwards respectively. The Thialf's Local Coordinate System (LCS) axis system has the same orientation, as have those of the Thialf's crane blocks. The LCS axis systems of the crane booms are inclined with respect to the horizontal plane: the x-axis is in-line with boom's orientation (diagonally upwards), the y-axis is sideways in the horizontal plane and the z-axis is perpendicular to the local xy-plane. The LCS axis systems of the H-542 and topsides are rotated 90 deg with respect to the GCS, such that their positive x-axis has the same orientation as the positive y-axis in the GCS.
The GCS is depicted in black and the LCSs are depicted in blue in figure 3.2. CoG locations in the GCS are given in section 3.3.2.

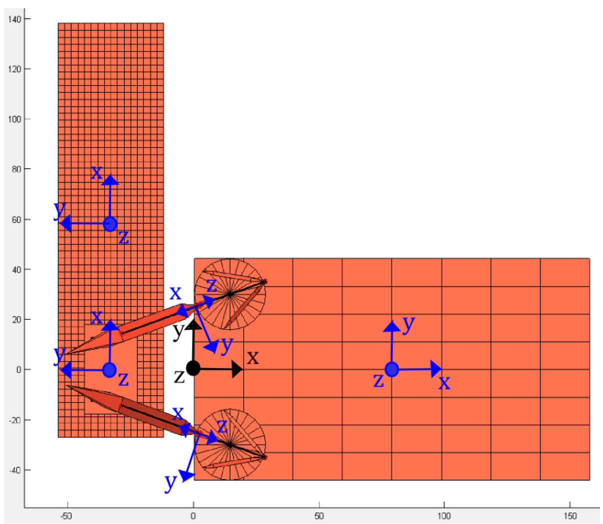

Figure 3.2: Liftdyn axis systems

3.3.2. Rigid body parameters

The topsides, H-542, Thialf, crane booms (mounted at the stern of the Thialf) and crane blocks are modelled as rigid bodies in Liftdyn. The mass and inertia properties, locations and orientations with respect to the GCS, and PoIs of each of these bodies are listed in tables 3.1 through 3.5 below. Coordinates are given with respect to the GCS unless stated otherwise.

Table 3.1: Liftdyn model - Thialf properties

Property	Magnitude	Unit
Mass	*stage dependent (s.d.)*	[mT]
CoG	*[s.d., s.d., s.d.]*	[m]
Hor. & vert. rotations LCS w.r.t. GCS	[0, 0]	[∘]
Hydrodynamic origin	[72.53, 0, 0]	[m]
Radii of gyration (around LCS-axes)	[38, 59, 65]	[m]
PoI 1: SB boom hinge	[2.21, -25.62, 47.28]	[m]
PoI 2: SB top A-frame	[28.20, -35.08, 118.61]	[m]
PoI 3: PS boom hinge	[2.21, 25.62, 47.28]	[m]
PoI 4: PS top A-frame	[28.20, 35.08, 118.61]	[m]

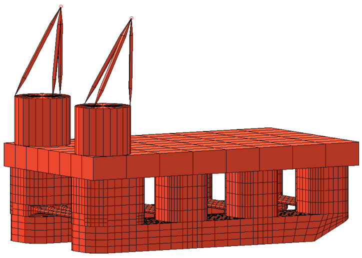

Figure 3.3: Liftdyn panel model - Thialf

Table 3.2: Liftdyn model - Crane booms properties

Property	Magnitude	Unit
Mass	1003.7	[mT]
SB boom CoG	[-21.23, -17.09, 103.27]	[m]
PS boom CoG	[-21.23, 17.09, 103.27]	[m]
SB Hor. & vert. rotations LCS w.r.t. GCS	[160, 66.18]	[∘]
PS Hor. & vert. rotations LCS w.r.t. GCS	[200, 66.18]	[∘]
Radii of gyration (around LCS-axes)	[1, 36.05, 36.05]	[m]
SB PoI 1: Boom hinge	[2.21, -25.62, 47.28]	[m]
PS PoI 1: Boom hinge	[2.21, 25.62, 47.28]	[m]
SB PoI 2: Suspension point	[-28.91, -14.29, 131.42]	[m]
PS PoI 2: Suspension point	[-28.91, 14.29, 131.42]	[m]
SB PoI 3: Main fall axle	[-33.25, -12.72, 123.92]	[m]
PS PoI 3: Main fall axle	[-33.25, 12.72, 123.92]	[m]

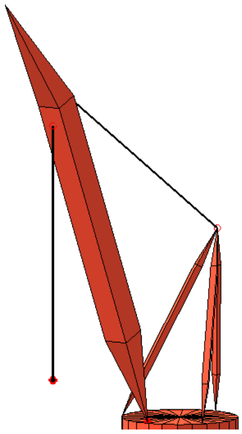

Figure 3.4: Liftdyn panel model - Crane booms

Table 3.3: Liftdyn model - Blocks properties

Property	Magnitude	Unit
Mass	186.2	[mT]
SB block CoG	[-33.23, -12.72, *s.d.*]	[m]
PS block CoG	[-33.23, 12.72, *s.d.*]	[m]
Hor. & vert. rotations LCS w.r.t. GCS	[0, 0]	[∘]
Radii of gyration (around LCS-axes)	[1, 1, 1]	[m]

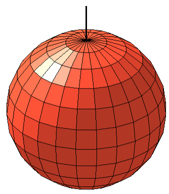

Figure 3.5: Liftdyn panel model - Blocks

Table 3.4: Liftdyn model - H-542 properties

Property	Magnitude	Unit
Mass	28890.12	[mT]
CoG	[-33.23, 53.72, *s.d.*]	[m]
Hor. & vert. rotations LCS w.r.t. GCS	[90, 0]	[∘]
Hydrodynamic origin	[-33.23, 55.52, 0]	[m]
Radii of gyration (around LCS-axes)	[11.29, 44.95, 45.99]	[m]
PoI 1: Grillage (topsides connection)	[-33.23, -1.90, *s.d.*]	[*m*]

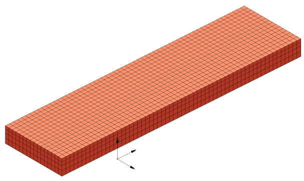

Figure 3.6: Liftdyn panel model - H-542

Table 3.5: Liftdyn model - Topsides properties

Property	Magnitude	Unit
Mass	5300	[mT]
CoG location	[-33.23, -1.90, *s.d.*]	[m]
Hor. & vert. rotations LCS w.r.t. GCS	[90, 0]	[∘]
Radii of gyration (around LCS-axes)	[16.23, 13.54, 16.09]	[m]
PoI 1: SB lift point #1	[-24.85, -12.50, *s.d.*]	[m]
PoI 2: SB lift point #2	[-41.61, -12.50, *s.d.*]	[m]
PoI 3: PS lift point #1	[-24.85, 12.50, *s.d.*]	[m]
PoI 4: PS lift point #2	[-41.61, 12.50, *s.d.*]	[m]
PoI 5: Grillage (H-542 connection)	[-33.23, -1.90, *s.d.*]	[m]

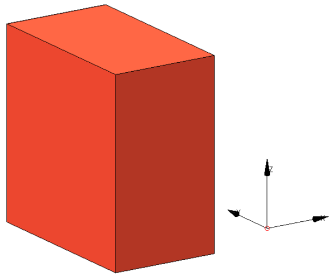

Figure 3.7: Liftdyn panel model - topsides

3.3.3. Connectors

All cable-like elements are modelled as linear spring-dampers. Grommets, which are wire ropes in an endless loop, are used to connect lift points on top of the topsides to the crane blocks. They run up and down twice in the configuration that was used, which means that the total cross-sectional area of the connector is $4 \cdot A_{grom}$. The boom suspension and main hoist wire consists of a system of reeved wire rope running over sheaves at either end of the connector: the total cross-sectional area of these connectors is $56 \cdot A_{rope}$ and $80 \cdot A_{rope}$ for the boom suspension and main hoist respectively. The cross-sectional area of a wire rope is calculated as follows [HMC, 2005]:

$$A_{wire} = 0.44 \frac{\pi}{4} D_{wire}^2 \tag{3.1}$$

where D_{wire} is the outer diameter of a wire rope. The factor 0.44 results from the rope being made up of strands, which do not fully cover the area corresponding to the outer diameter. This effective cross-sectional area convention will be used for elasticity calculations throughout this report. Wire rope stiffness is non-linear and dependent on loading history. A linear elasticity E of 70 GPa was used in the models [HMC, 2005], which is roughly a third of the stiffness of solid steel.All the connectors used in the models, along with their attachments and stiffnesses are listed in table 3.6 below. Please refer to tables 3.1 through 3.5 for the locations of the PoIs mentioned. In Liftdyn, all connectors have a damping at 1.5% of the critical damping by default. The values have been omitted from the table since it does not have a significant influence in the frequency range of interest.

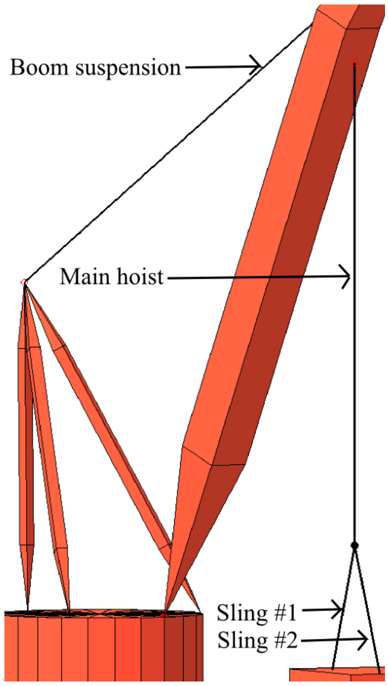

Figure 3.8: Liftdyn connectors

Table 3.6: Liftdyn model - Connector properties

Connector	Attachment #1	Attachment #2	D_{single} [mm]	#	EA [kN]
SB boom suspension	Thialf PoI 2	SB boom PoI 2	61.7	56	5,157,021.63
PS boom suspension	Thialf PoI 4	PS boom PoI 2	61.7	56	5,157,021.63
SB main hoist	SB boom PoI 3	SB block CoG	61.7	80	7,367,173.76
PS main hoist	PS boom PoI 3	PS block CoG	61.7	80	7,367,173.76
SB grommet #1	Topsides PoI 1 #1	SB block CoG	299	4	8,650,534.97
PS grommet #1	Topsides PoI 3 #1	PS block CoG	231	4	5,163,266.59
SB grommet #2	Topsides PoI 2 #2	SB block CoG	299	4	8,650,534.97
PS grommet #2	Topsides PoI 4 #2	PS block CoG	231	4	5,163,266.59

3.3.4. Lift stages considered & Corresponding model modifications

For each of the lift stages described in chapter 1, a separate Liftdyn model has been created. As can be seen in section 3.3.2 above, some model parameters are different for each stage. This is mainly due to mean hook load differences (re-distribution of load over the Thialf and H-542) and assymetric crane loading ($PS_{load} \approx 0.77 \cdot SB_{load}$). The Thialf was assumed to be ballasted such that it maintains a constant mean draft (of 26.6 m) throughout the lift operation, which means its displacement will have to remain the same for all stages (equation 3.2). For this to be the case, it has to de-ballast a weight in water exactly equal to the loads suspended from the cranes, such that the total weight of the Thialf and the topsides combined remains the same. Furthermore it was assumed to maintain an even mean heel and trim. In order to achieve this, its CoG will have to move (by means of changing ballastwater configuration) in order to compensate for the moments resulting from the hook loads (equation 3.3).

$$M_{loaded} = M_{unloaded} - SB_{load} - PS_{load} \tag{3.2}$$

$$CoG_{loaded} = \frac{M_{unloaded} \cdot CoG_{unloaded} - SB_{load} \cdot PoI_{SBmainfall} - PS_{load} \cdot PoI_{PSmainfall}}{M_{loaded}} \tag{3.3}$$

where M_{loaded},CoG_{loaded}, $M_{unloaded}$ and $CoG_{unloaded}$ are the Thialf's mass and CoG coordinates for the loaded and unloaded cases respectively. M_{SBload}, $PoI_{SBmainfall}$, M_{SBload} and $PoI_{SBmainfall}$ are the masses and locations where they act on the Thialf (the boom main fall axles) for SB and PS hook loads respectively. In the models, mean hook loads during the lift-off and set-down stages were adjusted to match measured mean hook loads during these stages. The SB mean hook loads turned out to be ca. 1950mT and 1200mT (ca. 65% and 40% of the total hook load during the free-hanging stage) for the lift-off and set-down stages respectively (figure 3.9 below). During the set-down stage, there was no time interval with more or less constant mean hook loads unfortunately. For the free-floating and free-hanging stages, naturally the hook loads were at 0% and 100% of the topsides weight respectively.

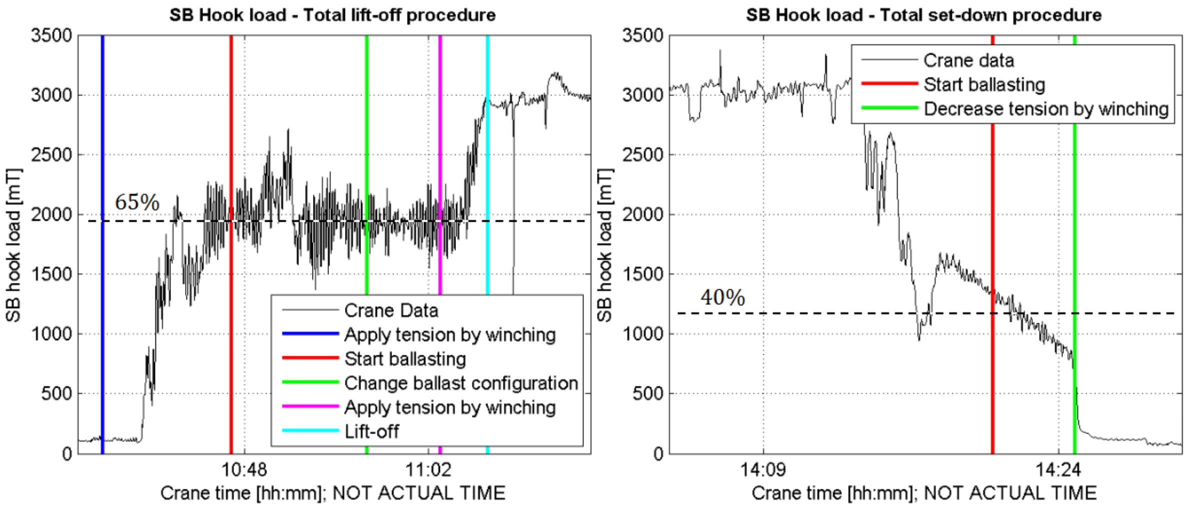

Figure 3.9: SB hook load time trace - Lift-off and set-down stages

In contrast to the Thialf, the H-542 does not ballast or de-ballast in order to maintain draft and an even heel and trim during lift operations. Draft differences are accounted for in the models. This results in turn to vertical displacements of all PoIs related to the elevation of the H-542: the topsides CoG, lift points, and the SB and PS blocks. The differences in heel and trim (due to the topsides not being positioned straight above the centre of floatation of the barge) have not been accounted for in the model. High hydrostatic restoring coefficients make that mean heel and trim variations are very small, which, in combinations with its simple box-shape, makes this influence on hydrodynamic properties marginal [Journée & Massie, 2001].

A visualisation of the different models used for each stage is given in figures 3.10 through 3.13 below. For stage specific parameters, please refer to appendix B.

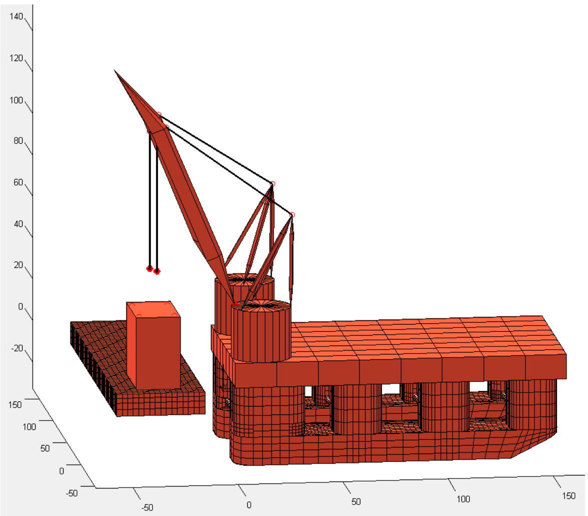

Figure 3.10: Free-floating stage - Liftdyn visualisation

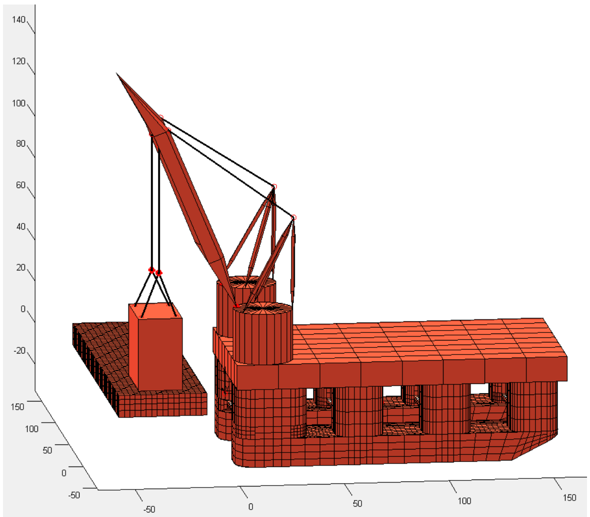

Figure 3.11: Lift-off stage - Liftdyn visualisation

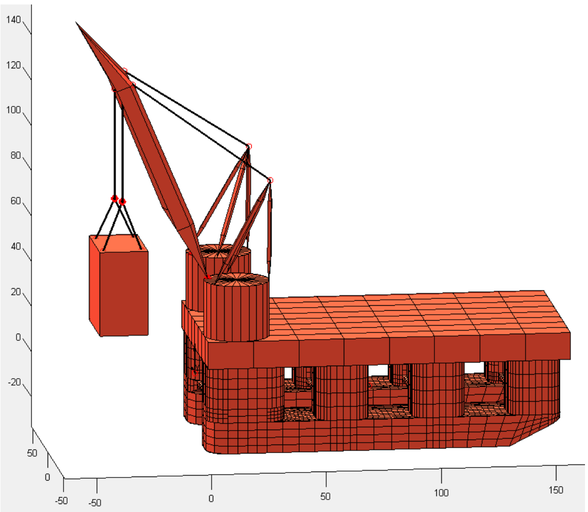

Figure 3.12: Free-hanging stage - Liftdyn visualisation

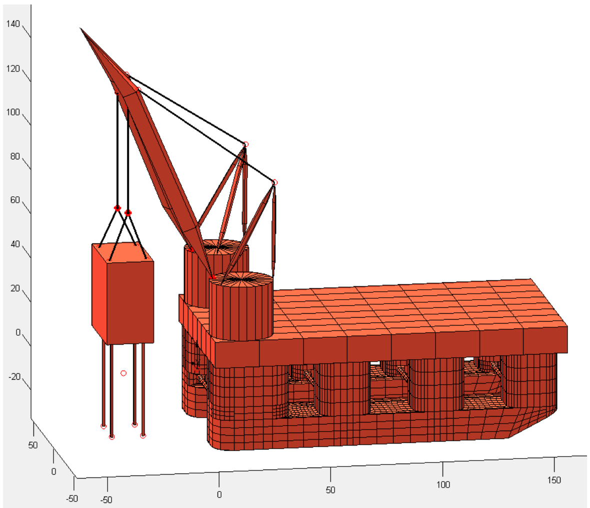

Figure 3.13: Set-down stage - Liftdyn visualisation

3.4. Wave forcing, added mass and damping

In standard engineering practices at HMC, wave forcing, hydraulic damping and added mass input for the floating bodies in a Liftdyn model are obtained from single-body diffraction analyses. For HMC's own SSCVs and barges, standard hydrodynamic databases containing this data are available for an (assumed) infinite water depths and standard shallow water depths (38.6 m deep in case of the Thialf). Since possibilities for SSCV/barge combinations and their positioning with respect to each other are endless, using two of these single-body hydrodynamic databases in the models is very practical, and saves an engineer the effort of conducting project specific multi-body diffraction analyses at the project's actual water depth.

This is generally considered to give a good approximation for engineering purposes. In this section, the influence of applying a multi-body analysis instead of two separate single-body diffraction analyses, and the influence of using the actual as opposed to an infinitely assumed water depth for this specific project are discussed. For a brief introduction on diffraction analyses and potential theory, please refer to chapter 2.

3.4.1. Diffraction analysis - Single- vs. Multi-body

During free-floating and lift-off stages, the H-542 is in very close proximity to the Thialf (ca. 12 m away from its stern). In a single-body diffraction analysis, there are no boundary conditions other than those at its own hull, the sea bed and the waterline. If there are two or more vessels in close proximity to one another however, waves reflected and radiated from one body influence the other bodies' wave fields.

Traditionally, these interaction effects have been neglected in the heavy lifting industry. In the past, conducting (especially multi-body) diffraction analyses was an expensive task, which required a lot of time or high computational power which was not readily available. It has been concluded in a recent study however [Ayaz et al., Saipem UK, 2014], that there are noticeable response differences for all the floating bodies involved with a lift operation when multi-body instead of single-body diffraction is used. For responses of vessels being shielded by much larger vessels, this influence was significant. However, the influence of mechanical coupling between two floating bodies (e.g. hoist wires and grommets as is the case during lift-off) was found to be much larger for the cases considered. Nevertheless, when there is no mechanical coupling, shielding effects can become influential on vessel motions [Ayaz et al., Saipem UK, 2014].

The configuration of the H-542 and Thialf with respect to the incoming waves was such (during the free-floating and lift-off stages) that significant shielding effects can be expected for the H-542. For the free-hanging and set-down stages, there were no (large) bodies in close proximity of the Thialf, except for the jacket structure, which consists of relatively thin tubular elements. These are considered not to influence the surrounding wave field significantly (Morison elements). Moreover, the Thialf and jacket structure are to a much lesser extent in-line with respect to the prevailing wave direction (figure 3.15).

Top views of vessel orientations during the lift operation are plotted over the corresponding 3D wave spectra in figures 3.14 (free-floating and lift-off) and 3.15 (free-hanging and set-down) below. In the figures, the Thialf, H-542 and topsides are depicted in green, yellow and red respectively. The prevailing wave direction is depicted by a black arrow.

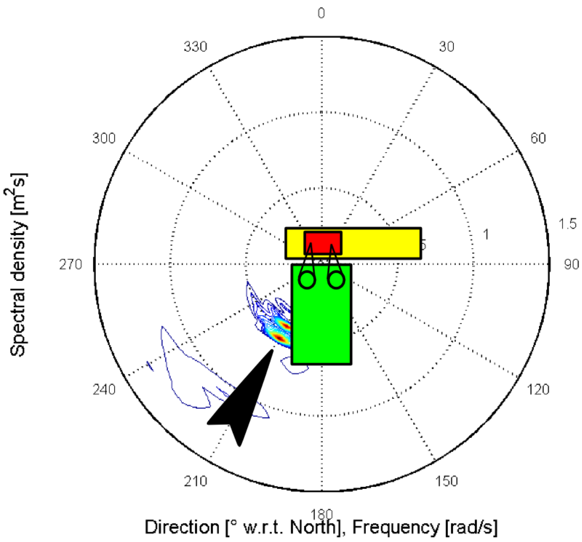

Figure 3.14: 3D wave spectrum and configuration
Free-floating & lift-off stages

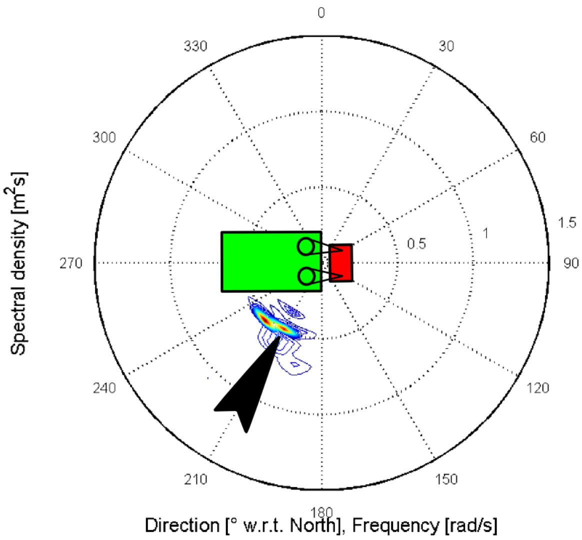

Figure 3.15: 3D wave spectrum and configuration
Free-hanging & set-down stages

These days, with advancement of technology, computational possibilities have increased and WAMIT also comes with the option to include multiple floating bodies in a single diffraction analysis. Therefore, for the free-floating and lift-off stages, both a single- and a multi-body diffraction analysis have been conducted.

ALTERED/OMITTED FOR CONFIDENTIALITY REASONS: All single vs. multi-body diffraction comparison plots for wave forcing RAOs, added mass and damping for the H-542 and Thialf can be found in appendix C. As expected, differences in wave forcing RAOs are largest for the H-542 (roll & pitch depicted in figures 3.16 *and 3.17 below). It can be seen wave forcing is much less smooth for the multi-body case: this is a well-known result for multi-body diffraction analyses. The peaks are caused by standing waves in between adjacent bodies. In reality, these resonant effects are smaller as compared to idealized potential flow, due to flow separation and viscous damping [Sun et al., 2010].*

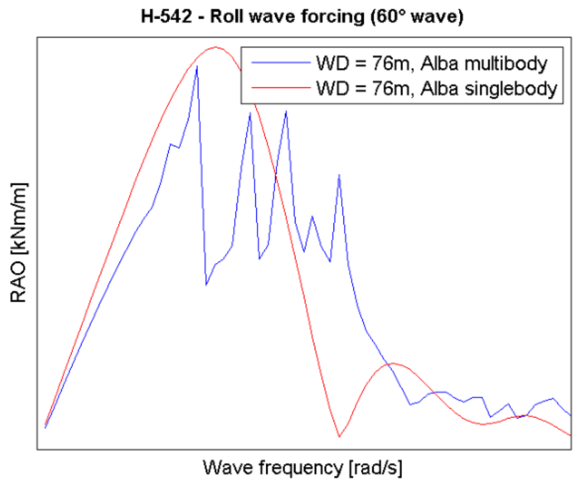

Figure 3.16: H-542 wave forcing lift-off stage - Roll Single- vs. Multi-body diffraction

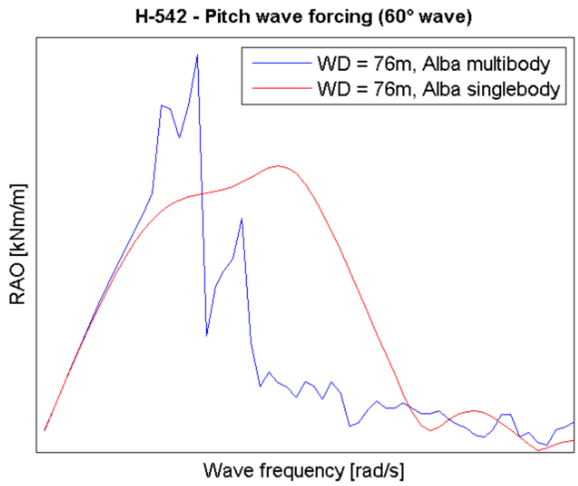

Figure 3.17: H-542 wave forcing lift-off stage - Pitch Single- vs. Multi-body diffraction

3.4.2. Diffraction analysis - Infinite vs. Actual water depth

Initially, the diffraction analyses for all stages were conducted at infinite WD. In reality the ocean's bottom will influence the ocean waves. The longer a wave, the more it will be influenced by the boundary condition at the seabed, according to the dispersion relationship [Holthuijsen, 2006]:

$$\lambda = \frac{gT_p^2}{2\pi} tanh\left(\frac{2\pi WD}{\lambda}\right) \tag{3.4}$$

where λ [m] is wave length and T_p [s] is wave period. $tanh\left(\frac{2\pi WD}{\lambda}\right) \approx 1$ for $WD = \frac{\lambda}{2}$. Therefore, as a rule of thumb, bottom influence starts becoming significant when:

$$WD < \frac{\lambda}{2} \tag{3.5}$$

For the project considered, where $WD \approx 76$ m, this means bottom influence becomes significant for waves longer than approximately 152 m. From the dispersion relationship, the following relation between wave length and wave period follows:

$$\lambda \approx 1.56 \cdot T_p^2 \tag{3.6}$$

which means that, at the location of the project under consideration, for waves with a period longer than approximately $T_p \approx \sqrt{\frac{152}{1.56}} \approx 10$ s bottom influence starts to become influencial. Since the project is situated in West-Africa, an area known for its swell sea states, using the actual WD instead of an infinite WD in the diffraction analysis could make a significant difference on wave forcing, added mass and damping in the frequency range of interest. Therefore, (multi-body) diffraction analyses for several WDs have been conducted in order to gain some understanding as to what extent the sea bed influences hydrodynamic properties for this project.

ALTERED/OMITTED FOR CONFIDENTIALITY REASONS: For several WDs, diffraction comparison plots for wave forcing RAOs, added mass and damping for the H-542 and Thialf can be found in appendix C. As expected, differences between the analyses are largest in the lower frequency ranges (roll & pitch depicted in figures 3.18 and 3.19 below).

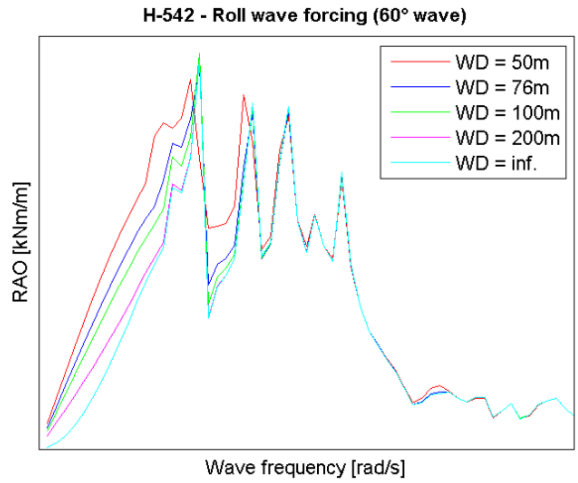

Figure 3.18: H-542 wave forcing lift-off stage - Roll
Increasing WD diffraction

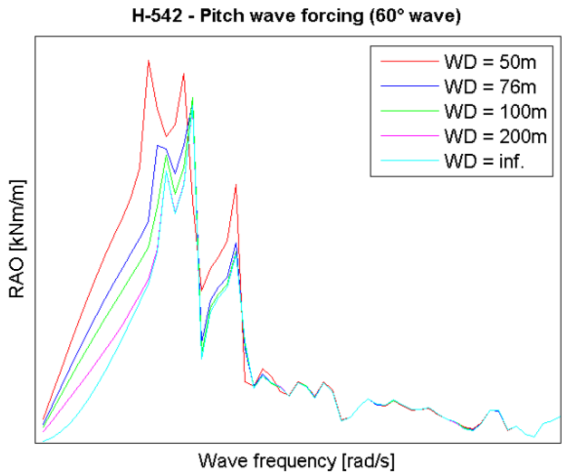

Figure 3.19: H-542 wave forcing lift-off stage - Pitch
Increasing WD diffraction

3.4.3. Diffraction analysis - Selected methods

Regarding single- vs. multi-body: multi-body output for wave forcing on the H-542 is significantly different from that of the single-body diffraction analysis, which is what was expected. Accounting for the exaggerated resonant peaks can be done by means of applying some extra damping on the free surface (referred to as applying a 'lid'). This is a large amount of work, and will not influence outcomes in the order searched for. However, these peaks do exist, and vessel response can be larger for some headings due to multi-body interaction. Therefore it has been decided to use the hydrodynamic properties resulting from the multi-body diffraction analysis for the free-floating and lift-off stages.

Regarding the WD: wave forcing, added mass and damping are somewhat different at the (very) low frequencies for the WDs considered. Since the wave spectra during project execution contained a lot of energy around 0.5 rad/s, and some at even lower frequencies, these differences could have an influence on vessel hydrodynamics. Therefore it has been decided to conduct the diffraction analyses with the actual WD for all stages.

An overview of the diffraction analysis configurations used to obtain hydrodynamic data for each stage is given in table 3.7 below.

Table 3.7: All stages - Diffraction analysis configurations

Diffraction analysis method	**WD [m]**	**Stages**	
Multi-body	76	Free-floating	Lift-off
Single-body	76	Free-hanging	Set-down

3.5. Level of pretension influence

OMITTED FOR CONFIDENTIALITY REASONS

4
Measurement campaign & data processing

4.1. Introduction

The discrepancy observed is one between modelled hook load fluctuations and measured hook load fluctuations. This discrepancy can therefore either be due to (1.) inaccurately modelled hook load fluctuations (which could in turn be due to inaccurately modelled vessel hydrodynamics) or (2.) inaccurate registration of actual hook load fluctuations by the measuring device (which could be due to the measured tension fluctuations not being representative for the actual hook load fluctuations), or a combination of both.

In order to assess which, and to what extent, each of these explanations applies, comparisons (1.) & (2.) below need to be made. The data required is listed for both comparisons:

1. Full scale measured motions spectra vs. Liftdyn modelled motions spectra
   - Vessel motion measurements
   - Liftdyn modelled RAOs
   - Measured wave spectrum
2. Full scale measured vs. Calculated hook load fluctuations spectra
   - Hook load measurements
   - Main hoist elongation measurements
   - Main hoist stiffness properties

Hook loads are measured by default, obviously, and wave spectra are either obtained from a forecast or measured on-site by a WRB. Regarding motion measurements, HMC has several systems at its disposal. The Thialf's motions are measured by default, as these are required as input for the vessel's dynamic positioning system. Offshore motion monitoring of other items (like barges or lift objects) can be done with portable motion monitoring units. These sensors are used for most of HMC's heavy lift projects, especially for critical lifts (lifts which require nearly the full crane capacity) or for research purposes. Since the dynamic tension in the main hoist (assuming wire rope has a certain stiffness) is directly related to it's length fluctuations, ideally motion measurements of both the main fall axle and the main block are obtained. Directly measuring main block motions is not feasible, due to power supply and space issues. A motions sensor on the lift object is possible however. Measuring crane boom motions (near the main fall axle) is not standard practice, but it has been done for the Thialf once before. This project concerned decommissioning of a jacket support structure and transportation of the jacket to a decommissioning yard while being suspended from the cranes [el Marini, 2014]. It did not include lifting an object of a floating barge, the operation specifically interesting for this thesis's topic.

Therefore, a recent offshore monitoring campaign for a topsides heavy lift operation has been expanded to include crane boom motions monitoring, especially for this thesis. This measurement campaign, the measurement equipment involved and processing of data obtained from these measurements are discussed in this chapter.

4.2. Measurement devices & Locations

4.2.1. SIRI motions sensors

A motion measuring system used by HMC is the Siri system. It consists of four 6 DoF motion sensors and a display and logging system which can be operated from the Thialf's bridge. Three sensors (S1, S2 & S3) are inside a portable container (figure 4.1) and transmit their measured signals to the display and logging system, where they are timestamped and saved. In addition, sensors S1 and S2 have their own hard drives as a backup, and they are equipped with larger batteries and solar panels which enable them to operate for extended periods of time (for instance on barges during transport). Sensor S3 has to be connected to a power supply during operation. The fourth sensor (S4) is permanently installed below the floor of the Thialf's bridge. The sensors measure translational accelerations and rotational velocities. Some important properties of the Siri motion sensors are given in table 4.1 below.

Table 4.1: Siri sensor properties

Property	Magnitude	Unit
Translations	*accelerations*	[m/s^2]
Rotations	*velocity*	[°/s]
Dynamic tran. accuracy	ca. 0.005	[m/s^2]
Dynamic rot. accuracy	ca. 0.2	[°/s]
Transmittal frequency	ca. 25	[Hz]

Figure 4.1: Siri sensor S1 during operation: fixed to topsides deck

For this specific project, sensors S1 and S2 (both portable sensors) were used, apart from sensor S4 which is used by default (figure 4.2). S1 was fixed to the floor of one the topsides' outside corridors. S2 was fixed to a frame inside the Thialf's SB crane boom, very near the SB main fall axle. The sensors were oriented such that their axis systems correspond to that of the LCS of the body they are attached to. Their coordinates in the LCS of the corresponding body are given in table 4.2 below.

Table 4.2: Siri sensor locations - Local coordinates

Sensor	Location (in LCS) [m]
S1 (w.r.t. Topsides CoG)	[0, -20.88, -15.29]
S2 (w.r.t. SB boom hinge)	[85., 0, -3.55]
S4 (w.r.t. Thialf CoG)	[47.95, 0.97, 48.39]

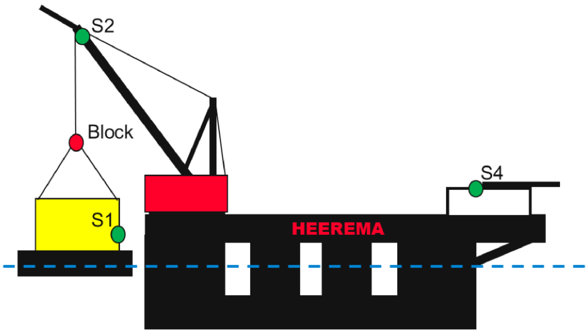

Figure 4.2: Siri sensor locations - SB sideview

4.2.2. Thialf - Motion Response Unit

Apart from Siri sensor S4, there is another motion measurement sensor for the Thialf: the so-called MRU. This device is also located inside the Thialf's accommodation, a few floors below the bridge. It processes translational acceleration and rotational velocity measurements real-time, by estimating for which filter cut-off frequencies errors are minimized (which are in turn dependent on mean wave height and noise a.o.), filtering and then integrating raw measurements [Godhavn, 2000]. It only registers heave, roll & pitch motions unfortunately; it is not possible to download raw data from this unit. However, these measurements are generally considered to be very accurate. They can be used to cross-check the heave, roll and pitch motions obtained from sensor S4.

Table 4.3: Thialf MRU properties

Property	Magnitude	Unit
Location (w.r.t. Thialf CoG)	[50.5, -7.2, 42.3]	[m]
Heave	*displacements*	[m]
Roll & Pitch	*rotations*	[°]
Dynamic tran. accuracy	ca. 0.05	[m]
Dynamic rot. accuracy	ca. 0.05	[°]
(Filtered) frequency	ca. 10	[Hz]

Figure 4.3: Thialf MRU

4.2.3. Load Measuring Pins

The Thialf main hoists are part of a complex system of wire rope running over sheaves. For each crane, this system consists of two winches at the base of the crane ('front drum' & 'rear drum' in figure 4.4), to which both ends of a long wire rope are connected. The resulting wire rope loops are reeved through a system of sheaves, including those in the main fall and main block axles. As a result of this, the crane blocks move up or down when the winches are wound in or out respectively, and the centre of the wound out wire loop will remain in the same position (if the wire would have an infinite axial stiffness and sheaves were frictionless). Each drum covers one half of a crane block, so winding in and out always happens in tandem. Standard is the so-called '4 × 20' main hoist reeving, which means four sets of 20 sheaves are used: 20 for both the main fall and main block axle, for both winches. In this configuration, crane capacity is highest, but lowering depth is limited since the amount of wire rope on the drums is finite. A schematic side view of the sheaves arrangement can be seen in figure 4.4 below. Please refer to appendix A for a more detailed drawing of the '4 × 20' reeving arrangement.

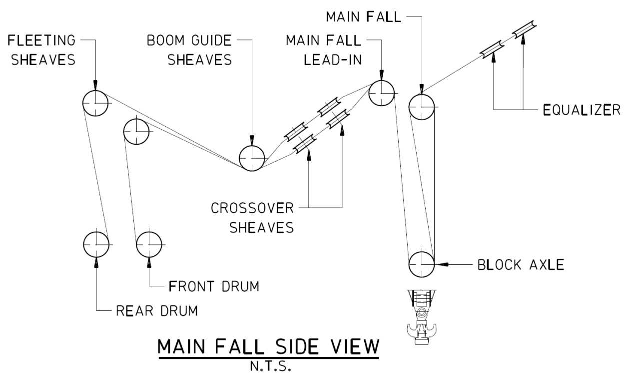

Figure 4.4: Wire & sheaves arrangement - Schematic

The hook load measurement, which is at the very core of this thesis's topic, is done by two so-called Load Measuring Pins (LMPs) [Huisman-Itrec, 2007]. Such a LMP is basically a sheave axis with strain gauges inside (figure 4.5 below). These strain gauges' resistance changes when deformed, thereby regulating the current within a range of 4 - 20 mA. These current values are then transformed to a force on the LMP by means of a static(!) calibration. Since the sheaves next the the sheaves containing the LMPs are fixed, the angle (β in figure 4.6) the wire ropes make with respect to the measurement direction of the LMP are known, and the measured force can be translated to axial tension in the wire rope running over the sheave. The axial tension of a single wire rope cross-section can then be multiplied by the number of cross-sections in the main hoist, since theoretically a (massless) wire rope experiences the same tension everywhere along it's length. Each of the Thialf's cranes is equipped with two LMPs: one for each wire rope loop (they act as axes for the 'Equalizer' sheaves in figure 4.4, see figure A.2 for details). The wire rope tension measured by one LMP therefore roughly corresponds to one-eightieth of the total hook load in the '4 × 20' reeving arrangement. Note however that the (static) calibration for Thialf's hook load measurement has been conducted with actual calibration loads on the crane hook, with the LMPs in place.

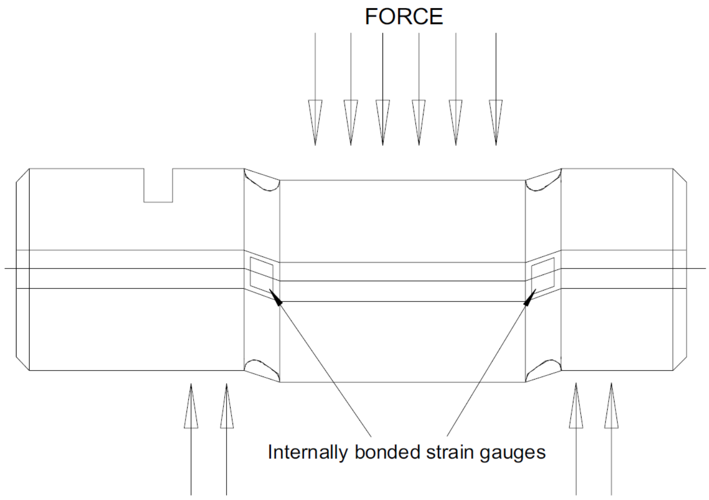

Figure 4.5: LMP - Strain gaugs

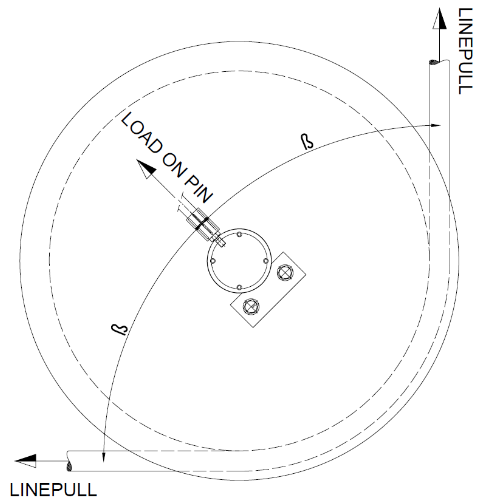

Figure 4.6: LMP - Wire tension calculation

4.2.4. Sheaves motions behaviour - Main block camera

As explained in the section above, the total hook load measurement is based on the tension measurements in two single sections in the wire rope/sheaves system (one for each wire loop). Although these registered loads have been statically calibrated, one could wonder if the dynamic tension at the measurement locations represents the average dynamic tension of all cross-sections in the main hoist. Maybe stuck sheaves, slip-stick rotation mechanisms or sheave inertia properties influences the re-distribution of wire rope over the sheaves such, that this is not the case.

One way of learning about this potential influence of relative sheave movements on registered hook loads, is by means of video footage of the sheaves in the main fall or main block axles. The view on the main fall axle is obstructed by fenders and not easily accessible. Therefore, it was decided to film the sheaves on the main block axle, using a standalone camera fixed to the main block. This comes with some difficulties, like power supply, safe and sturdy connection (dropped objects) and remote control. Eventually it was decided to combine a high-definition action camera (GoPro) with a high-capacity power bank (figure 4.7) in a see-through watertight box, which allows for the camera to maintain standby mode with Wifi (for remote control) switched on for 3-4 days. This period is long enough for the camera assembly to be attached to the main block during crane hook inspection (after which the main block is not accessible anymore), which can be several days in advance of a lift.

It was decided on-site to change the camera assembly's location from the side of the SB main block to the centre of the block, in between the reeved hoist wires (encircled in red in 4.8 below). As a result of this, the block's steel and hoist wires were in between the camera and the remote control, which may have caused the Wifi signal to be blocked. In any case, the signal proved to be not strong enough for the camera to be switched on. Therefore this attempt at obtaining video footage of relative sheave movement during a heavy lift operation has failed unfortunately.

Figure 4.7: Camera assembly

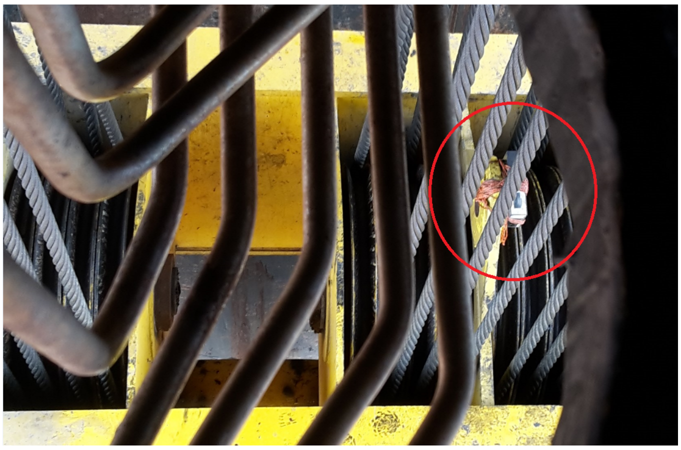

Figure 4.8: Camera assembly - Connected to main block

4.2.5. Wave Rider Buoy

In order to take wave forcing input in this comparison study out of the equation, modelled motions and hook load spectra were calculated using the wave spectra measured during the corresponding lift stage. These wave spectra were obtained from a WRB. WRB measurements are generally considered to be very accurate. Some properties of the WRB used are listed in table 4.4 below [Datawell, 2016]. The WRB measures heave motion (wave height) time traces, and calculates wave direction from measured roll and pitch motions.

Table 4.4: WRB properties

Property	Magnitude	Unit
Heave range	(-20) - (+20)	[m]
Heave resolution	0.01	[m]
Heave accuracy	<1%	[m]
Directional range	0 - 360	[°]
Directional resolution	1.4	[°]
Directional accuracy	ca. 0.5	[°]
Period range	1.6 - 30	[s]

4.3. Motion measurements processing - Initial approach

Please refer to appendix D for some example plots of the different Siri measurement data processing steps.

4.3.1. Siri signals - Synchronisation & Filtering

Since Liftdyn calculates RAOs in the frequency domain, measurements do not have to be exactly synchronized, for as long as the time window of the measurements is from the corresponding stage, a spectral comparison can be made. For calculating the elongation of the main hoist however, ideally two exactly synchronized motion signals of both the main fall axle and the crane block are used. Also for time series comparison of multiple motion sensors or load signals, the sensors' timestamp should be exactly the same ideally.

Although sample rate varies a little bit per Siri sensor (in order for the sensors not to interfere; all ca. 25 Hz), all Siri sensor signals are timestamped by the same computer. Therefore, after resampling, the discrete time signals are exactly synchronised. Bandpass filtering was conducted according to the method explained in chapter 2.

4.3.2. Siri signals - Accounting for gravity

The raw Siri translational acceleration measurements also contain a gravitational component. The magnitude of these components depends on the orientation of the sensor. Therefore, for each time step, the gravitational acceleration component in each translational direction has to be determined using the rotations occurring at that time step.
To that end, the relative unit length of each axis of a sensor's LCS with respect to the GCS's z-axis (the axis along which g acts). The three Euler angles (α, β and γ in figure 4.9) can be used to define the orientation of any 3D axis system with respect to another axis system. The following rotation matrices can be used for transforming coordinates in a certain coordinate system to coordinates in the system obtained after rotating along the corresponding angle.

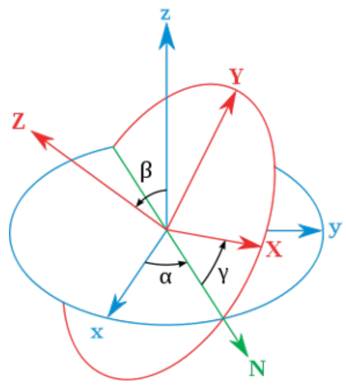

Figure 4.9: Euler angles

$$A_\alpha = \begin{bmatrix} cos\alpha & -sin\alpha & 0 \\ sin\alpha & cos\alpha & 0 \\ 0 & 0 & 1 \end{bmatrix}, \quad A_\beta = \begin{bmatrix} 1 & 0 & 0 \\ 0 & cos\beta & -sin\beta \\ 0 & sin\beta & cos\beta \end{bmatrix}, \quad A_\gamma = \begin{bmatrix} cos\gamma & -sin\gamma & 0 \\ sin\gamma & cos\gamma & 0 \\ 0 & 0 & 1 \end{bmatrix} \tag{4.1}$$

These rotation matrices are used for transforming coordinates in a sensor's LCS to coordinates in the GCS. In order to account for local roll (local pitch & yaw can be accounted for in β and γ respectively), an extra rotation matrix is introduced:

$$A_\delta = \begin{bmatrix} 1 & 0 & 0 \\ 0 & cos\delta & -sin\delta \\ 0 & sin\delta & cos\delta \end{bmatrix} \tag{4.2}$$

These four matrices combined form the total rotation matrix required for transforming local coordinates to global coordinates. The inverse of this matrix is used to find the gravity components in each translational acceleration in the LCS.

$$A_{rot} = A_\alpha A_\beta A_\gamma A_\delta, \qquad \bar{x}_{GCS} = A_{rot}\bar{x}_{LCS}, \qquad g_{LCS} = {A_{rot}}^{-1} \begin{bmatrix} 0 \\ 0 \\ g \end{bmatrix} \tag{4.3}$$

The mean orientation of a sensor can be accounted for in α, β and γ. The filtered rotation time signals in the LCSs for roll, pitch and yaw (obtained from integrated velocities) can be accounted for in δ, β and γ respectively. An example (S2 sensor heave in LCS, governed by local pitch) is given in figure 4.10 below.

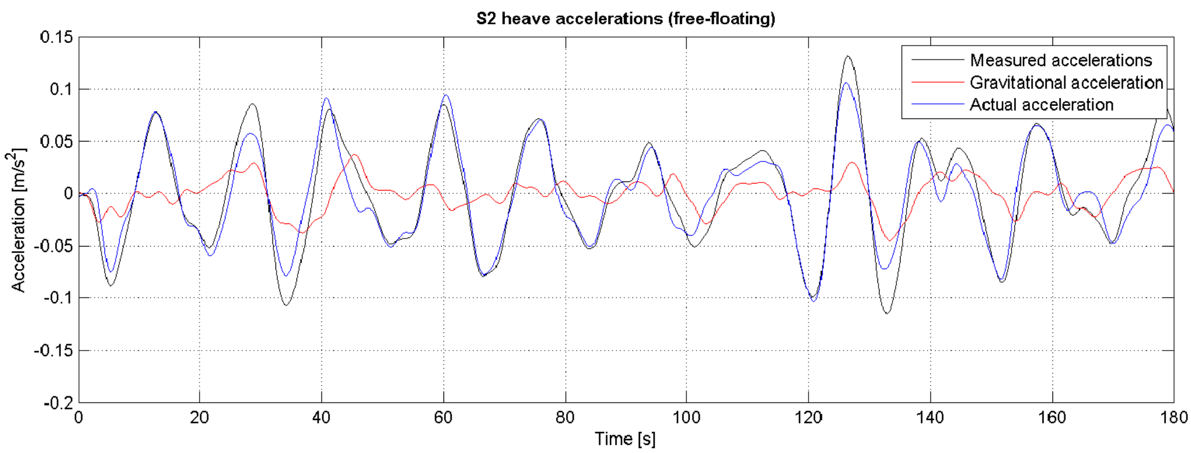

Figure 4.10: S2 sensor heave - Gravity deduction (free-floating)

4.3.3. Siri signals - Integration

The Siri signals contain translational accelerations and rotational velocities. These signals have to be integrated over time, two and one time(s) respectively. Two simple integration methods have been tested:

- Euler forward method: $x(n+1) = x(n) + \dot{x}(n+1)\Delta t$
- Central difference method: $x(n+1) = x(n) + \frac{(\dot{x}(n+2) + \dot{x}(n))}{2}\Delta t$

where Δt is the time step in between each sequential sample. The initial displacement or velocity ($x(0)$) is not known. The initial value was therefore set at 0, which results in an offset of the integrated signal. High-pass filtering then brings the mean signal back to zero. Both methods yield virtually the same results.

4.3.4. Siri signals - Transformation

In rigid body dynamics, rotations everywhere on a body are assumed to be the same. In order to obtain translations at a certain location on a body, the translations resulting from rotations have to be accounted for:

$$x_{PoI} = x_{sensor} + z_{arm} sin\theta - y_{arm} sin\psi \tag{4.4}$$
$$y_{PoI} = y_{sensor} - z_{arm} sin\phi + x_{arm} sin\psi \tag{4.5}$$
$$z_{PoI} = z_{sensor} + y_{arm} sin\theta - x_{arm} sin\phi \tag{4.6}$$

where x_{PoI}, y_{PoI} and z_{PoI} are the translations of the desired point, x_{sensor}, y_{sensor} and z_{sensor} are the translations at the sensor location and x_{arm}, y_{arm} and z_{arm} are the distances between the sensor and the PoI in the LCS.

Transformation has been used to obtain the topsides' and Thialf's CoG translations from Siri sensors S1 and S4 respectively, as well as for obtaining the motions of the topsides SB lift points. Plots of the obtained motion time traces are omitted from appendix D and given when relevant.

5
Motions & hook load comparison study

5.1. Introduction

The first part of this chapter covers the validation of Liftdyn modelled motions (and hook load fluctuations resulting from it). This roughly corresponds to assessing if root cause (1.), as explained in chapter 1, contributes to the observed discrepancy between modelled and measured hook load fluctuations. This validation is done by means of a comparison study of Liftdyn modelled motion and hook load fluctuations spectra (chapter 3) to measured motion and hook load fluctuations spectra (chapter 4).

The second part of this chapter concerns calculating hook load fluctuations, with measured main hoist elongations as input. If it is assumed these measurements and wire rope stiffness properties are accurate, this exercise roughly corresponds to checking for contributions of root causes (2.) and (3.) (as described in chapter 1) to the observed discrepancy between modelled and measured hook load fluctuations.

5.2. Measured vs. Liftdyn modelled - Motions & hook loads

In sections 5.2.1 to 5.2.4 below, for each lift stage considered the measured hook load spectrum ('Crane data' in legends) and the Liftdyn modelled hook load spectrum are plotted in the same figure, for both the SB and PS cranes. The measured hook load spectrum multiplied by ten has been plotted as well, for clarity (since measured hook load fluctuations are indeed much smaller than modelled fluctuations, i.e. the motive for this thesis). 3D (directional) and 2D (predominant direction) wave spectra, as measured by the WRB onsite, have been included as well. The 3D data was used for computing Liftdyn calculated responses according to equation 2.7. This data was available in 1° intervals, whereas wave forcing RAOs have been computed in 15° intervals. Mean spectral densities of each 15° interval were multiplied by the corresponding RAO (squared) in order to obtain modelled response spectra.

ALTERED/OMITTED FOR CONFIDENTIALITY REASONS: For plots of measured vs. Liftdyn modelled motions spectra for all DoFs (in LCS), bodies and stages, please refer to appendix E. These measured response spectra have been taken from time signals obtained according to the method described in chapter 4, using the theory explained in chapter 2.

For each lift stage, specific observations are given in the corresponding section. Observations that apply to all lift stages are discussed in chapter 7.

5.2.1. Free-floating stage

Hook load fluctuations

Peaks at ca. 0.4 - 0.45 rad/s observed in the Liftdyn calculated spectra correspond to the SB and PS blocks' pendulum motions (appendix B). In reality, the slack grommets (which have not been included in the model) will apply some damping and restoring forces on motions of the crane blocks. Hook load fluctuations during this stage are small, therefore they will not be further elaborated on in this thesis.

Motions

Measured vs. Liftdyn calculated motions are particularly interesting for the free-floating stage, since there is no mechanical coupling between the Thialf and H-542 yet. Specifically for this stage, the large discrepancies for roll and pitch of both the H-542 and Thialf are striking. For the Thialf, hardly any roll was measured, and measured peak pitch frequency is lower than the modelled peak frequency. For the H-542, spectral shapes roughly correspond, but measured roll and pitch amplitudes are around two times as large as those modelled.

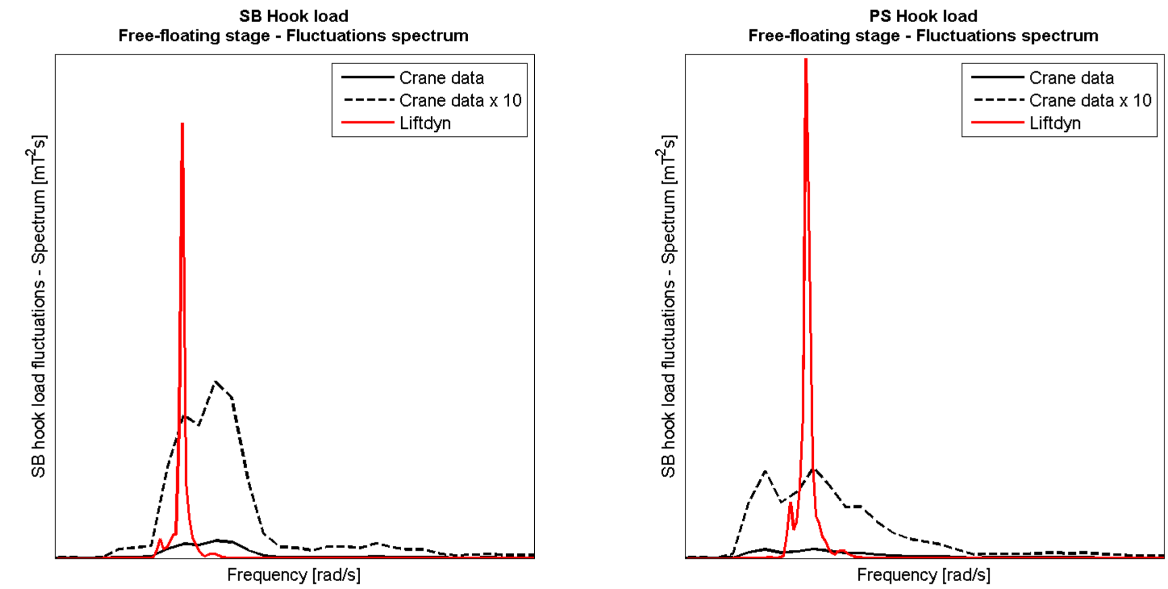

Figure 5.1: SB and PS hook load fluctuations spectra (free-floating stage)

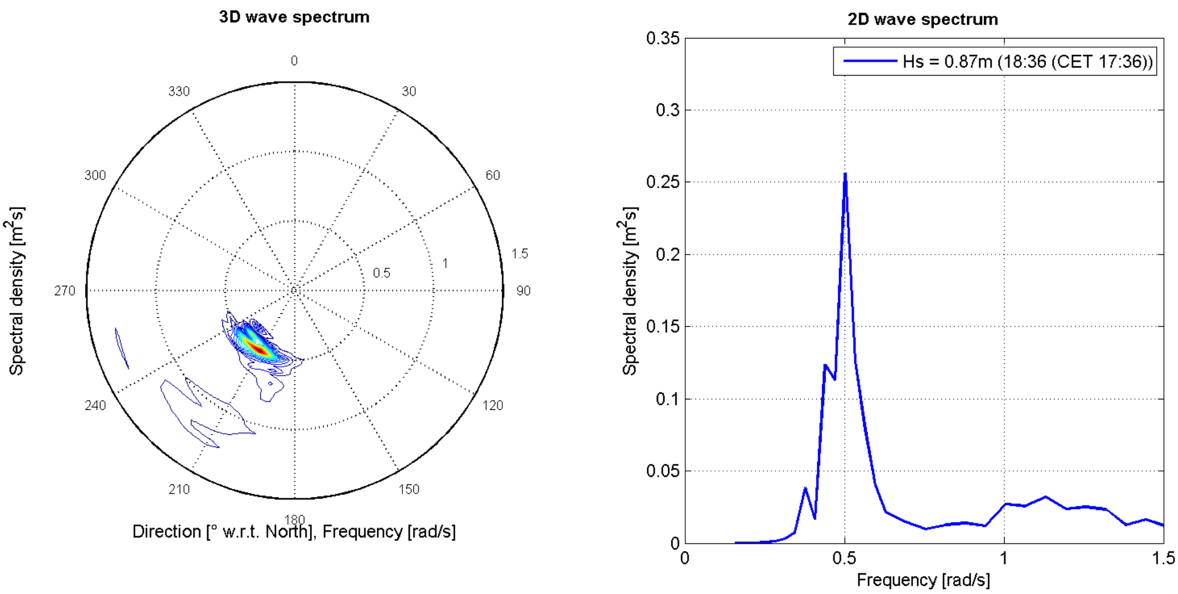

Figure 5.2: 3D and 2D wave spectra (free-floating stage)

5.2.2. Lift-off stage

Hook load fluctuations

This comparison is the original motive for this study. What is most striking is that there is no peak observed in the Liftdyn modelled SB hook load spectrum at 0.5 rad/s. Apparently, the modelled vertical motions of the SB main block and main fall at that frequency are in phase and of similar magnitude. The original observation - that modelled hook load fluctuations spectra overestimate those measured - holds.

Motions

Motions behaviour is similar to that during the free-floating stage, regarding roll and pitch motions for the Thialf and H-542. The Thialf's pitch spectral shapes better correspond to one another. For H-542 measured pitch motions however, a low frequency peak is present (at =0.2 rad/s) which was much smaller for the free-floating stage.

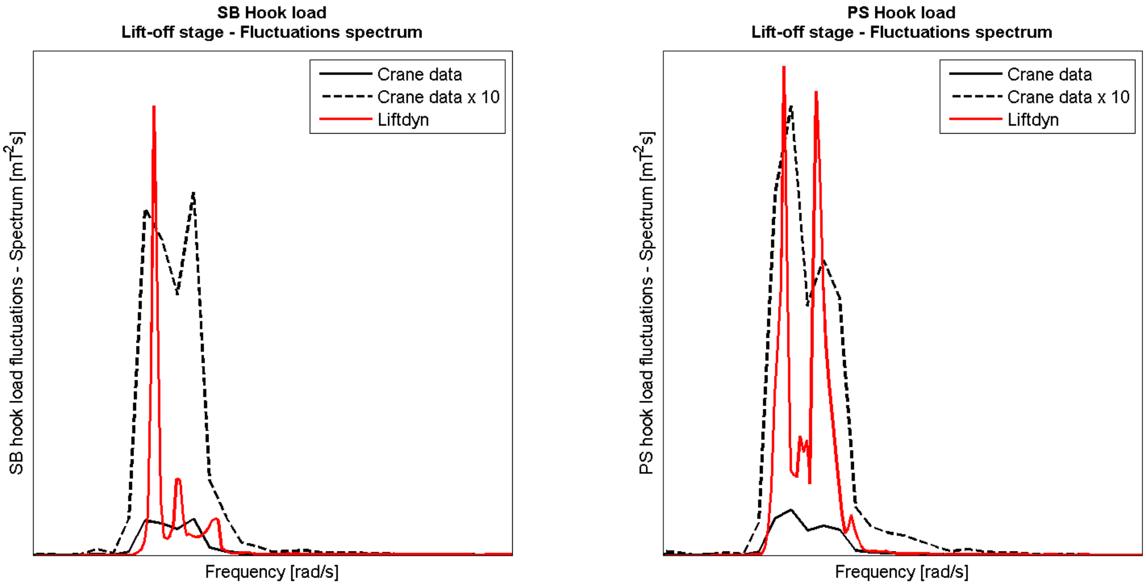

Figure 5.3: SB and PS hook load fluctuations spectra (lift-off stage)

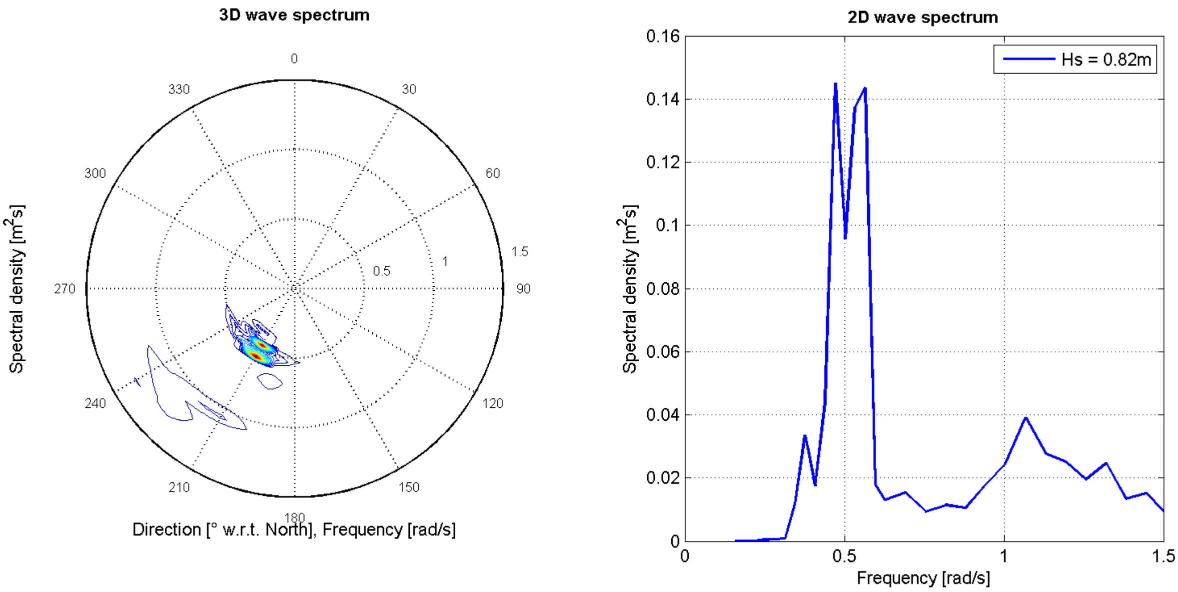

Figure 5.4: 3D and 2D wave spectra (lift-off stage)

5.2.3. Free-hanging stage

Hook load fluctuations

It becomes clear that a hook load discrepancy is not exclusive for the lift-off stage. During the free-hanging stage differences between modelled and measured hook load fluctuations are large as well. These can only be attributed to a relative motion of the topsides resulting from its own inertia and damping properties, since the topsides are not subject to wave forcing (through the H-542) anymore.

Motions

During the free-hanging stage, again, measured roll for the Thialf is much smaller than modelled roll. Most notably, the modelled peak at 0.45 rad/s is not measured. Other than this, overestimations of all topsides' DoFs except for heave are observed.

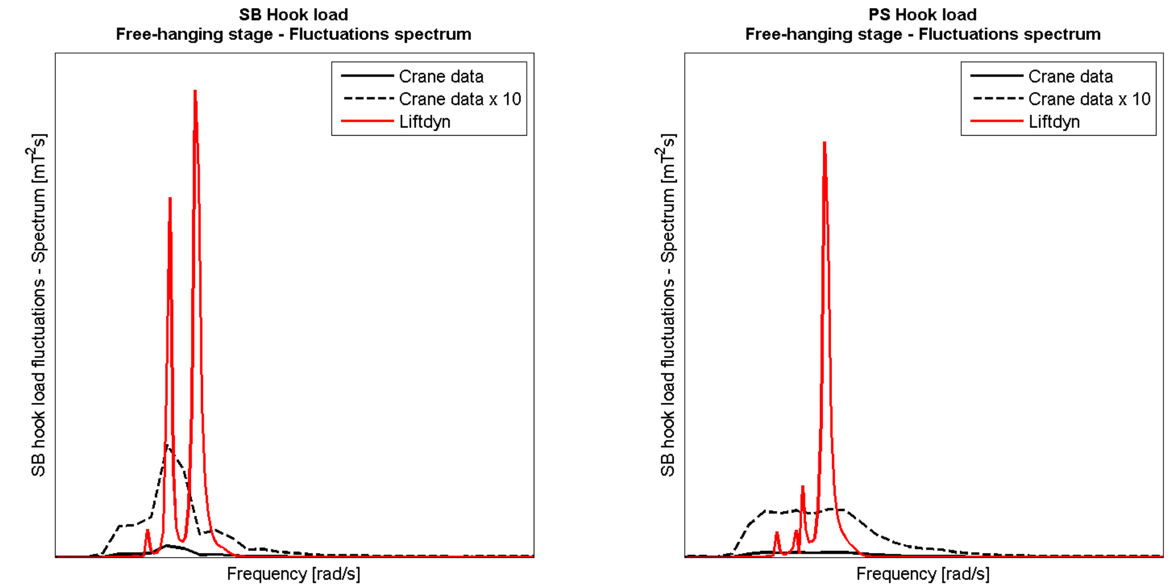

Figure 5.5: SB and PS hook load fluctuations spectra (free-hanging stage)

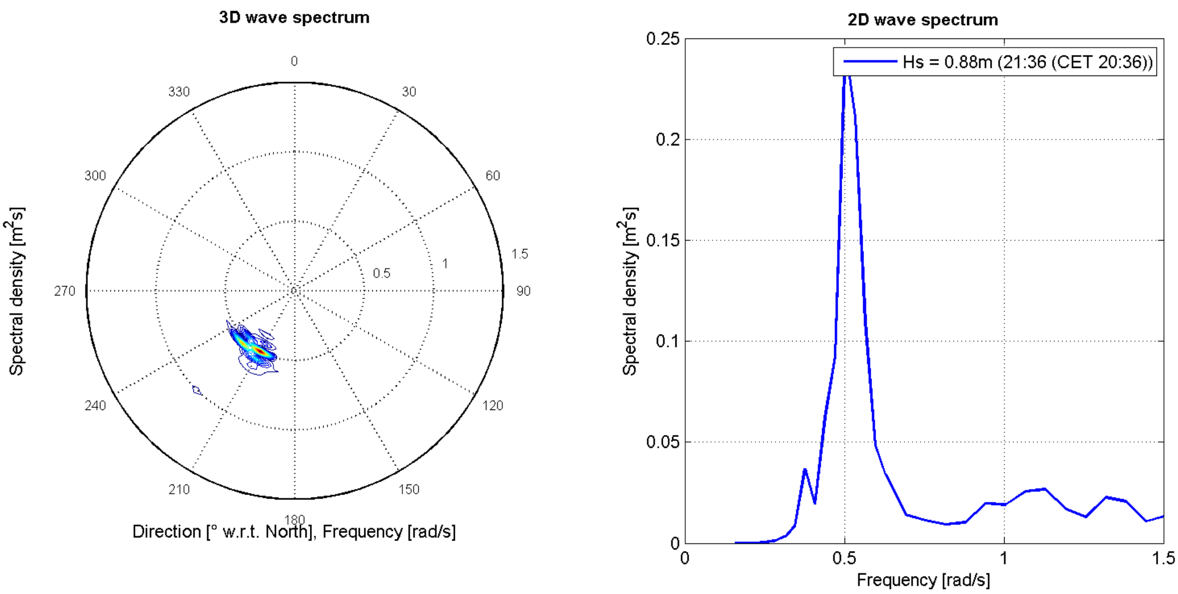

Figure 5.6: 3D and 2D wave spectra (free-hanging stage)

5.2.4. Set-down stage

Hook load fluctuations

As compared to the other lift stages, hook load fluctuations spectra during the set-down stage show more energy around 0.55 rad/s. This seems to be mainly caused by the Thialf's heave and roll motions, and since the topsides is fixed this leads to hook load fluctuations at the same frequency ranges.

Motions

The Thialf's translational response discrepancies are similar to those in the other stages. However, especially Thialf pitch response is highly underestimated in the model. A possible explanation for this could be the sudden decrease of hook load, which induces a natural pitch motion. A (near) stationary response will therefore, most probably, not have been reached for the set-down stage. The difference in Thialf pitch in turn leads to similar differences for the main fall's surge and heave directions.

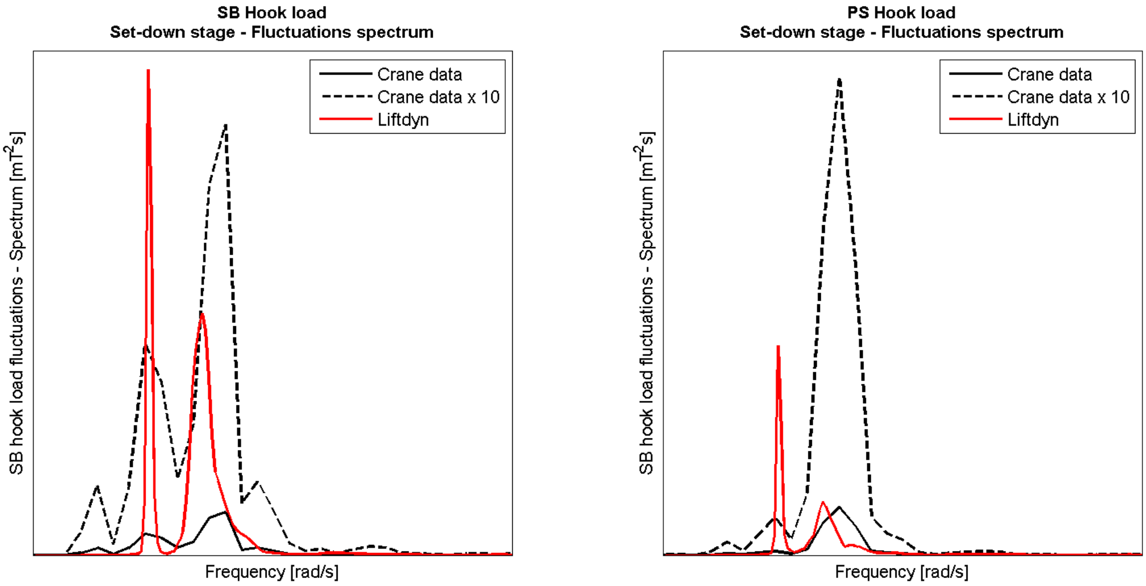

Figure 5.7: SB and PS hook load fluctuations spectra (set-down stage)

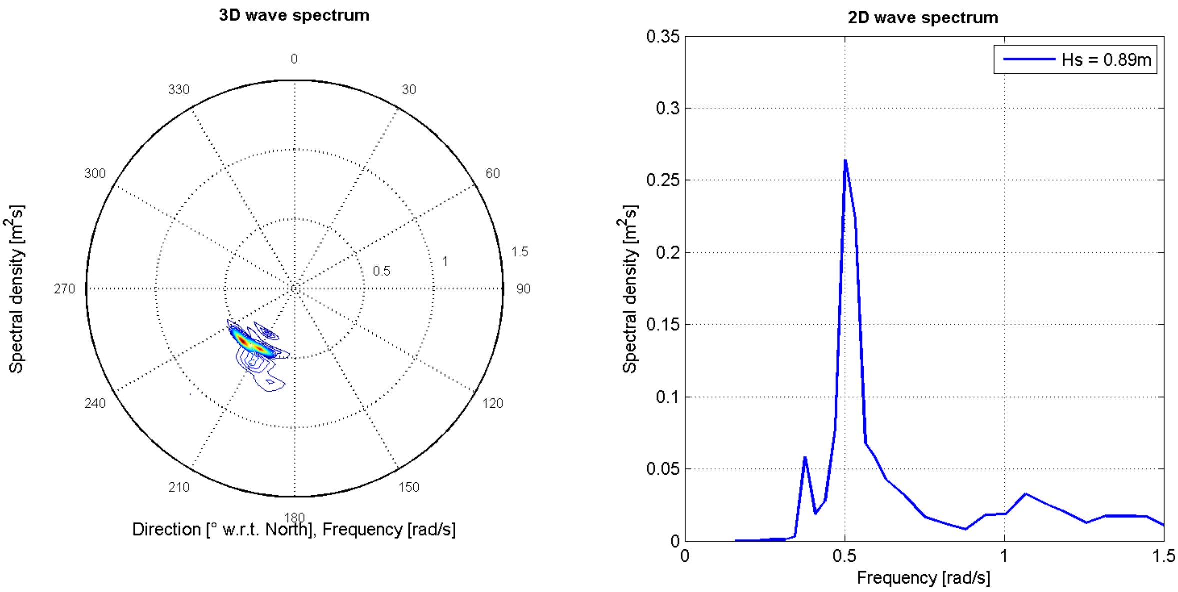

Figure 5.8: 3D and 2D wave spectra (set-down stage)

5.3. Measured vs. Calculated - Hook loads

As was demonstrated in the previous section, some modelled motion responses are more accurate than others. These inaccuracies can already give rise to discrepancies between modelled and measured hook load fluctuations, regardless of wire rope stiffness properties and hook load measurements being accurate. In order to check for discrepancy contributions thereof, modelled motion inaccuracies need to be taken out of the equation. To that end, dynamic hook loads that should occur in the SB main hoist are calculated using measured motions of sensors S1 (topsides) and S2 (main fall axle) as input. Assuming the reeved main hoist can be modelled by a linear spring, it is checked if hook load fluctuations calculated from the relative motions of these points correspond to measured hook load fluctuations.

If a discrepancy still holds after this comparison, contributions of root causes (2.) and (3.) as described in chapter 1 add to the overall discrepancy between measured and modelled hook load fluctuations.

5.3.1. Calculation method

Ideally, main hoist elongations are calculated using measurements at the SB main fall axle and directly at the SB main block. Unfortunately, this was not possible due to restricted accessibility and space (as explained in chapter 4). Therefore motion measurements of sensor S1 (topsides) have to be used as input for motions of the SB main block. The topsides is still assumed to be a rigid body. Since grommets have a certain elasticity (in the order of magnitude of the main hoist's elasticity), there will be relative motions of the main blocks with respect to the topsides. Moreover, the blocks have a significant mass (186 mT) which could induce main block oscillations relative to main fall and main block motions. The EoMs of the SB main block therefore need to be solved in order to obtain its position. Since all forces act on the same point on the block, only force equilibrium needs to hold:

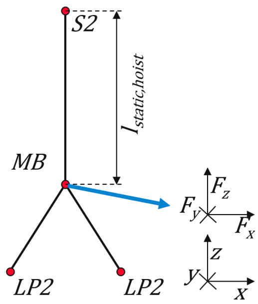

Figure 5.9: Force equilibrium - Main block

$$\begin{bmatrix} \Sigma F_x(t) \\ \Sigma F_y(t) \\ \Sigma F_z(t) \end{bmatrix} = \begin{bmatrix} 0 \\ 0 \\ 0 \end{bmatrix} \tag{5.1}$$

The natural periods for the SB main block surge and heave motions are under half a second for all stages (except for the free-floating stage, which is not relevant for this comparison; appendix B), as a result of high stiffnesses of the grommets and main hoist. Main hoist elongations are mostly in the order of 10 - 15 s. For simplicity's sake, the main blocks are therefore assumed to move quasi-statically with respect to main fall axle and main block motions. Damping is also negligible since motions are well out of the resonance region. Therefore, only spring term components (resulting from elasticity of the main hoist and grommets) to each DoF of the block need to be taken into account, and the position of the SB main block can be calculated as if it has reached static equilibrium for each timestep.

$$\begin{bmatrix} ((x_{LP1}-x_{MB})\alpha_{LP1}+(x_{LP2}-x_{MB})\alpha_{LP2})EA_{grom}+(x_{S2}-x_{MB})\alpha_{S2}EA_{hoist} \\ ((y_{LP1}-y_{MB})\alpha_{LP1}+(y_{LP2}-y_{MB})\alpha_{LP2})EA_{grom}+(y_{S2}-y_{MB})\alpha_{S2}EA_{hoist} \\ ((z_{LP1}-z_{MB})\alpha_{LP1}+(z_{LP2}-z_{MB})\alpha_{LP2})EA_{grom}+(z_{S2}-z_{MB})\alpha_{S2}EA_{hoist}-gM_{MB} \end{bmatrix} = \begin{bmatrix} 0 \\ 0 \\ 0 \end{bmatrix} \tag{5.2}$$

where x, y and z [m] are the global coordinates of the respective points, EA_{grom} and EA_{hoist} [kN] are the stiffnesses of the grommets and main hoist (given in chapter 3) and α_{point} [m^{-1}] determines the directional component of each force contribution, which is given below:

$$\alpha_{point} = \left(\frac{1}{\sqrt{(x_{point}-x_{MB})^2+(y_{point}-y_{MB})^2+(z_{point}-z_{MB})^2}} - \frac{1}{l_{static}} \right) \tag{5.3}$$

where l_{static} [m] is the static length of the grommet or main hoist (given in chapter 3). Positions of the main fall axle and lift points 1 and 2 are known for each time step. The position of the SB main block (x_{MB}, y_{MB} and z_{MB}) were solved according to this system of equations in Matlab. Finally, expected hoak load time traces are calculated by multiplying SB main hoist strain by its stiffness:

$$F_{hook}(t) = \left(\frac{\sqrt{(x_{S2}(t) - x_{MB}(t))^2 + (y_{S2}(t) - y_{MB}(t))^2 + (z_{S2}(t) - z_{MB}(t))^2}}{l_{hoist,static}} - 1 \right) EA_{hoist} \tag{5.4}$$

5.3.2. Results - All lift stages

Expected hook load fluctuations were calculated according to the method described in the section above for the lift-off, free-hanging and set-down stages. For motions of the main fall axle and lift points 1 and 2, several input time traces were tried:

- Motions obtained from the 'raw' sensor file (translational accelerations and rotational velocities)
- Motions obtained from the 'raw' sensor file; gravity component not accounted for (explained below)
- Motions obtained from the 'accelerations' sensor file (accelerations for all DoFs)

The resulting hook load fluctuations spectra are plotted over the measured spectra below for each stage considered. Findings and conclusions drawn from the spectral comparisons are given in chapter 7.

Results - Raw sensor file

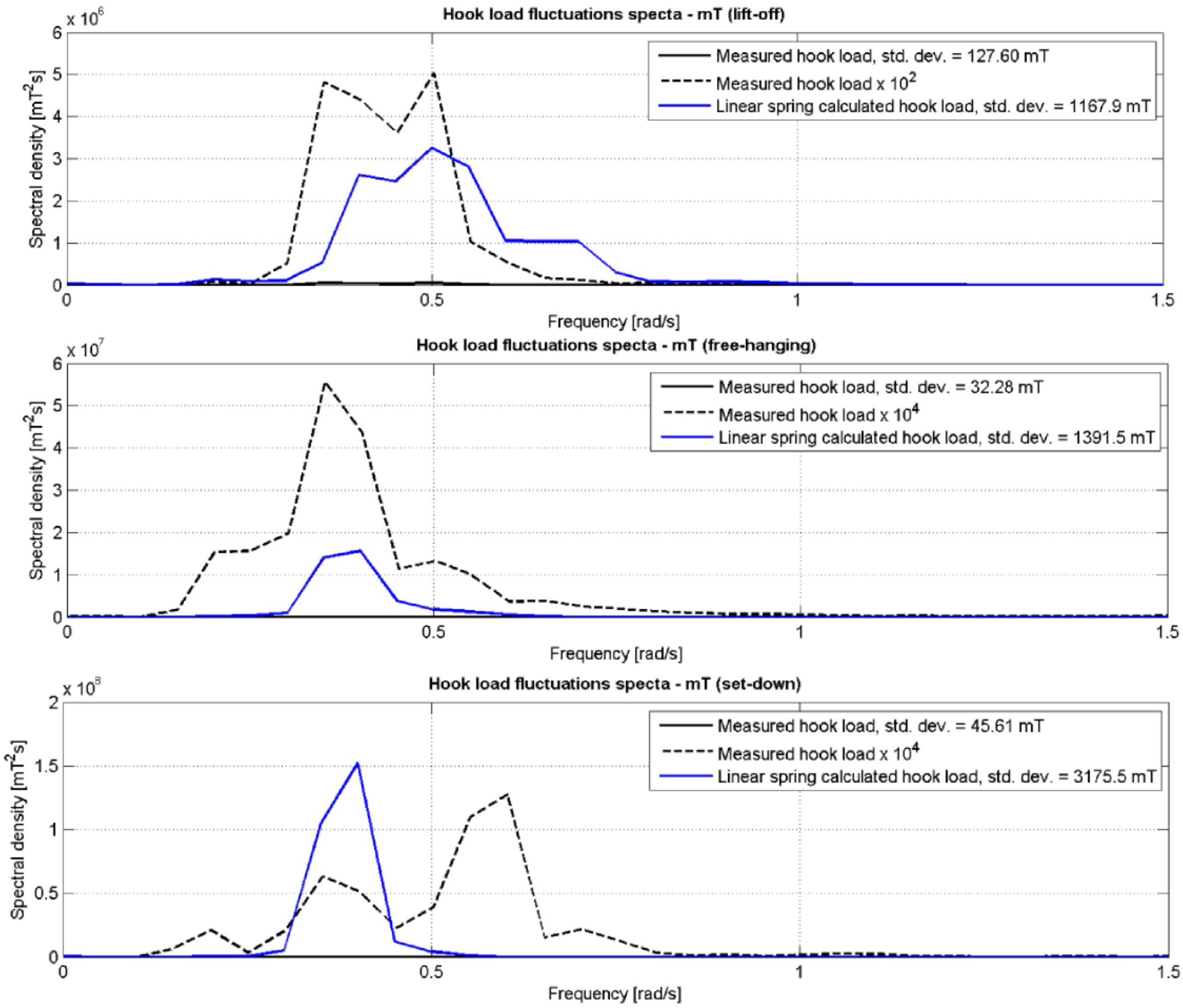

Figure 5.10: Measured vs. Calculated hook load fluctuations spectra - Raw sensor file

Results - Pre- vs. Post-accounting for gravity terms

As was demonstrated in chapter 4, gravity components in translational accelerations are not accurate. However, a sensor orientation change results in an increase of the gravity component in one or two translational directions, but a decrease thereof in the remaining direction(s). The total vertical gravity component will remain the same: g. Therefore, measured vertical acceleration fluctuations in the GCS, and thus hook load fluctuations should remain the same if gravity components have not been accounted for.

Indeed, this proves to be the case. Calculated hook load fluctuations spectra are virtually the same as those calculated with motion input files where gravity components were accounted for. Only small differences in standard deviation are observed: 1163, 1390 and 3174 mT as opposed to 1168, 1392 and 3176 mT for the lift-off, free-hanging and set-down stages respectively. These are attributed to numerical errors.

Spectra obtained for the case where gravity components were not accounted for are omitted, since differences with the spectra presented above are marginal.

Results - Accelerations sensor file

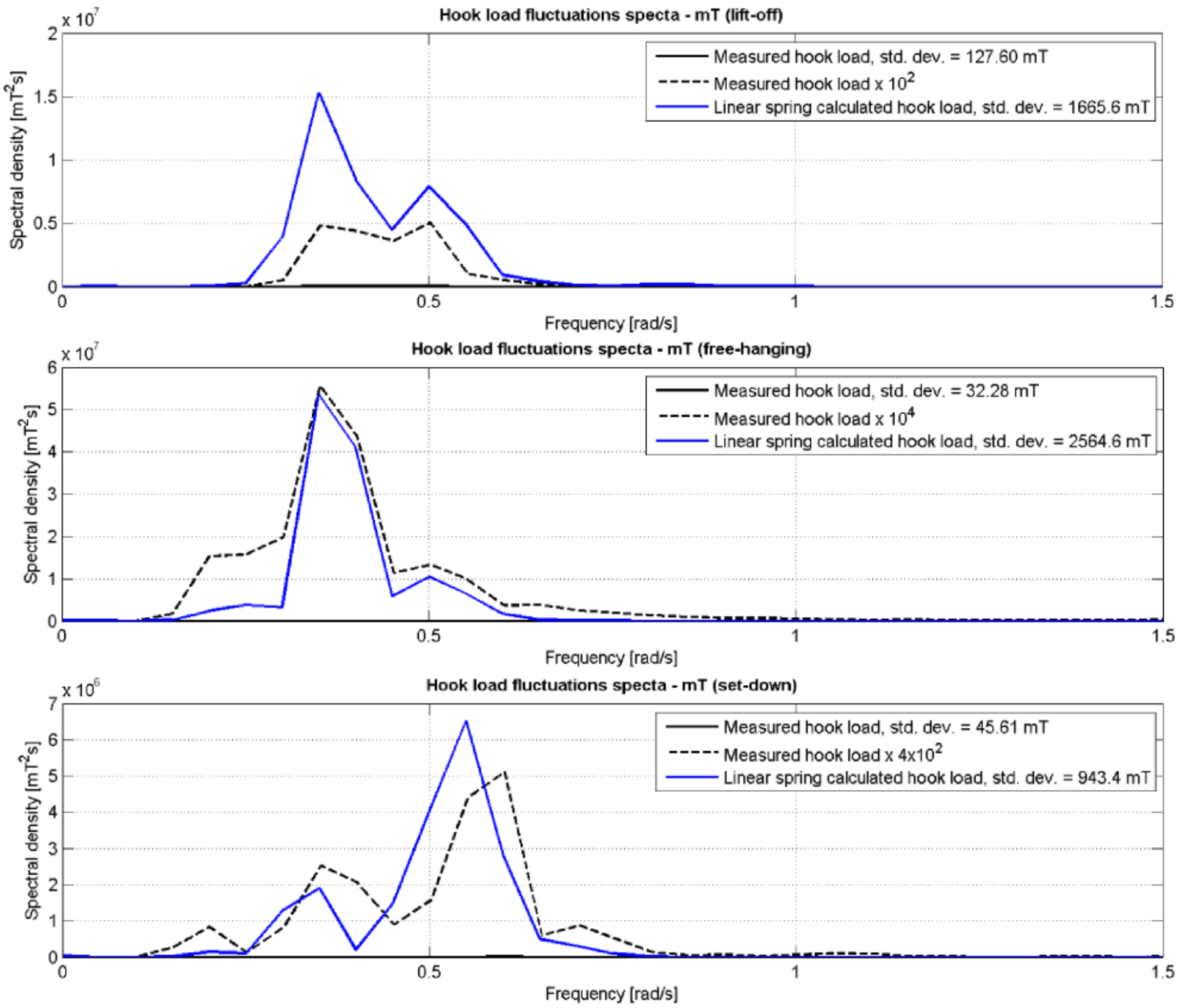

Figure 5.11: Measured vs. Calculated hook load fluctuations spectra - Accelerations sensor file

6

Obtaining elasticity & damping properties

6.1. Introduction

The original (and obvious) hypothetical explanation for the discrepancy between measured and modelled hook load fluctuations, was a wire rope stiffness overestimation in the models. In section 5.3 it was demonstrated that, if the Young's modulus of the hoist wire rope and grommets is 70 kN/mm^2 (wire rope stiffnesses are assumed to be roughly in between 70 [HMC, 2005] and 100 kN/mm^2 [Bridon, 2016]), calculated hook load fluctuations using measured motions are far greater than those measured. The factor by which they deviate is different for each lift stage. Also, these factors were considered to be too large to solely be attributed to a severe wire rope stiffness overestimation. However, it may well be that stiffness is lower than 70 kN/mm^2, and thus has a significant influence on force fluctuations. Furthermore, phasing between crane boom tip and topsides vertical motions implies an underestimation of wire rope damping properties in the models.

A suggested method for estimating more accurate (linearized) stiffness and damping properties for the wire rope sections in the crane system is presented in this chapter.

6.2. Elasticity - Modes during free-hanging stage

6.2.1. Simplified 2DoF dynamic model

An indication of the stiffness properties of the crane boom suspension wires, and the main hoist and grommets (combined), can be obtained from a simplified model of the crane and topsides during the free-hanging stage. Measured natural frequencies of topsides heave and boom pitch motions are used as input. A schematic representation of this model is given in figure 6.1 below:

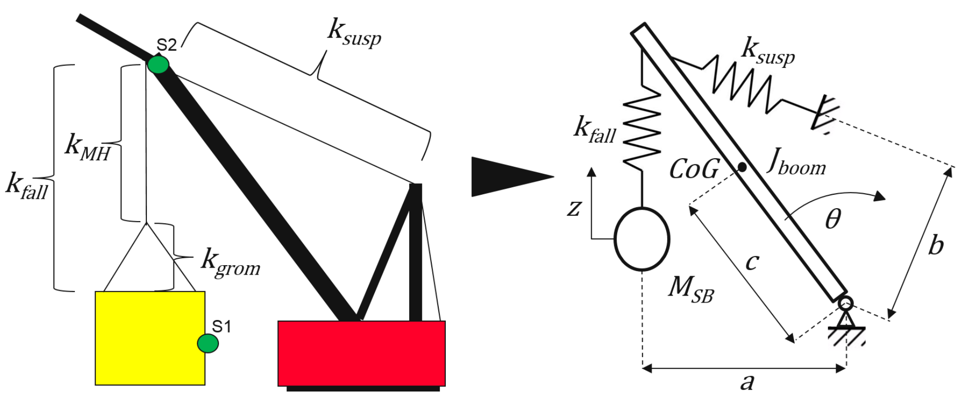

Figure 6.1: 2DoF crane model - Free-hanging stage

Only two DoFs have been included: vertical motions z[m] of the topsides, and boom rotations θ[rad] in-plane with the main hoist, grommets and boom suspension wires. The other DoFs have a marginal influence on the mode shapes searched for. Furthermore, it is assumed there are no imposed motions of the crane base (resulting from vessel motions), which is not the case in reality. The mode shapes searched for are expected to be well out of the range of vessel motions however, so this is deemed appropriate for the purpose of this exercise. The EoMs of this simplified system are as follows:

$$\begin{bmatrix} M_{SB} & 0 \\ 0 & J_{boom} \end{bmatrix} \begin{bmatrix} \ddot{z} \\ \ddot{\theta} \end{bmatrix} + \begin{bmatrix} k_{fall} & -ak_{fall} \\ -ak_{fall} & a^2 k_{fall} + b^2 k_{susp} - cM_{boom} g \end{bmatrix} \begin{bmatrix} z \\ \theta \end{bmatrix} = \begin{bmatrix} 0 \\ 0 \end{bmatrix} \tag{6.1}$$

Substituting a general solution for z and θ (with amplitudes $\hat{z}$ and $\hat{\theta}$) and then superpositioning the mass and stiffness matrices yields the following system:

$$\begin{bmatrix} k_{fall} - M_{SB}\omega^2 & -ak_{fall} \\ -ak_{fall} & a^2 k_{fall} + b^2 k_{susp} - cM_{boom} g - J_{boom}\omega^2 \end{bmatrix} \begin{bmatrix} \hat{z} \\ \hat{\theta} \end{bmatrix} = \begin{bmatrix} 0 \\ 0 \end{bmatrix} \tag{6.2}$$

A non-trivial solution to this system only exists when its determinant equals zero:

$$(k_{fall} - M_{SB}\omega^2)(a^2 k_{fall} + b^2 k_{susp} - cM_{boom} g - J_{boom}\omega^2) - a^2 k_{fall}^2 = 0 \tag{6.3}$$

$$M_{SB} J_{boom}\omega^4 - (M_{SB}(a^2 k_{fall} + b^2 k_{susp} - cM_{boom} g) + J_{boom} k_{fall})\omega^2 + k_{fall}(b^2 k_{susp} - cM_{boom} g) = 0 \tag{6.4}$$

The solutions for ω_1^2 and ω_2^2 are then given by the equations below:

$$\omega_1^2 = \frac{-B - \sqrt{B^2 - 4AC}}{2A}; \quad \omega_2^2 = \frac{-B + \sqrt{B^2 - 4AC}}{2A} \tag{6.5}$$

where

$$A = M_{SB} J_{boom}; \quad B = -(M_{SB}(a^2 k_{fall} + b^2 k_{susp} - cM_{boom} g) + J_{boom} k_{fall}); \quad C = k_{fall}(b^2 k_{susp} - cM_{boom} g) \tag{6.6}$$

Measured acceleration signal spectra are searched for spectral peaks, which correspond to modes ω_1 [rad/s] and ω_2 [rad/s]. Values for all other parameters in these equations are presented in table 6.1 to the right. M_{SB} is the mass suspended from the SB crane. The rotational inertia of the boom around its hinge, J_{boom}, is approximated as if its mass is distributed evenly along its length ($J = \frac{1}{3}Ml^2$, where M and l are the boom's mass and length). Arms a and b follow from crane geometry (section 3.3.2)

Table 6.1: 2DoF dynamic model parameters

Parameter	**Value**	**Unit**
M_{SB}	3000	mT
J_{boom}	$4.988 \cdot 10^6$	mTm^2
a	37.7	m
b	44.3	m

Thus, k_{fall} [kN/m] and k_{susp} [kN/m] are the only remaining unknowns in these two equations (6.5) and the system can be solved.

6.2.2. Supposed modes & Corresponding stiffnesses

Unfiltered raw acceleration signals are searched for natural frequencies. Sensor S1 local heave natural frequencies can be used as input for $z[\omega]$. Sensor S2 local heave natural peaks correspond to crane boom pitch rotations if the crane boom is assumed to be rigid. Since translational accelerations measured contain much less noise than rotational velocity measured signals, the S2 local heave accelerations signal is therefore searched for response peaks used as input for $\theta[\omega]$. Sensor S1 and S2 local heave acceleration spectral densities (during the free-hanging stage) are depicted in blue in figure 6.2 below, for a frequency range between 3 and 12 rad/s. The modes searched for should be within this range, for wire rope elasticities to have a plausible value.

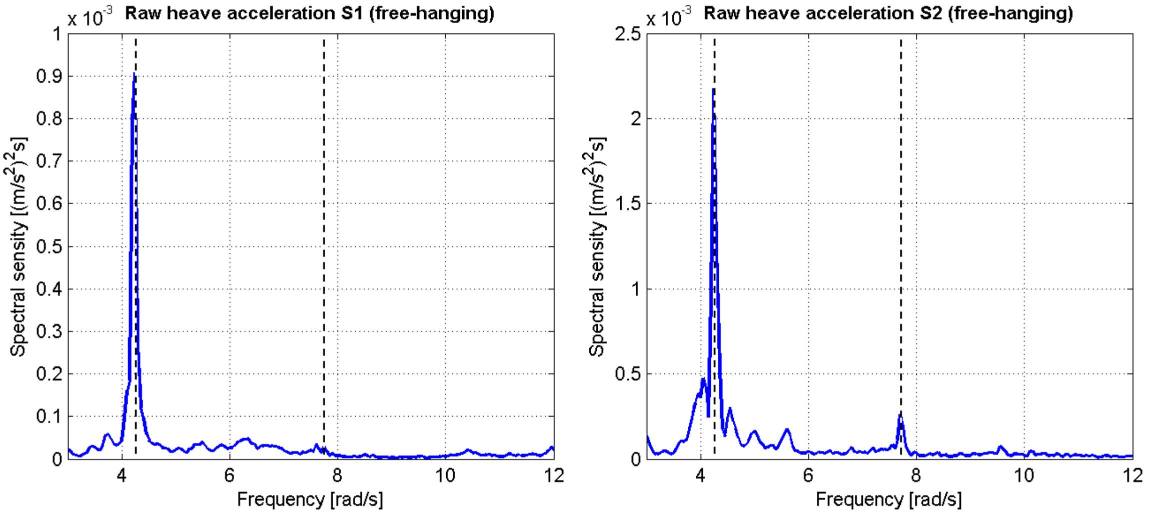

Figure 6.2: S1 (left) & S2 (right) local heave accelerations spectra - Natural frequencies (free-hanging)

A response peak at ca. 4.25 rad/s is quite apparent for both signals. From the Liftdyn model of the free-hanging stage (using a Young's modulus of 70 GPa for all wire rope sections), followed a topsides natural heave frequency of ca. 4.2 rad/s and a crane boom natural pitch frequency of ca. 9.7 rad/s. Therefore it is likely that the 4.25 rad/s response peak is due to the natural heave frequency of the topsides. That this peak is larger for the S2 local heave signal than for the S1 local heave signal follows from the fact that the S2 sensor is inclined, at ca. 65°. If the main hoist and grommets system would be completely rigid, S2 local heave amplitudes would have to be approximately $\frac{\cos 65°}{1} \approx 2.4$ times as high as those of S1. The spectral response peaks measured correspond to maximum acceleration amplitudes of roughly $\sqrt{2 \cdot 0.9 \cdot 10^{-3}}$ m/s^2 and $\sqrt{2 \cdot 2.2 \cdot 10^{-3}}$ m/s^2 for sensors S1 and S2 respectively. This yields a ratio of ca. $\frac{\sqrt{2 \cdot 0.9 \cdot 10^{-3}}}{\sqrt{2 \cdot 2.2 \cdot 10^{-3}}} \approx 1.6$, which is smaller than 2.4 due to elasticity of the main hoist and grommets and inertia of the boom. Response peaks that could correspond to the natural pitch motion of the SB boom are less explicit. Since this frequency is expected to be much higher than the natural heave frequency of the topsides, topsides response to natural pitch motions of the boom should be minimal. Vice versa, the pitch response of the boom to the natural heave motion of the topsides should be almost in the quasi-static region. This is confirmed by the response at 4.25 rad/s in the boom's local heave signal, as demonstrated above. A response peak in the boom's local heave spectrum is observed at ca. 7.75 rad/s, which is present much less so in the topsides local heave spectrum. This peak could be due to the natural pitch motion of the boom.

Frequencies 4.25 rad/s and 7.75 rad/s are substituted for ω_1 and ω_2 in equations 6.5 in order to solve for k_{fall} and k_{susp}. However, this simplified system cannot be solved for the supposed natural frequencies found in the measured signals. Apparently no combination of k_{fall} and k_{susp} exists for which the roots of equation 6.4 are equal to 4.25^2 and 7.75^2. A simplified Liftdyn model has been developed, which is exactly the same as the 2DoF model presented in figure 6.1. A wire rope elasticity of 70 GPa has been used for all connectors in this model. Solving equations 6.5 for natural frequencies obtained from the Liftdyn model (3.42 and 9.09 rad/s respectively) yields values for k_{fall} and k_{susp} which correspond to elasticities of 70 GPa. Hence, the Liftdyn model and model presented in figure 6.1 are cross-checked and verified. Unfortunately, it therefore has to be concluded that no mistakes have been made and this combination of natural frequencies cannot exist for this 2DoF model. Model parameters should be accurate, since masses and geometries are known quite well. Therefore the only remaining explanation for the system not being solvable is that the response peaks found at 4.25 and 7.75 rad/s are not caused by mode shapes.

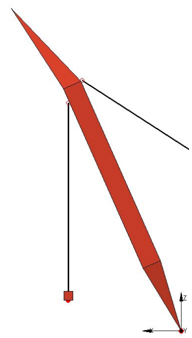

Figure 6.3: 2DoF Liftdyn model - Free-hanging stage

The peak observed at 4.25 rad/s was observed for other measured signals as well. For instance, the peak was observed in the topsides heave signal during the free-floating and lift-off stages, although a factor ten smaller (peak at ca. $1 \cdot 10^{-4}$ $(m/s^2)^2 s$). During these stages the natural heave motion of the free-hanging topsides cannot exist. Even though the spectral density peak is a factor ten larger during the free-hanging stage, chances therefore are that this peak is due to something else than the topsides natural heave motion. Regarding the natural pitch motion of the boom, no other explicit response peaks were found within a frequency range that makes equations 6.5 solvable, using 4.25 rad/s as input for the topsides natural heave frequency. Unfortunately, stiffness properties for k_{fall} and k_{susp} can therefore not be obtained using the measurements available.

If k_{fall} and k_{susp} would have been obtained, the equivalent stiffness k_{fall} could easily have been split in k_{hoist} and k_{grom} for the main hoist and grommets respectively. Both the main hoist and boom suspension are made up of a reeved system of the same type of wire rope, therefore it can be assumed that they have the same Young's modulus. Since there are 80 and 56 single wire ropes in their cross-sections respectively, the following relation between k_{hoist} and k_{susp} can be obtained:

$$E_{hoist} = E_{susp} \tag{6.7}$$

$$\frac{k_{hoist} l_{hoist}}{A_{hoist}} = \frac{k_{susp} l_{susp}}{A_{susp}} \tag{6.8}$$

$$k_{hoist} = \frac{80}{56} \frac{k_{susp} l_{susp}}{l_{hoist}} \approx 2.33 k_{susp} \tag{6.9}$$

Now that k_{hoist} is known, k_{grom} can simply be deduced from the relation of equivalent spring stiffness, since k_{fall} is known:

$$\frac{1}{k_{fall}} = \frac{1}{k_{hoist}} + \frac{1}{k_{grom}} \tag{6.10}$$

$$k_{grom} = \frac{k_{hoist} k_{fall}}{k_{hoist} - k_{fall}} \tag{6.11}$$

6.2.3. Alternative elasticity estimations

Wire rope elasticity has been set at 70 GPa for all wire rope sections in the models used. However, other sources within HMC propose using an elasticity of 35 GPa for grommets, and 100 GPa for the main hoist and boom suspension wires [HMC, 2005].

A possible explanation for this could be that grommets are often loaded relatively lightly, due to safety factors and availability of used grommets. This is true for the grommets used during the project considered in this study. As a result of the strands in the grommet being able to settle against each other, the stiffness of these relatively lightly loaded grommets can be lower. Moreover, loading history of these grommets is not known. In figure 6.4, a stress over strain graph is depicted of the first three load cycles of a new wire rope (30mm Outer Diameter (OD)). It is quite clear that on initial loading, stiffness is substantially lower (and non-linear), especially for relatively low loading (with respect to the wire rope's Minimum Breaking Load (MBL)). Nonlinearities are expected to remain even after initial loading for relatively low loading (under 10-15% of the MBL), so linearized stiffnesses could be much lower than that observed in between 25-50% in this test [Bridon, 2016].

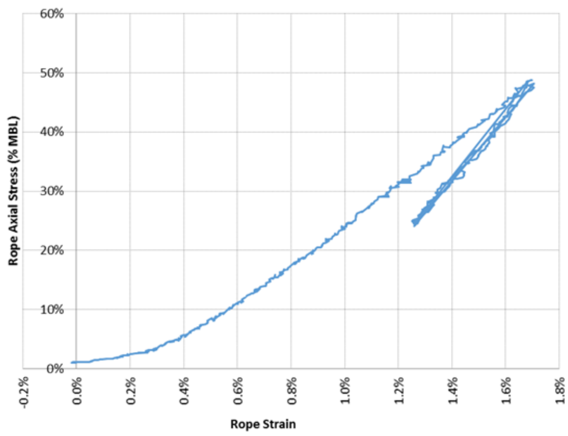

Figure 6.4: 30mm OD wire rope - Stiffness test [Bridon, 2016]

Wire rope (initial) cross-sectional elasticities are obtained from figure 6.4 by taking the derivatives of the curve at the proper relative loading level, and divided by the connector's cross-section A in order to obtain a Young's modulus for each connector:

$$E_i = \frac{1}{A}\frac{dT}{d\epsilon} \tag{6.12}$$

where E_i [GPa] is the Young's modulus corresponding to initial loading, A [mm^2] is the connector's cross-sectional area, T [kN] is the mean tension in the connector and ϵ [m/m] is strain. The linearized initial elasticity properties of all wire rope elements in the system corresponding to the relation presented in figure 6.4 are given in table 6.2 below.

Table 6.2: Wire ropes & grommet elasticities - From stiffness test [Bridon, 2016]

Stage	**Connector**	T **[kN]**	MBL **[kN]**	T/MBL **[%]**	EA **[kN]**	A **[mm^2]**	E_i **[GPa]**
Lift-off (65%)	SB grommets	$1.04 \cdot 10^4$	$2.56 \cdot 10^5$	4.1	$4.90 \cdot 10^6$	$1.24 \cdot 10^5$	39.5
	PS grommets	$7.92 \cdot 10^3$	$1.78 \cdot 10^5$	4.4	$4.00 \cdot 10^6$	$7.38 \cdot 10^4$	54.2
	SB main hoist	$2.10 \cdot 10^4$	$2.59 \cdot 10^5$	8.1	$7.31 \cdot 10^6$	$1.05 \cdot 10^5$	69.6
	PS main hoist	$1.65 \cdot 10^4$	$2.59 \cdot 10^5$	6.4	$6.73 \cdot 10^6$	$1.05 \cdot 10^5$	64.1
	SB suspension	$1.97 \cdot 10^4$	$1.81 \cdot 10^5$	10.9	$5.42 \cdot 10^6$	$7.37 \cdot 10^4$	73.5
	PS suspension	$1.65 \cdot 10^4$	$1.81 \cdot 10^5$	9.1	$5.11 \cdot 10^6$	$7.37 \cdot 10^4$	69.3
Free-hanging (100%)	SB grommets	$1.60 \cdot 10^4$	$2.56 \cdot 10^5$	6.3	$6.74 \cdot 10^6$	$1.24 \cdot 10^5$	54.3
	PS grommets	$1.22 \cdot 10^4$	$1.78 \cdot 10^5$	6.9	$4.75 \cdot 10^6$	$7.38 \cdot 10^4$	64.3
	SB main hoist	$3.13 \cdot 10^4$	$2.59 \cdot 10^5$	12.1	$8.23 \cdot 10^6$	$1.05 \cdot 10^5$	78.3
	PS main hoist	$2.44 \cdot 10^4$	$2.59 \cdot 10^5$	9.4	$7.59 \cdot 10^6$	$1.05 \cdot 10^5$	72.3
	SB suspension	$2.71 \cdot 10^4$	$1.81 \cdot 10^5$	15.0	$5.47 \cdot 10^6$	$7.37 \cdot 10^4$	74.2
	PS suspension	$2.22 \cdot 10^4$	$1.81 \cdot 10^5$	12.3	$5.47 \cdot 10^6$	$7.37 \cdot 10^4$	74.2
Set-down (40%)	SB grommets	$6.42 \cdot 10^3$	$2.56 \cdot 10^5$	2.5	$2.99 \cdot 10^6$	$1.24 \cdot 10^5$	24.1
	PS grommets	$4.87 \cdot 10^3$	$1.78 \cdot 10^5$	2.7	$2.25 \cdot 10^6$	$7.38 \cdot 10^4$	30.4
	SB main hoist	$1.36 \cdot 10^4$	$2.59 \cdot 10^5$	5.2	$5.89 \cdot 10^6$	$1.05 \cdot 10^5$	56.1
	PS main hoist	$1.09 \cdot 10^4$	$2.59 \cdot 10^5$	4.2	$4.91 \cdot 10^6$	$1.05 \cdot 10^5$	46.7
	SB suspension	$1.44 \cdot 10^4$	$1.81 \cdot 10^5$	8.0	$4.92 \cdot 10^6$	$7.37 \cdot 10^4$	66.7
	PS suspension	$1.25 \cdot 10^4$	$1.81 \cdot 10^5$	6.9	$4.53 \cdot 10^6$	$7.37 \cdot 10^4$	61.4

Mean relative loading of the grommets during this project was well under 7% of their MBLs during the free-hanging stage, which is the stage during which mean wire connector tensions are the highest. Grommet plastic and elastic properties are therefore assumed to follow the non-linear behaviour observed in figure 6.4 for all stages considered, regardless of loading history. The main hoist and boom suspension wires have been replaced in April '15 and June '14 respectively. Several very heavy lifts (ca. 8,000 - 10,000 mT, which corresponds to ca. 4,500 mT per crane) have been conducted since then, which means the wire ropes have been subject to tensions of ca. 20% of their MBL several times when this project was executed in January '16. Higher linear elasticities than those observed for the initial load cycle in figure 6.4 can therefore be expected.

The more or less linear stiffness behaviour for load cycles two and three, observed between ca. 25-50% of MBL in figure 6.4, corresponds to a Young's modulus of ca. 135 GPa. Stiffness tests with multiple load cycles in between 5-15%, which is the range of relative loads of the main hoist and boom suspension wires for all stages considered, are not available unfortunately. However, mean relative loading of the main hoist and boom suspension wires are under 15% of their MBLs during the free-hanging stage. Non-linearities, or linearized stiffnesses smaller than those observed in between 25%-50% of MBL in figure 6.4, are therefore very likely for all stages considered. A linearized Young's modulus of 100 GPa, as proposed by one source in [HMC, 2005], might therefore be a good approximation for engineering purposes.

6.3. Damping - Topsides time trace modelling during free-hanging stage

6.3.1. Simplified 1DoF dynamic model

There is a slight phase lag of the topsides vertical motions behind the vertical motions of the main fall axle during the free-hanging stage. This can be observed in figure F.7 in appendix F. In the Liftdyn models, phase lag between these motions is nearly zero, for all frequencies. This implies that damping properties might be substantially underestimated in the models.

In an attempt to obtain more accurate damping properties of the main hoist and grommets as a system, a simplified 1DoF model of the the topsides hanging of the SB crane during the free-hanging stage has been set up. This model representation only has a single DoF: topsides vertical motions z. Measured vertical motions of the crane boom tip (z_{fall}) are imposed on a mass-spring-damper system, where the mass M_{SB} is the topsides component suspended from the SB crane (same as M_{SB} in figure 6.3) and k_{fall} and c_{fall} are the equivalent stiffness and damping of the main hoist, main block and grommets combined. A schematic representation of this system is depicted in figure 6.5 (right).

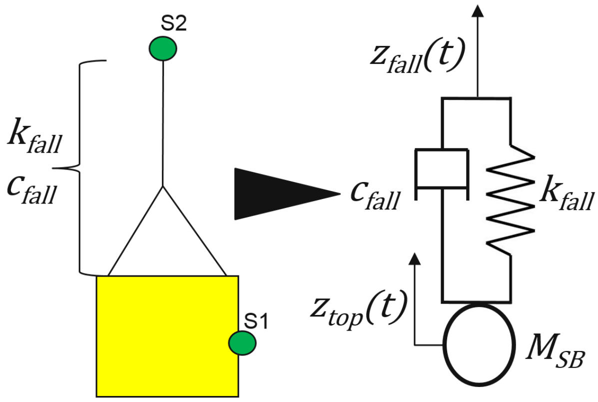

Figure 6.5: 1DoF crane model - Free-hanging stage

The state-space representation of the EoM of this mass-spring-damper system is given below:

$$\begin{bmatrix} \dot{z} \\ \ddot{z} \end{bmatrix} = \begin{bmatrix} 0 & 1 \\ -\frac{k_{fall}}{M_{SB}} & -\frac{c_{fall}}{M_{SB}} \end{bmatrix} \begin{bmatrix} z \\ \dot{z} \end{bmatrix} + \begin{bmatrix} 0 \\ \frac{k_{fall}}{M_{SB}} z_{fall}(t) \end{bmatrix} \tag{6.13}$$

Initial values for z and $\dot{z}$ are taken from the measured topsides vertical motions signal. $\ddot{z}$ on this time instant can be derived from equation 6.13, which can be integrated using an Ordinary Differential Equation (ODE) solver in Matlab in order to obtain z and $\dot{z}$ for the next time step. Thus, the modelled topsides vertical motions response to an imposed motions time trace $z_{fall}(t)$ at the boom tip is modelled. The purpose is to model topsides vertical motions $z(t)$ such that they best correspond to measured topsides vertical motions. To that end, damping values c_{fall} are varied in order to obtain a minimal phase lag between measured and modelled topsides vertical motions. M_{SB} = 3000mT, and k_{fall} can be obtained from equation 6.10, using values for k_{grom} and k_{hoist} corresponding to elasticities found in section 6.2.3:

$$k_{fall} = \frac{k_{hoist} k_{grom}}{k_{hoist} + k_{grom}} \tag{6.14}$$

During the free-hanging stage, main hoist and boom suspension Young's moduli for initial loading are 70-80 GPa, as opposed to 135 GPa for a well bedded and relatively heavily loaded wire rope. Since the wire ropes are relatively lightly loaded, a Young's modulus of 100 GPa is taken for the main hoist and boom suspension in accordance with [HMC, 2005]. This yields a main hoist stiffness of $k_{hoist} = \frac{E_{hoist} A_{hoist}}{l_{hoist}} \approx \frac{100 \cdot 1.05 \cdot 10^5}{44.4} \approx 2.36 \cdot 10^5 kN/m$. For the two grommet connectors, of which are at an angle $\alpha \approx 21°$ w.r.t. to vertical, the following equivalent stiffness in vertical direction can be derived:

$$k_{grom} = 2 \cos\alpha \frac{E_{grom} A_{grom}}{l_{grom}} \approx 2 \cos 21° \frac{6.74 \cdot 10^6}{23.4} \approx 5.38 \cdot 10^5 kN/m \tag{6.15}$$

Substituting k_{hoist} and k_{grom} in equation 6.14 yields the following equivalent stiffness:

$$k_{fall} = \frac{2.36 \cdot 10^5 5.38 \cdot 10^5}{2.36 \cdot 10^5 + 5.38 \cdot 10^5} \approx 1.64 \cdot 10^5 kN/m \tag{6.16}$$

6.3.2. Modelled time trace - 'Raw' vs. 'Accelerations' sensor file

As was explained in chapters 4 and 5, some haziness exists as to which of two measured signals of each motions sensor is most accurate. However, it was noticed that for the 'accelerations' signal vertical motions of the topsides are generally larger than those of the main fall axle during the free-hanging stage. Since topsides motions are mainly governed by imposed motions at the crane boom tip, this implies topsides motions are excited by these motions. For that to be the case, the equivalent stiffness of the main hoist and grommets combined would have to be such that resonance can occur. This means the stiffness of the main hoist and grommets combined k_{fall} has to be around $M_{SB}\omega^2$, where ω [rad/s] is the wave frequency at which the topsides vertical motions are most excited.

Using the 1DoF model depicted in figure 6.5 and described by equation 6.13, it is possible to achieve similar resonant topsides behaviour as that registered in the 'accelerations' measured signal. This is demonstrated in figure 6.6 below:

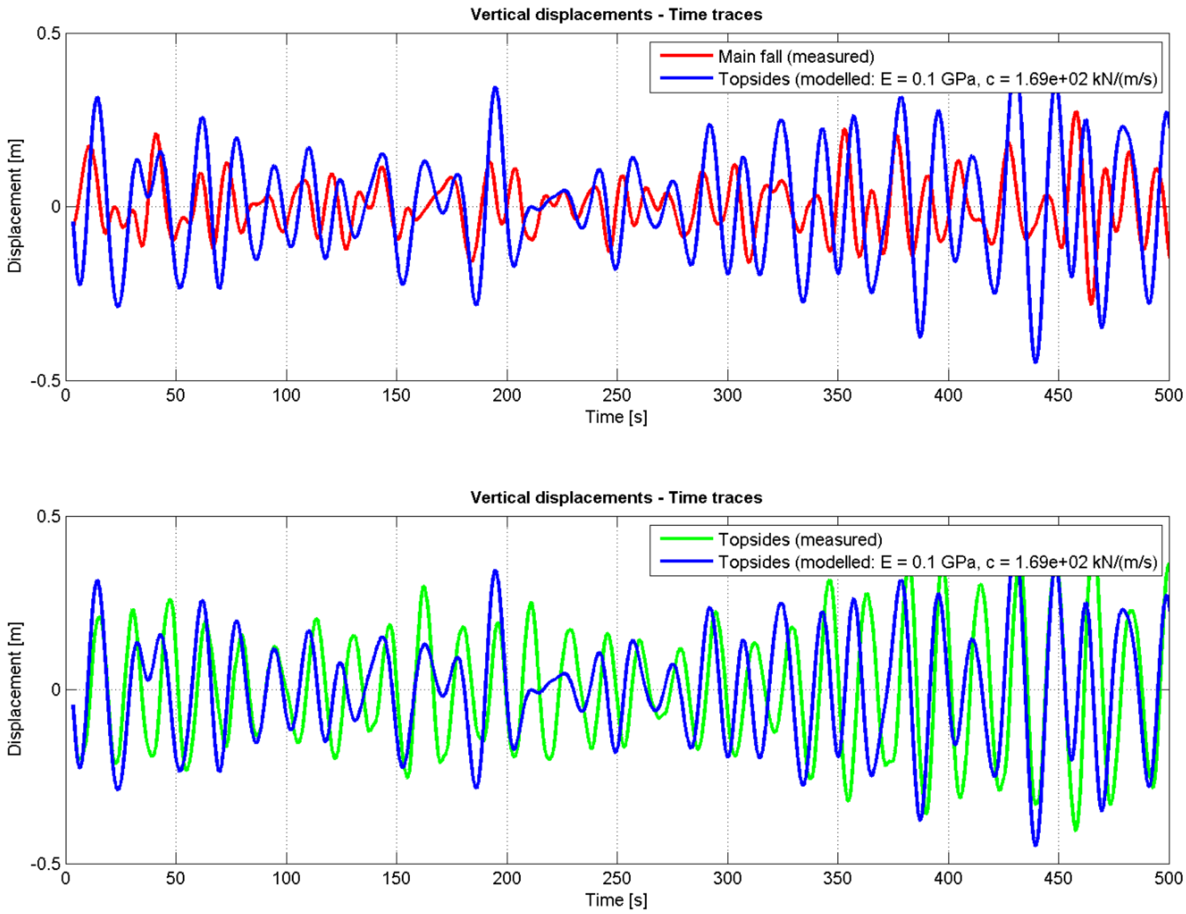

Figure 6.6: Modelled topsides heave time trace - Resonant from 'accelerations' signal

However, main fall stiffnesses required to obtain this behaviour are so low that they correspond to Young's moduli as low as 0.1 GPa. This is as low an elasticity as is typical for stiff rubbers, which is out of the question. Therefore, it can be concluded that the measurements registered in the 'accelerations' signal cannot be correct, and that they should not be used.

6.3.3. Damping properties obtained

As was demonstrated in the section above, the 'accelerations' measured signals cannot be used. The 'raw' measured signals are therefore used as input for $z_{fall}(t)$ in the model described by equation 6.13. Damping values c_{fall} are varied such that topsides vertical motions $z_{top}(t)$ best correspond to the time trace registered in the 'raw' measurement signal.

By default, connector damping values in Liftdyn models are set at 1.5% of their critical damping. For the 1DoF system described by equation 6.1, this yields a damping of [Blaauwendraad, 2010]:

$$c_{fall} = 1.5\% c_{cr} = 1.5\% \cdot 2\sqrt{k_{fall} M_{SB}} = 1.5\% \cdot 2\sqrt{1.64 \cdot 10^5 \cdot 3000} \approx 665 kN/(m/s) \tag{6.17}$$

The phasing ϕ [rad] between z_{fall} (the imposed motions forcing this 1DoF system) and modelled motions z_{top} for each forcing wave frequency is defined as follows:

$$\phi(\omega) = \arctan\left(\frac{-c_{fall}\omega}{k_{fall} - M_{SB}\omega^2}\right) \tag{6.18}$$

For the measured vertical motions of the topsides during the free-hanging stage, a phase lag of roughly 1s was observed with respect to vertical motions of the main fall axle, for vertical motion periods of roughly 16s (please refer to figure F.7). This corresponds to a phase lag ϕ of ca. $\frac{\pi}{8}$ rad, for a frequency of $\frac{\pi}{8}$ rad/s. Rewriting equation 6.18 and substituting $\phi\left(\frac{\pi}{8}\right) = \frac{\pi}{8}$ rad and $\omega = \frac{\pi}{8}$ rad/s yields the following value for c_{fall}:

$$c_{fall} = \frac{\tan\phi(\omega)\left(M_{SB}\omega^2 - k_{fall}\right)}{\omega} = \frac{\tan\left(\frac{\pi}{8}\right)\left(3000 \cdot \left(\frac{\pi}{8}\right)^2 - 1.64 \cdot 10^5\right)}{\left(\frac{\pi}{8}\right)} \approx 1.72 \cdot 10^5 kN/(m/s) \tag{6.19}$$

This corresponds to almost $4 \cdot c_{cr}$, and almost 260 times as much damping as the original value of $1.5\% c_{cr}$. This The fact that $c_{fall}/c_{cr} > 1$, and the system is thus critically damped, could also explain that no explicit response peaks corresponding to natural frequencies were found in section 6.2. The huge difference with original default damping values in Liftdyn will have a significant influence on modelled hook load fluctuations.

Note that this linearized equivalent damping was found using a roughly estimated phase lag for a single (dominant) wave frequency of $\left(\frac{\pi}{8}\right)$ rad/s. It could well be that damping values are different for other forcing frequencies. Moreover, damping can be highly non-linear depending on the origin of energy dissipation. For instance, mean wire rope tensions have a large influence on the curvatures wire ropes attain when they are bent over a sheave. Variations in axial tensions influence these curvatures, which can induce internal friction inside wire ropes near sheaves. Linearized damping values may therefore be different for other stages than the free-hanging stage.

For measured vs. modelled topsides time traces for both the original (1.5% of critical) damping value and the damping value found in equation 6.19, please refer to appendix G. A phase plot has been included for both cases as well. Since the distribution of energy dissipation is not quantitatively known, it is assumed that damping is proportionally divided over the main hoist and grommets. Since the static length and cross-sections of both the grommets and main hoist are known, the following relation between their respective damping approximations can be derived:

$$c_{hoist}\frac{l_{hoist}}{A_{hoist}} = c_{grom}\frac{l_{grom}}{A_{grom}} \quad \rightarrow \quad c_{grom} = c_{hoist}\frac{A_{grom} l_{hoist}}{A_{hoist} l_{grom}} \approx 2.24 \cdot c_{hoist} \tag{6.20}$$

Substituting c_{hoist} and c_{grom} in the damping equivalent of equation 6.14 yields the following equation:

$$c_{fall} = \frac{2.24 \cdot c_{hoist}^2}{3.24 \cdot c_{hoist}} \quad \rightarrow \quad c_{hoist} = \frac{3.24}{2.24} \cdot c_{fall} \tag{6.21}$$

Substituting $c_{fall} = 1.72 \cdot 10^5$ kN/(m/s) in equations 6.20 and 6.21 yields proportionally divided damping values for the SB grommets and main hoist. Damping values for the PS grommets and boom suspension wires are obtained in a similar manner, based on their cross-sectional area and static length. The procedure used to obtain damping properties from a simplified 1DoF model during the free-hanging stages is not possible for other lift stages unfortunately. Damping properties are therefore assumed to be the same for all stages considered.

Damping values thus obtained for all connectors in the models are given in table 6.3 below.

Table 6.3: Damping values obtained from 1DoF model - All connectors

Connector	A **[mm^2]**	l **[m]**	c **[kN/(m/s)]**
SB grommets	$1.24 \cdot 10^5$	23.4	$5.57 \cdot 10^5$
PS grommets	$7.38 \cdot 10^4$	19.7	$3.94 \cdot 10^5$
SB main hoist	$1.05 \cdot 10^5$	44.4	$2.49 \cdot 10^5$
PS main hoist	$1.05 \cdot 10^5$	48.5	$2.72 \cdot 10^5$
SB suspension	$7.37 \cdot 10^4$	72.4	$2.84 \cdot 10^5$
PS suspension	$7.37 \cdot 10^4$	72.4	$2.84 \cdot 10^5$

6.4. Obtained wire rope dynamic properties - Hook load fluctuations

The original Liftdyn models (described in chapter 3) are adjusted. Stiffness and damping properties are changed, according to the values obtained in sections 6.2 and 6.3 above.

Modelled hook load fluctuations spectra are different than those calculated using the original model (please refer to section 5.2), however they do not necessarily correspond better to measured hook load fluctuations spectra. Motion response spectra are omitted from this report. The motions behaviour of the floating bodies (H-542 and SSCV Thialf) is virtually the same as that modelled using the original damping and elasticity parameters.

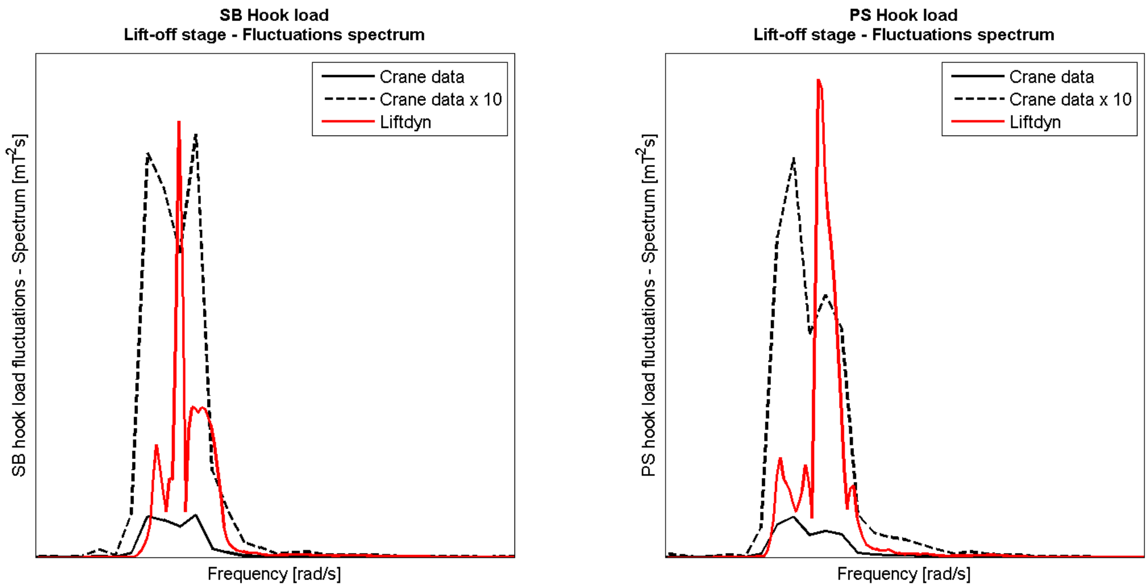

Figure 6.7: SB and PS hook load fluctuations spectra (lift-off stage) - Adjusted connector properties

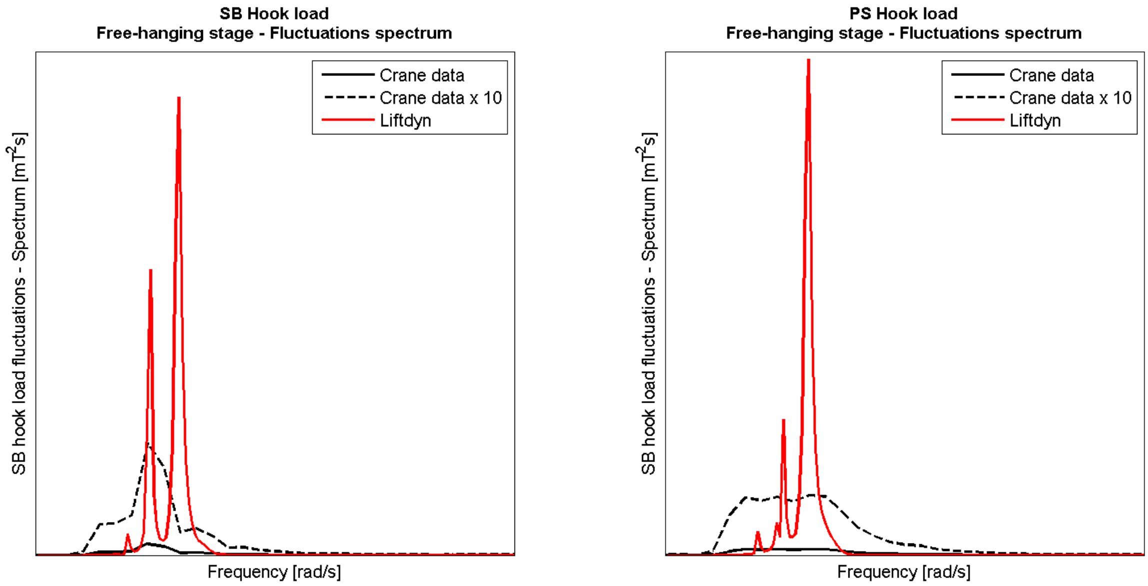

Figure 6.8: SB and PS hook load fluctuations spectra (free-hanging stage) - Adjusted connector properties

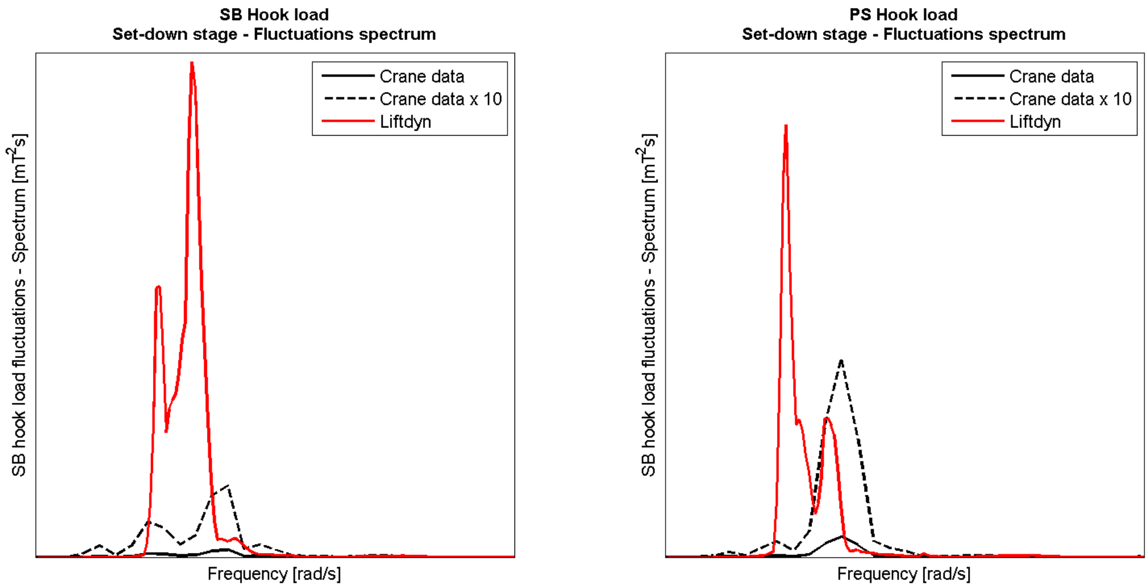

Figure 6.9: SB and PS hook load fluctuations spectra (set-down stage) - Adjusted connector properties

7
Discussion

7.1. Introduction

The goal of this thesis is to ascertain what causes the discrepancy observed between measured and modelled hook load fluctuations of a heavy lift operation. In order to do so, a step-by-step approach was proposed and partially carried out to systematically eliminate or confirm contributions of several root causes to this discrepancy. The focus lies on the first potential root cause identified: a discrepancy between actual and modelled hydrodynamics. The assessment of this contribution was based mainly on a comparison study between measured and modelled hydrodynamics, and attempts were made to obtain more accurate model parameter values.

The measurements used, methods applied, and results obtained from this research are discussed in this chapter. These observations and considerations lead to conclusions and recommendations regarding future research, modelling practices and measuring equipment used, which are presented in chapter 8.

7.2. Hydrodynamic modelling - Wave forcing, added mass and damping

Please refer to chapter 3 and appendix C for details.

7.2.1. Diffraction analysis - Infinite vs. Actual water depth

When waters are sufficiently deep, the bottom has an insignificant influence on ocean waves according to equation 3.4. The advantage of this is that hydrodynamic properties of a certain floating body, obtained from a single diffraction analysis using an infinite water depth, can be used for all projects for which the ocean is sufficiently deep. Since the water depth for the lift operation considered in this research is in the range where the ocean floor starts influencing ocean waves, a diffraction analysis has been conducted for both an infinite and the actual water depth. Using hydrodynamic properties obtained from an analysis conducted using the actual instead of an infinite water depth proved to have an insignificant influence on calculated responses for the water depth and sea state (as was to be expected from equation 3.4).

7.2.2. Diffraction analysis - Single- vs. Multi-body

In [Ayaz et al., Saipem UK, 2014], is was concluded that the influence adjacent bodies have on each other's hydrodynamic properties, are noticable for modelled responses of all cases considered. When the adjacent bodies are mechanically coupled however, the influence of applying a multi-body instead of a single-body diffraction analysis was found to have an insignificant influence on calculated responses as compared to the influence of mechanical coupling. For the case considered in this study, it was concluded that some (especially H-542) calculated response differences can be considered significant during the lift-off stage, when the Thialf and H-542 are mechanically coupled.

For engineering purposes, using a single-body instead of a multi-body diffraction analysis is more convenient. It is important to notice, however, that applying a single-body diffraction analysis is not necessarily conservative. While in most cases operations are optimized by using vessel shielding to an advantage, hydrodynamic forcing can be larger due to multi-body interaction when incoming waves come from another direction. When it is not possible to change heading for an operation (due to restricted motions of either the SSCV or lift-off or set-down location), hydrodynamic response can be underestimated when results from a single-body diffraction analysis are used. For critical operations where this is the case, it is therefore advisable to conduct a multi-body diffraction analysis. A downside of multi-body diffraction analyses are exaggerated peaks, which originate from standing waves in between adjacent floating bodies. This is already observed for the RAOs obtained for the Thialf in a single-body diffraction analysis (figures **??** to C.1), due to its hull being made up of multiple (adjacent) columns. Flow separation and viscosity are not accounted for in a diffraction analysis (since these are based on potential theory), which causes these peaks to be exaggerated [Sun et al., 2010]. A possibility to account for this is by applying a so-called 'lid', which dampens water elevations in between adjacent vessels, which complicates the effort of conducting a multi-body diffraction analysis even more. This has not been done for the multi-body diffraction analyses conducted for this research.

7.3. Measurements used - Accuracy

Methodologically speaking, the approach for obtaining translations and rotations described in chapter 4 is correct. However, some haziness exists as to which of multiple measured signals (measured by each sensor) is most accurate. Furthermore, especially the measured signals of sensor rotations contain quite some noise.

Please refer to chapter 4 and appendix D for details.

7.3.1. Siri signals - 'Accelerations' signal vs. 'Raw' signal

The 6DoF motion sensors used at HMC have been used for several years. The sensors register several signals:

- A 'raw' signal, which contains translational accelerations and rotational velocities, and requires post processing for obtaining correct (SI) units and signs [HMC, 2012].
- An 'accelerations' signal, which contains accelerations for al 6DoFs. The internal sensor processing algorithm used to obtain this signal is unknown.
- Rotations and heave signals. These are obtained during operation, by integrating measured velocities and accelerations real-time using an algorithm [Godhavn, 2000]. A phase lag is introduced, and the algorithm is known to be inaccurate [SIRI Marine, 2016]. Especially heave was found to be very far off (when compared to the Thialf's MRU system; described below). These signals should not be used for post-processing purposes.

The 'raw' sensor file is normally used for post-processing purposes at HMC. However, when hook load fluctuations are calculated based on hoist wire elongations (described in section 5.3, it turns out that using translations of the 'accelerations' signal results in a hook load fluctuations spectral shape which corresponds much better to the measured hook load fluctuations spectrum than when 'raw' signal translations are used. Why this is the case remains unclear. In section 6.3 however, it was demonstrated that for the 'accelerations' signal to be correct, elasticity values of the main hoist would have to be as low as 0.1 GPa, which is nonsense.

This, along with the overall haziness of the origin of the 'accelerations' signal and the way it is obtained, renders the 'accelerations' measured signal unreliable. In line with HMC practices, using the 'raw' sensor file for this research is therefore the best option (from measured signals available).

7.3.2. Siri signals - Rotational velocity measurements

The rotational velocity measurements proved to be very noisy: the dynamic error amounts to ca. 0.2 °/s (example S4 raw roll velocity signal in figure 7.1). Also, the rotational velocity signals contain an offset, of which the cause is not known.

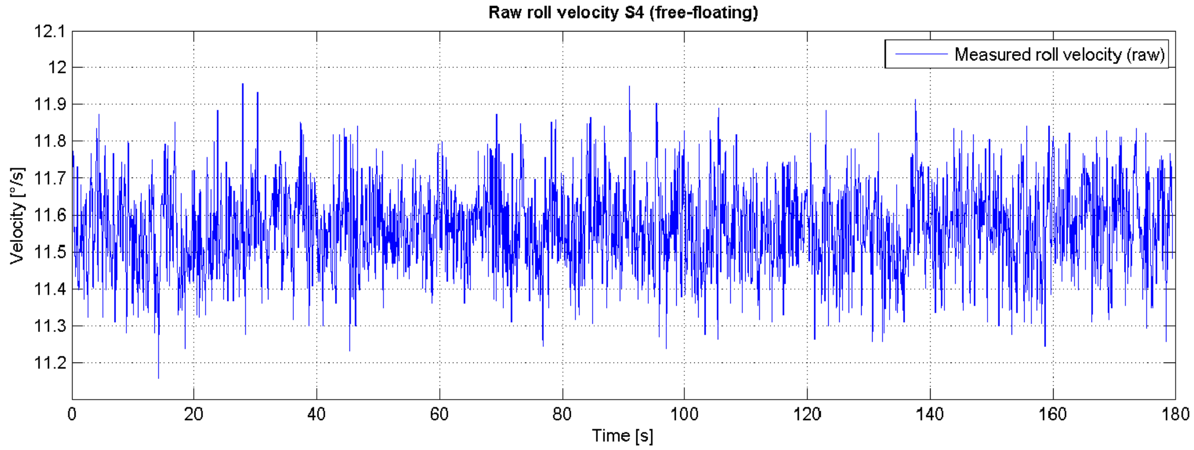

Figure 7.1: S4 raw - Roll velocity (free-floating)

This is a very large relative error. During the lift operation of which measurements have been obtained, sea states were very benign (please refer to section 5.2). The rotational motions behaviour was therefore in the same order of magnitude as the error. Moreover, this error results in inaccurately calculated gravity components in the translational accelerations: for a horizontal sensor, an error as little as 0.1° in roll and pitch measurements results in an error of the gravity component in the sensor's sway and surge directions of $gsin(0.1) \approx 0.017$ m/s^2. This too is in the order of magnitude of translational accelerations for this specific project. For the S4 sensor, a cross-check with the Thialf's MRU can be conducted for heave, roll and pitch:

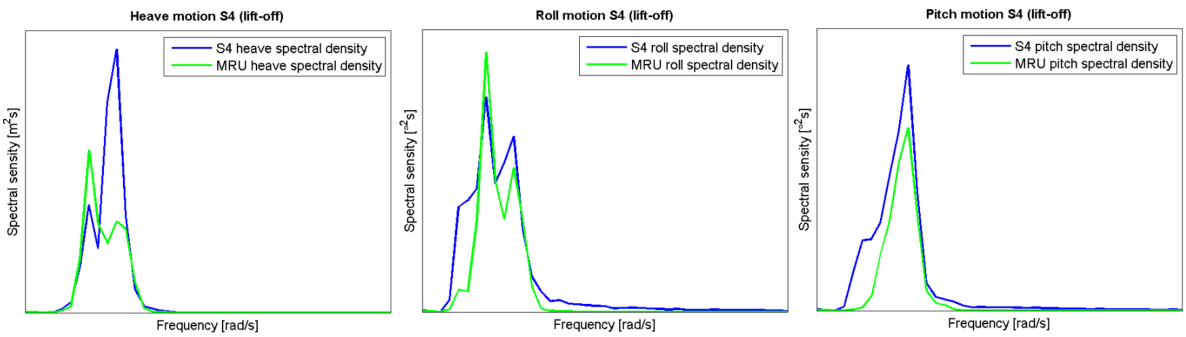

Figure 7.2: S4 vs. MRU comparison - Heave, roll and pitch spectra (lift-off)

For other stages, results were similar (appendix D). As can be seen in figure 7.2 above, the signal spectra still match fairly well, rendering the Siri rotational signals not completely useless. However, the gravity component in vertical accelerations of a mean horizontal accelerometer (the heave direction of sensor S4) hardly changes as a result of roll and pitch motions (for $cos\phi \approx 1$ for small angles). Surge and sway signals of the horizontal Siri sensors are influenced heavily by gravity components. Unfortunately, no MRU signals for surge and sway are available for cross-checking with the Siri S4 obtained surge and sway signals.

Fortunately, S1 and S4 surge and sway motions play a marginal role in hook load fluctuations as compared to heave, roll and pitch. For the S2 sensor however, which is positioned at an angle in the SB crane boom, especially surge and heave motions (in the sensor's LCS) contain strongly varying gravity components dependent on the sensor's rotations. Errors therein therefore affect local translational acceleration, which all contribute to vertical accelerations in the GCS, and could thus influence the main hoist's perceived elongation and hook load fluctuations. However, it was found that errors in gravity components in the LCS cancel each other out in the GCS. This is clarified by the 2D example below:

$$\ddot{z}_{global} = (\ddot{x}_{local} + g_{local,x})\sin\alpha + (\ddot{z}_{local} + g_{local,z})\cos\alpha \quad (7.1)$$

$$\ddot{z}_{global} = \ddot{x}_{local}\sin\alpha + \ddot{z}_{local}\cos\alpha + g(\sin^2\alpha + \cos^2\alpha) \quad (7.2)$$

$$\ddot{z}_{global} = \ddot{x}_{local}\sin\alpha + \ddot{z}_{local}\cos\alpha + g \quad (7.3)$$

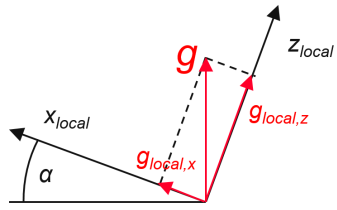

Figure 7.3: Vertical gravity component in GCS

Errors in local translational accelerations therefore do not introduce errors in accelerations in the GCS.

7.3.3. S2 rotations - Alternative approach

A possible method for obtaining more accurate rotations of the main fall axle (S2 location), is by using the Thialf's MRU signal according to the following procedure:

- Synchronise Siri S4 and Thialf MRU heave signals, which are quite accurate for both units
- Transform Thialf translations to translations at SB crane boom hinge and top of SB A-frame
- Include boom and suspension wires in model described in section 5.3
- Use motions of topsides and motions obtained from transforming MRU signals to calculate SB boom motions

This complicates the model significantly, and introduces other error sources, like vessel deformations.

For the purpose of this thesis, it turns out this effort is not required. Even though errors in calculated gravity components are in the order of magnitude of measured accelerations, the total vertical gravity component in the measured translational accelerations will always remain the same: g. Errors in calculated gravity components therefore cancel eachother out (in the GCS), as was demonstrated in the section above. In section 5.3 it is proven that accounting for gravity components indeed has no influence on calculated hook load fluctuations.

7.4. Measured vs. Liftdyn modelled - Motions

Please refer to chapter 5 and appendix 5 for details.

The general observation is that motions are modelled quite well by Liftdyn. Dynamic properties like mass and radii of gyration of all the bodies are assumed to be accurate: both the Thialf and H-542 have been owned and operated by HMC for many years, and the topsides comes with a detailed weight report supplied by the client. Other potential errors can result from rigidly assumed bodies, and assumed linearity and stationarity. The errors these assumptions introduce cannot be checked individually with a frequency domain analysis, since these factors are time dependent. Some modelled response spectra deviate more from measured response spectra than others. These discrepancies are discussed in the sections below.

7.4.1. Horizontal plane motions floating bodies

High-pass filtering was conducted at a frequency of 0.2 rad/s. Therefore, all motions at a lower frequency are taken out of the measured signals. However, already just above 0.2 rad/s a lot of energy was observed in the spectra obtained from measurements. This is attributed to second order wave forces [Journée & Massie, 2001]. These have not been included in the Liftdyn models, since the RAOs are computed by calculating steady state responses to individual regular waves at each frequency. Response spectra have been calculated according to equation 2.7. Since phasing between the different regular waves in the spectrum is not known, floating body response to wave groups cannot be modelled in this manner. Moreover, stiffness properties in the horizontal plane (mooring lines and DP systems) were not known for the project for which measurements have been obtained. Since this data was not readily available, stiffnesses in the horizontal plane were chosen somewhat arbitrarily in the Liftdyn models. Motions in the horizontal plane have a marginal influence on hook load fluctuations, which are governed by heave, roll and pitch. Therefore excluding second order vessel motions from the models is deemed appropriate for the purpose of this thesis.

7.4.2. Spectral peakedness

For practically all stages and DoFs, modelled response spectra contain sharper peaks than measured wave spectra and measured response spectra. This is especially true for the free-floating and lift-off stages, where multi-body interaction may lead to standing waves (as explained in section 3.4 [Sun et al., 2010]). The same effect on modelled responses can, to a lesser extent, be witnessed for the Thialf during the free-hanging and set-down stages. This is because the Thialf itself can be considered to consist of multiple bodies, from a diffraction analysis point of view. This is also evident from the RAOs presented in appendix C.

HMC has standard RAOs available for most of their vessels and barges, which are validated by model tests and adjusted accordingly. Since it was decided to use hydrodynamic properties of multi-body diffraction analyses for the free-floating and lift-off stages, for comparison purposes new (single-body) diffraction analyses have been conducted for the free-hanging and set-down stages as well. RAOs obtained from these analyses also feature these sharp peaks due to the Thialf's hull shape, as explained above. Obviously, this proves to have a large influence on modelled hook load fluctuations as well, which is discussed in section 7.5 below.

7.4.3. H-542 roll (free-floating and lift-off stages)

During the free-floating and lift-off stages, measured topsides roll (which was connected to the H-542 for the stages considered) is a factor two larger than modelled. An explanation for (part) of this behaviour could be that the free surface of ballast water inside the H-542 has not been accounted for in these Liftdyn models. It is possible to include dynamic forces and moments resulting from sloshing in the diffraction analysis application used [WAMIT, 2015]. It is advisable to account for these free surfaces in order not to underestimate vessel motions. Other explanations could be that hydrodynamic properties, obtained from WAMIT, are incorrect. Ascertaining the origin of this relatively large discrepancy is left out of scope for this thesis.

7.4.4. Topsides motions (free-hanging stage)

All measured topsides motions during the free-hanging stage, except for heave, are far smaller than those measured. This is attributed to the tugger winches not being included in the Liftdyn model. In reality, these winches are used to stabilize the motions of a lift object relative to the Thialf during operation. Heave motions are not compensated by the tugger winches, which explains why measured topsides heave response does correspond well to modelled response (figure E.15). The topsides surge (pendulum) motion being restricted also explains the smaller measured than modelled roll response of the Thialf during the free-hanging stage.

7.4.5. S2 (SB main fall) motions

SB boom motions are strongly related to motions of the Thialf. The only motions it has relative to motions of the Thialf (assuming both bodies are rigid), is caused by elasticity of boom suspension wires. The SB boom is boomed up at an angle of 60° with respect to the horizontal, at a 20° horizontal angle with respect to the Thialf's x-axis. As a result of this orientation, SB boom roll, pitch and yaw are similar to Thialf yaw, pitch and roll respectively.

7.4.6. Stationarity

Regarding stationarity: for the set-down stage, there was a clear influence of non-stationary behaviour (figure E.20), resulting from the sudden decrease in hook load just prior to the comparison interval. The pitch motion of the Thialf was far greater than modelled, which is attributed to the sudden decrease of hook load and expected to decline over time as a result of (mainly) hydrodynamic damping. These increased pitch motions can pose a threat of slack rigging, if the load is almost completely supported by the support structure. In practice, hook load is rapidly lowered by winching at this stage.

7.4.7. General findings

All in all, motions obtained from Liftdyn are considered to model reality quite well. The (especially rotational) motion measurements used for the comparison are quite noisy, which in combination with a mild sea state results in a relatively large error. Still, comparison to another measuring device (Thialf MRU, figure 7.2) increases confidence in the measurements used for the comparison study. Note that for this comparison study, the actual measured wave spectrum was used to model responses in retrospect. For engineering purposes, an extra error is introduced since forecasted wave spectra are used. The suggestions for obtaining more accurately modelled motions have not been applied to the models used for this comparison study, because the motions relevant for main hoist elongations (and thus hook load fluctuations) are deemed accurate enough for the purpose of this thesis.

No model perfectly describes reality, and a contribution of root cause (1.) will always add to the overall discrepancy. The order of magnitude by which modelled hydrodynamics deviate from measurements however is smaller than the order of the discrepancy between measured and modelled hook load fluctuations. A contribution of root causes (2.) and/or (3.) is thereby deemed proven.

7.5. Measured vs. Liftdyn modelled - Hook load fluctuations

Please refer to chapter 5 and appendix F for details.

7.5.1. Liftdyn vs. Measured hook load fluctuations spectra

What is clear from the comparison study between measured and Liftdyn modelled hook load fluctuations spectra (figures 5.1 to 5.7), is that discrepancies are not exclusive for the lift-off stage, but observed for all other stages of a lift operation as well. Similar to modelled motions, modelled hook load fluctuations response is much more sharp peaked than measured. These (exaggerated) peaks complicate a spectral shape comparison of both response spectra. However, the standard deviations of modelled spectra are ca. two times as high as those of measured spectra for all stages considered. The discrepancies observed in earlier hook load fluctuations comparison studies (provoking this study) were somewhat larger: a factor three. Still, the discrepancy observed originally holds for the lift operation considered in this research.

7.5.2. Measured vs. Calculated hook fluctuations spectra

Main hoist elongation time traces, which are directly related to hook load fluctuations, are calculated from relative motions between the crane boom tip and lift object. Hook load fluctuation time traces corresponding to these elongations can be calculated, assuming that wire rope elasticity properties are known. This is done for the lift-off, free-hanging and set-down stages, for both the 'raw' and 'accelerations' measured signals (described in section 7.3.1). Standard deviations for measured and calculated hook load fluctuations spectra, along with their ratios for both methods are presented in table 7.1 below.

Table 7.1: Measured vs. Calculated hook load fluctuations - Standard deviations

Stage	$\sigma_{measured}$ **[mT]**	σ_{raw} **[mT]**	σ_{acc} **[mT]**	$\frac{\sigma_{raw}}{\sigma_{measured}}$ **[-]**	$\frac{\sigma_{acc}}{\sigma_{measured}}$ **[-]**
Lift-off	127.6	1168	1666	9	13
Free-hanging	32.28	1392	2565	43	79
Set-down	45.61	3176	943.4	70	21

7.5.3. Linearisation

It was found that accounting solely for vertical motions instead of motions in all directions yields nearly identical main hoist elongations, as can be seen for the lift-off stage in figure 7.4 below (free-hanging and set-down stages yielded identical results as well).

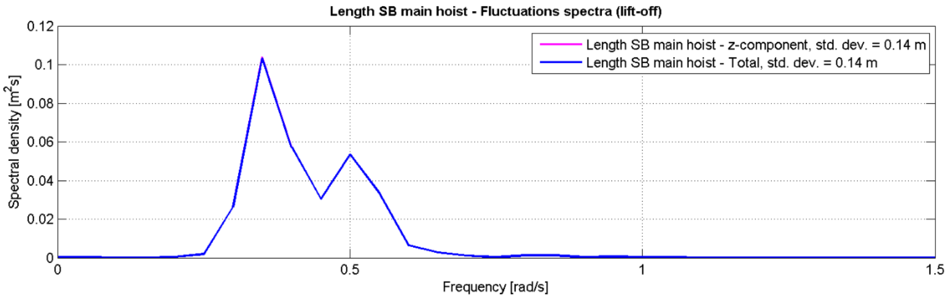

Figure 7.4: SB main hoist elongations spectra - Total vs. z-component lift-off)

7.5.4. General findings

The first thing that stands out from the comparison between measured and calculated hook load fluctuations spectra, is that discrepancies are (very) large for both measured signals. Discrepancies with measured hook load fluctuations are so large, that a wire rope stiffness overestimation contribution to the discrepancy is deemed possible. This cannot be the only origin of discrepancies, since the factor by which they deviate is very different for each stage. A stage dependent influence of root cause (2.) and/or (3.) are therefore considered possible. The second thing that strikes, is that the shapes of fluctuations spectra calculated with motions obtained from 'accelerations' measured signals correspond much better to those of the measured spectra than those using motions obtained from 'raw' measured signals as input. Especially the calculated spectrum for the set-down stage (using 'raw' measured signals as input) seems to be missing a lot of energy around 0.55 rad/s. Hook load fluctuations spectra calculated using motions obtained from 'accelerations' signals as input however are quite similar in shape to measured hook load fluctuations spectra. The 'accelerations' measured signals should not be used however, as was demonstrated in section 7.3.1. The high fluctuations cannot be attributed to sensors S1 and S2 (for some reason) not being in synch: also for the set-down stage, when the topsides are fixed, much larger vertical motions for the main fall axle are measured than those modelled.

Above all, measurement inaccuracies and uncertainties are of paramount importance to the reliability of these results. Note that, if wire rope elasticities are assumed to be 70 GPa, a hook load increase of 100mT corresponds to a main hoist elongation of ca. 1cm. One could argue therefore that the measurement equipment used is much too inaccurate, and not suitable for this purpose.

7.6. New wire rope dynamic properties obtained

Please refer to chapter 6 and appendix G for details.

7.6.1. Elasticity

The method proposed in section 6.2 for obtaining wire rope stiffness properties, using a simplified 2DoF system with measured natural frequencies as input, could have worked. However, for the most explicit and probable response peaks found in the measured signals, this system cannot be solved. If hoist wire rope damping properties are indeed supercritical, as follows from the analysis presented in section 6.3, no natural frequencies can occur in this system, which would explain the absence of response peaks corresponding to the modes searched for.

The alternative elasticity properties presented, obtained from a stiffness test [Bridon, 2016], are similar to elasticities proposed by other sources [HMC, 2005]. They correspond fairly well to the elasticity values used originally in the Liftdyn models. In normal Liftdyn modelling practices however, relative loading and loading history of the wire rope sections in the models is not accounted for. Wire rope elasticity is highly dependent on this however. Therefore, it is advisable to take this into account when modelling hydrodynamics for critical lift operations.

7.6.2. Damping

Whereas high stiffness and relatively low damping of the main hoist in the models makes that modelled vertical motions of the topsides and main fall axle are almost exactly in-phase for all frequencies considered, delayed motions of the topsides with respect to the main fall axle are observed in measured signals of their vertical motions (figure F.7). This phase lag observed between measured topsides and crane boom tip vertical motions (of ca. 1s) during the free-hanging stage implies significant damping in the the main hoist and grommets. A damping of ca. $4 \cdot c_{cr}$, as opposed to the original default value of $0.015 \cdot c_{cr}$, is found to yield a much better correspondence of modelled topsides motions to measured topsides motions. This is a very large difference with respect to the default damping values in Liftdyn models, which will have a significant influence on modelled hook load fluctuations.

Again, the reliability of this result is highly dependent on the accuracy of measurements, especially on the measured signals used being in synch. If the supposed phase lag of ca. 1s for the measured topsides motions originates from inaccurate signal timestamping, damping values obtained in this manner is heavily overestimated. However, the measured signals of both sensors S1 and S2 are time stamped by the same computer, and thus they have the same reference time. There is no reason to believe that the signals used are not in synch.

7.6.3. Influence on modelled hook load fluctuations

The elasticity values obtained are similar to those used in the original Liftdyn models, this will therefore have an insignificant influence on modelled hook load fluctuations. A logical consequence of the very high (supercritical) damping values found, is that phasing between the motions of the lift object, crane boom, and the Thialf increases, which in turn leads to higher hook load fluctuations. Indeed, this is observed in figures 6.7 to 6.9.

Unfortunately, this finding increases the discrepancy between modelled and measured hook load fluctuations even more. The revised hoist wire properties obtained therefore are no explanation for the problem treated in this research.

7.7. Overall discrepancy & root cause contributions

After assessment of root cause (1.), no explanation for the discrepancy observed has been found. Motions behaviour in general appears to be modelled quite accurately in Liftdyn, however results obtained from assessment of root cause (1.) are highly dependent on the reliability of measurements used, as explained above.

Mainly the factor by which calculated hook load fluctuations differ from the measured values, which is different for each stage considered, implies that measured hook load fluctuations are dependent on mean hook load and main hoist length. (Large) contributions of root causes (2.) and (3.) are therefore deemed very likely. The sheaves, especially those neighbouring the sheaves which contain the LMPs (please refer to appendix A), have a high influence on which dynamic tensions are actually measured. If this is indeed the case, hook load fluctuations modelled by Liftdyn can indeed occur, however they are not registered properly. In a worst case scenario, actual hook load fluctuations may even be higher as a result of damping values being underestimated in current modelling practices.

It therefore cannot, under no circumstances, be concluded that Liftdyn overestimates hook load fluctuations from the outcome of this research. A repetition of methods used in this thesis, using accurate measuring equipment, is necessary in order to become confident about the dynamic properties of the wire ropes used, and thus be confident about the actual hook loads that are occurring. Then, known hook load fluctuations can be compared to hook loads measured and registered, in order to gain insight in possible contributions of root causes (2.) and (3.). Due to time constraints, this was left out of scope for this thesis.

8 Conclusions & Recommendations

8.1. Conclusions

Based on the observations made in chapter 7, several conclusions can be drawn. They are listed per topic below.

8.1.1. Diffraction analysis

- Multi-body diffraction analyses result in exaggerated sharp peaks in RAOs. Applying hydrodynamic properties in Liftdyn models obtained from a multi-body diffraction analysis, where no damping lid was used in between adjacent bodies, is not appropriate therefore.
- Current (single-body diffraction) practices are only slightly conservative when vessel shielding is used. For unfavourable wave directions however, single-body modelled response can underestimate actual response due to multi-body interaction. Therefore multi-body diffraction analyses should be conducted for critical lift operations, for which vessel heading cannot be chosen freely.

8.1.2. Siri motion measurement system

- Some haziness exists as to which of two measured signals is most accurate: the 'raw' signal or the 'accelerations' signal. Rotations obtained from the 'raw' file compare much better to the Thialf's MRU measurements.
- Using the 'accelerations' signals for topsides motions during the free-hanging stage implies resonance. This is not considered to be possible, based on topsides mass and main hoist elasticity. Moreover, it is unclear how these 'accelerations' signals are obtained. Therefore it is concluded that they should not be used.
- Measured rotational velocities are quite noisy. This is in turn leads to inaccurately calculated gravity components in translations accelerations.
- Especially horizontal motions are subject to inaccuracies resulting from inaccurate gravity components. For this thesis's purpose, this was not a problem since hook load fluctuations are governed by vertical motions. Inaccurately calculated gravity components in translational accelerations do not influence vertical motions in the GCS. Errors cancel each other out.

8.1.3. Modelled motions

- In general, motions are found to be modelled quite accurately by Liftdyn. Still, contributions of root cause (1.) as explained in chapter 1 can add to the overall discrepancy. The error introduced by (inaccurate) motion modelling is of a smaller order than the hook load fluctuations discrepancy observed.

- 2nd order motions have not been included in the Liftdyn models. They are not relevant for the main goal of this thesis, but they should be included if one is interested in these motions, since they are quite substantial compared to 1st order motions.
- Stationarity assumption is not always appropriate. This is especially true for the set-down stage, and to a lesser extent the lift-off stage.

8.1.4. Modelled hook load fluctuations

- Discrepancies between measured and modelled hook load fluctuations are not exclusive to the pretension condition during lift-off. They have been observed for all lift stages considered: free-floating, lift-off, free-hanging and set-down.
- Spectral shape of modelled hook load fluctuations spectra differs more from measured hook load fluctuations spectra than was the case in earlier studies. This is attributed to exaggerated peaks resulting from multi-body diffraction analysis.

8.1.5. Calculated hook load fluctuations

- Discrepancies between measured hook load fluctuations and hook load fluctuations calculated from measured displacements are enormous. Calculated hook load fluctuations are far greater.
- The factor by which measured hook load fluctuations deviate from measured hook load fluctuations is different for each stage considered. This implies that measured hook load fluctuations are dependent on mean hook load and main hoist length. The higher the ratio between calculated and measured hook fluctuations standard deviations, the shorter the length of the main hoist for the corresponding stage (appendix B).
- This cannot be attributed solely to a possible overestimation of wire rope elasticity; differences are too large, and the different factor per stage implies a contribution of root causes (2.) and/or (3.).
- Spectral shape of the hook load fluctuations spectra calculated using measurements of the 'accelerations' signals corresponds better to the spectral shape of measured hook load fluctuations. However, as stated in section 8.1.2, these signals are unreliable.
- Hook load fluctuations are governed by vertical elongations. Influence of horizontal motions is insignificant.

8.1.6. Wire rope dynamic properties

- Accurate wire rope elasticity properties could not be obtained from the measurements used. There is no reason to believe wire rope elasticity properties are significantly lower than is assumed in current Marine Engineering modelling practices at HMC [HMC, 2005].
- A supercritical damping of $4 \cdot c_{cr}$ has been found, as opposed to a default damping of $1.5\% \cdot c_{cr}$ in Liftdyn. This is very much dependent on the synchronisation of measurements used.
- Applying these new elasticities and damping properties in the Liftdyn models does not result in modelled hook load fluctuations spectra that correspond better to measured hook load fluctuations spectra.

8.1.7. Overall discrepancy & root cause contributions

- From the outcome of this research, it cannot be concluded that Liftdyn overestimates hook load fluctuations. Results are highly dependent on the accuracy of the measurements used.
- It is likely that actual hook load fluctuations are larger than those measured.
- Location of LMP is not ideal. Dynamic tension fluctuations in the wire segment that is measured may not be representative for average hook load fluctuations in the main hoist (root cause (2.)).

8.2. Recommendations

Regarding hydrodynamic modelling practices, measuring equipment and future research, these conclusions lead to the followings recommendations:

8.2.1. Hydrodynamic modelling

- Stick to applying hydrodynamic properties in Liftdyn models obtained from single-body diffraction analyses for relatively simple lift operations where shielding can be used.
- Conduct a multi-body diffraction analysis, with a damping lid in between adjacent floating bodies, for critical lift operations where vessel heading cannot be chosen freely.
- Include second order wave forces in Liftdyn when vessel motions in the horizontal plane are limited.
- Take relative loading and loading history into account when selecting elasticities for each connector in a Liftdyn model. Generally, applying elasticities of 100 GPa for the main hoist and boom suspension wires, and 35 GPa for slings and grommets is a good approximation until further research on wire rope elasticity is conducted. This is in-line with present Marine Engineering conventions at HMC [HMC, 2005].
- Significantly increase connector damping values in Liftdyn models. This is very much dependent on the accuracy of measurements used in this research however.

8.2.2. Measuring equipment

- Acquire measuring equipment which is more transparent and less noisy.
- Consider moving LMPs to sheaves in the main fall axle. That way local dynamic tension differences in the main hoist wire system will not effect measured hook load fluctuations

8.2.3. Future research

- Repeat this research for other projects, using more accurate and reliable measuring equipment.
- If possible and economical, conduct tests for determining (dynamic) elasticity and damping properties of the wire ropes used on all SSCVs.
- If wire rope damping properties prove to be subcritical (when the method presented in section 6.3 is repeated using reliable measurements), obtain wire rope elasticity properties according to the method described in section 6.2.
- Film movement of sheaves neighbouring LMP sheave. Possibly, apply Particle Image Velocimetry (PIV) on the video material obtained in order to determine local hoist wire elongations and thus tensions.

A
Study method & Drawings

This appendix contains a flowchart of the suggested study approach for gaining understanding of the observed discrepancy between measured and modelled hook load fluctuations. Furthermore, some drawings with terminology of the SSCV Thialf and components relevant for this thesis are added.

1. SSCV Thialf - General crane arrangement
2. SSCV Thialf - Main hoist sheaves & wire rope 4×20 arrangement
3. Suggested approach - Flowchart

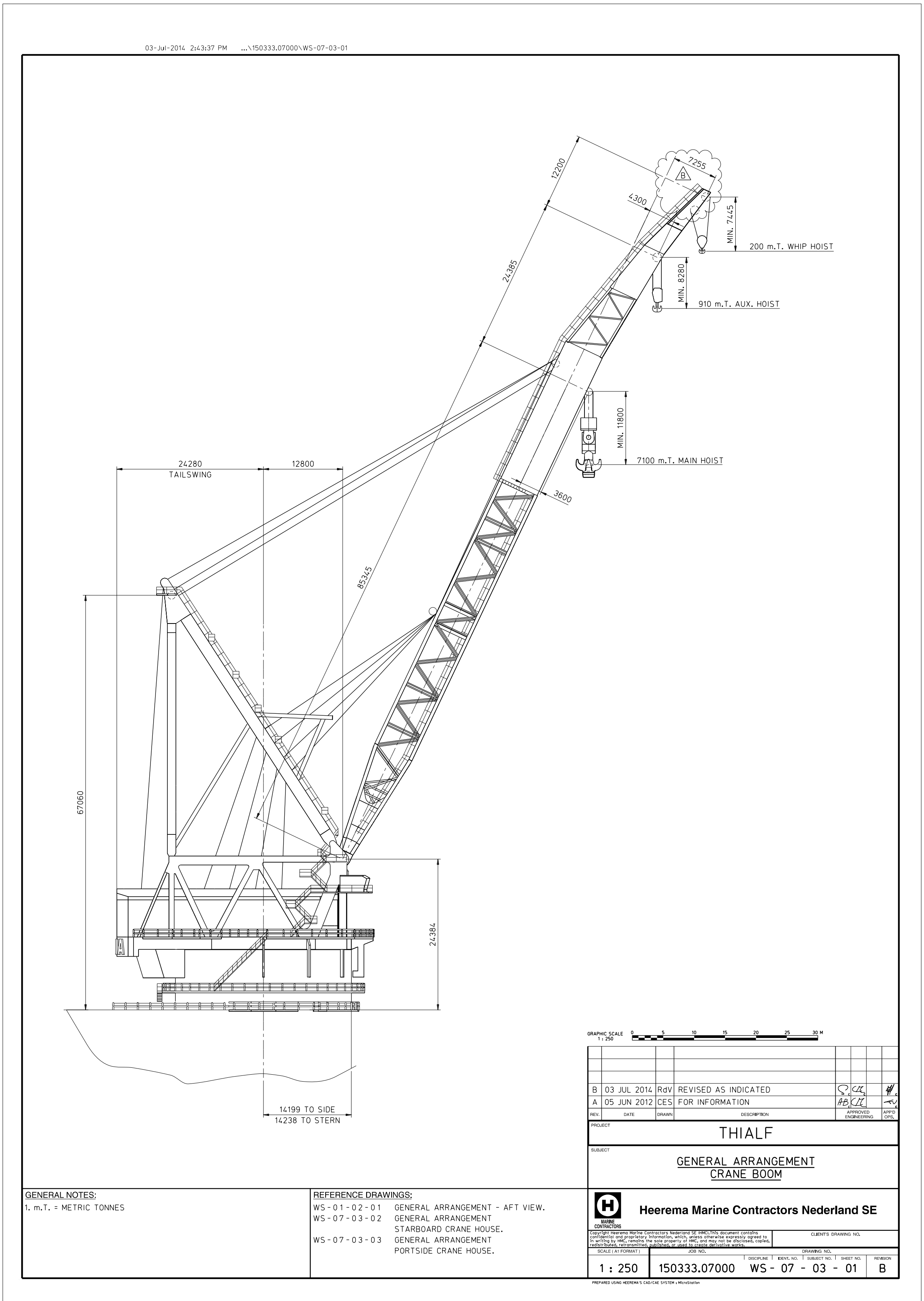

Figure A.1: SSCV Thialf - General crane arrangement

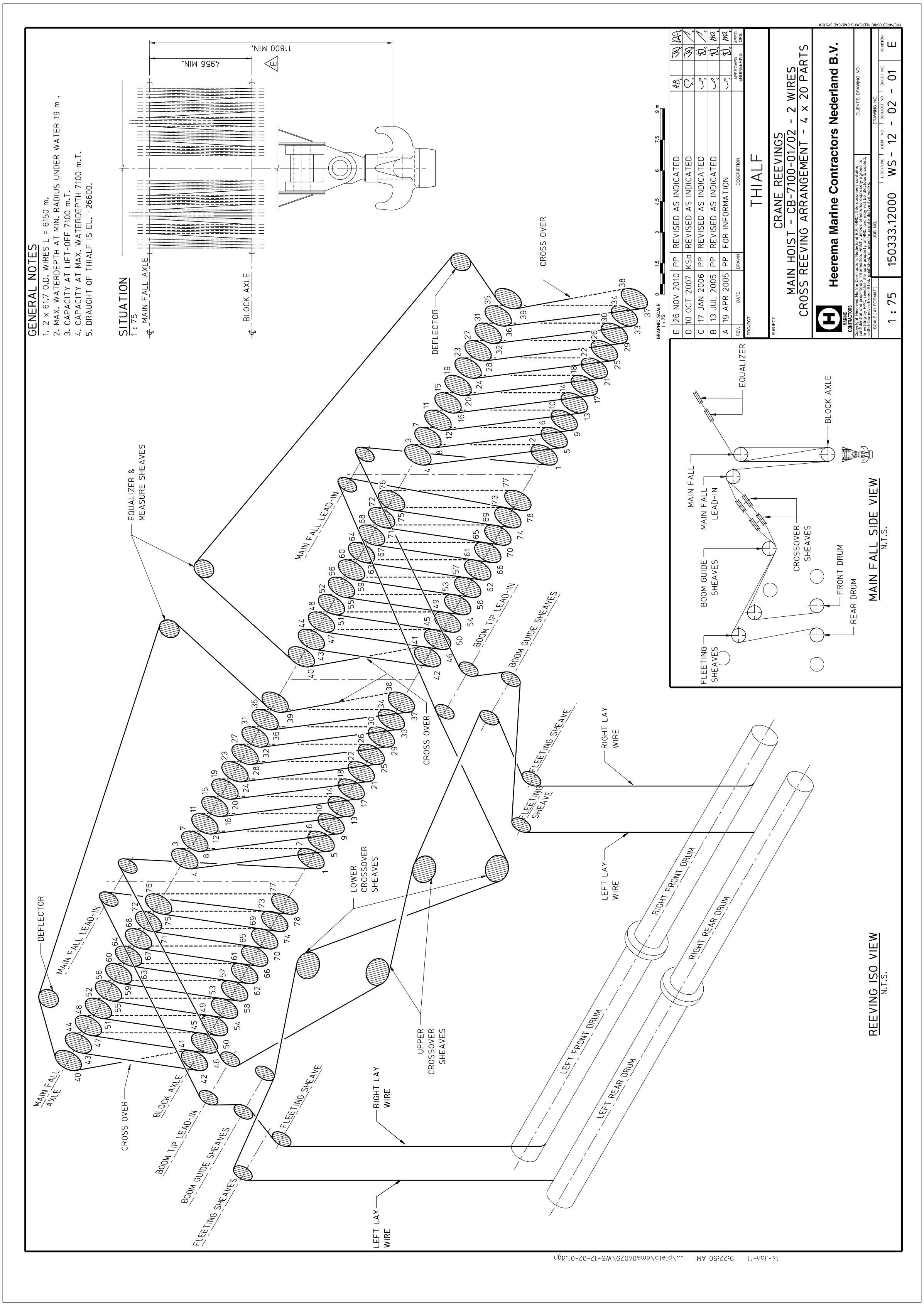

Figure A.2: SSCV Thialf - Main hoist sheaves & wire rope 4 × 20 arrangement

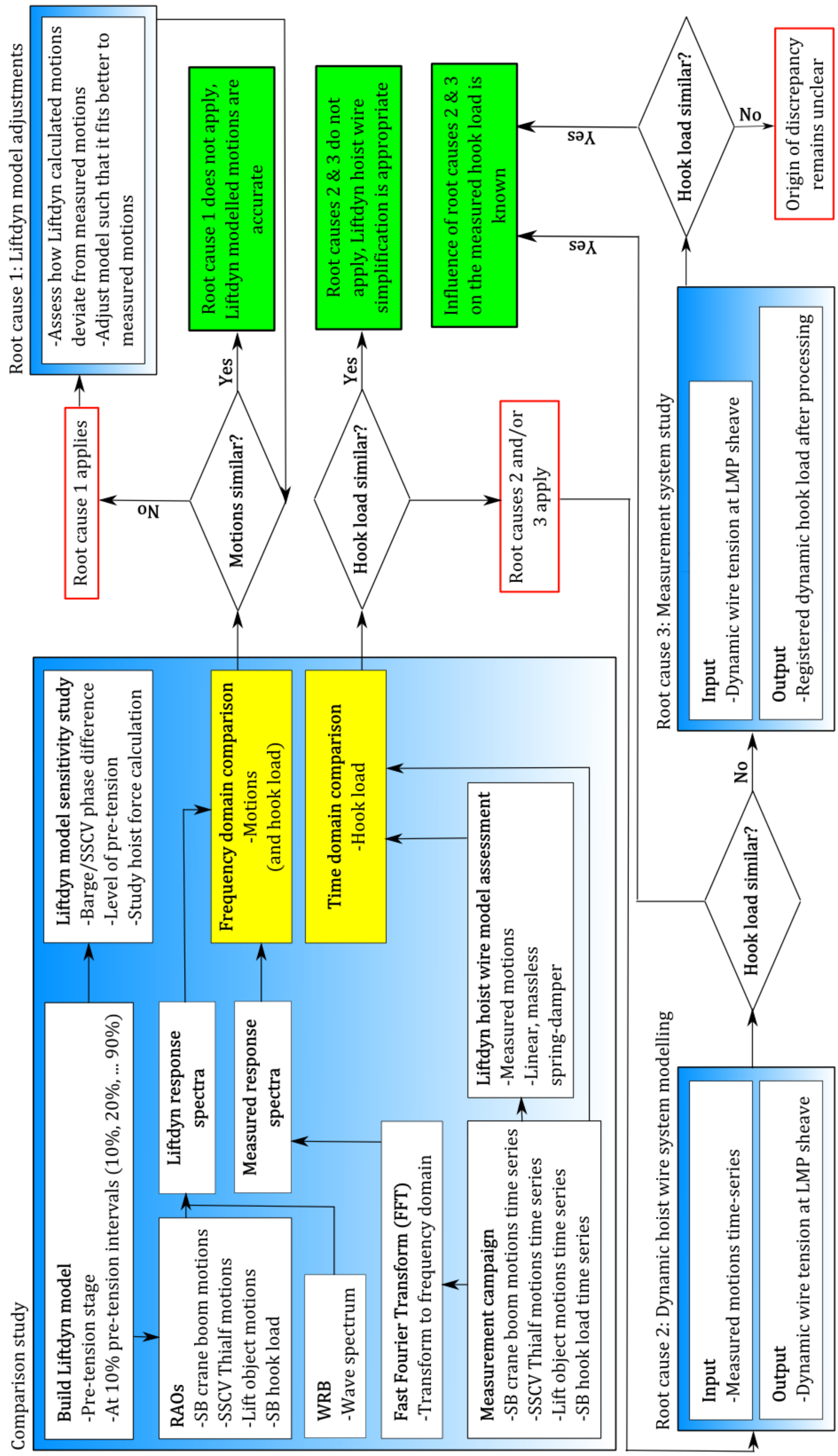

Figure A.3: Suggested approach - Flowchart

B

Stage specific parameters

This appendix contains lift stage dependent Liftdyn model parameter information. For other model parameters, which apply to all lift stages, please refer to section 3.3.2.

Table B.1: Free-floating stage - Model parameters

Thialf	
Mass $[mT]$	174,722
CoG $[m]$	[72.53, 0, -4.44]
z-coordinate in GCS	$[m]$
SB block	61.65
PS block	57.61
H-542 CoG	1.19
H-542 PoI 1	2.75
topsides CoG	19.89
topsides PoIs 1-4	39.81
topsides PoI 5	3.44

Table B.2: Lift-off stage - Model parameters

Thialf	
Mass $[mT]$	171,277
CoG $[m]$	[74.66, 0.03, -6.49]
z-coordinate in GCS	$[m]$
SB block	62.13
PS block	58.09
H-542 CoG	1.67
H-542 PoI 1	2.75
topsides CoG	20.37
topsides PoIs 1-4	40.29
topsides PoI 5	3.92

Table B.3: Free-hanging stage - Model parameters

Thialf	
Mass $[mT]$	169,462
CoG $[m]$	[75.84, 0.05, -7.62]
z-coordinate in GCS	$[m]$
SB block	79.48
PS block	75.44
topsides CoG	37.72
topsides PoIs 1-4	57.54
topsides PoI 5	21.27

Table B.4: Set-down stage - Model parameters

Thialf	
Mass $[mT]$	172,602
CoG $[m]$	[73.83, 0.02, -5.69]
z-coordinate in GCS	$[m]$
SB block	75.48
PS block	71.44
topsides CoG	33.72
topsides PoI 1-4	53.54
topsides PoI 5	17.27

C

Wave forcing, added mass & damping

ALTERED/OMITTED FOR CONFIDENTIALITY REASONS: This appendix contains hydrodynamic data obtained from WAMIT for the Thialf and H-542. This includes added mass and damping for the vessels' mode shapes, and wave forcing RAOs for the prevailing wave direction during lift-off ($150°$ *for the Thialf and* $60°$ *for the H-542 in local coordinates). Wave forcing for the free-floating stage is similar, since there is only a small draft difference influencing the analysis. For the free-hanging and set-down stages, wave forcing will be somewhat different (from the given Thialf single-body results), since the prevailing wave direction is different (*$240°$ *in local coordinates). Considering the Thialf's symmetry, and that the prevailing wave direction is roughly bow quartering for both cases, wave forcing RAOs for these stages have been omitted from this appendix.*

The following comparison plots are presented:

1. Single- vs. Multi-body - Thialf response (lift-off)
2. Single- vs. Multi-body - H-542 response (lift-off)
3. Infinite vs. Actual WD - Thialf response (lift-off)
4. Infinite vs. Actual WD - H-542 response (lift-off)

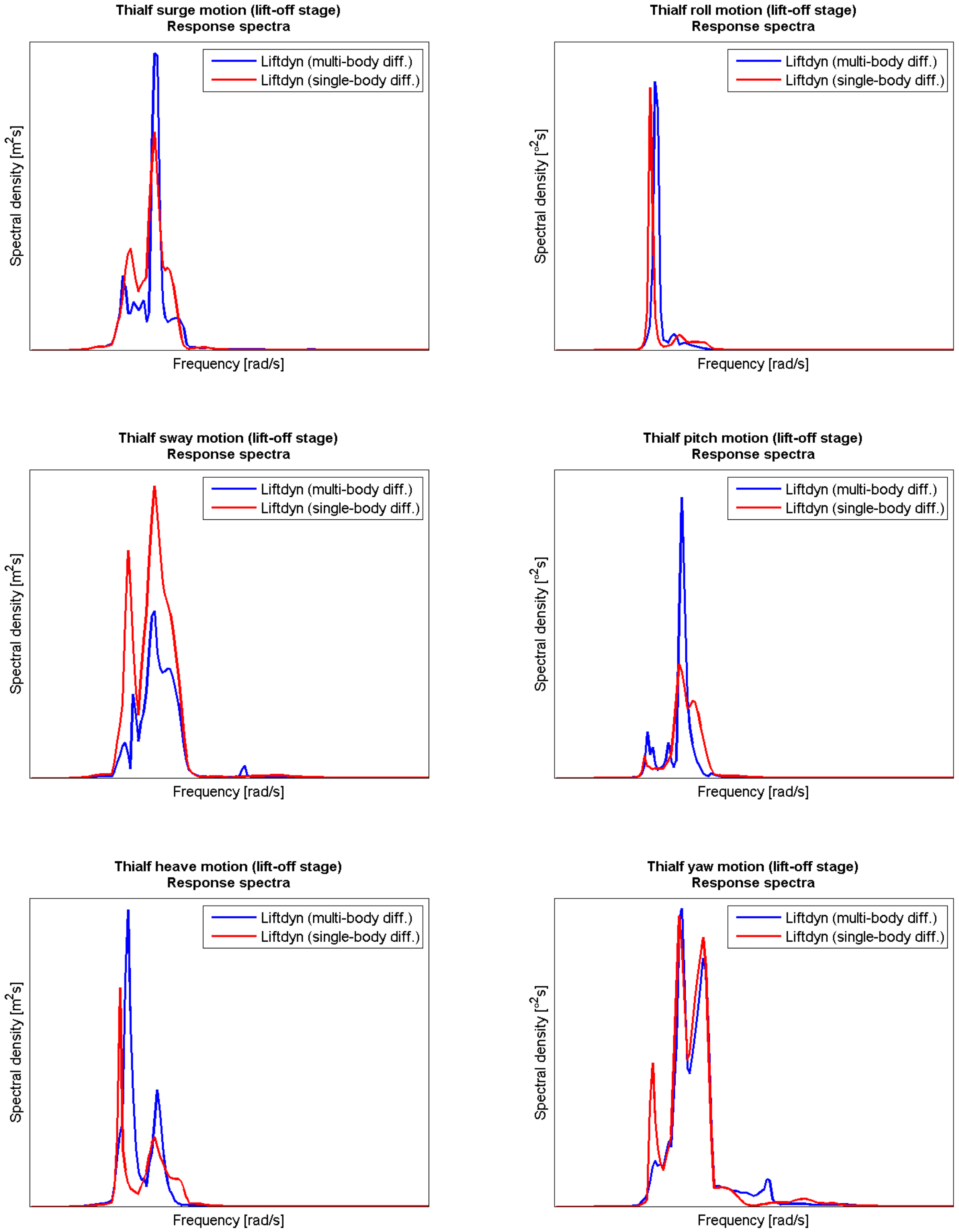

Figure C.1: Thialf response - Single- vs. Multi-body (lift-off)

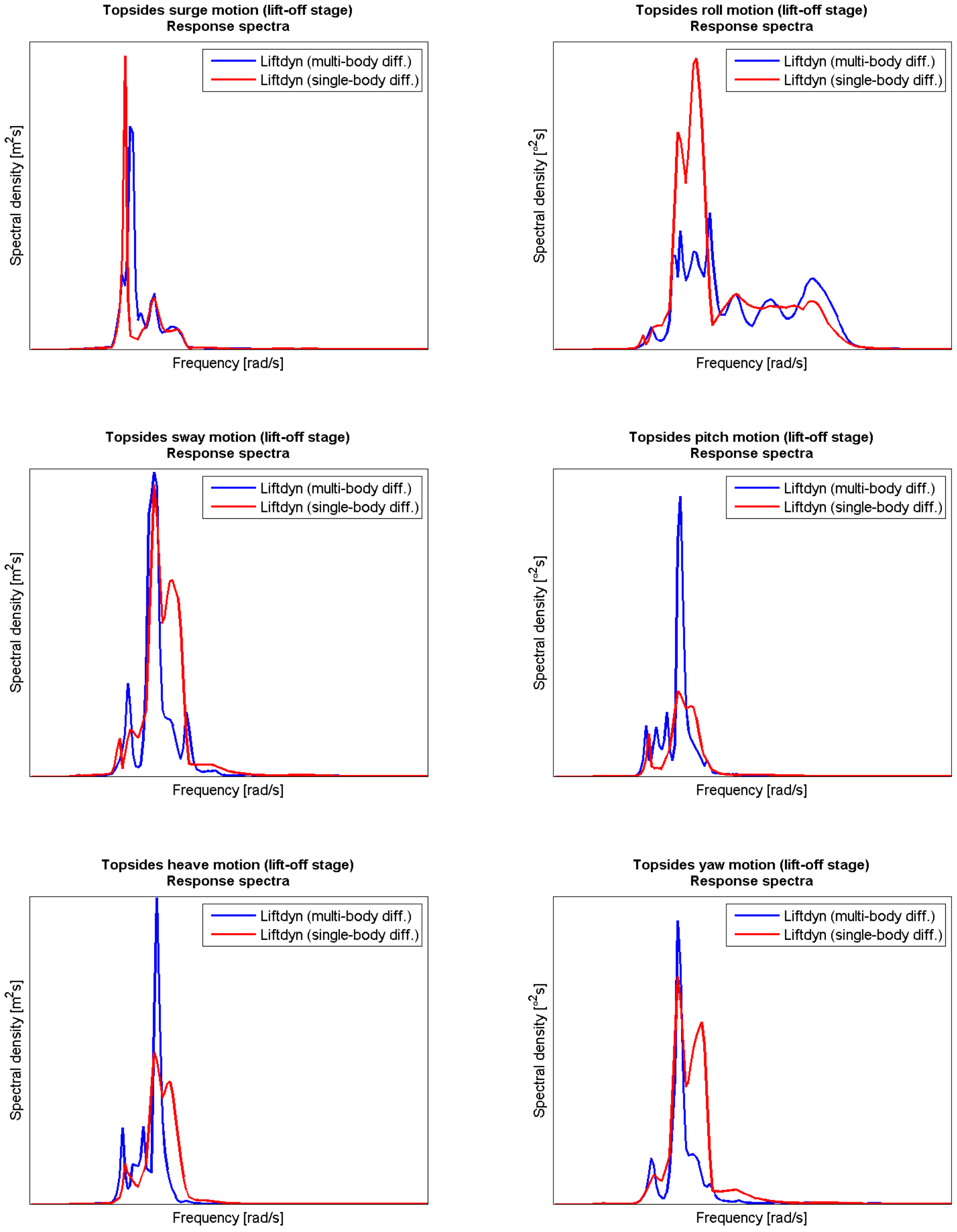

Figure C.2: Topsides/H-542 response - Single- vs. Multi-body (lift-off)

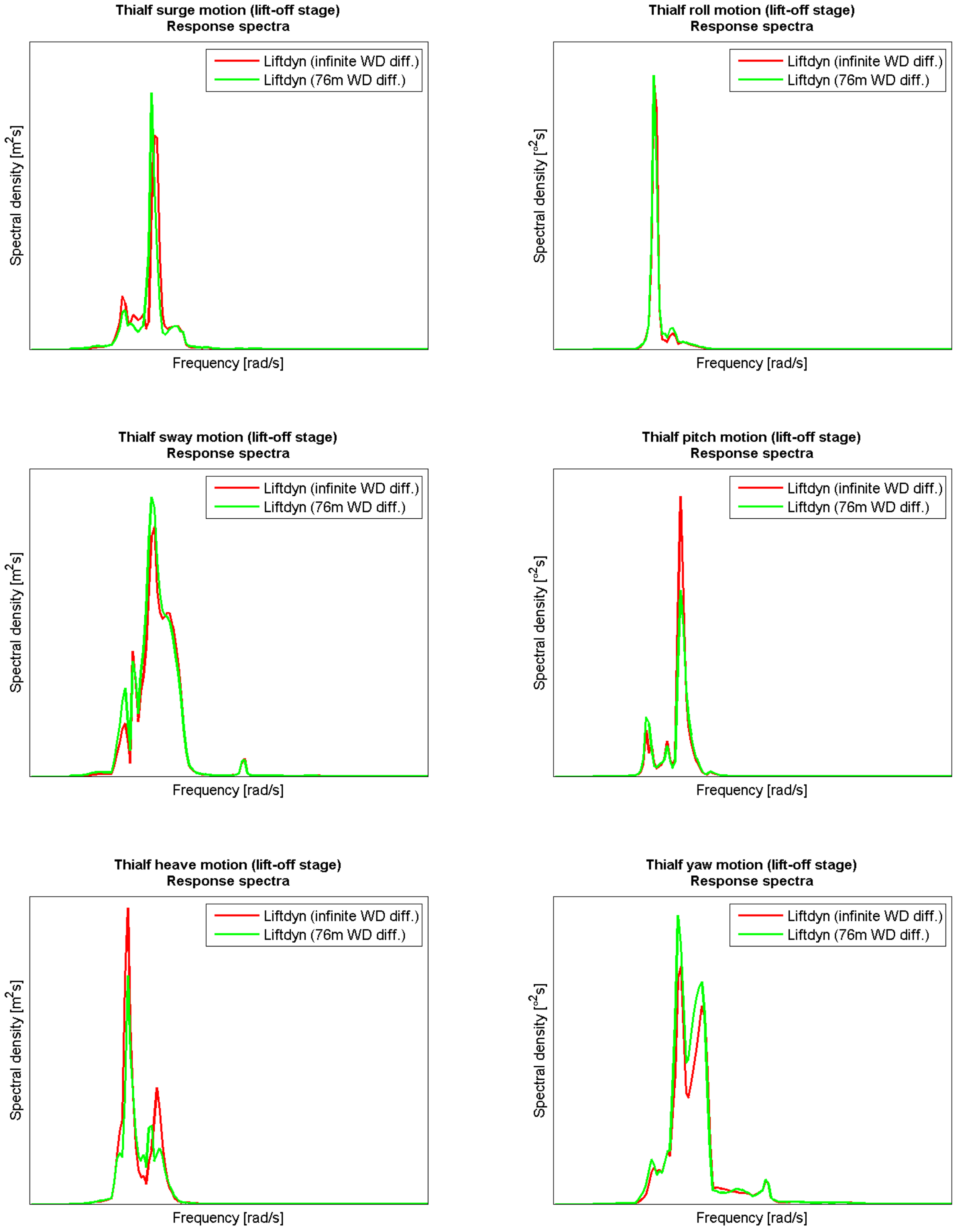

Figure C.3: Thialf response - Infinite vs. actual WD (lift-off)

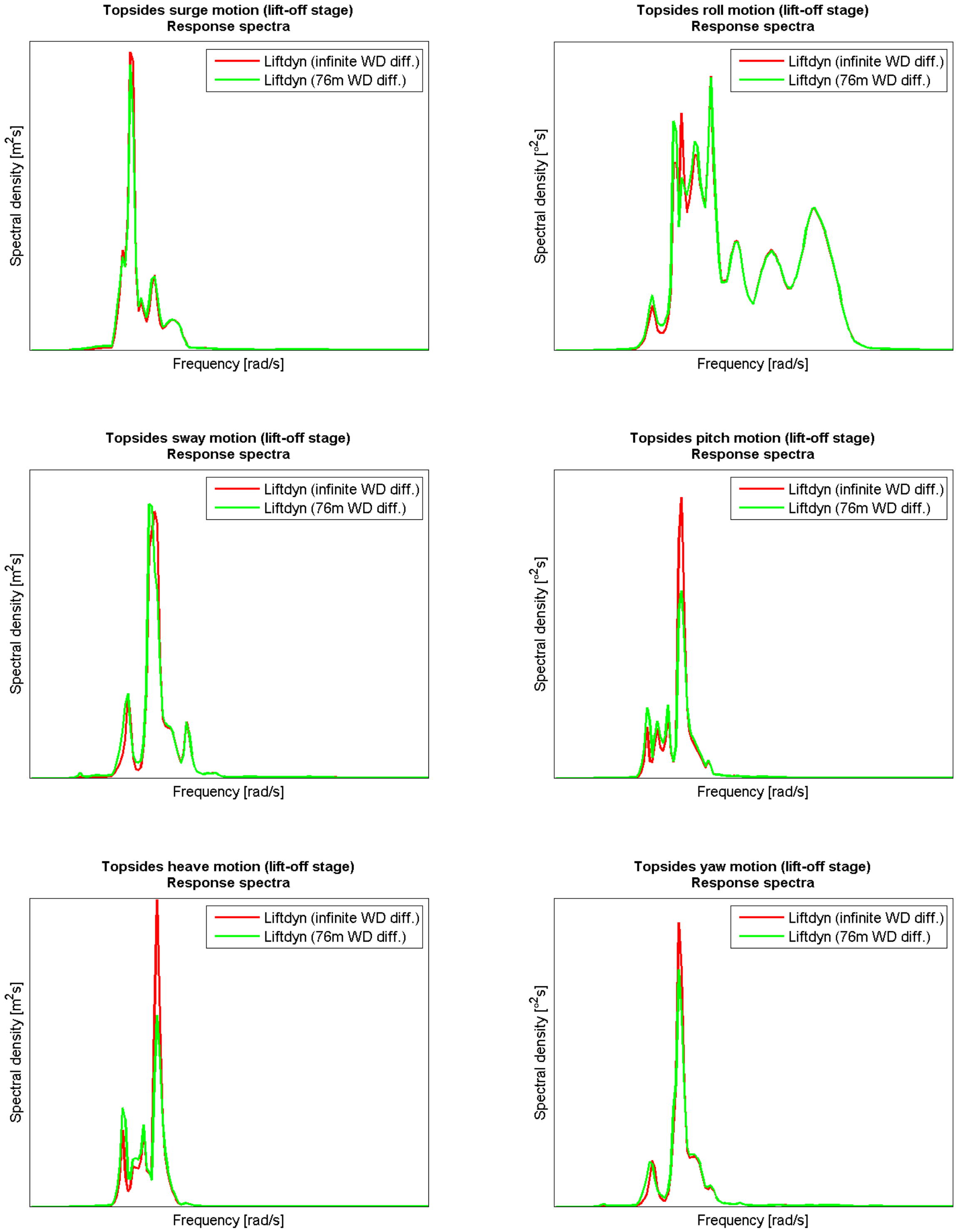

Figure C.4: Topsides/H-542 response - Infinite vs. actual WD (lift-off)

D

Motion measurement data processing

This appendix contains some example plots from the different steps taken for processing the raw Siri motion sensor signals.

Especially the rotational velocity measurements proved to be very noisy. The purpose of this appendix is to give the reader a general impression of the reliability of measurements. The data presented has been obtained for all sensors, lift stages and full time traces; results from the other sensors and stages were similar and have been omitted from this appendix. For sensor S4, the motions spectra have been given for all four stages, because for this sensor a cross-check comparison with the Thialf's MRU system was possible.

The results have been used for obtaining the motions spectra presented in appendix E.

1. S1 surge - Integrated accelerations (lift-off)
2. S1 sway - Integrated accelerations (lift-off)
3. S1 heave - Integrated accelerations (lift-off)
4. S1 roll - Integrated velocities (lift-off)
5. S1 pitch - Integrated velocities (lift-off)
6. S1 yaw - Integrated velocities (lift-off)
7. Subtracting gravity components - S1 (lift-off)
8. Subtracting gravity components - S2 (lift-off)
9. Subtracting gravity components - S4 (lift-off)
10. Siri vs. MRU - S4 (free-floating)
11. Siri vs. MRU - S4 (lift-off)
12. Siri vs. MRU - S4 (free-hanging)
13. Siri vs. MRU - S4 (set-down)

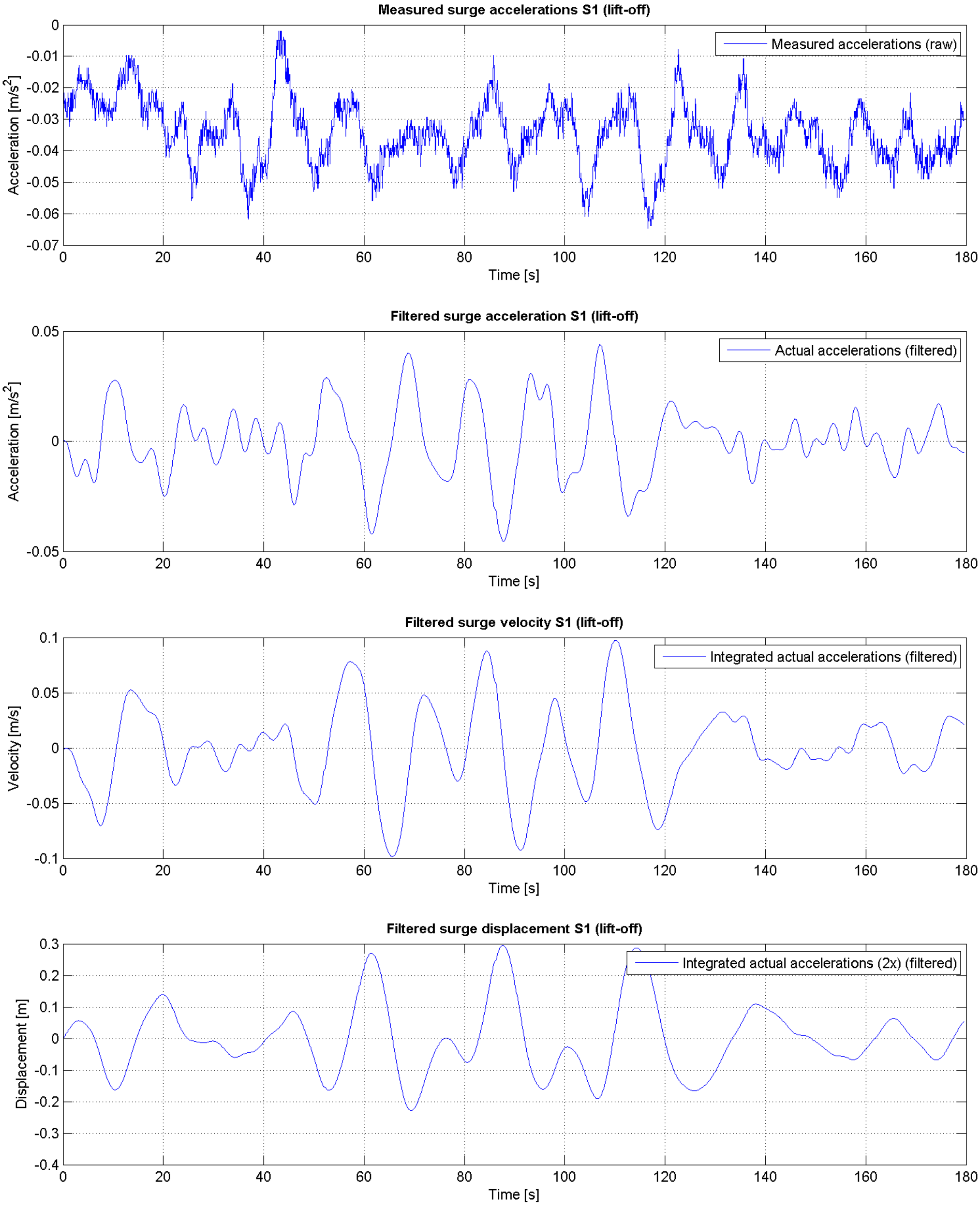

Figure D.1: Signal integration - S1 surge (lift-off)

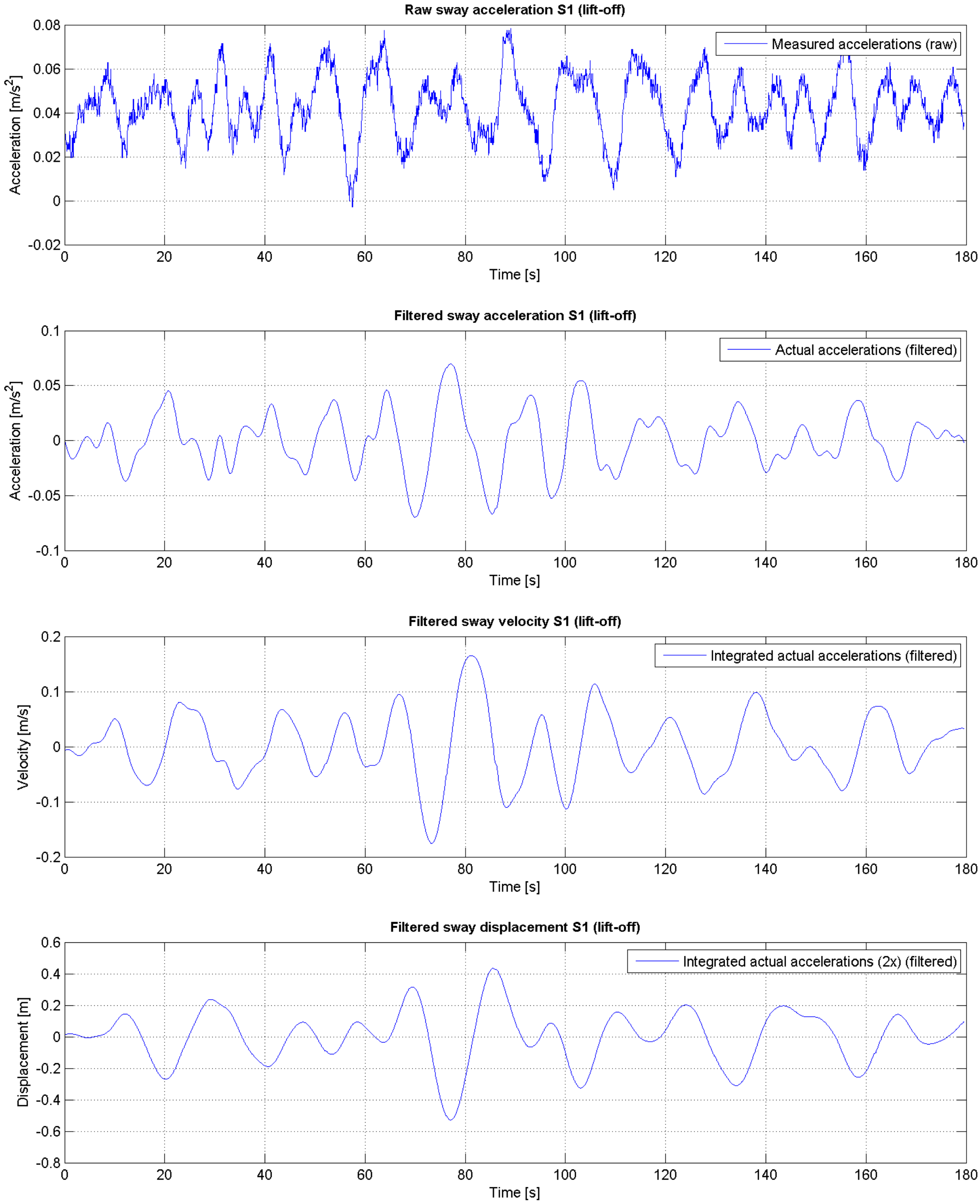

Figure D.2: Signal integration - S1 sway (lift-off)

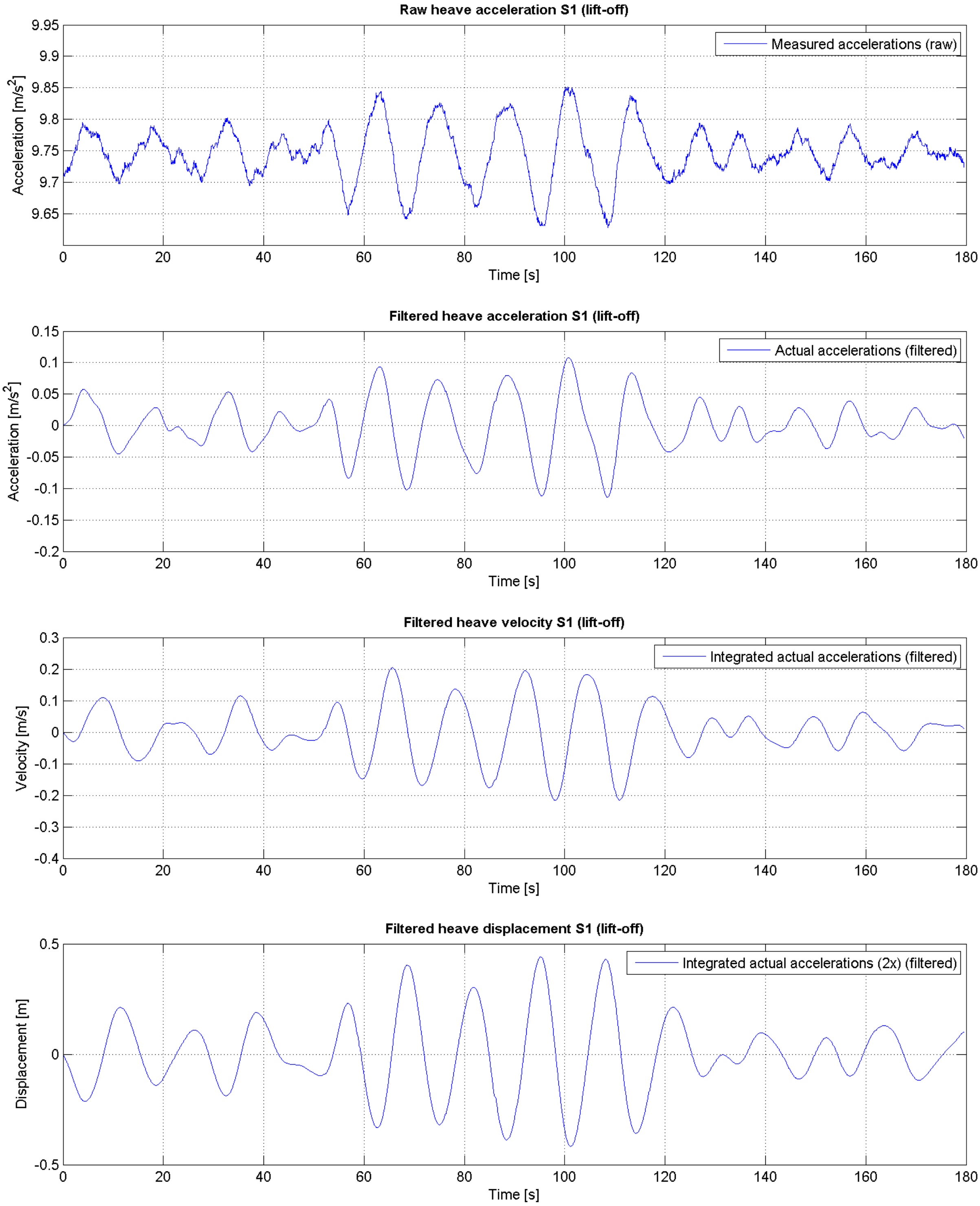

Figure D.3: Signal integration - S1 heave (lift-off)

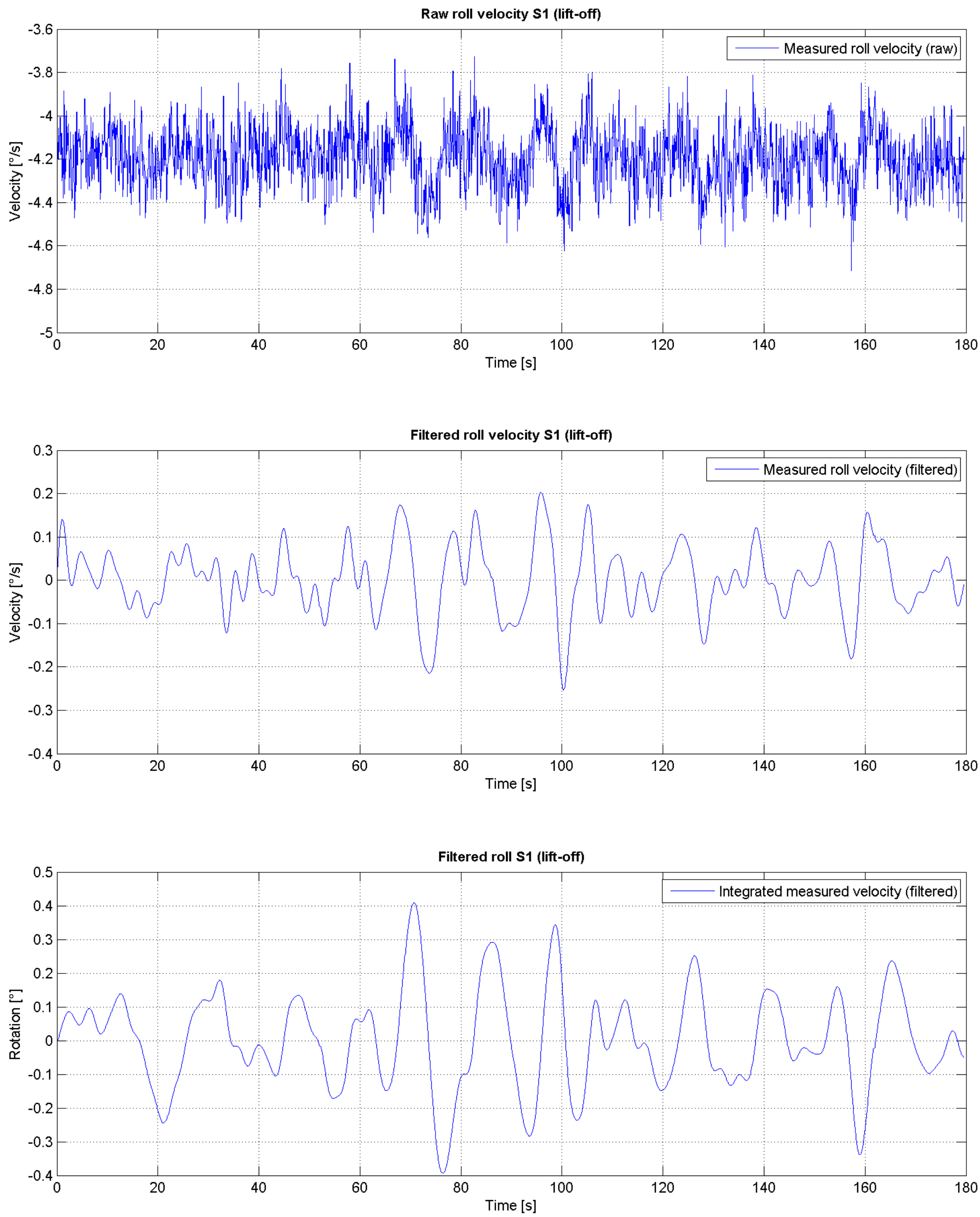

Figure D.4: Signal integration - S1 roll (lift-off)

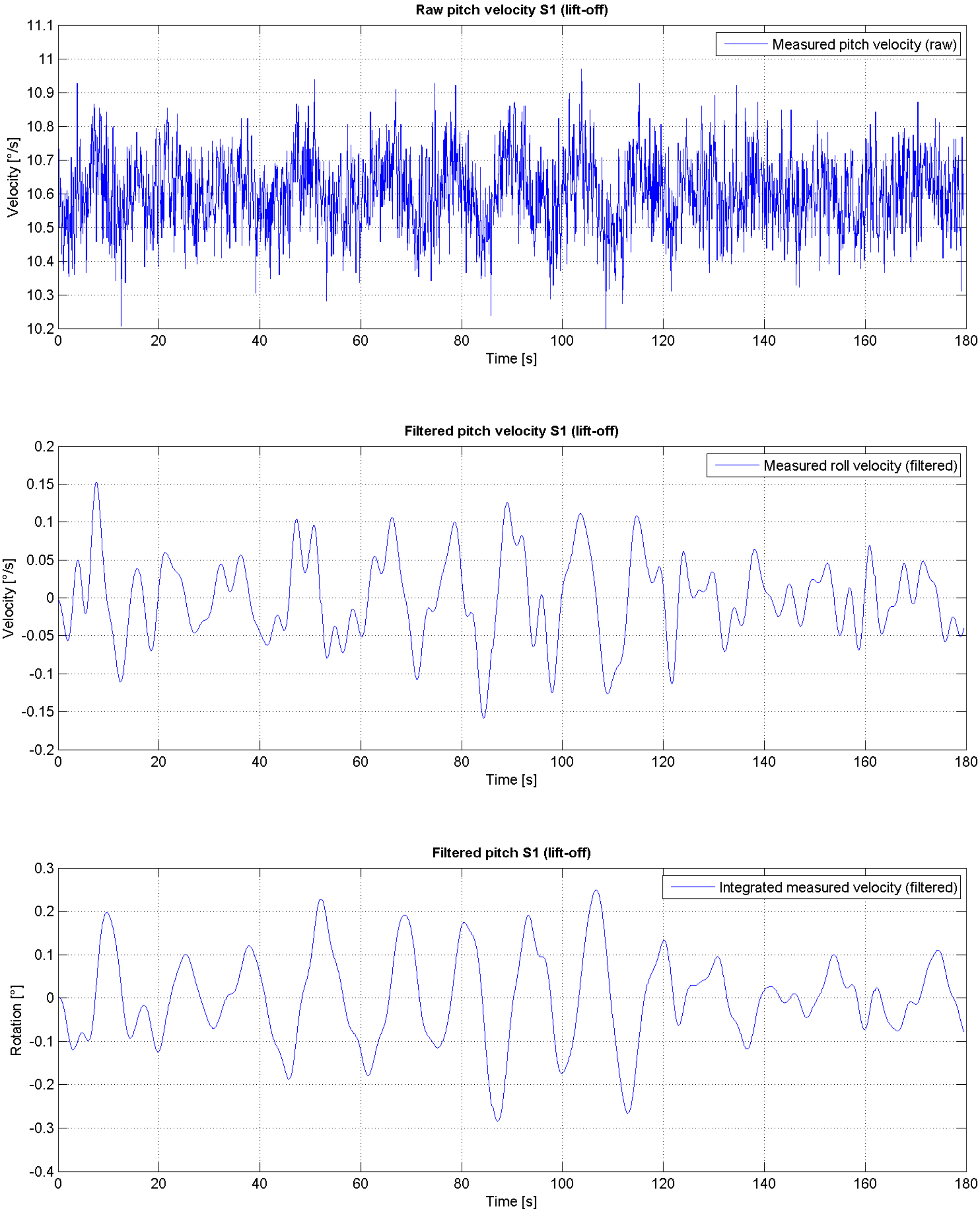

Figure D.5: Signal integration - S1 pitch (lift-off)

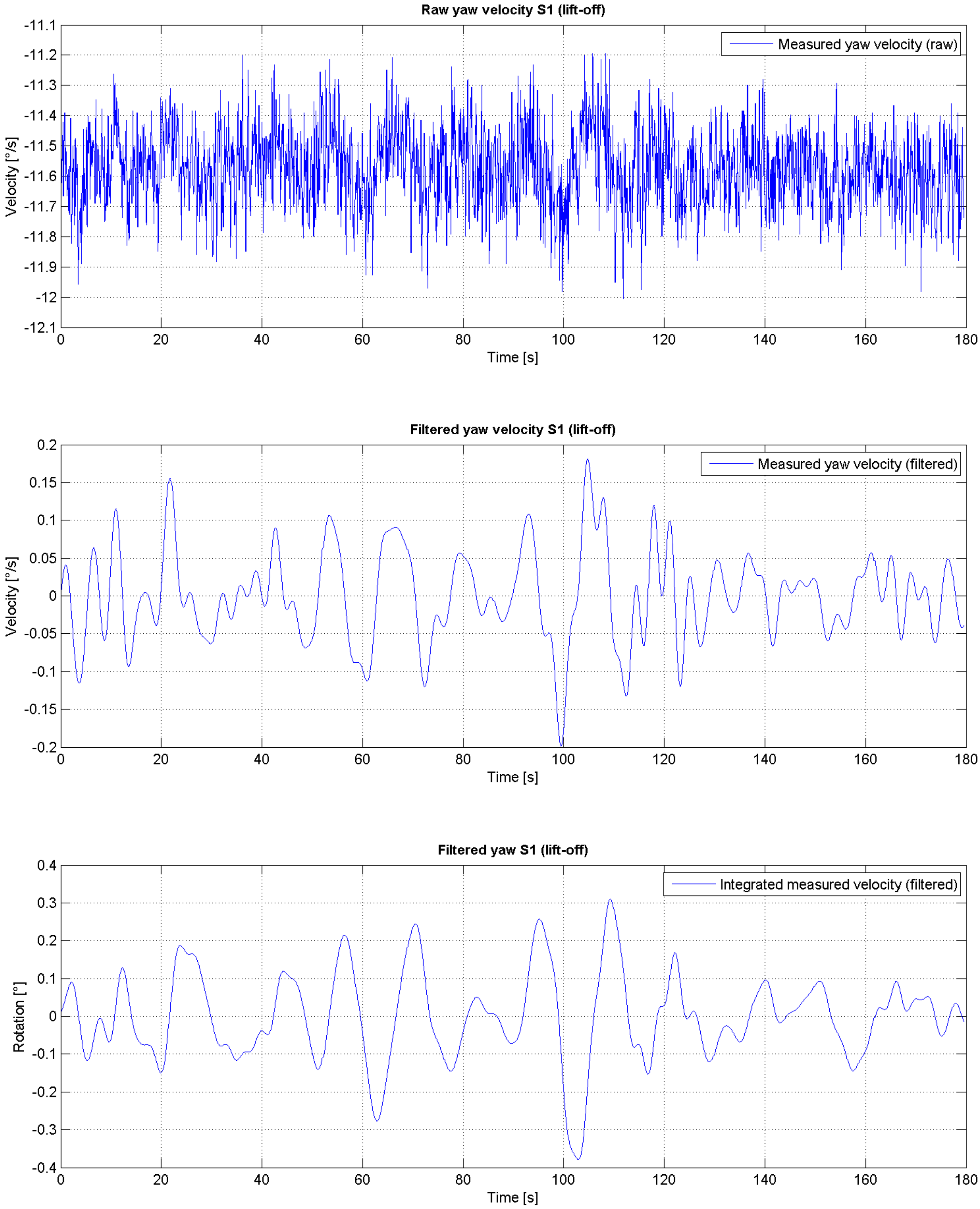

Figure D.6: Signal integration - S1 yaw (lift-off)

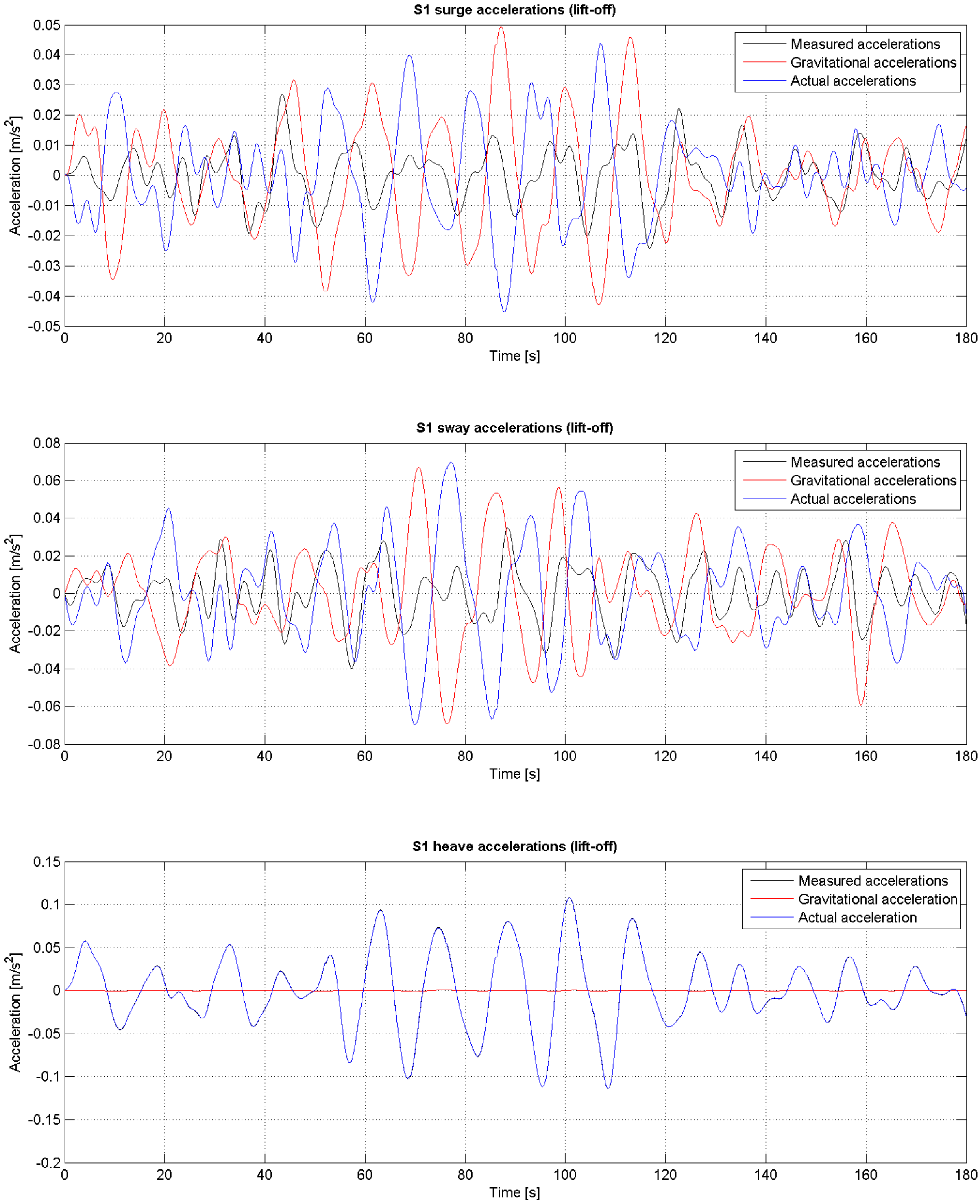

Figure D.7: Subtracting gravity components - S1 (lift-off)

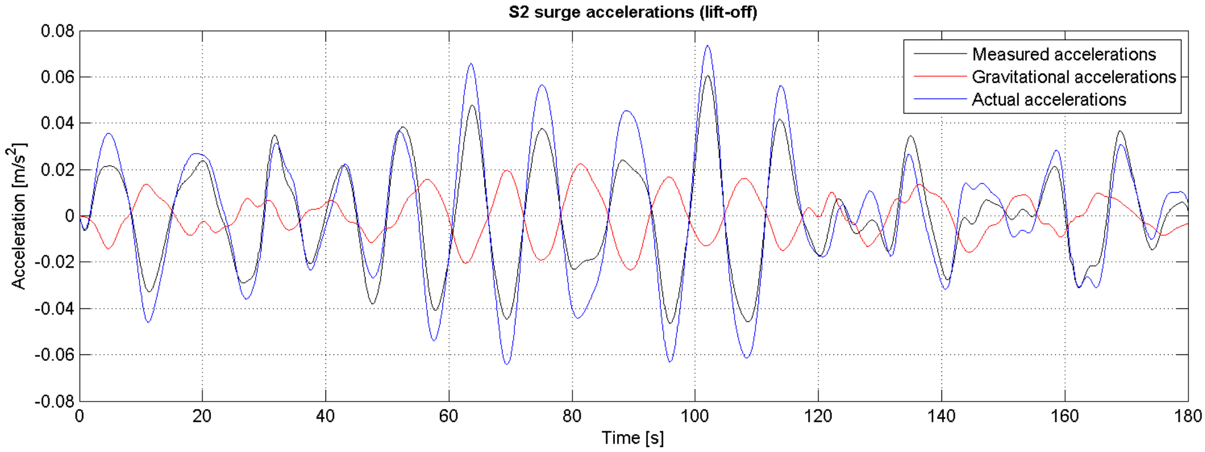

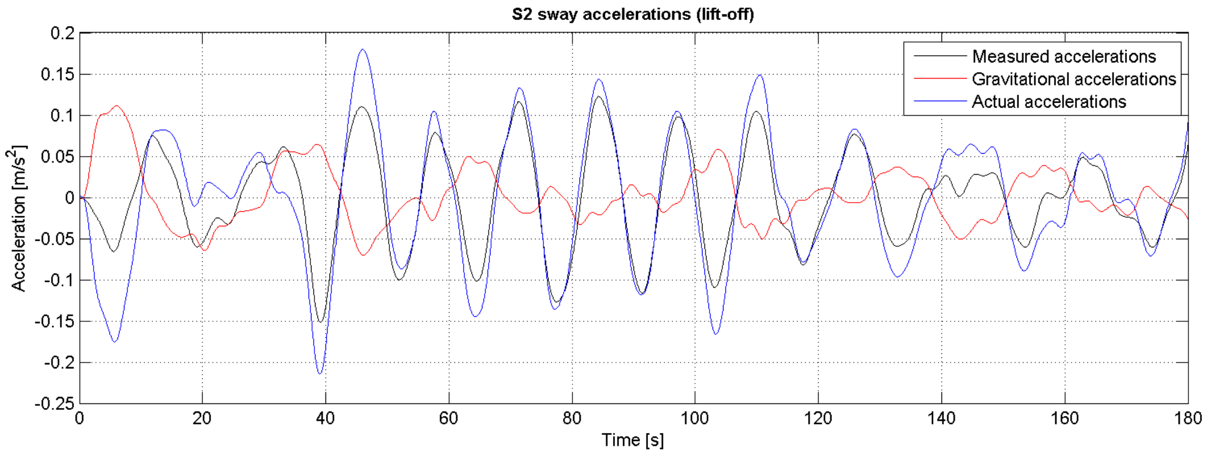

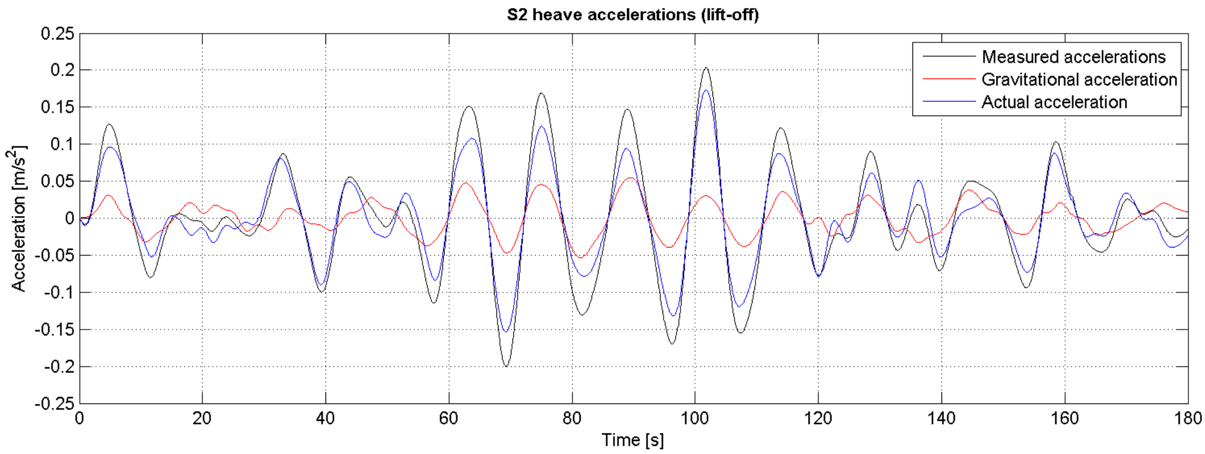

Figure D.8: Subtracting gravity components - S2 (lift-off)

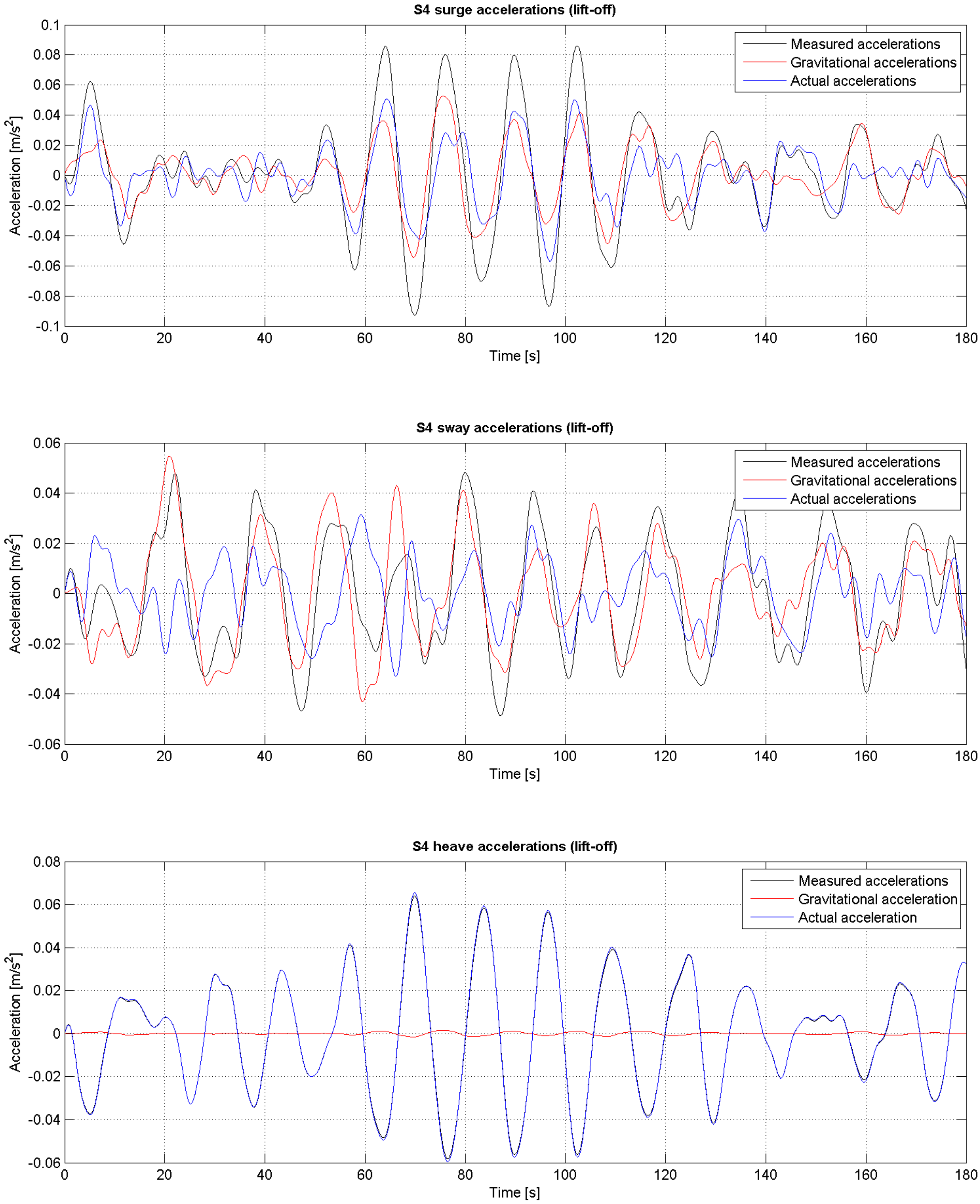

Figure D.9: Subtracting gravity components - S4 (lift-off)

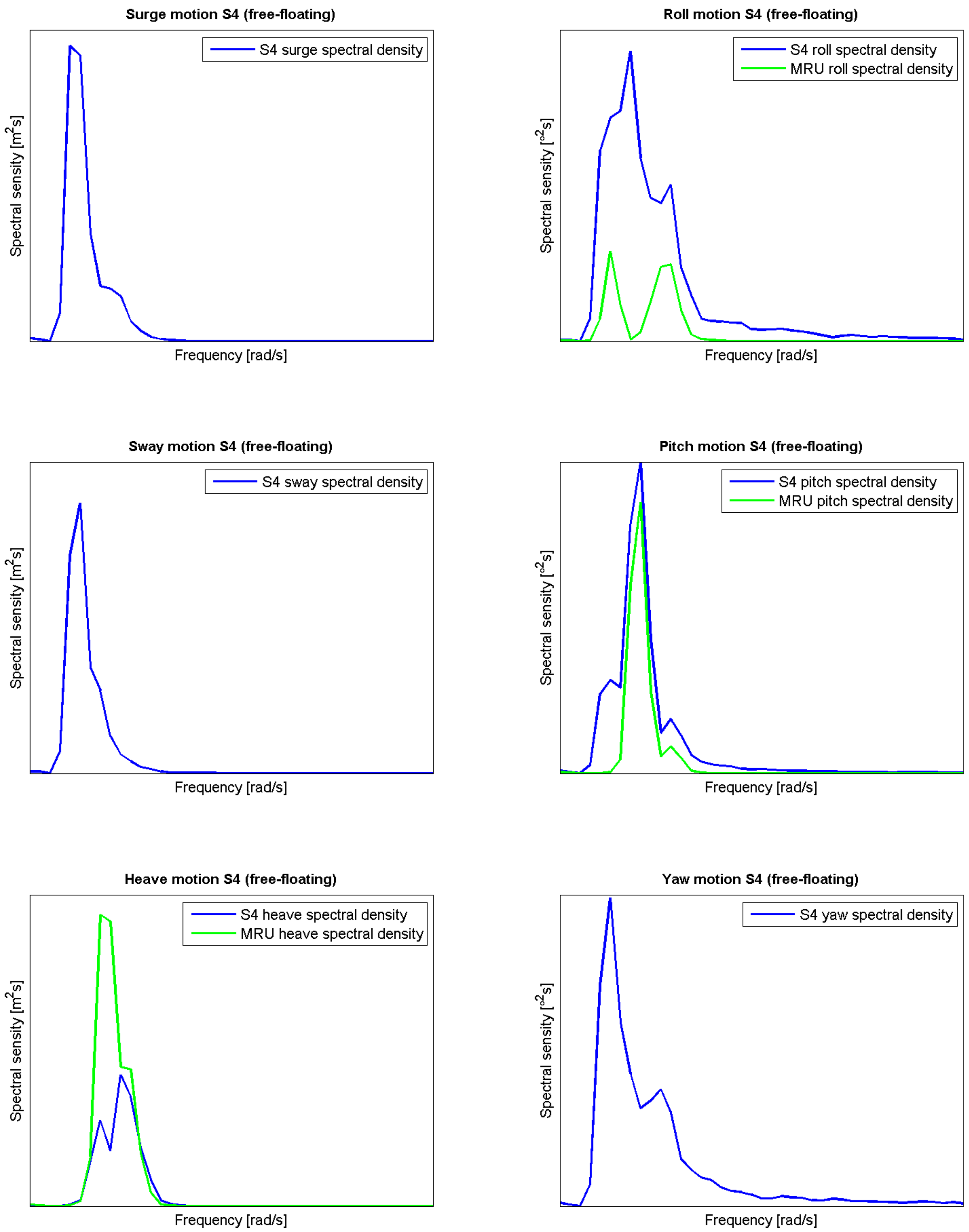

Figure D.10: Siri vs. MRU - S4 (free-floating)

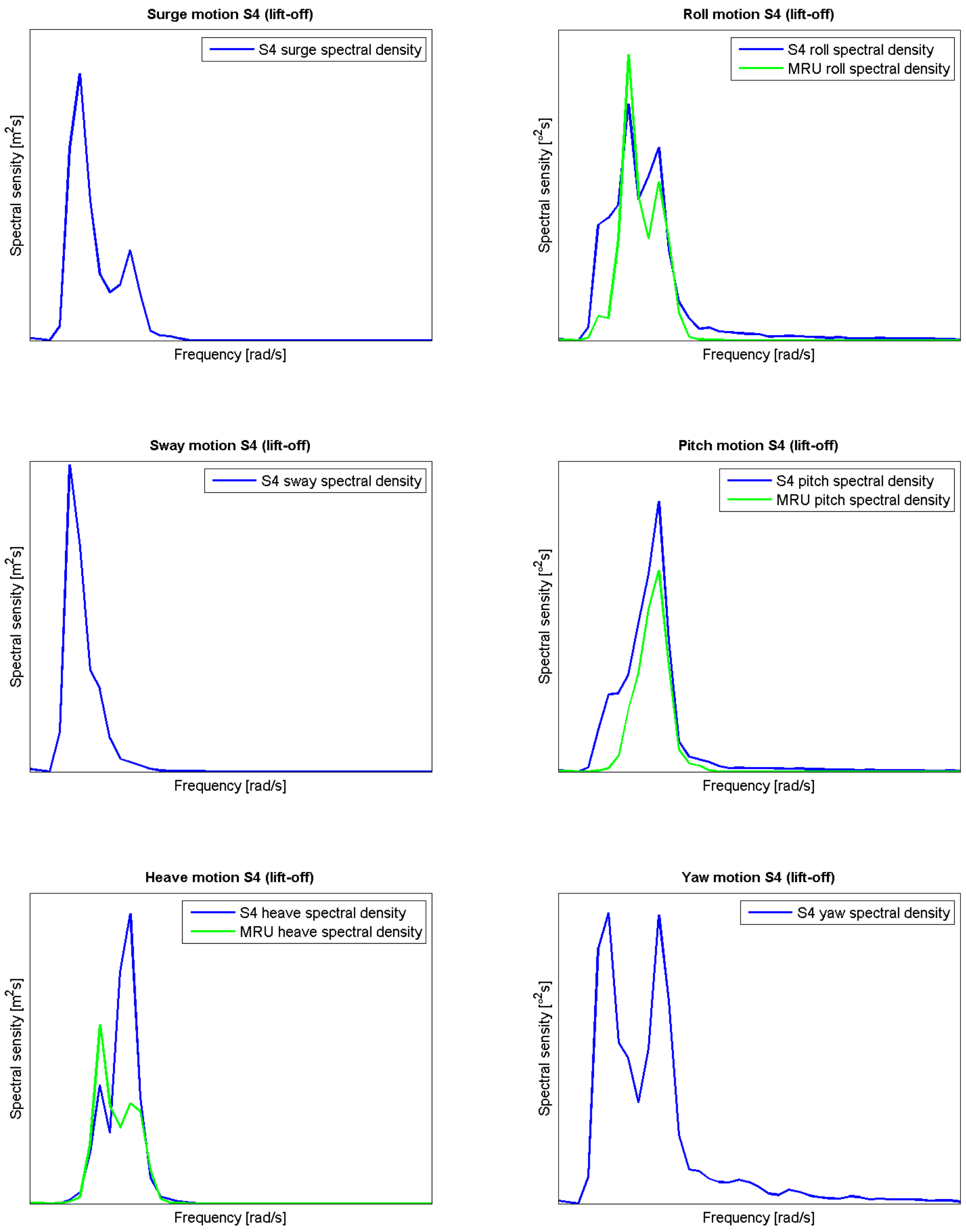

Figure D.11: Siri vs. MRU - S4 (lift-off)

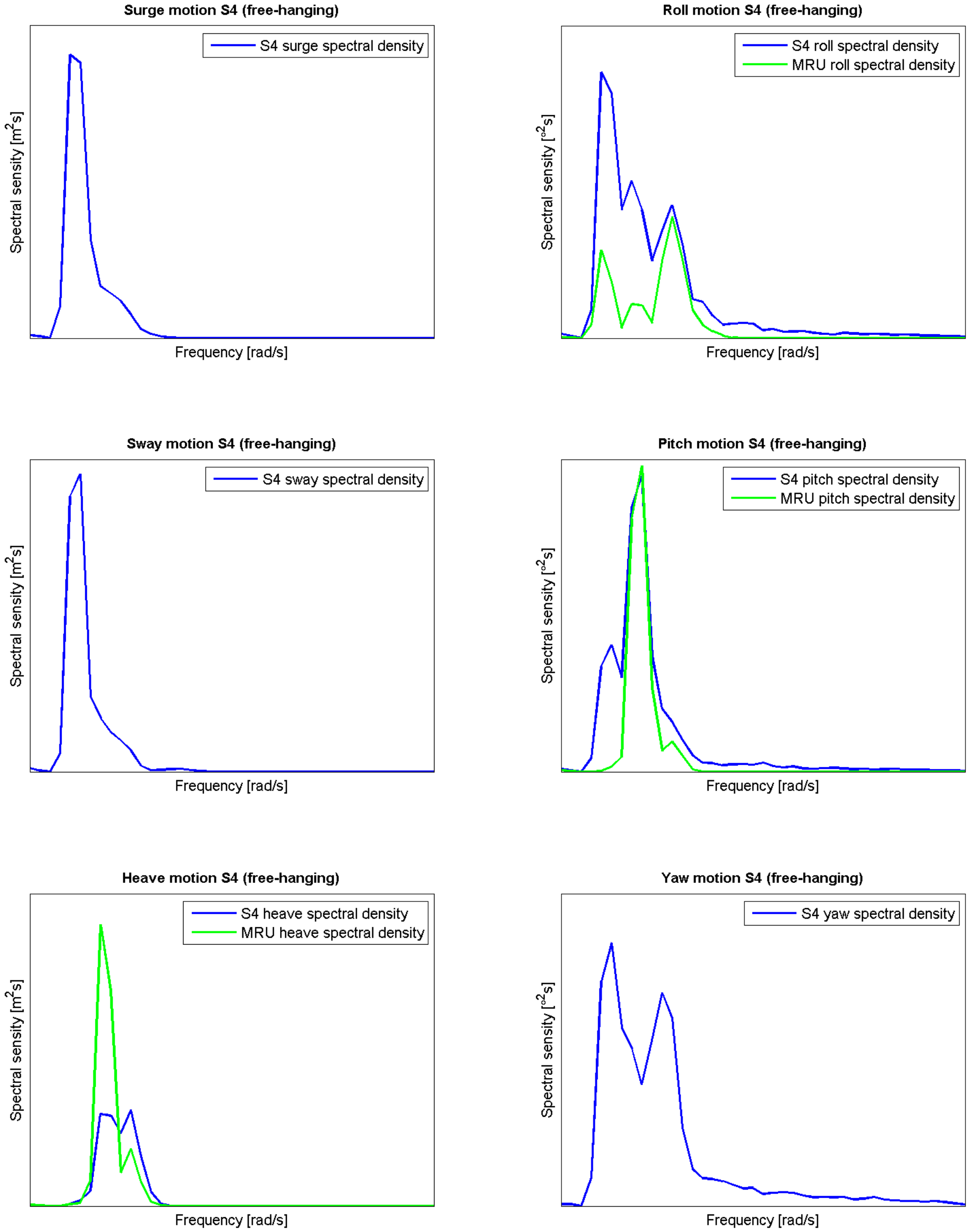

Figure D.12: Siri vs. MRU - S4 (free-hanging)

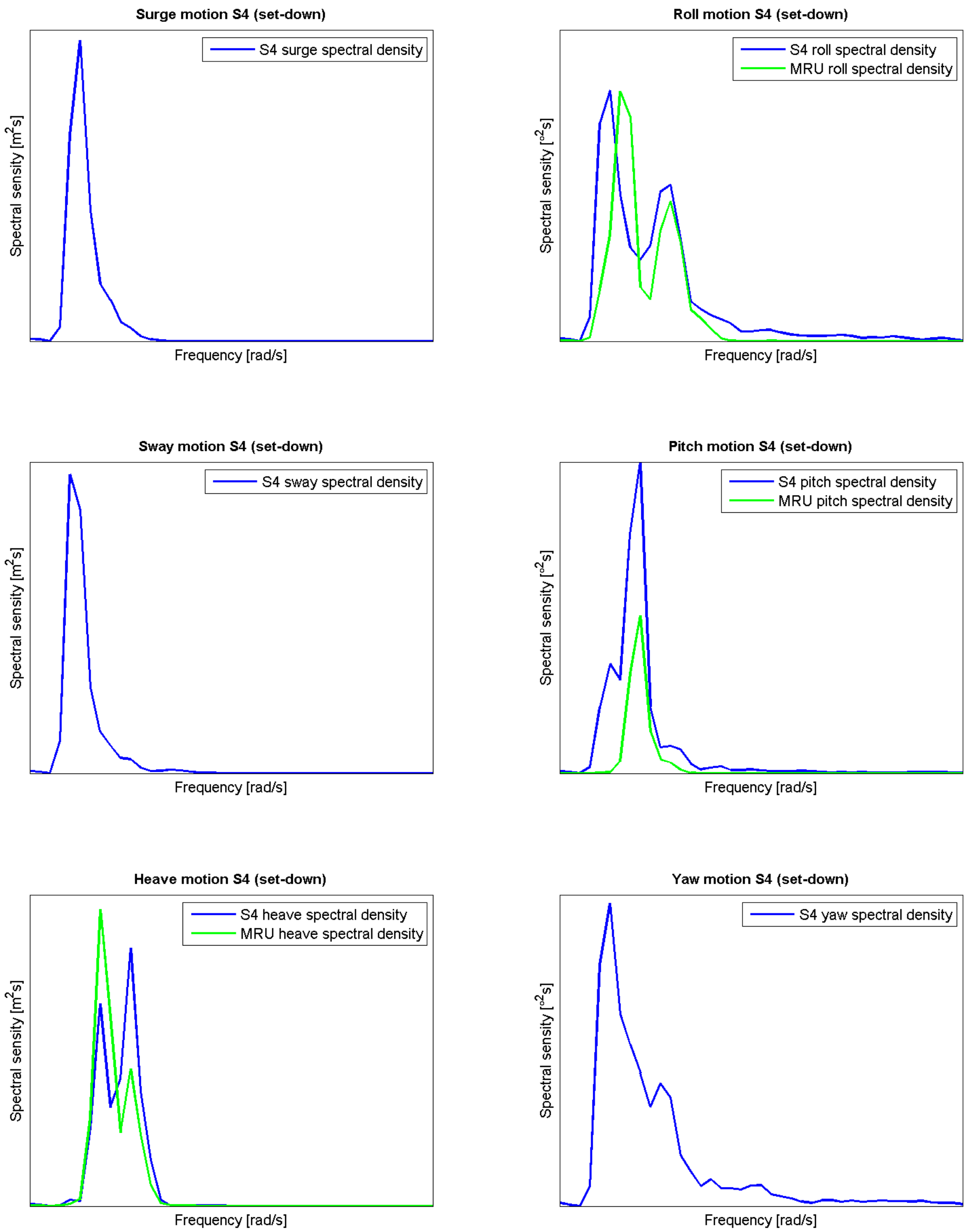

Figure D.13: Siri vs. MRU - S4 (set-down)

E

Modelled vs. measured motion response

ALTERED/OMITTED FOR CONFIDENTIALITY REASONS:This appendix contains measured motion time traces and modelled vs. measured response spectra, for all sensors (in local coordinates, please refer to section 3.3.1) and stages considered:

1. Free-floating stage - Thialf translations (at CoG)
2. Free-floating stage - Thialf rotations
3. Free-floating stage - Topsides translations (at CoG)
4. Free-floating stage - Topsides rotations
5. Free-floating stage - SB boom translations (at main fall axle (S2))
6. Free-floating stage - SB boom rotations
7. Lift-off stage - Thialf translations (at CoG)
8. Lift-off stage - Thialf rotations
9. Lift-off stage - Topsides translations (at CoG)
10. Lift-off stage - Topsides rotations
11. Lift-off stage - SB boom translations (at main fall axle (S2))
12. Lift-off stage - SB boom rotations
13. Free-hanging stage - Thialf translations (at CoG)
14. Free-hanging stage - Thialf rotations
15. Free-hanging stage - Topsides translations (at CoG)
16. Free-hanging stage - Topsides rotations
17. Free-hanging stage - SB boom translations (at main fall axle (S2))
18. Free-hanging stage - SB boom rotations
19. Set-down stage - Thialf translations (at CoG)
20. Set-down stage - Thialf rotations
21. Set-down stage - SB boom translations (at main fall axle (S2))
22. Set-down stage - SB boom rotations

(no topsides motions for set-down stage)

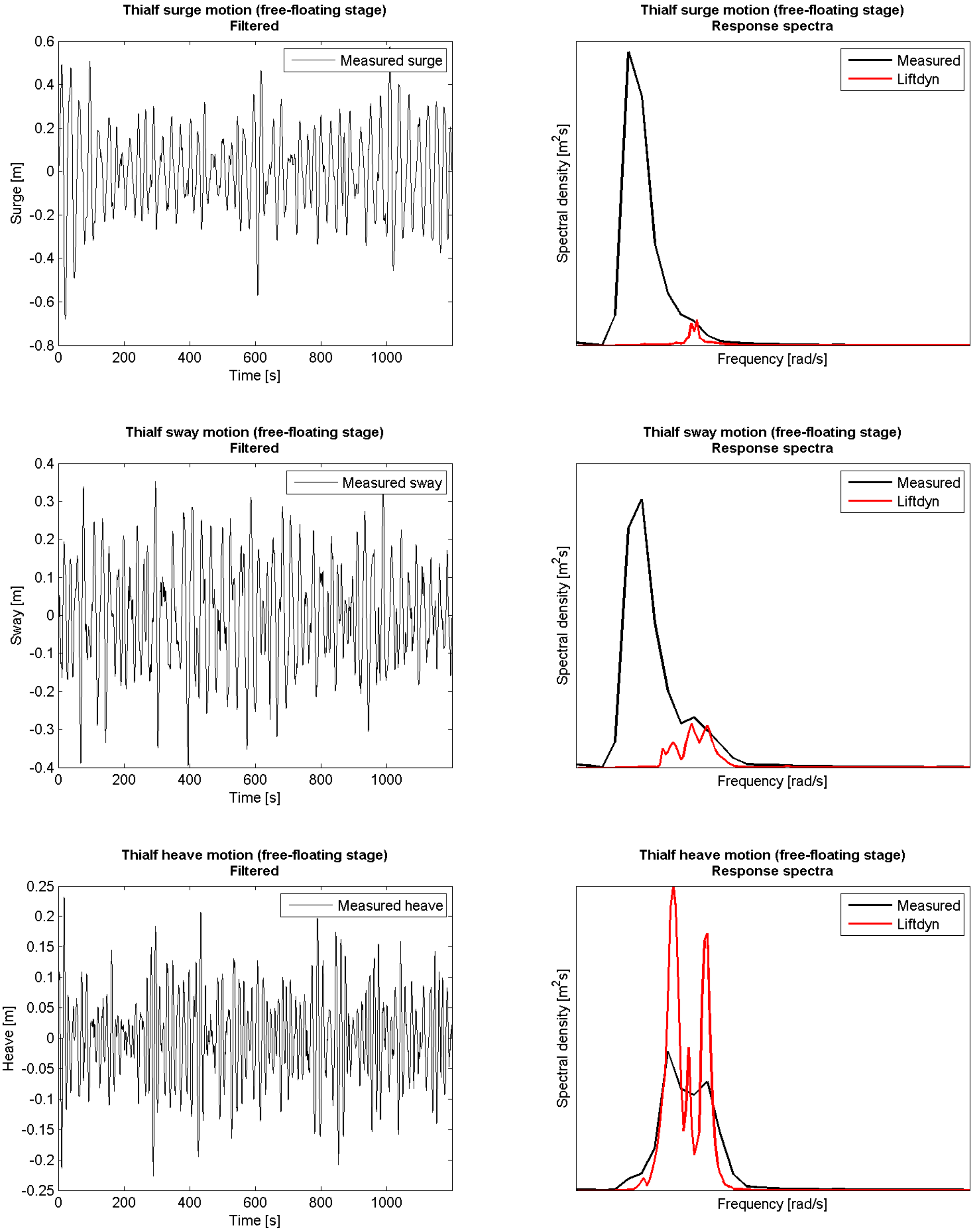

Figure E.1: Free-floating stage - Thialf translations (at CoG)

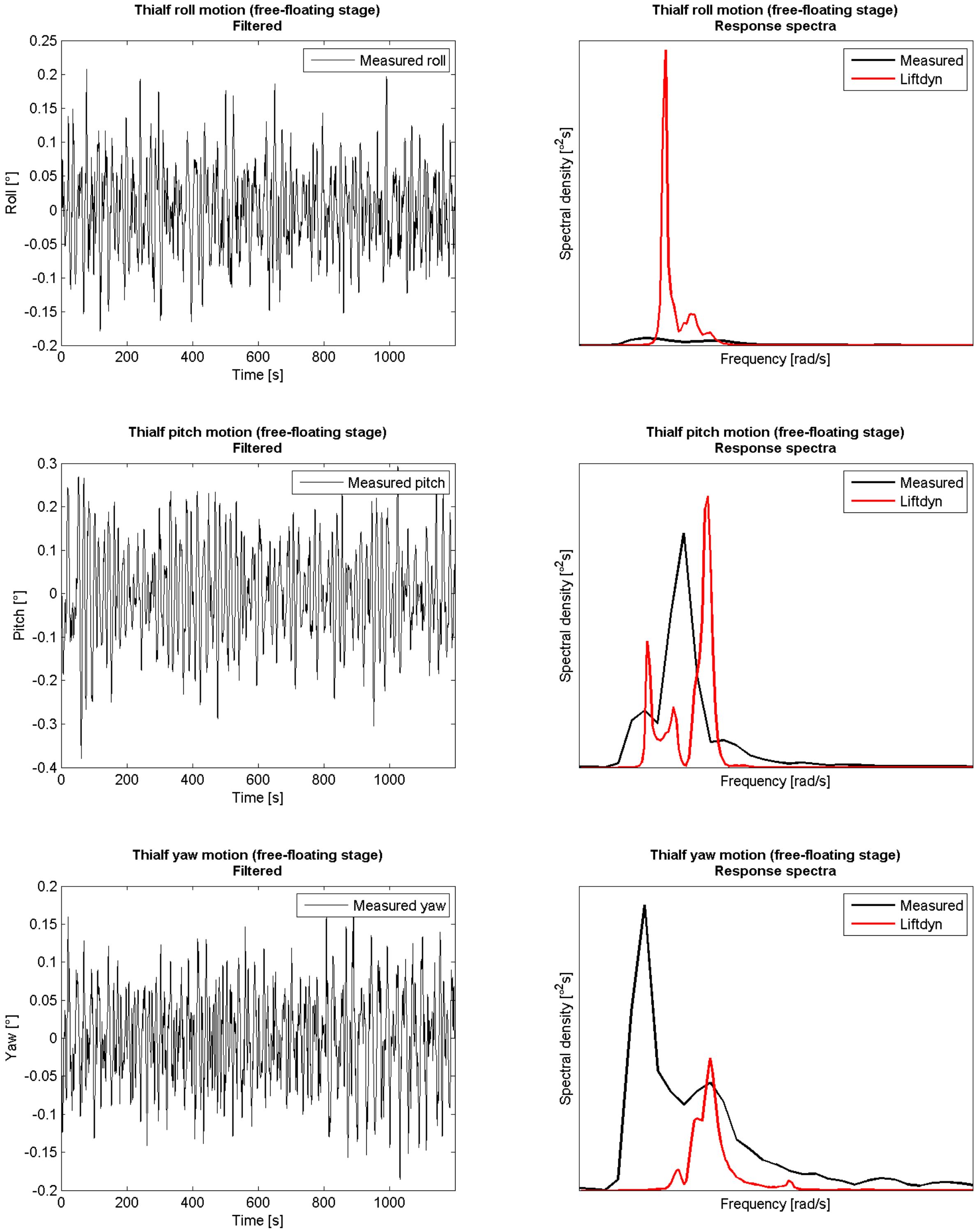

Figure E.2: Free-floating stage - Thialf rotations

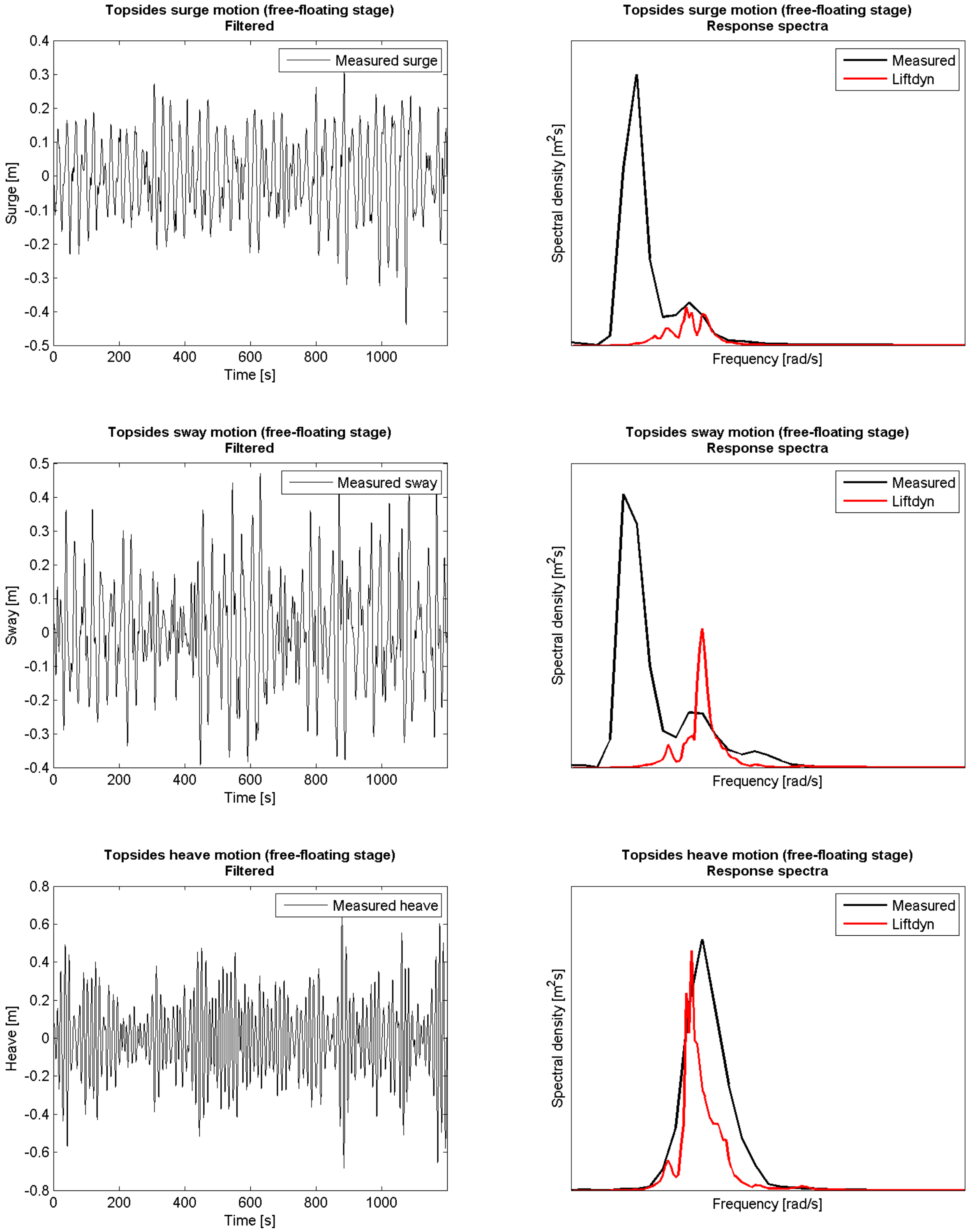

Figure E.3: Free-floating stage - Topsides translations (at CoG)

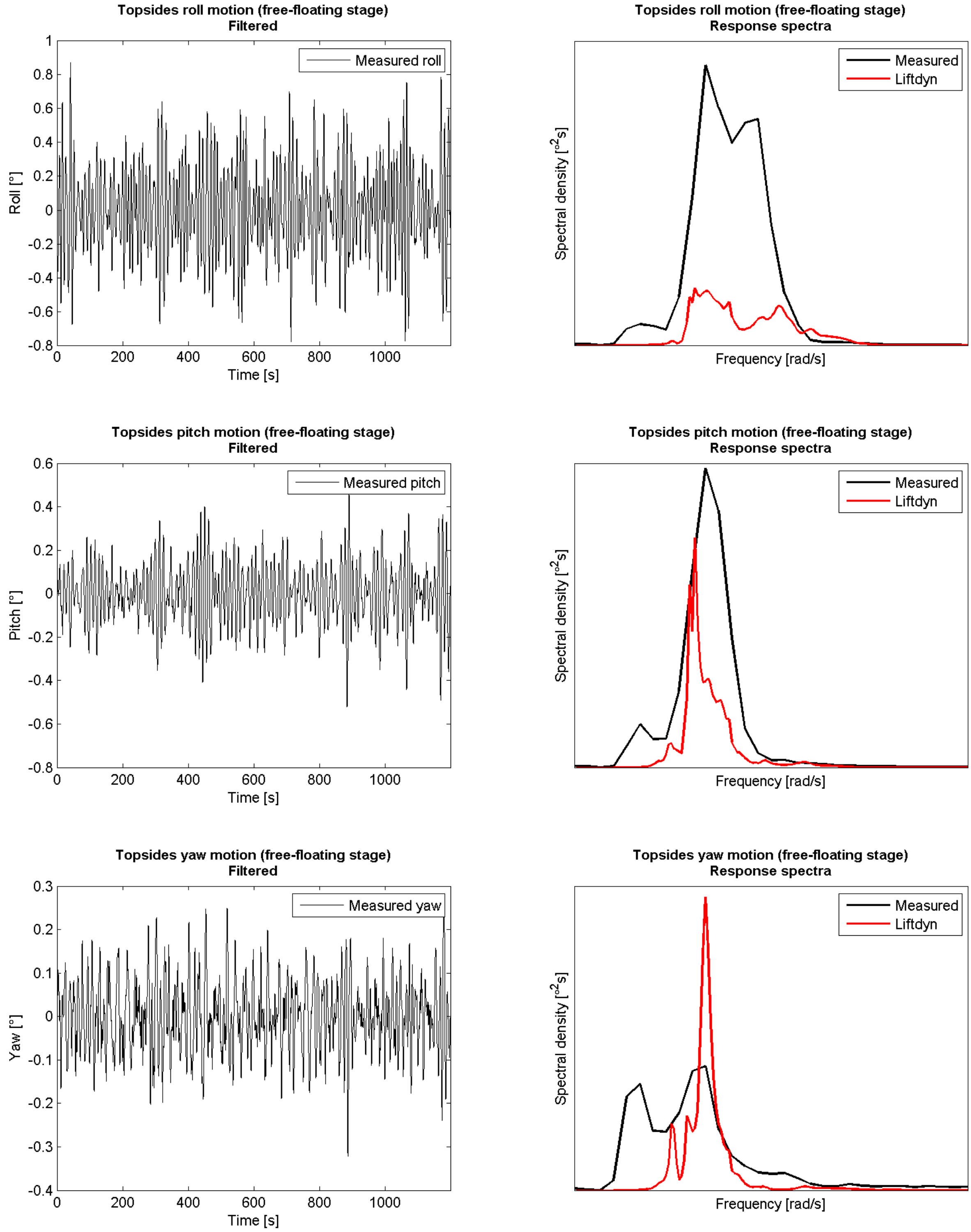

Figure E.4: Free-floating stage - Thialf rotations

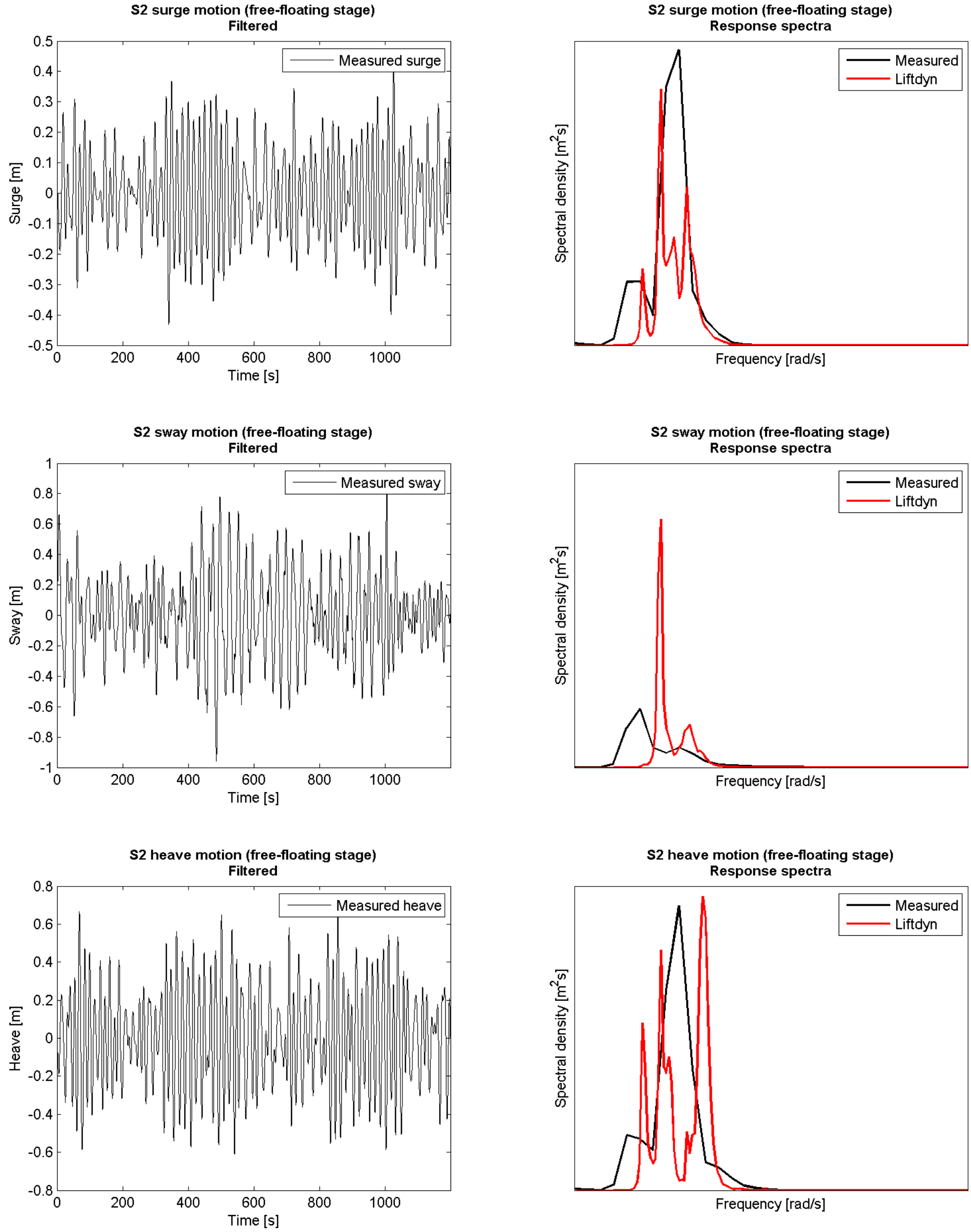

Figure E.5: Free-floating stage - SB boom translations (at main fall axle (S2))

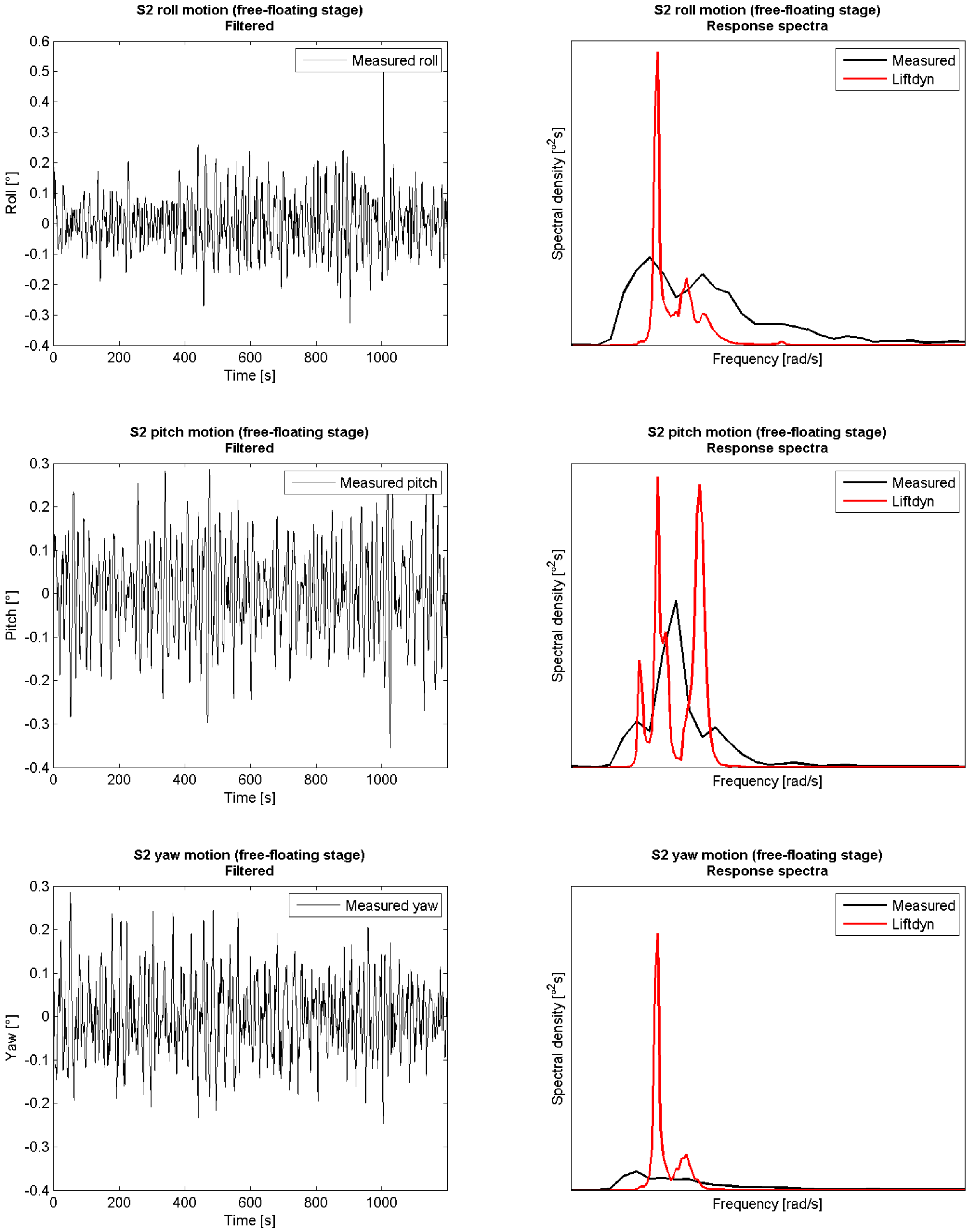

Figure E.6: Free-floating stage - SB boom rotations

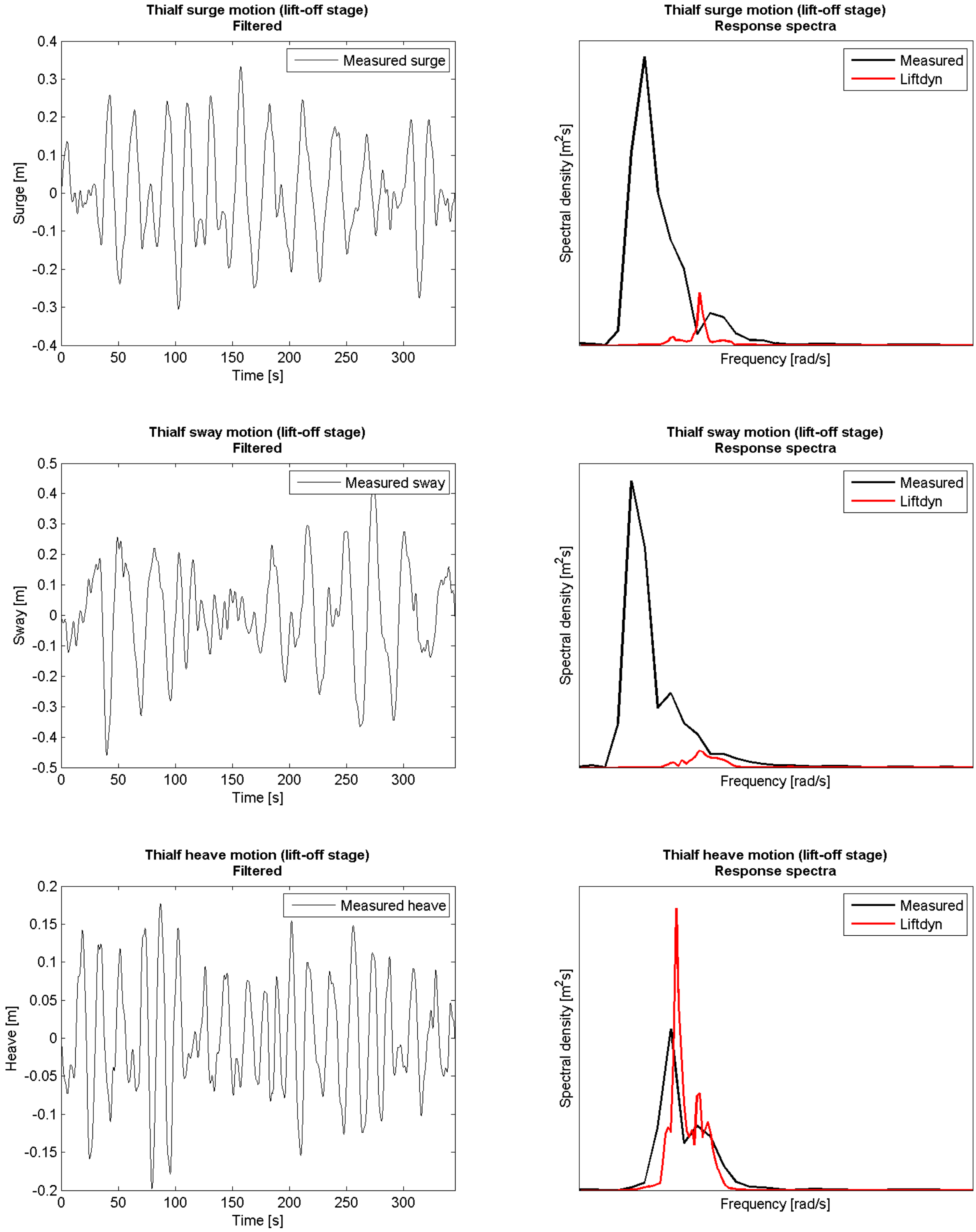

Figure E.7: Lift-off stage - Thialf translations (at CoG)

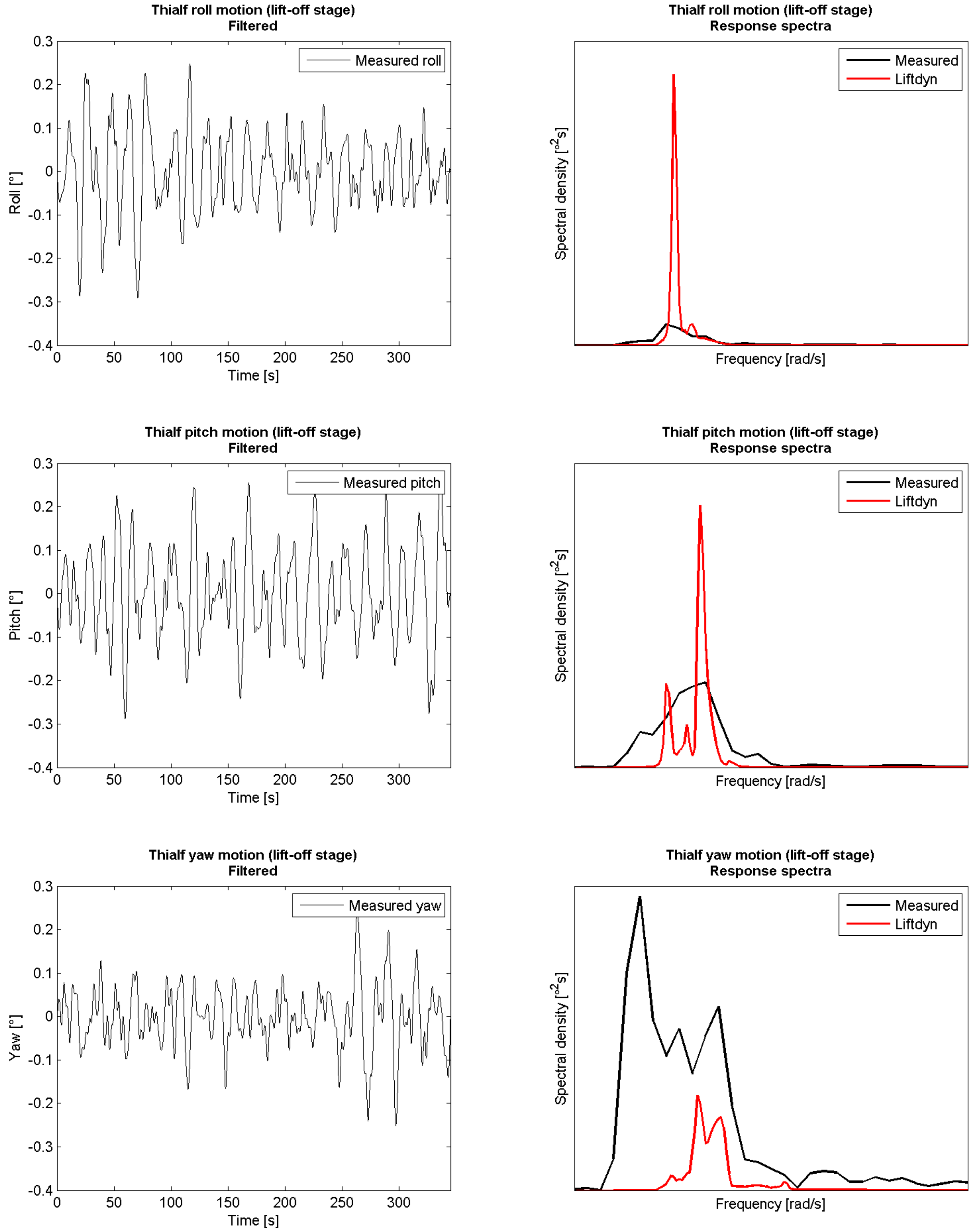

Figure E.8: Lift-off stage - Thialf rotations

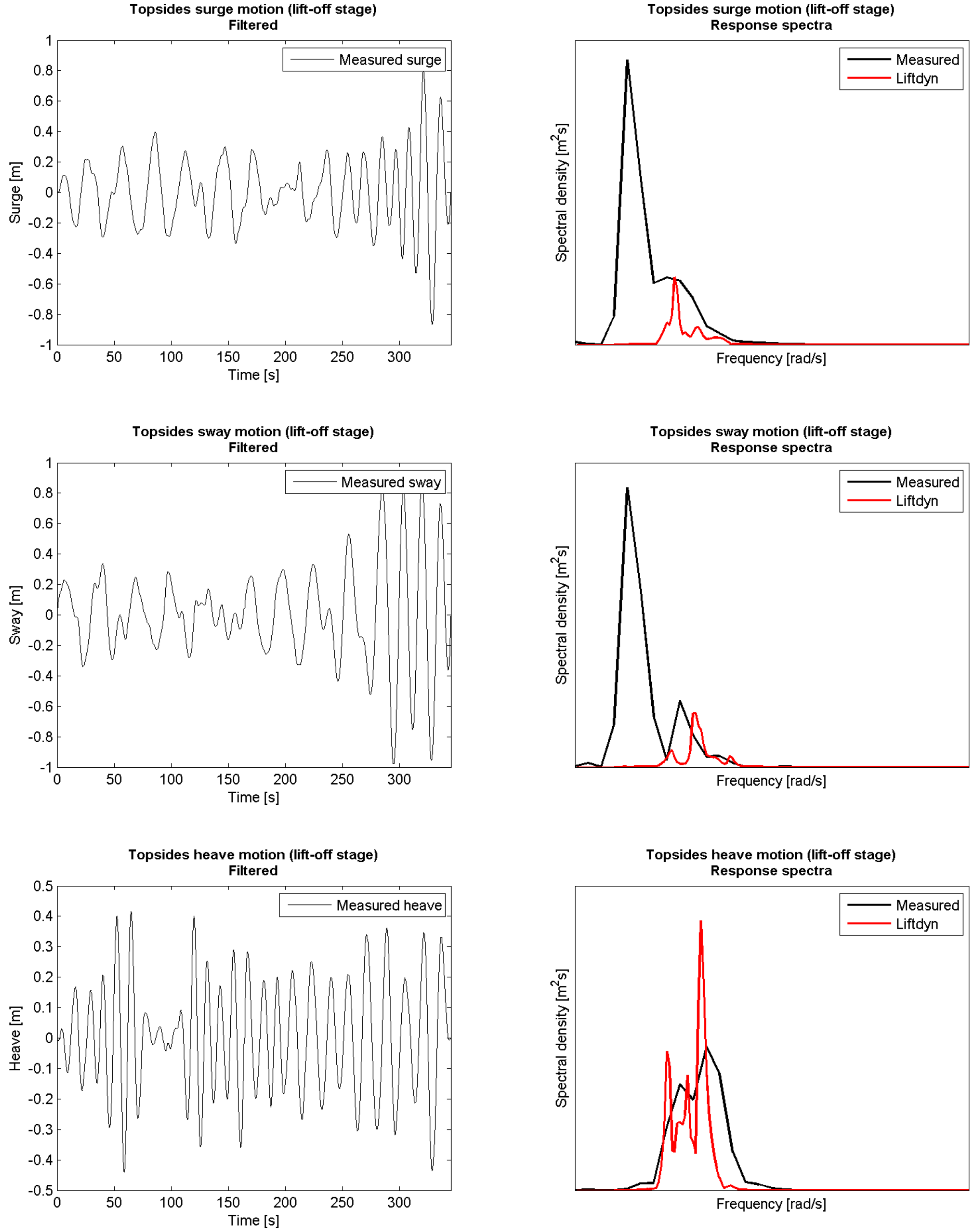

Figure E.9: Lift-off stage - Topsides translations (at CoG)

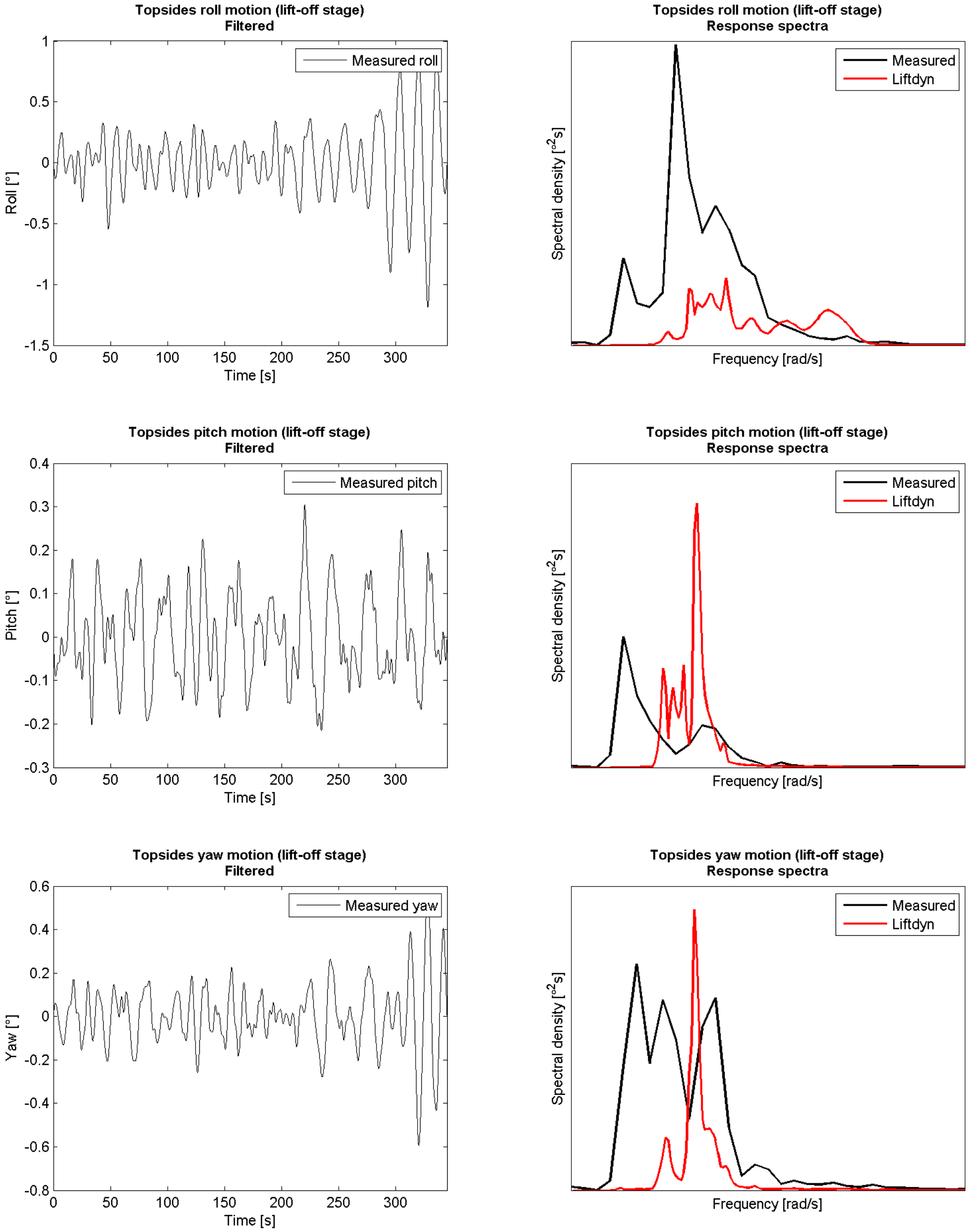

Figure E.10: Lift-off stage - Thialf rotations

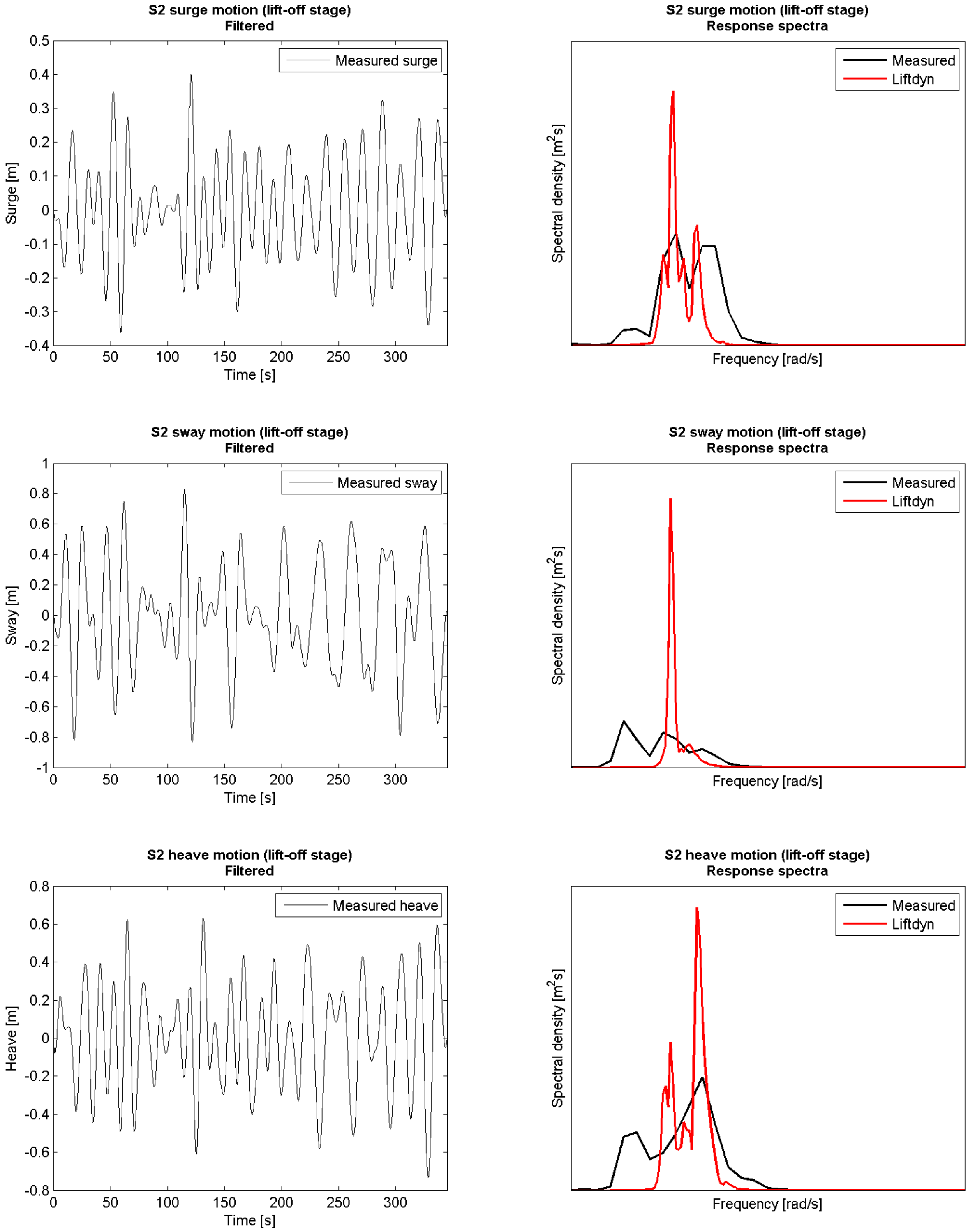

Figure E.11: Lift-off stage - SB boom translations (at main fall axle (S2))

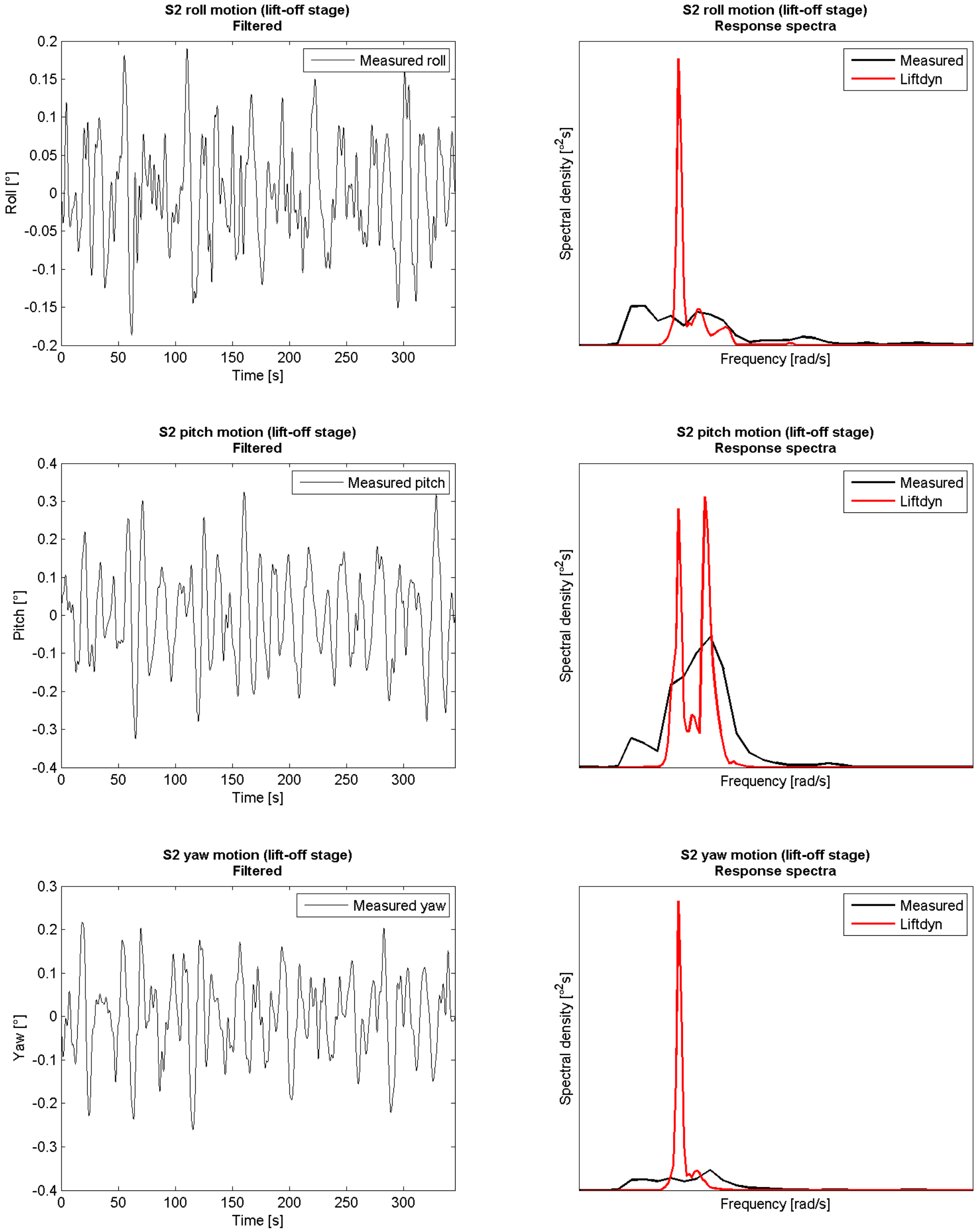

Figure E.12: Lift-off stage - SB boom rotations

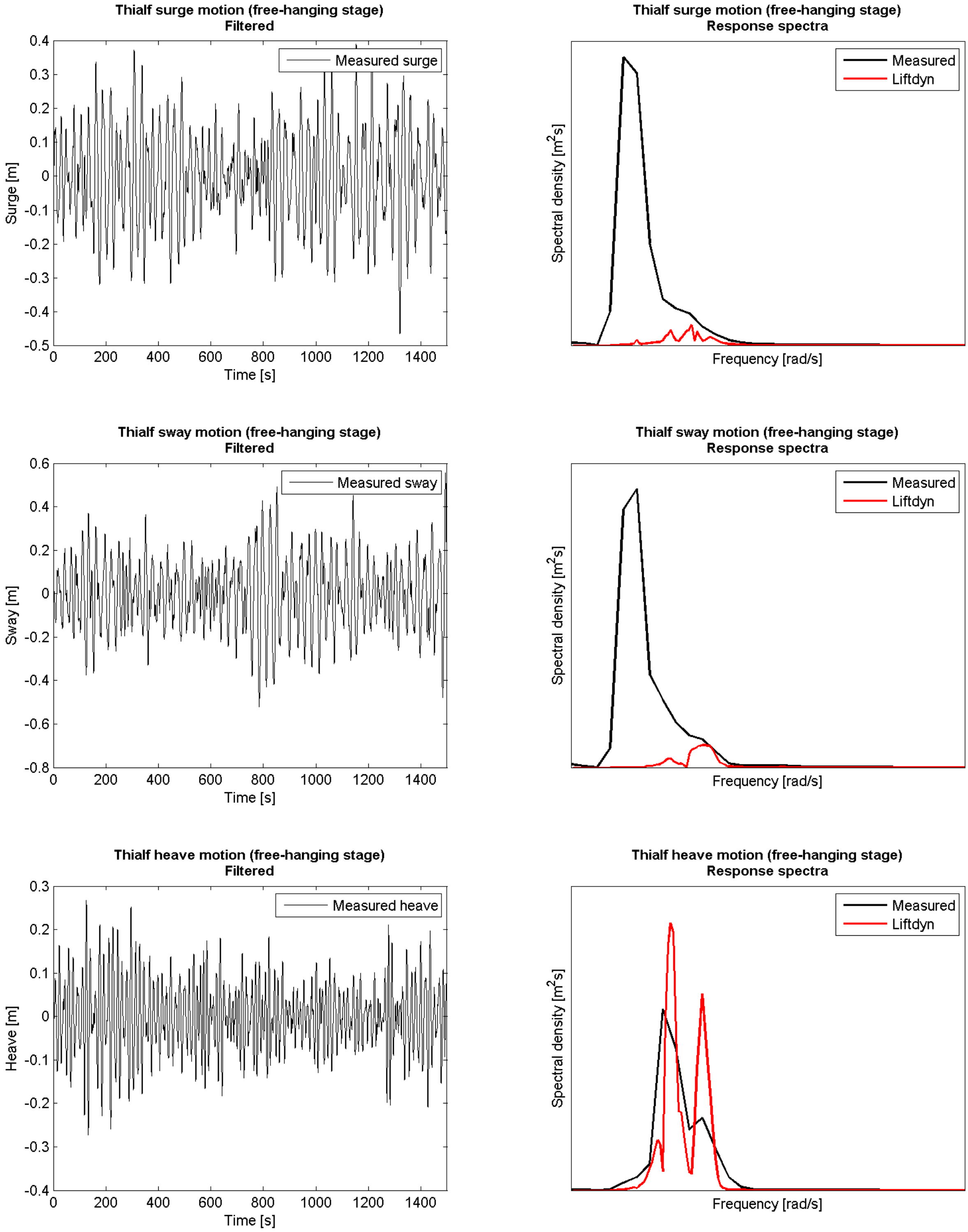

Figure E.13: Free-hanging stage - Thialf translations (at CoG)

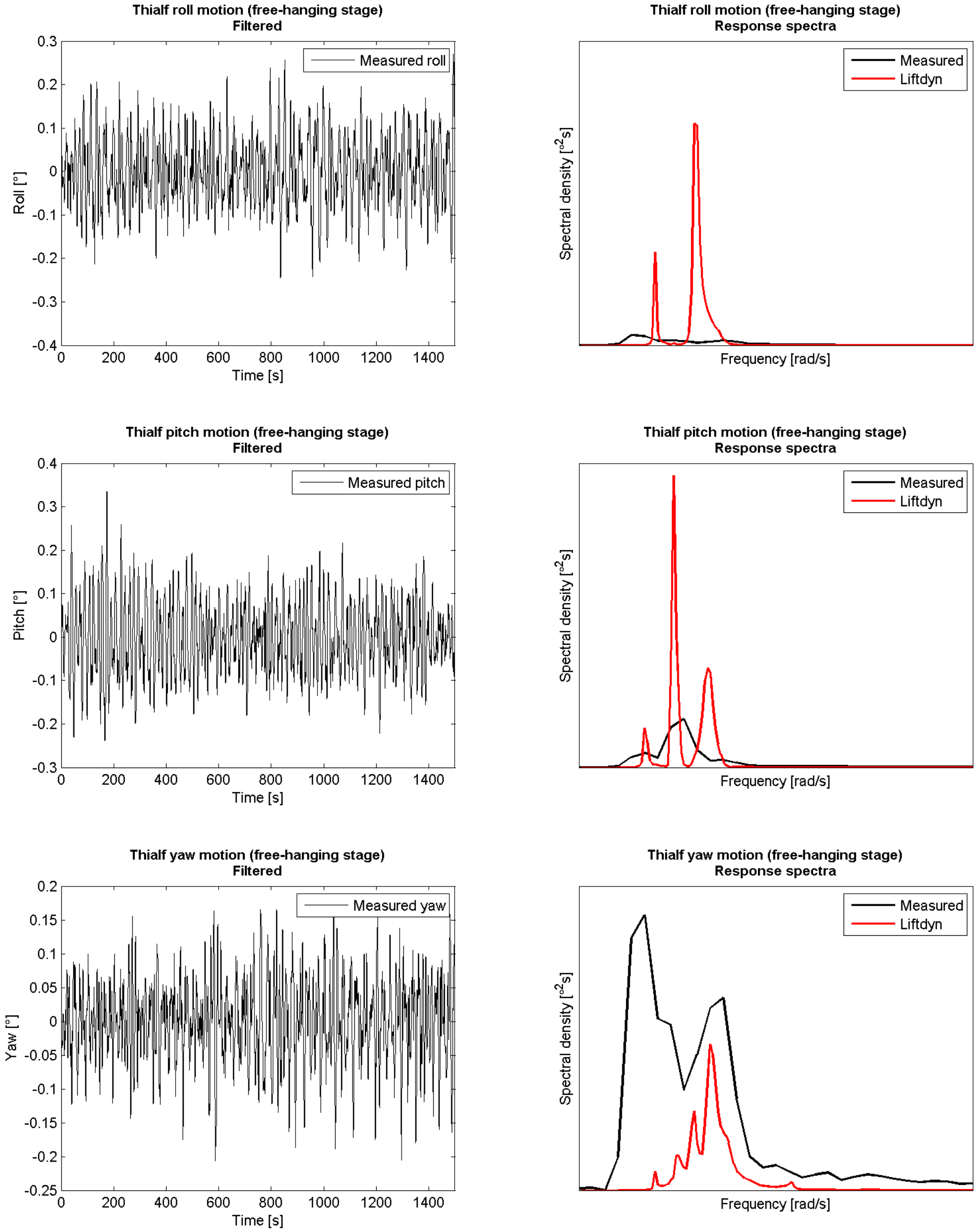

Figure E.14: Free-hanging stage - Thialf rotations

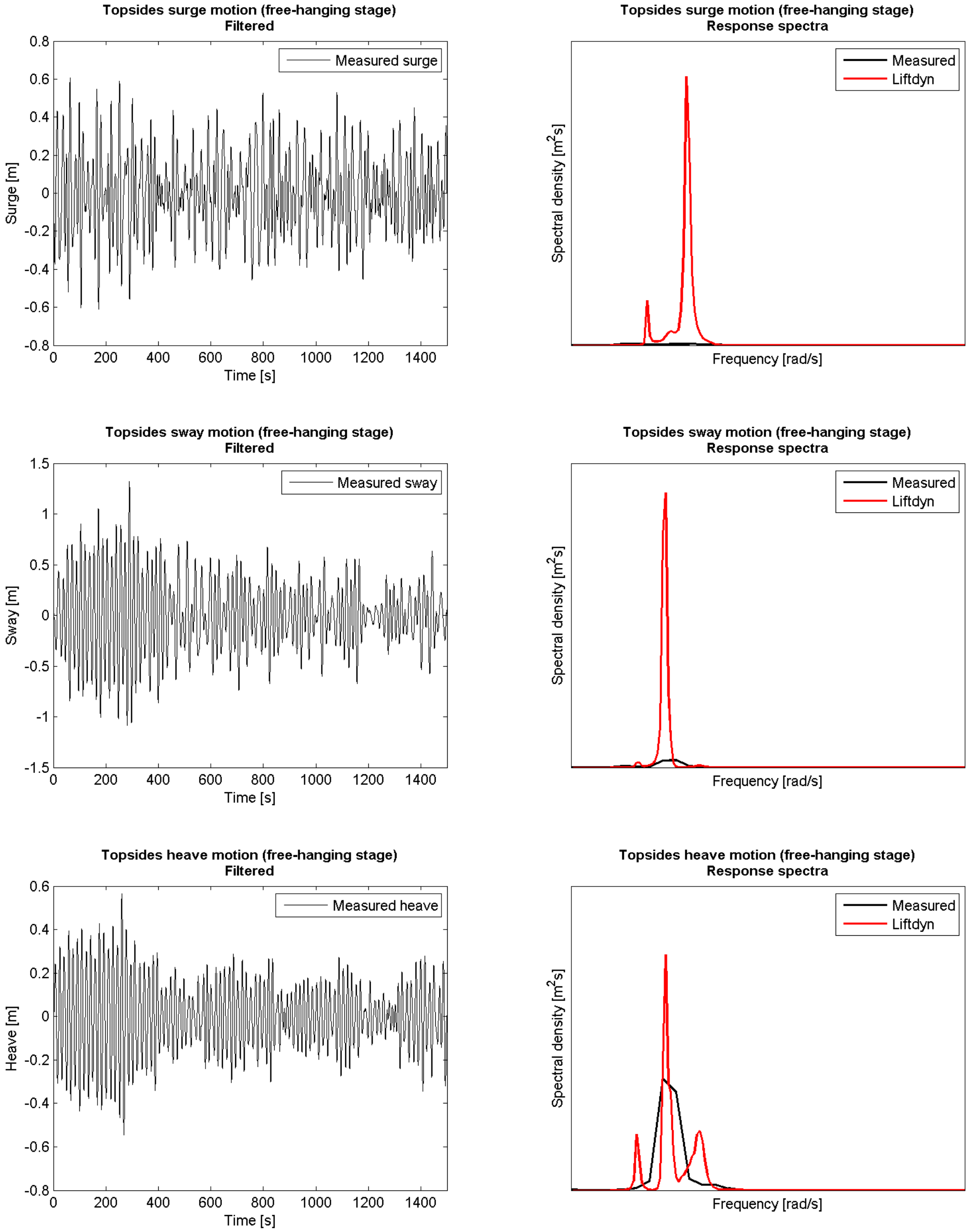

Figure E.15: Free-hanging stage - Topsides translations (at CoG)

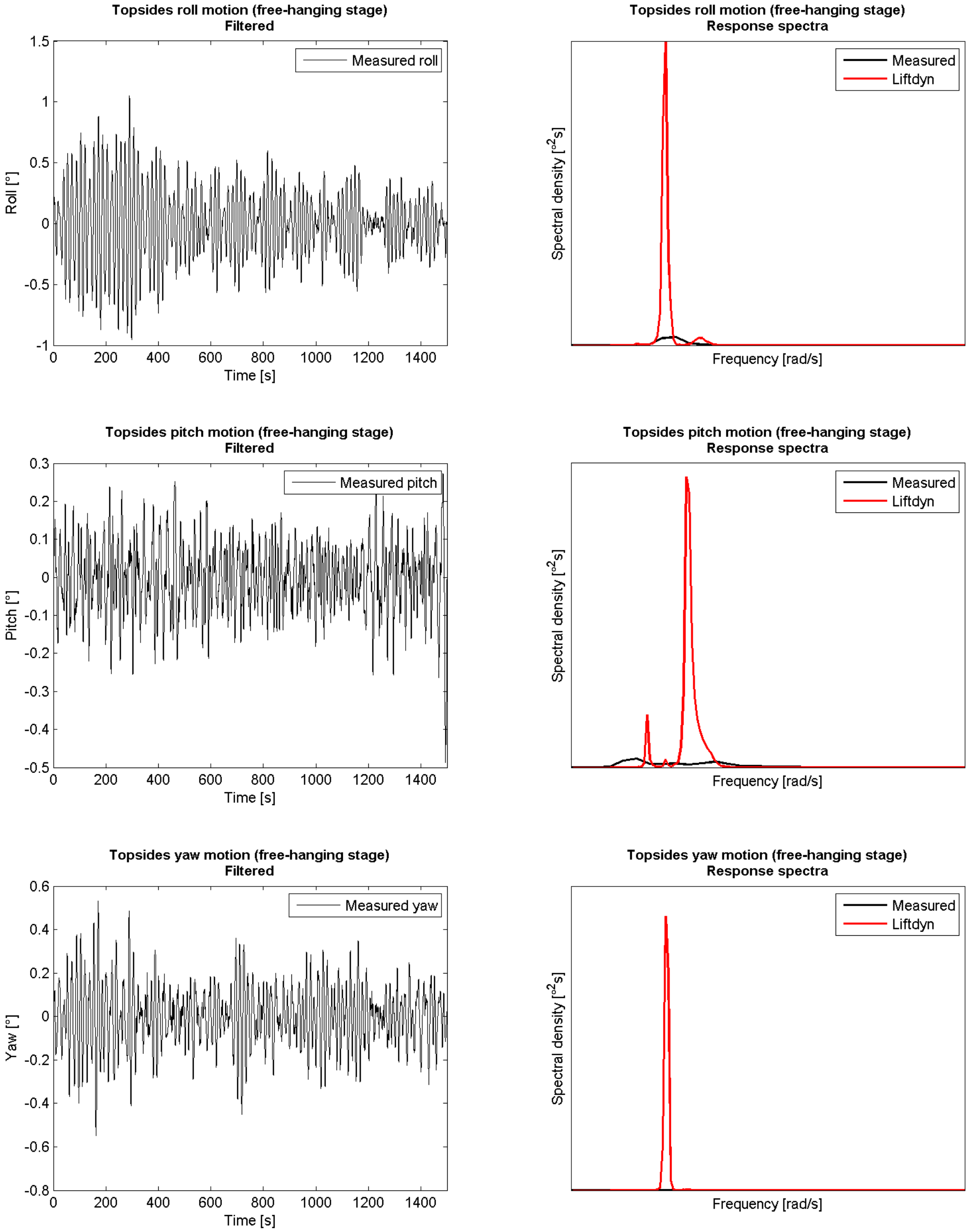

Figure E.16: Free-hanging stage - Thialf rotations

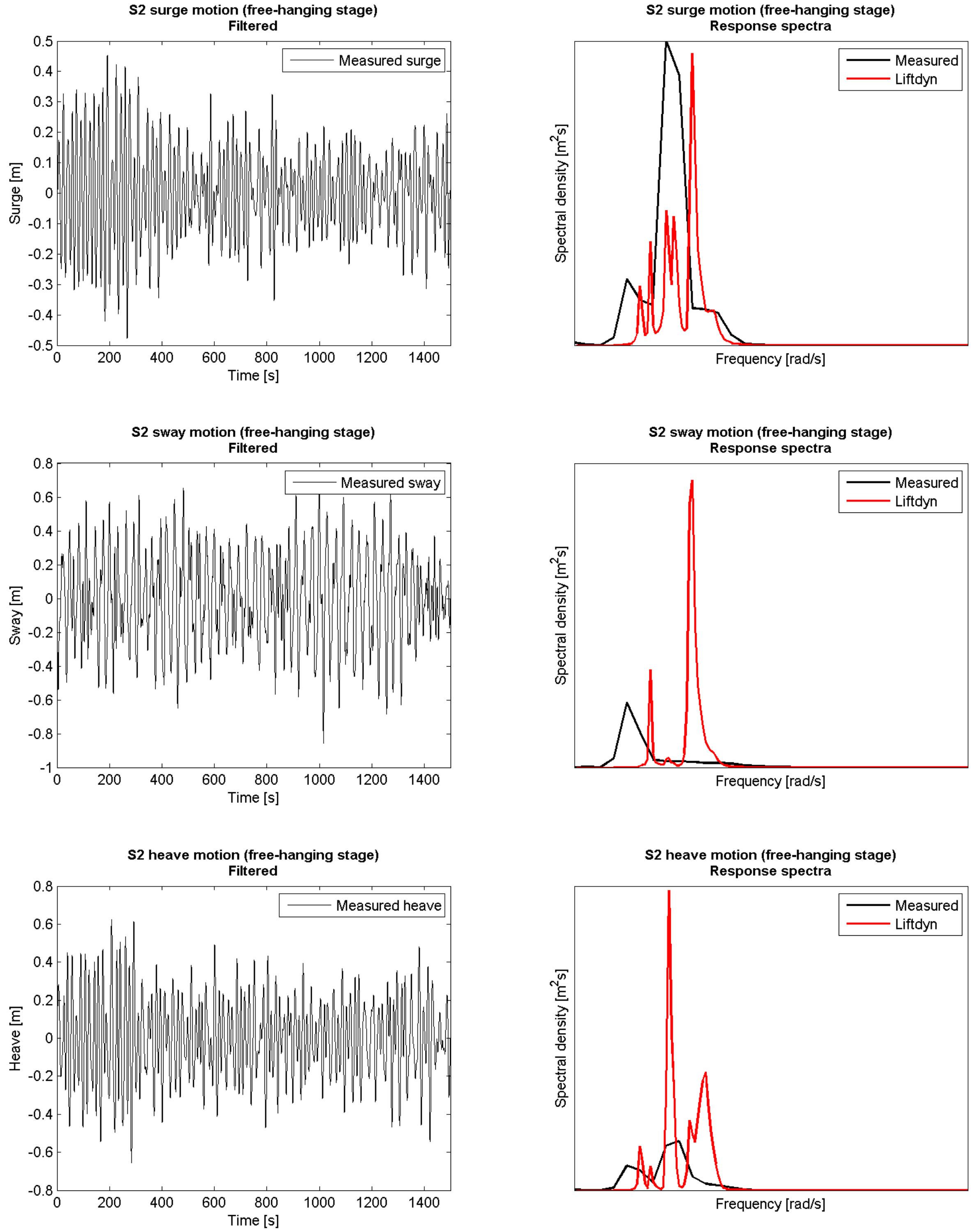

Figure E.17: Free-hangingg stage - SB boom translations (at main fall axle (S2))

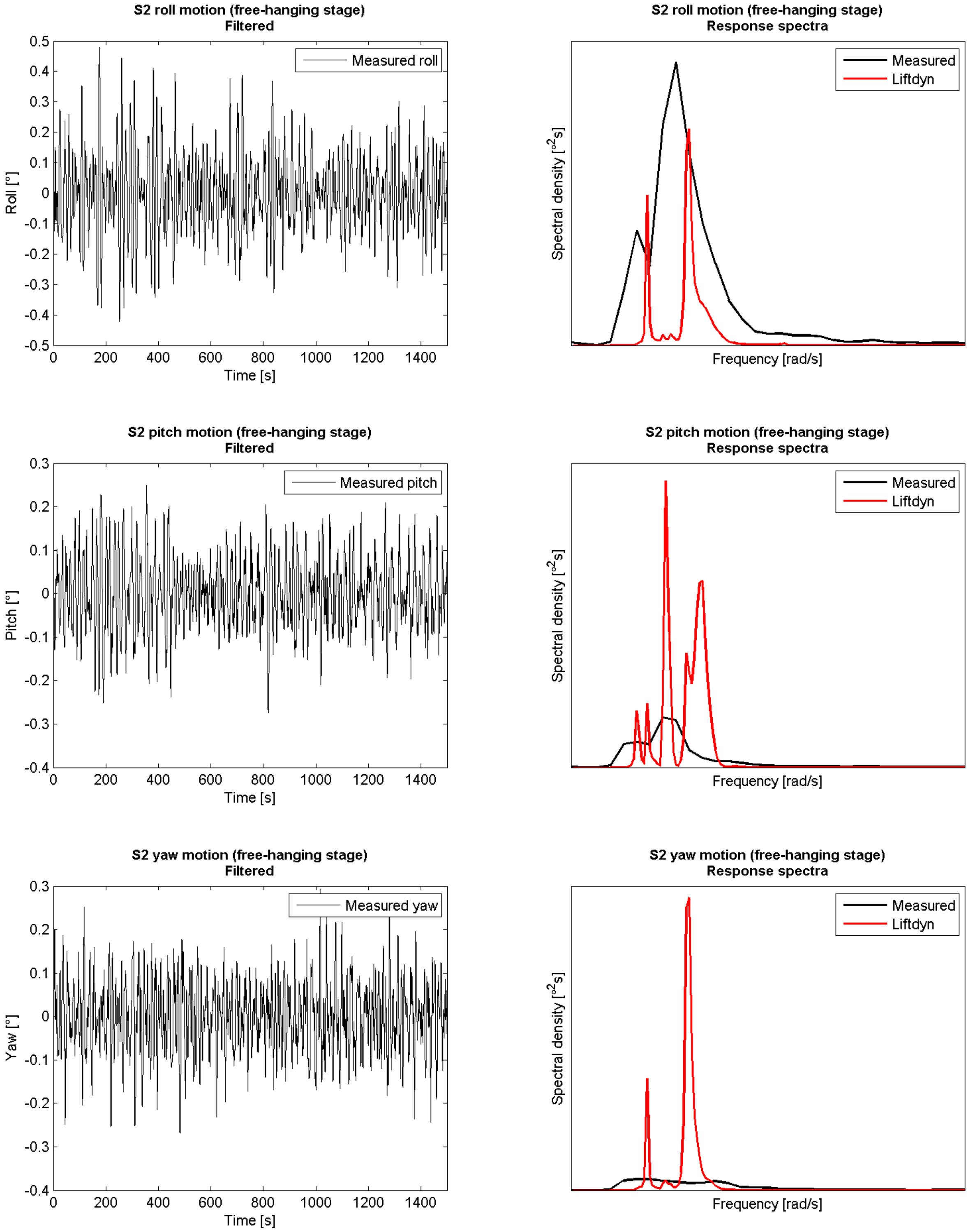

Figure E.18: Free-hanging stage - SB boom rotations

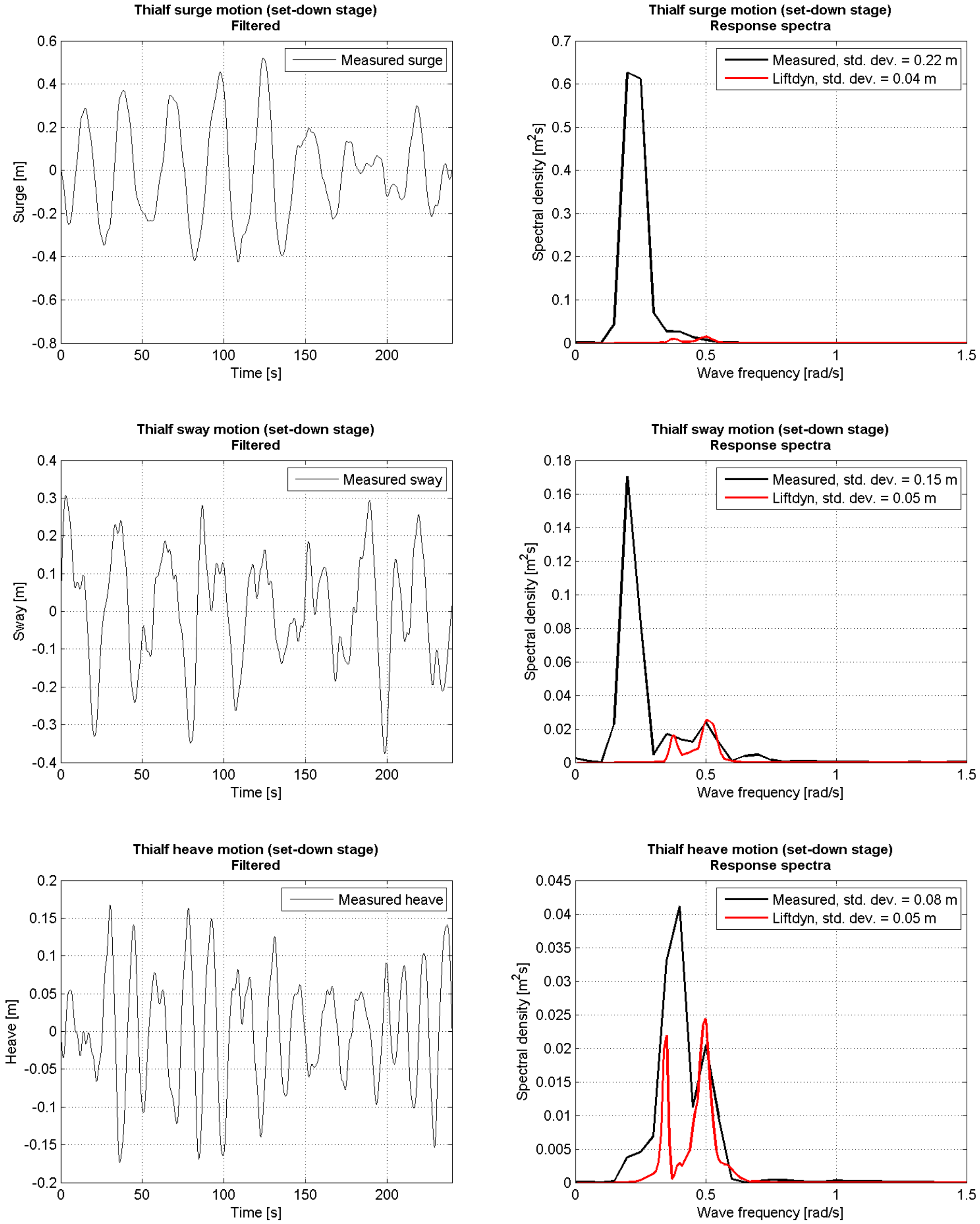

Figure E.19: Set-down stage - Thialf translations (at CoG)

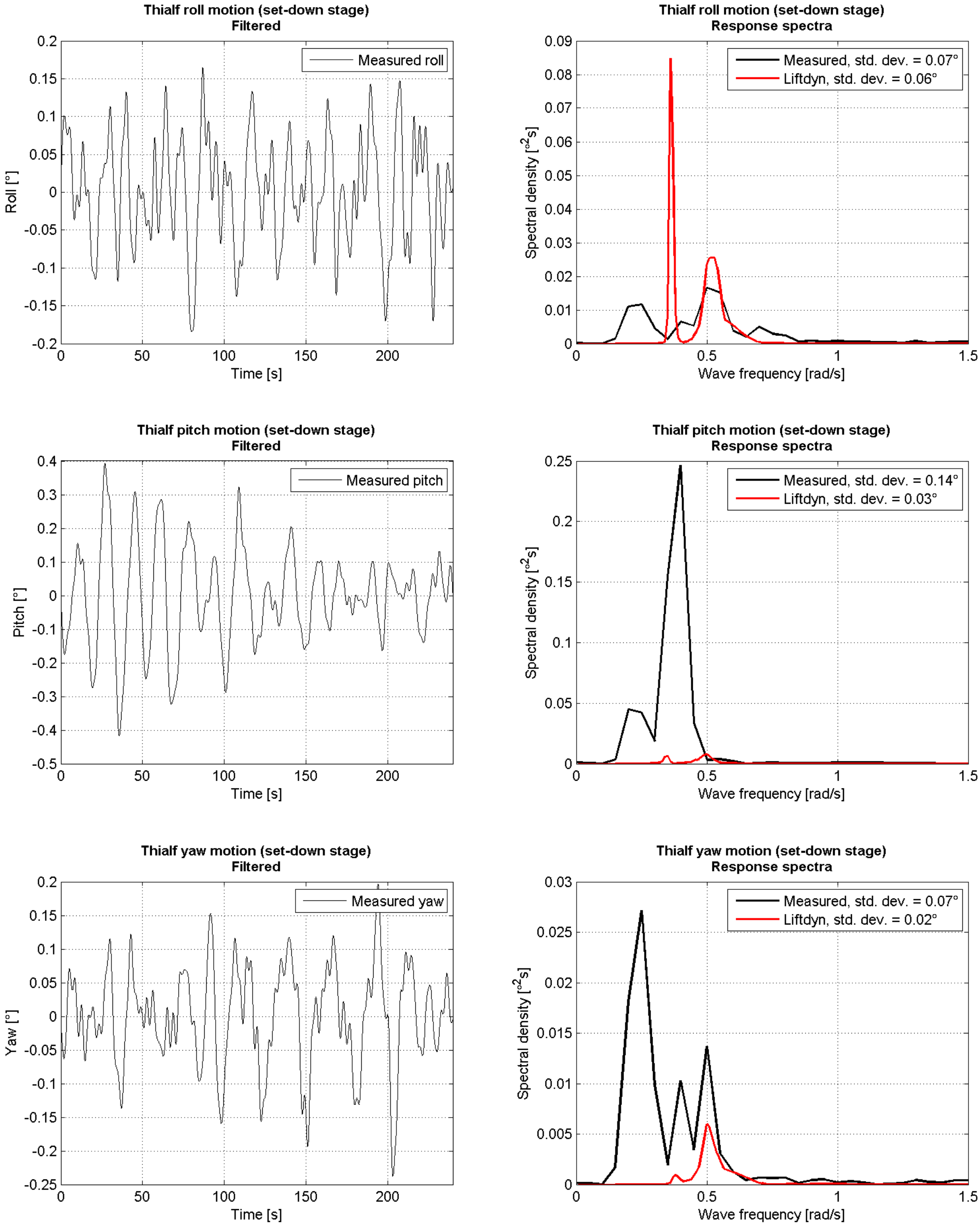

Figure E.20: Set-down stage - Thialf rotations

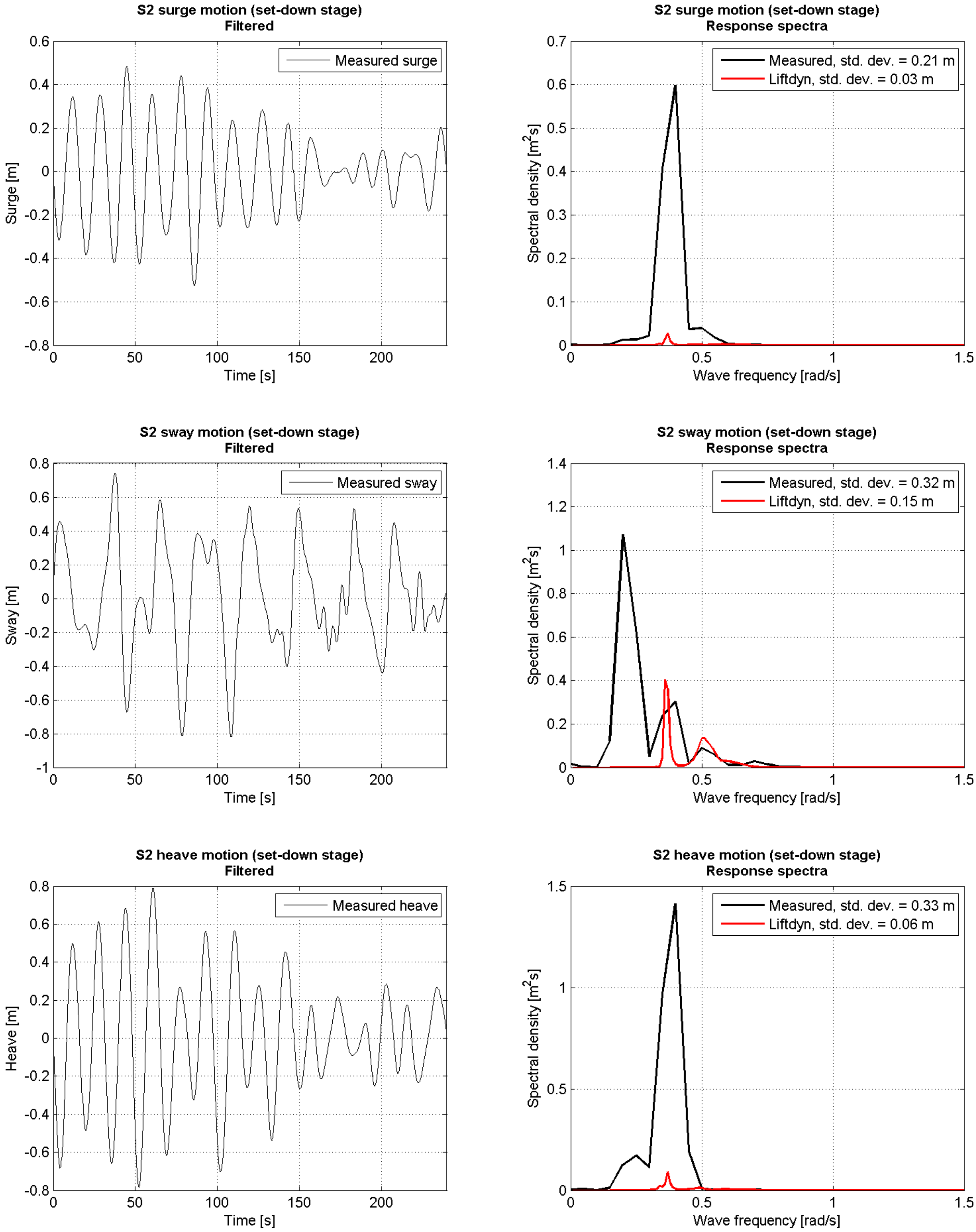

Figure E.21: Set-down stage - SB boom translations (at main fall axle (S2))

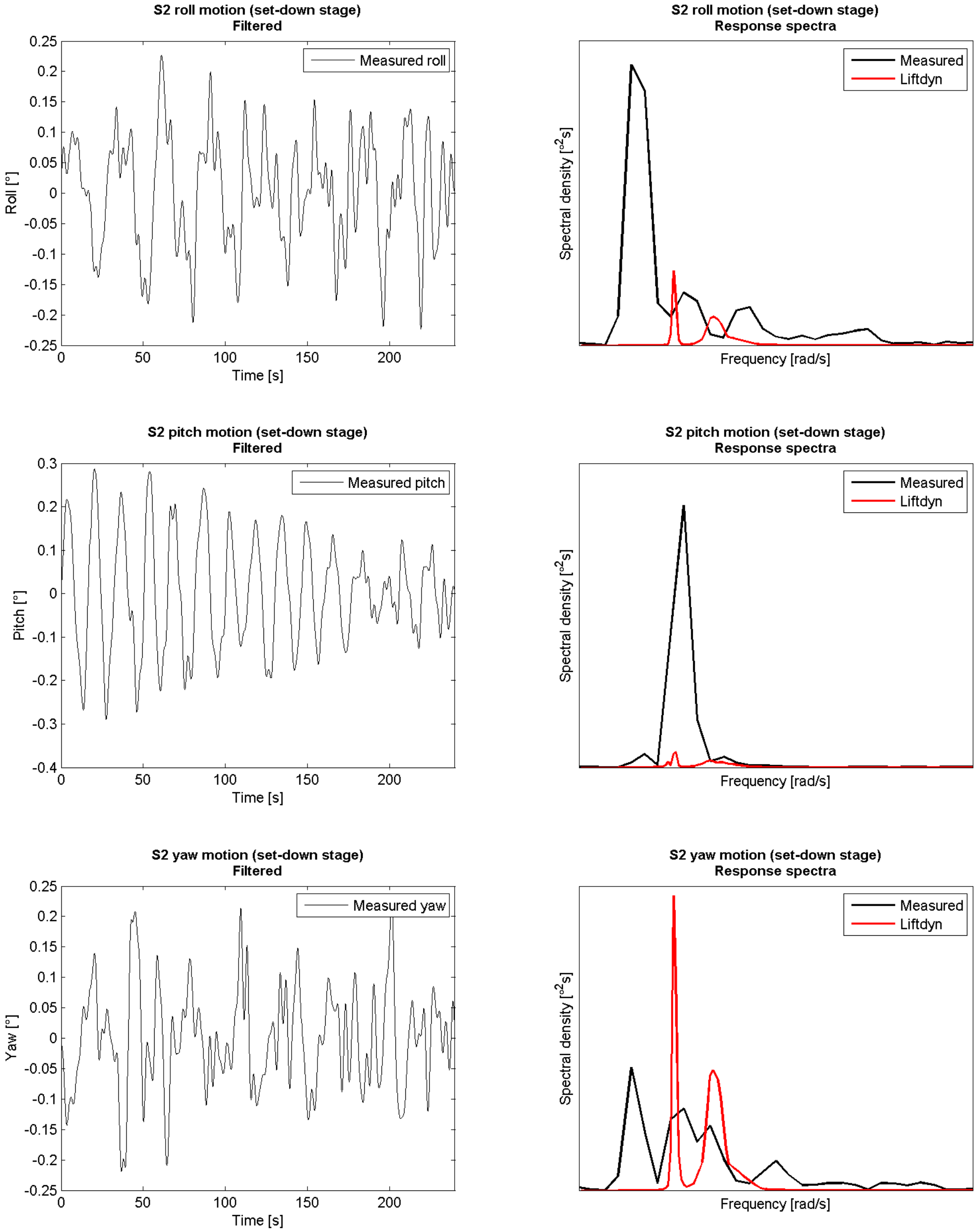

Figure E.22: Set-down stage - SB boom rotations

F
Motions governing main hoist elongations

This appendix contains measured time traces for all motions relvenant for SB main hoist elongations, and modelled SB main block motions as described in chapter 5. Furthermore measured (or modelled, in case of the main block) vs. Liftdyn vertical motions spectra are included. Jumps in the calculated main block's y-motions are attributed to numerical inaccuracies in the block position solver (stiffness in that direction is much smaller as compared to its x- and z-directions).

As explained in chapters 5 and 7, some haziness remains as to which measured signals are most accurate. Therefore, time traces and vertical motion response spectra obtained from both the 'raw' and 'accelerations' sensor files have been included in this appendix.

1. 'Accelerations' sensor file - SB motion time traces (lift-off)
2. 'Accelerations' sensor file - SB vertical motions spectra (lift-off)
3. 'Raw' sensor file - SB motion time traces (lift-off)
4. 'Raw' sensor file - SB vertical motions spectra (lift-off)
5. 'Accelerations' sensor file - SB motion time traces (free-hanging)
6. 'Accelerations' sensor file - SB vertical motions spectra (free-hanging)
7. 'Raw' sensor file - SB motion time traces (free-hanging)
8. 'Raw' sensor file - SB vertical motions spectra (free-hanging)
9. 'Accelerations' sensor file - SB motion time traces (set-down)
10. 'Accelerations' sensor file - SB vertical motions spectra (set-down)
11. 'Raw' sensor file - SB motion time traces (set-down)
12. 'Raw' sensor file - SB vertical motions spectra (set-down)

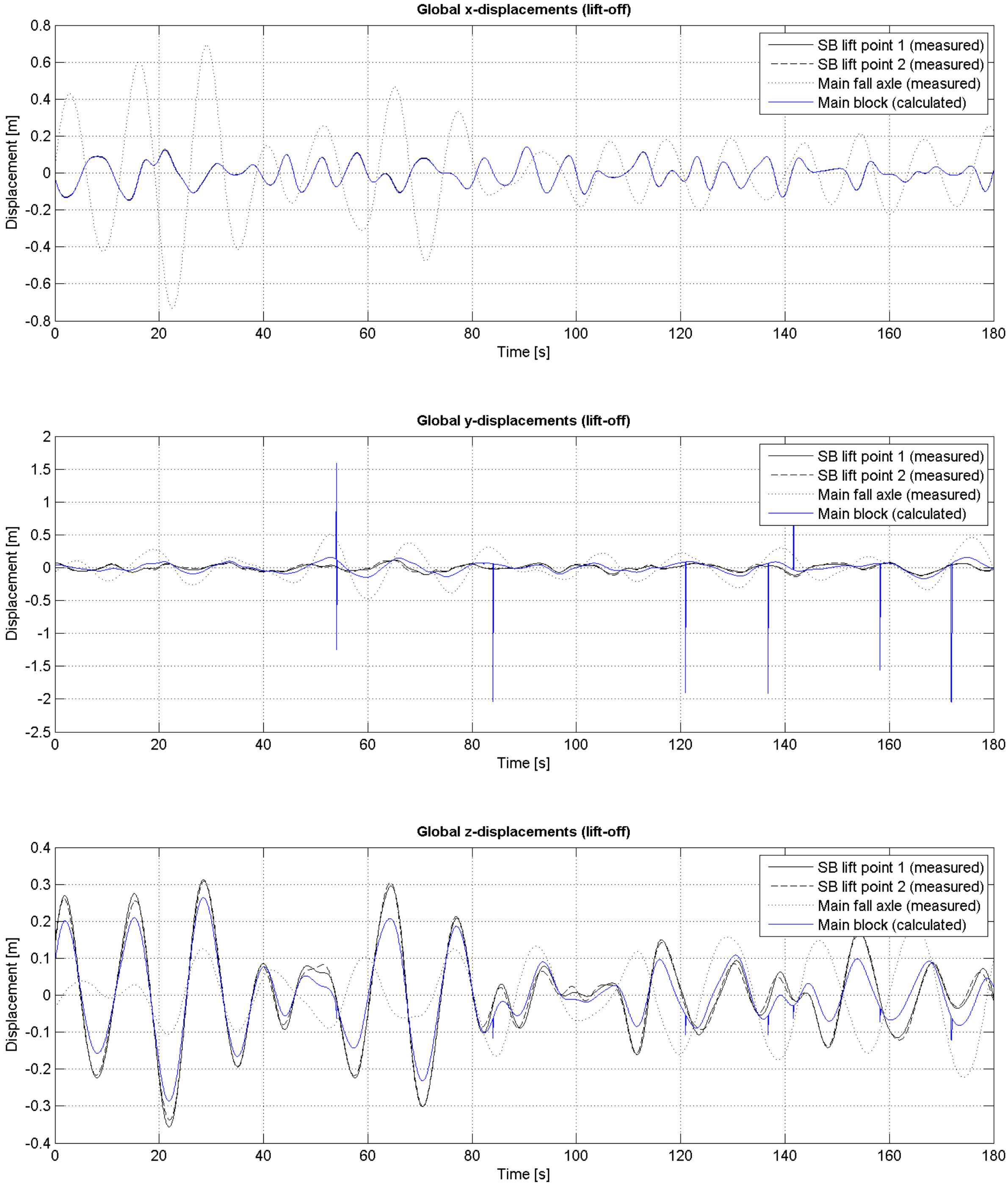

Figure F.1: 'Accelerations' sensor file - SB motion time traces (lift-off)

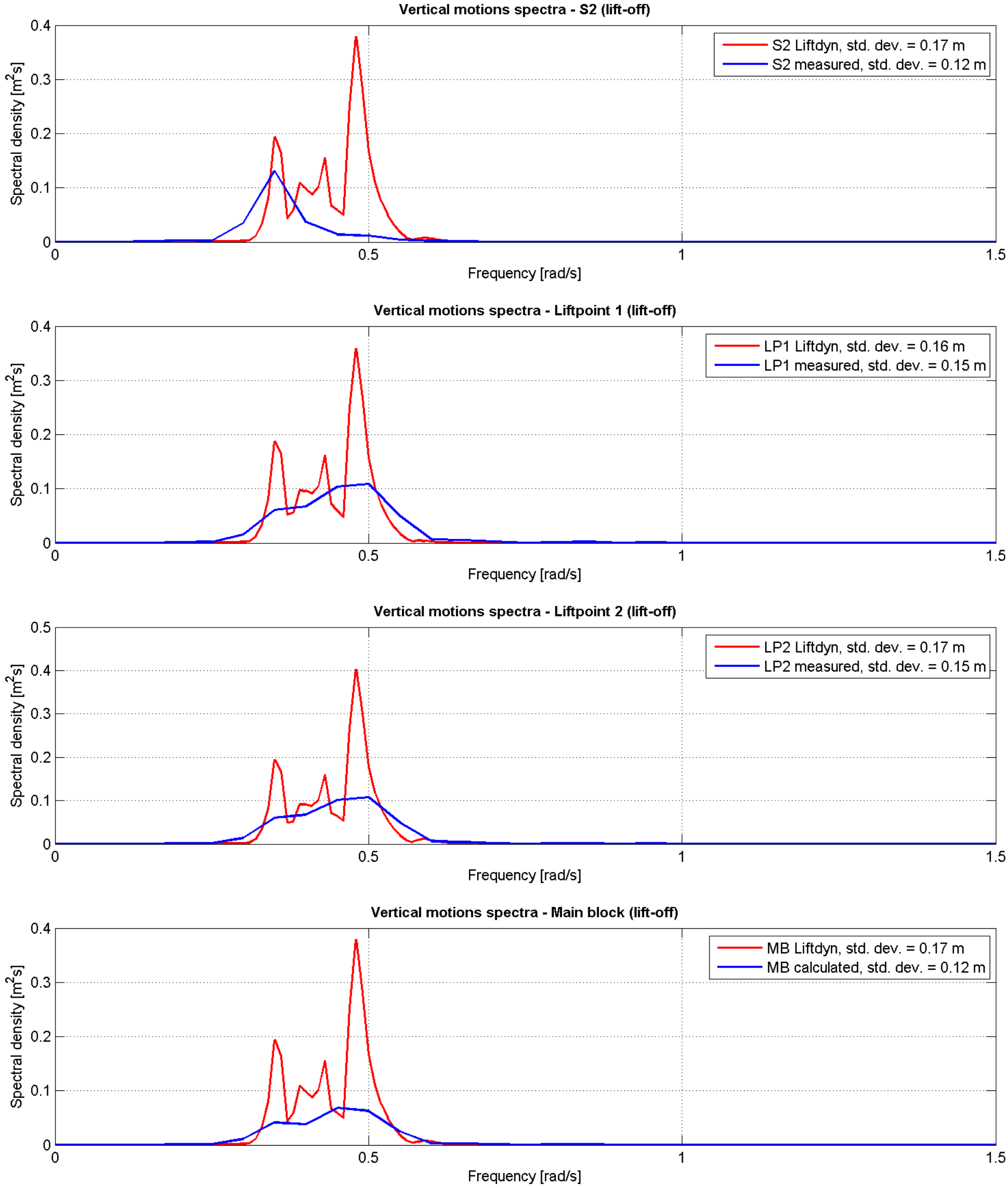

Figure F.2: 'Accelerations' sensor file - SB vertical motions spectra (lift-off)

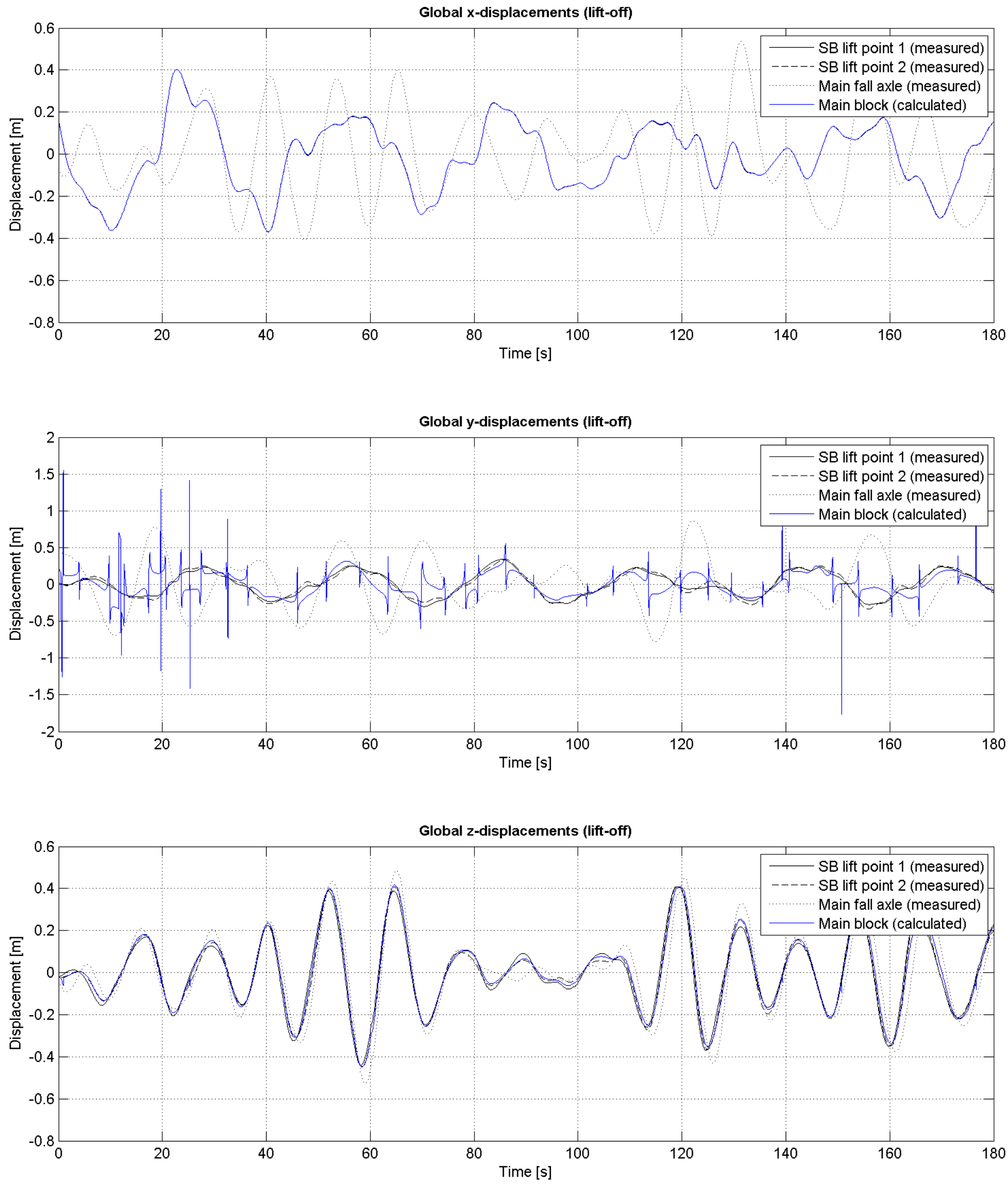

Figure F.3: 'Raw' sensor file - SB motion time traces (lift-off)

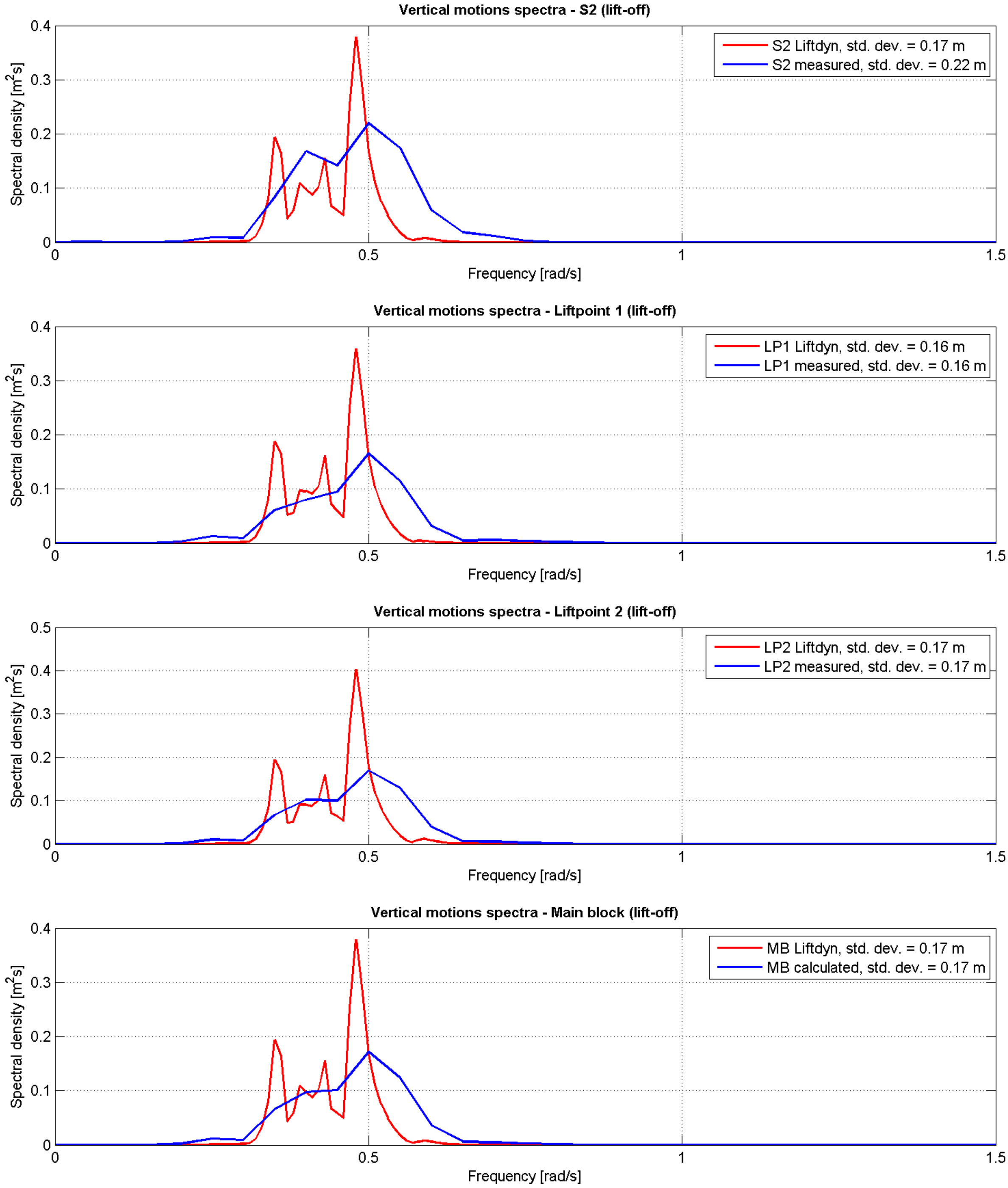

Figure F.4: 'Raw' sensor file - SB vertical motions spectra (lift-off)

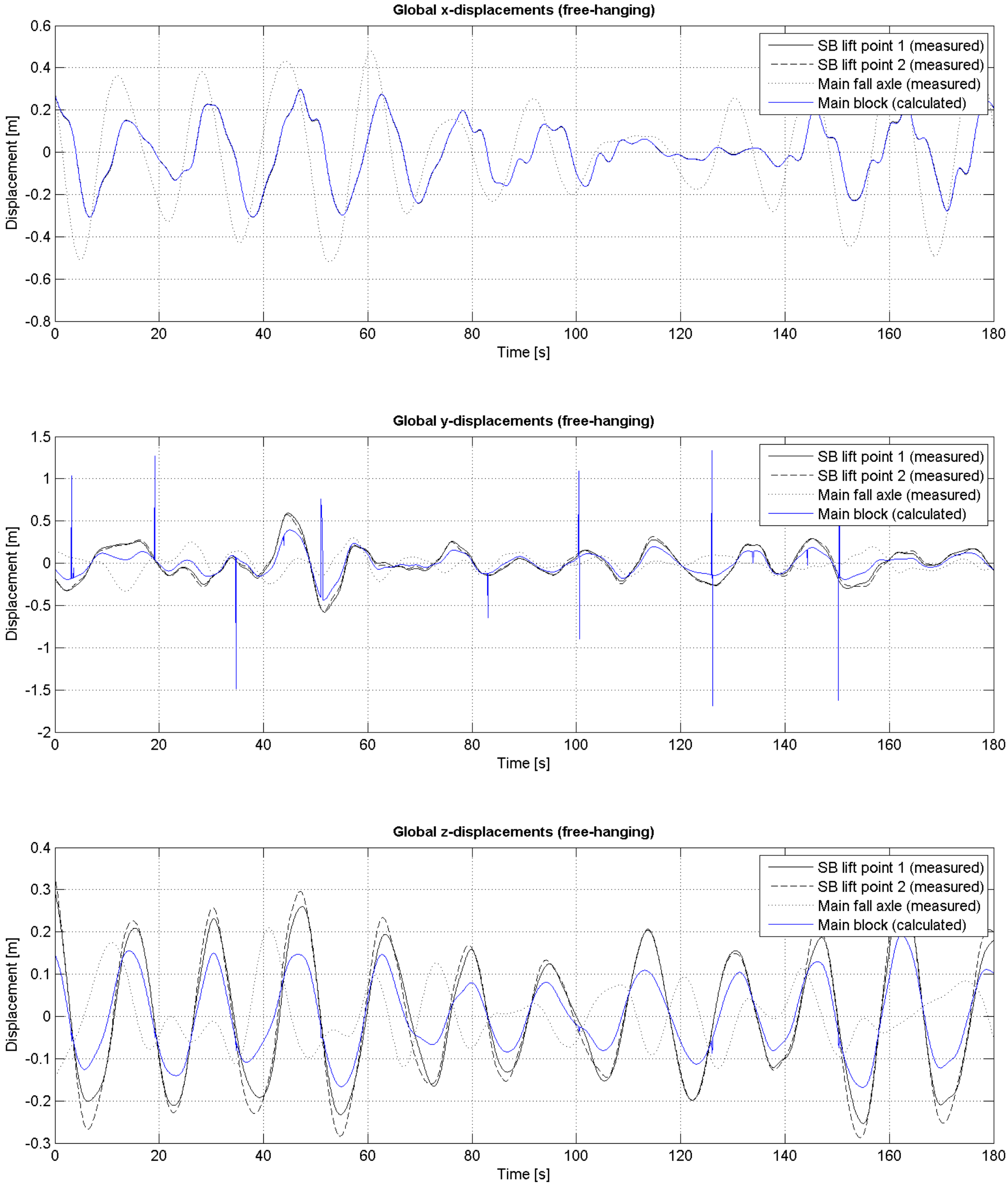

Figure F.5: 'Accelerations' sensor file - SB motion time traces (free-hanging)

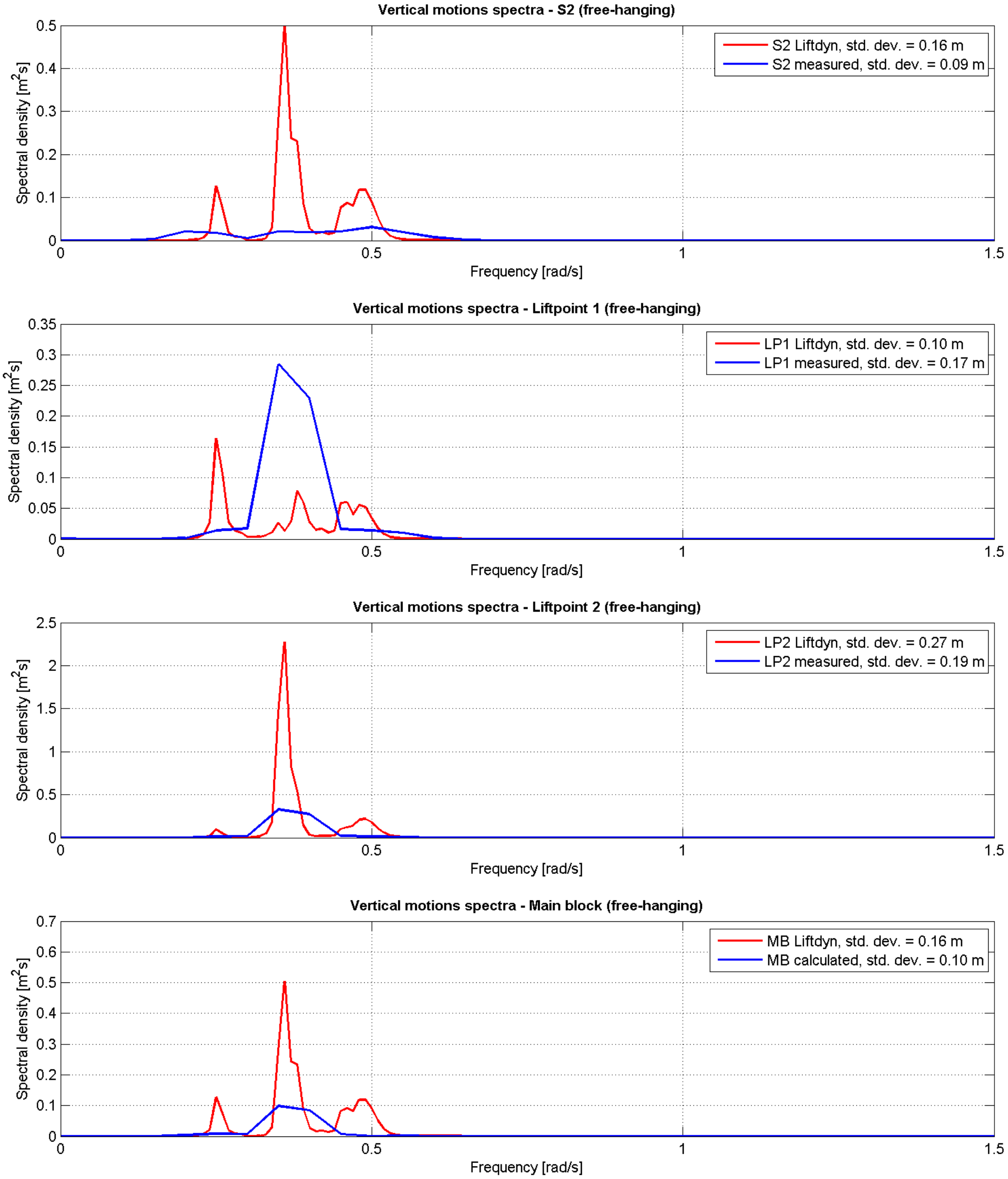

Figure F.6: 'Accelerations' sensor file - SB vertical motions spectra (free-hanging)

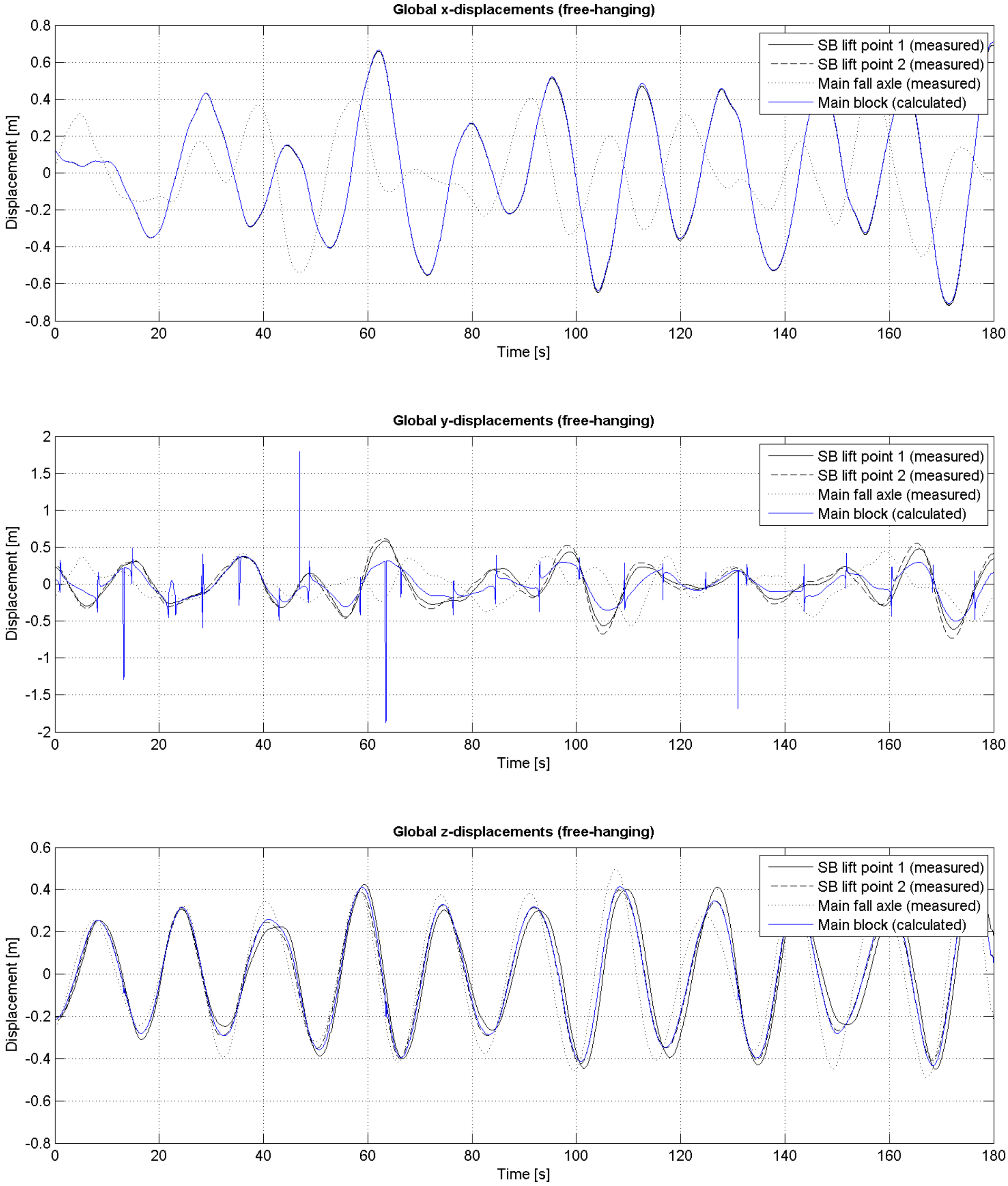

Figure F.7: 'Raw' sensor file - SB motion time traces (free-hanging)

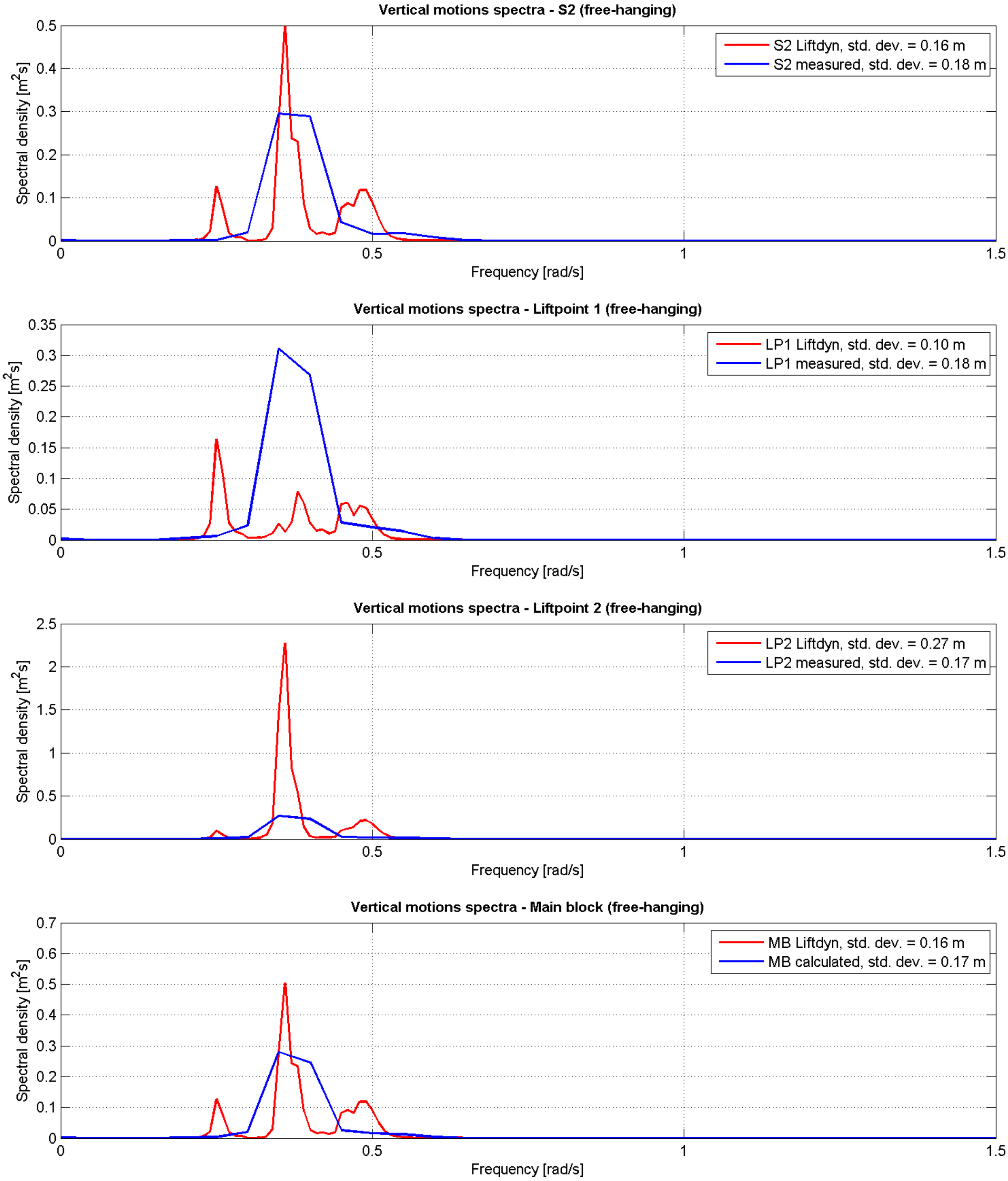

Figure F.8: 'Raw' sensor file - SB vertical motions spectra (free-hanging)

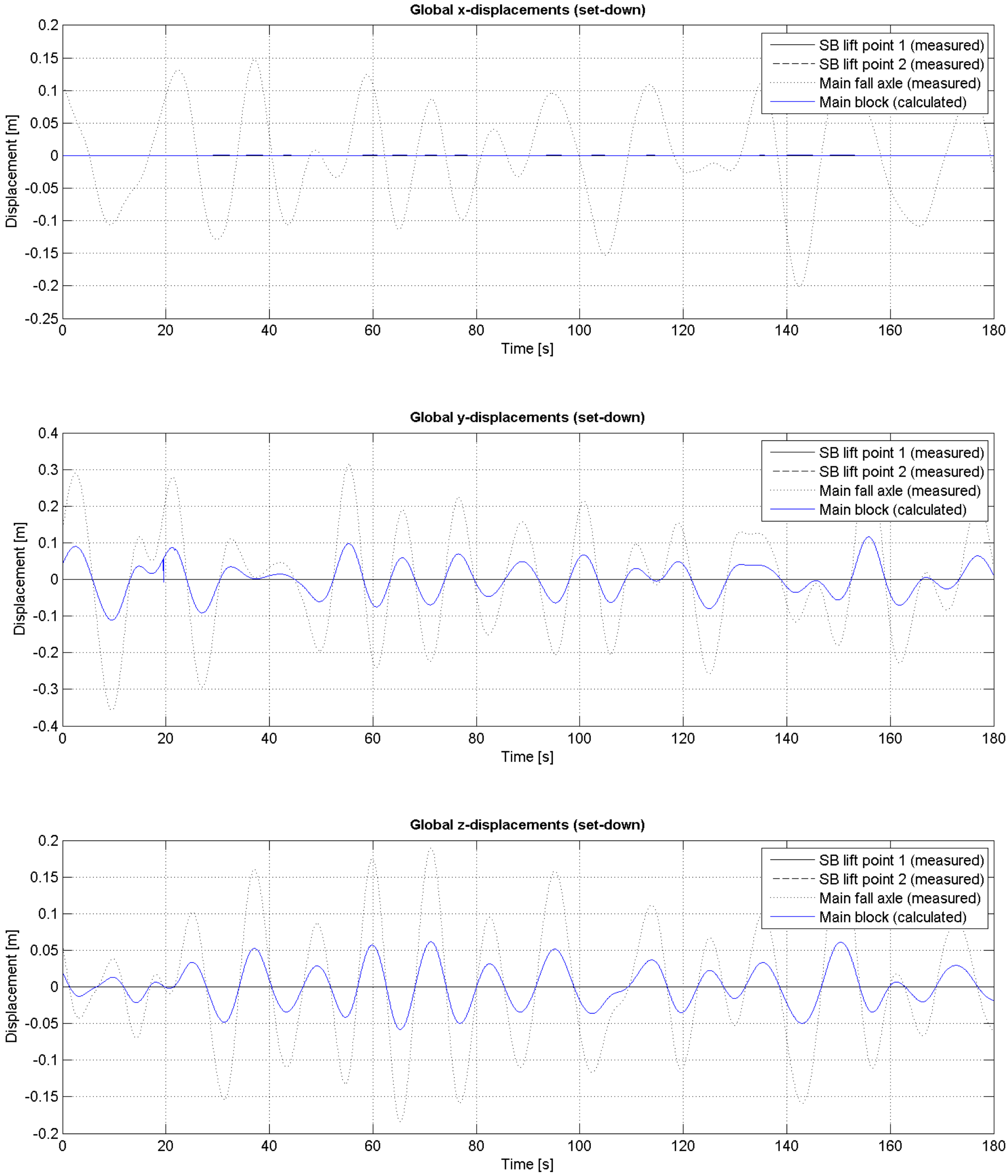

Figure F.9: 'Accelerations' sensor file - SB motion time traces (set-down)

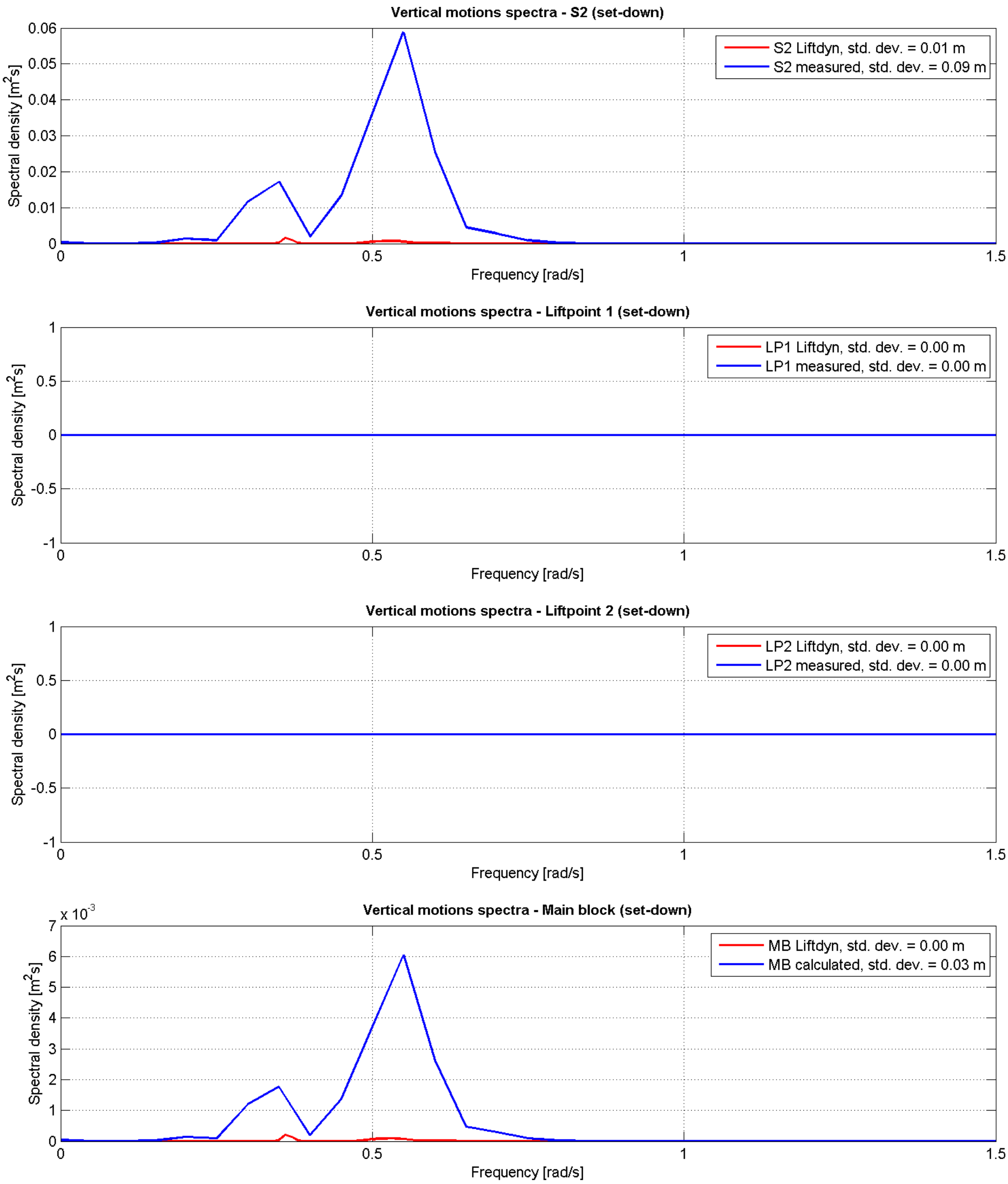

Figure F.10: 'Accelerations' sensor file - SB vertical motions spectra (set-down)

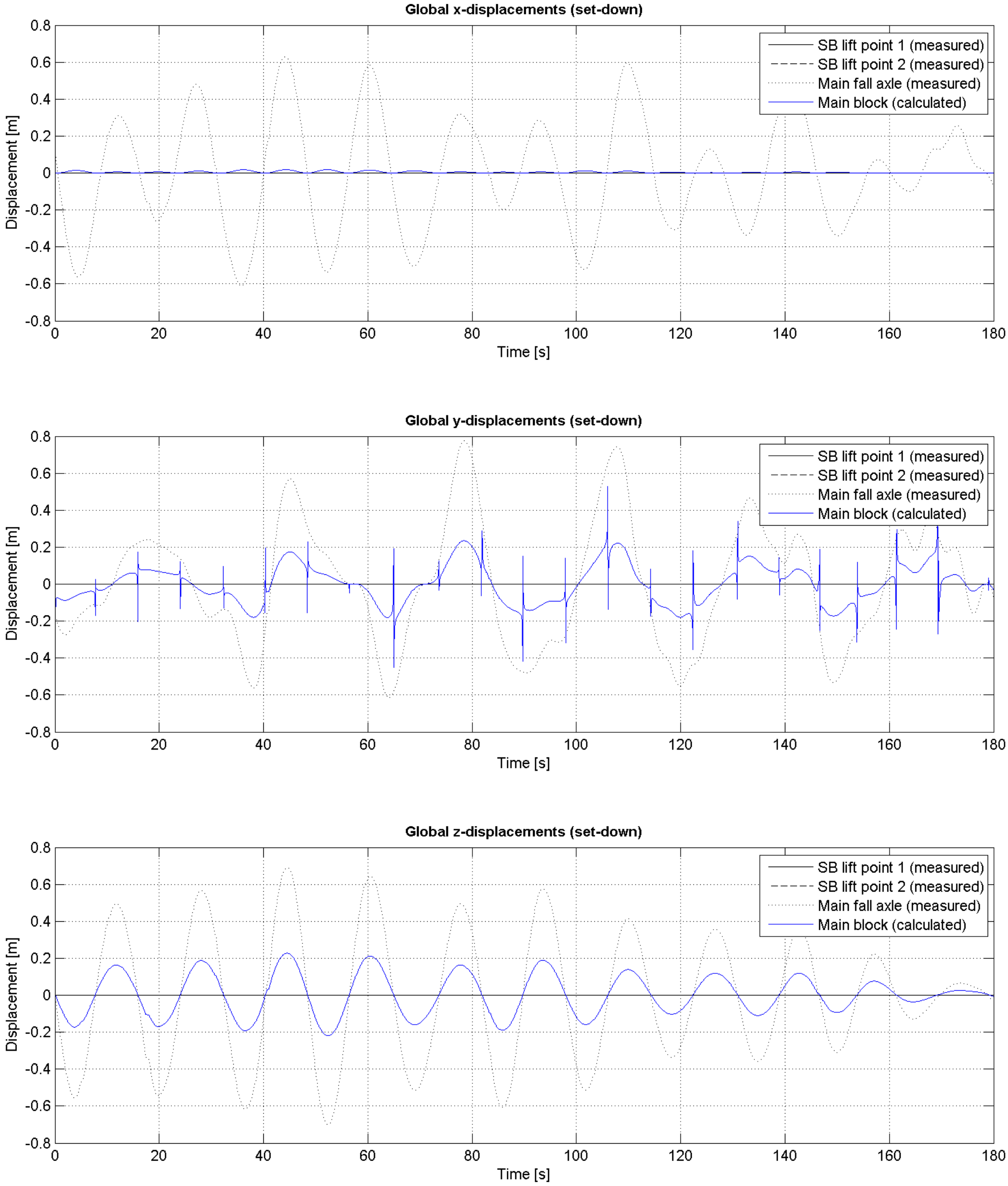

Figure F.11: 'Raw' sensor file - SB motion time traces (set-down)

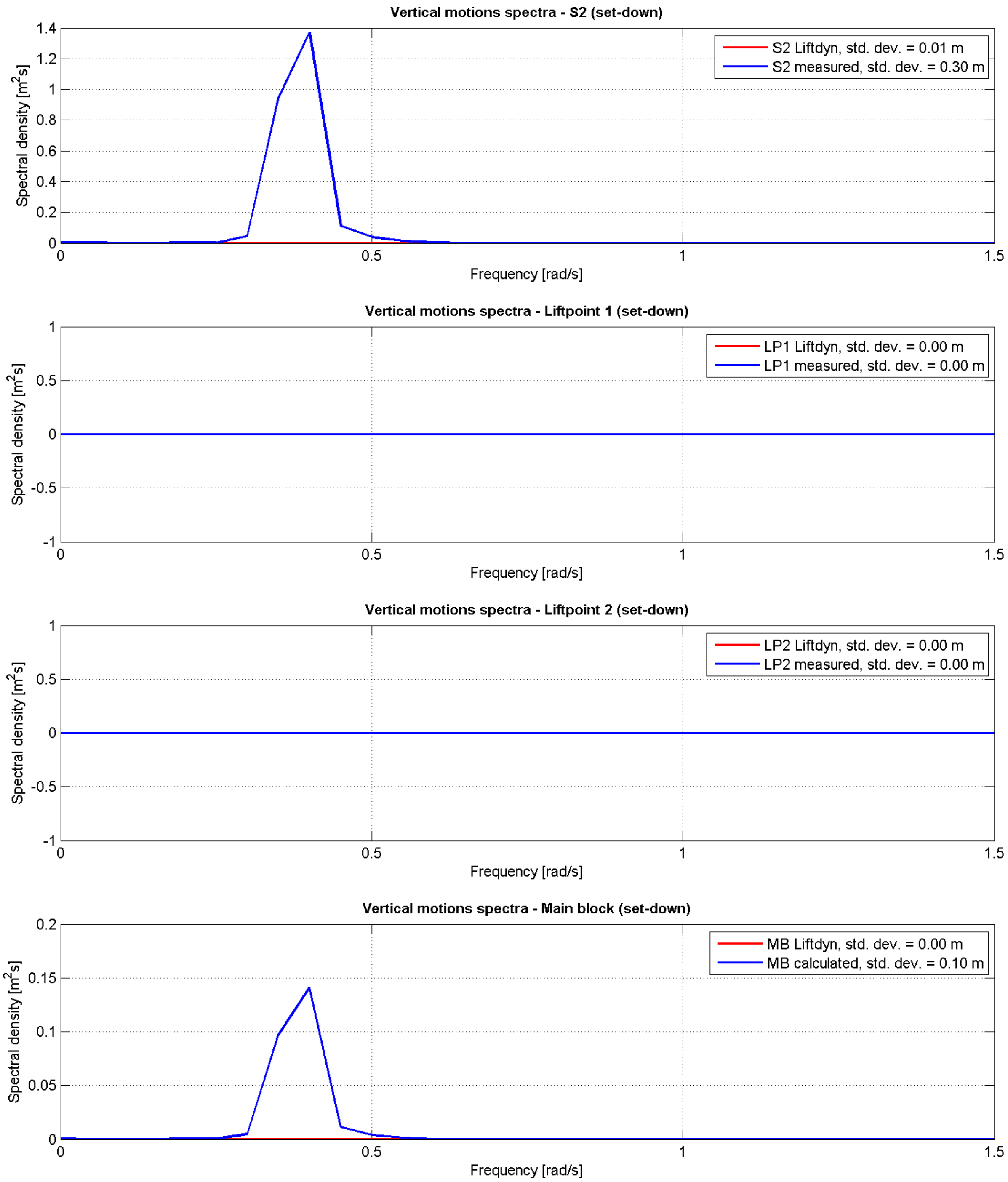

Figure F.12: 'Raw' sensor file - SB vertical motions spectra (set-down)

G

Damping from topsides modelled motions

This appendix contains modelled vs. measured topsides heave time traces, as explained in chapter 6. Modelled and measured topsides motions are plotted over each other for both the original damping properties used in Liftdyn (1.5% of critical damping), as well as the damping properties obtained in section 6.3. Furthermore, a phase lag plot with respect to the measured imposed motions of the main fall axle, for both the original and the obtained damping values.

1. Modelled topsides vertical motions - Phase lag behind imposed motions
2. Modelled vs. measured topsides vertical motions time trace - Original damping
3. Modelled vs. measured topsides vertical motions time trace - Obtained damping

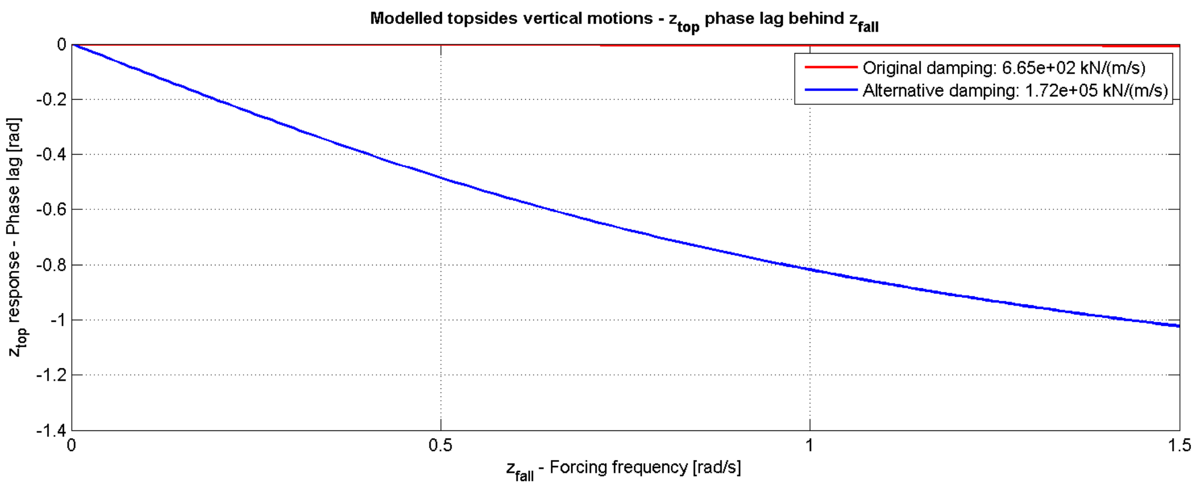

Figure G.1: Modelled topsides vertical motions - Phase lag behind imposed motions

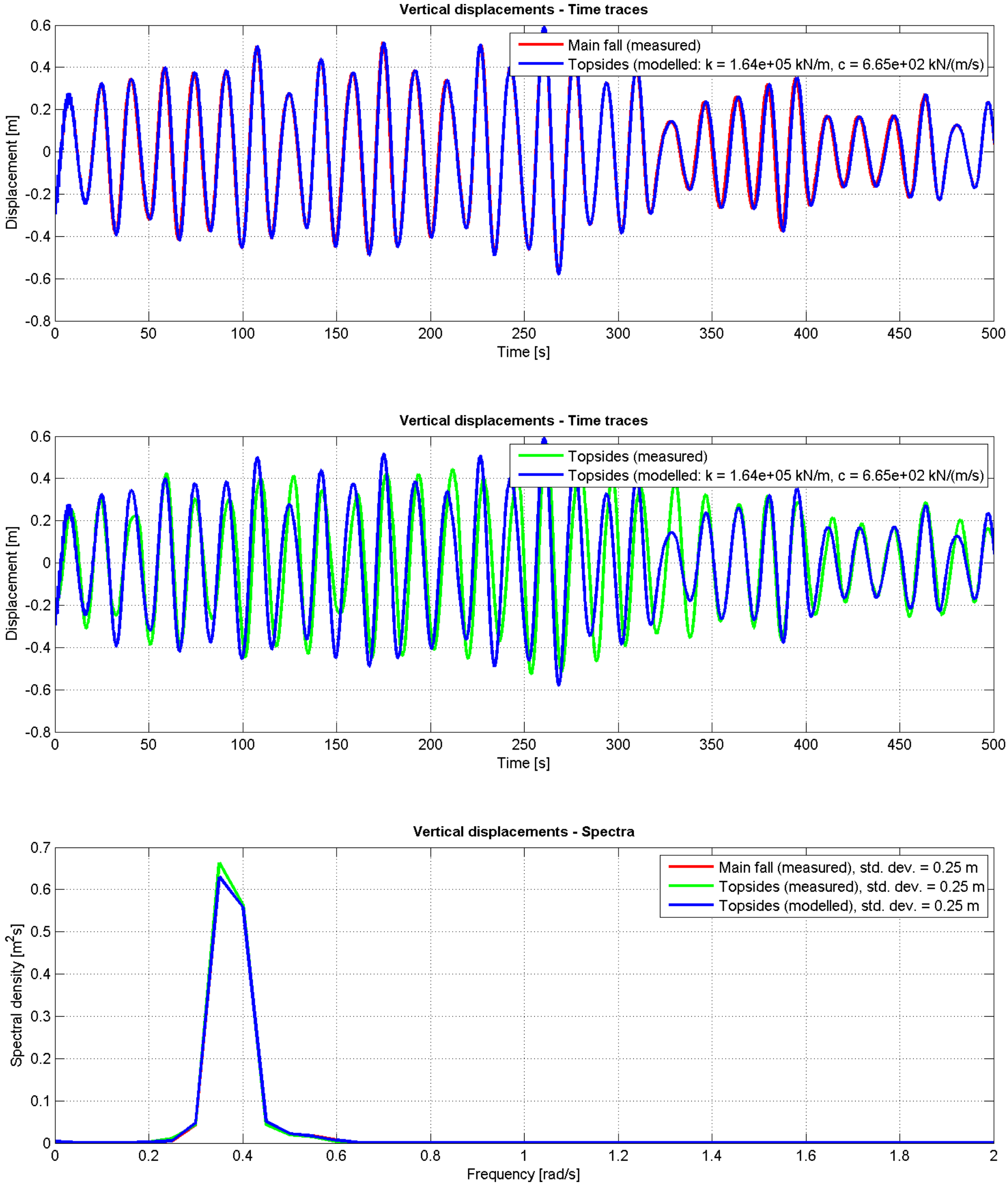

Figure G.2: Modelled vs. measured topsides vertical motions time trace - Original damping

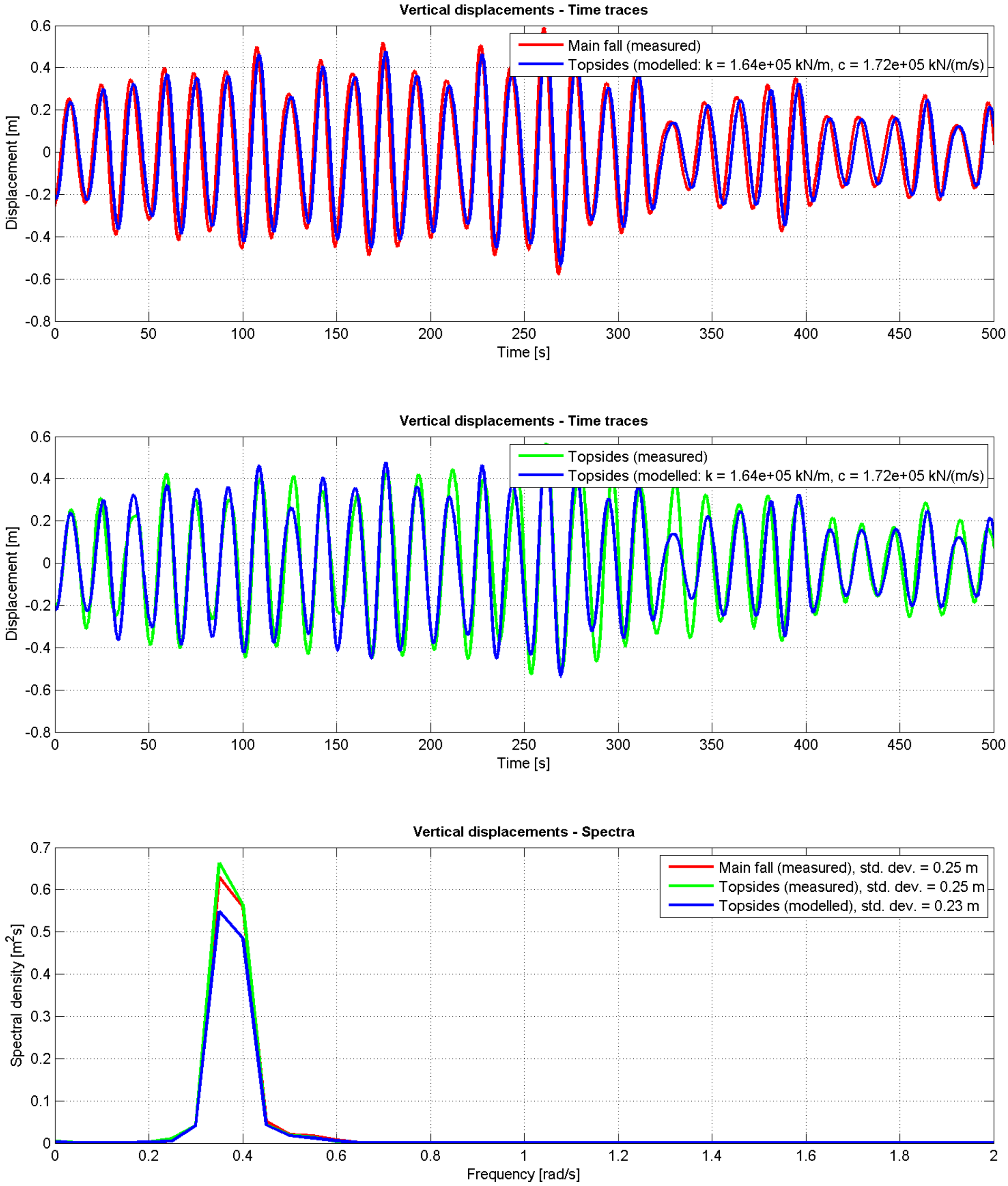

Figure G.3: Modelled vs. measured topsides vertical motions time trace - Original damping

Bibliography

Ayaz et al., Saipem UK. Hydrodynamic interaction between floating structures during heave lift operations - Is it worth analysing?, 2014.

Blaauwendraad. *Dynamica van Systemen.* 2010.

Bridon. (Large diameter) wire rope stiffness properties - E-mail correspondence, 2016.

Brown & Root Vickers. Heavy Lift Criteria - A Joint Industry Report, 1990.

Cooley & Tukey. An Algorithm for the Machine Calculation of Complex Fourier Series, 1964.

Datawell. *Directional Waverider MkIII*, 2016.

el Marini. Measurement-based dynamic analysis of the thialf cranes during suspended jacket transports. Master's thesis, TU Delft, 2014.

Godhavn. Adaptive tuning of heave filter in motion sensor, 2000.

HMC. Sling & Hoist wire stiffness, 2005.

HMC. Liftdyn theory manual, 2009.

HMC. Axis system for siri sensors, 2012.

HMC. Validation of Liftdyn Hookload fluctuations during pretension condition - Edvard Grieg Modules, July 2015, 2015.

Holthuijsen. *Waves in oceanic and coastal waters.* 2006.

Huisman-Itrec. Manual huisman load measuring pinsl, 2007.

Journée & Massie. *Offshore Hydromechanics.* 2001.

SIRI Marine. Signals measured - 6DoF motion sensors, 2016.

Spijkers, Vrouwenvelder & Klaver. *Dynamics of Structures - Part 1 Vibrations of Structures.* 2006.

Sun et al. First- and second-order analysis of resonant waves between adjacent barges, 2010.

WAMIT. *WAMIT User manual - Version 7.1*, 2015.